



University Library

Author/Filing Title HAZRA, K.

Class Mark T

Please note that fines are charged on ALL
overdue items.

FOR REFERENCE ONLY

0403271789



**The Influence of Stitch Architecture in Multiaxial Warp Knit
Fabrics on the Damage Tolerance and Environmental
Durability of Carbon Fibre Reinforced Composites**

by

Kalyan Hazra

*A Doctoral Thesis Submitted in Partial Fulfilment of the Requirements for the Award
of Doctor of Philosophy of Loughborough University*

Supervisor: Mr. J F Harper

Director of Research: Professor D J Hourston

Institute of Polymer Technology and Materials Engineering

Loughborough University

May 2006

© by Kalyan Hazra, 2006

 Loughborough University Pilkington Library
Date JAN 2007
Class T
Acc No. 0403271 789

To my wife Souroni, son Kabbyo, my Parents,

My Parents-in-laws and Sangeeta-di

ACKNOWLEDGEMENTS

I would like to thank the following people for their contributions to this work:

- Mr. John Harper for his overall guidance. I am indebted to him for his patience, support and perseverance throughout this project.
- Mr. Andrew Foreman of QinetiQ for his guidance over the years during this project.
- Mr. Andrew Mills for his valuable suggestions, at the beginning of this work, about RFI and for showing how it works.
- Mr. Ash Choudry of Advanced Composites Groups for his advice on the various issues regarding the resin MTM44.
- Prof. Doug Hourston for his help with the DMTA experiments, for letting me use his equipment and offering suggestion in interpreting the results.
- Prof. Jon Binner for his support as the departmental research co-ordinator during the first couple of years of this project.
- Dr. Xujin Bao and Dr. Leno Mascia for their valuable suggestions during the 1st and 2nd year assessment of this work.
- Mr. Andrew Woolley, Mr. Trevor Atkinson and Mr. Ray Owens for their technical assistance during various experiments.
- Mr. Mike Hallam, Workshop Supervisor, for his super effort to keep up with my demands.
- Dr. Simon FitzGerald of Horiba Jobin Yvon, for his assistance with Raman Spectroscopy.
- The Charles Wallace Bangladesh Trust (£2000), The SHA Ziauddin Trust (£500) and the University Hardship Fund (£500) for their financial help during the time of financial hardship.
- Finally all my near and dear ones for their support during this study.

ABSTRACT

Among all the 3D textile reinforcements, Multiaxial Warp Knit (MWK) fabrics have brought together the advantages of textile technology: high deposition rates, unlimited shelf-life, lower cost and finally an improvement in the damage tolerance by the use of stitching. However, the stitching in MWKs is slightly different from that traditionally used, i.e. over stitching. The effect of this type of stitching has been investigated and is reported in this work.

Three different variants of stitch architectures of carbon MWK, used in an epoxy matrix, were considered. Interlaminar shear strength, low energy impact, through penetration impact and compression strength testing were carried out on dry samples, while interlaminar shear strength, compression strength, DMTA, FTIR, Raman Spectroscopic analysis were carried out on aged samples.

In low energy impact high stitch density offered more damage resistance, being directly influenced by the complex fibre structure, which has been shown to stop or deviate crack propagation. Similar results were also found during through penetration impacts. Compression After Impact (CAI) properties were found to vary directly with the damage area. Whilst higher stitch density showed better residual strength properties after ageing, the percentage retention of the compression after impact strength was higher for low stitch density MWK.

Environmental durability testing showed higher water uptake by fabric with low stitch density. Chemical and thermal analysis showed that thermohumidity aided degradation of epoxy resin and formation of hydrogen bond with water molecules. Interlaminar shear strength and glass transition temperature were also found to decrease with the thermohumid ageing duration. Laminates with high stitch density reinforcement were found to have a higher compression strength and compression after impact strength reduction.

Key Words: Multiaxial Warp Knit Fabric; Stitch Density; Carbon Fibre Reinforced Plastics; Impact; Compression after Impact; Environmental Durability.

CONTENTS

ACKNOWLEDGEMENTS	I
ABSTRACT.....	II
CONTENTS	III
LIST OF FIGURES	IX
LIST OF TABLES	XIV
GLOSSARY	XV
CHAPTER 1	1
<hr/>	
INTRODUCTION AND AIM.....	1
1.1 INTRODUCTION	1
1.2 AIM AND OBJECTIVES	4
CHAPTER 2	5
<hr/>	
BACKGROUND AND MANUFACTURING VARIABLES.....	5
2.0 NON CRIMP FABRIC	5
2.1 MULTI-AXIAL WARP KNITTED FABRIC MANUFACTURING TECHNOLOGY	6
2.1.1 Manufacturing Variables	8
2.1.2 Disadvantages of MWK	13
2.1.3 Mechanical Properties of MWK Reinforced Composites	13
2.2 LIQUID COMPOSITE MOULDING (LCM).....	18
2.2.1 Resin Film Infusion (RFI)	19
2.3 RFI PROCESS VARIABLES AND EFFECTS.....	20
2.3.1 Newtonian Flow through a Porous Medium.....	20
2.3.2 Permeability of Fibrous Preforms.....	22
2.3.3 Resin Viscosity during Cure.....	23
2.3.4 Wettability of the Fibres	23
2.3.5 Compaction Behaviour of the Reinforcements.....	25

CHAPTER 3	26
<hr/>	
CHARACTERISATION OF COMPOSITE MATERIALS	26
3.1 INTRODUCTION	26
3.2 IN-PLANE PROPERTY CHARACTERISATION	27
3.2.1 Compression Strength and Modulus	27
3.2.2 Interlaminar Shear Strength (ILSS)	29
3.3 FRACTURE CHARACTERISATION	30
3.3.1 Introduction	30
3.3.2 Mechanism of Interlaminar Fracture	31
3.4 IMPACT AND DAMAGE TOLERANCE CHARACTERISTICS	35
3.4.1 Theoretical Aspect	35
3.4.2 Impact Characteristics	36
3.4.3 Effect of Material Properties and Fibre Architecture	36
3.4.4 Post Impact Mechanical Characteristics	38
3.5 ENVIRONMENTAL EFFECTS	39
3.5.1. Influence of Moisture Absorption	39
3.5.2 Theory of Diffusion	41
3.5.3 Influence of Moisture on Static Strength/Stiffness	44
3.5.4 The Influence of Temperature	45
3.5.5 Moisture/Temperature Interaction	46
CHAPTER 4	49
<hr/>	
EXPERIMENTAL.....	49
4.1 MATERIALS.....	49
4.1.1 Reinforcements	49
4.1.2 Matrix Material	50
4.2 LAMINATE MANUFACTURE	53
4.2.1 Examination of Cured Laminates	58
4.3 PHYSICAL PROPERTY TESTING	59
4.3.1 Density Measurement	59
4.3.2 Determination of Fibre Volume Fraction	59
4.3.3 Determination of Void Content	61

4.4 STATIC MECHANICAL TESTING.....	62
4.4.1 Interlaminar Shear Strength.....	62
4.5 DAMAGE TOLERANCE TESTING AND ASSESSMENT	63
4.5.1 Instrumented Low Energy Impact	63
4.5.2 Instrumented Through Penetration Impact	66
4.5.3 Impact Damage Assessment	67
4.6 COMPRESSION STRENGTH TESTING	70
4.7 THERMO-HUMID EFFECT TESTING AND ASSESSMENT	72
4.7.1 Accelerated Ageing in Water.....	72
4.7.2 Dynamic Mechanical Thermal Analysis	73
4.7.3 Raman and Infra-red (IR) Spectroscopy.....	75
4.7.4 Inter-laminar Shear Strength (ILSS) Analysis.....	77
4.7.5 Damage Tolerance Analysis.....	78
4.7.6 Hardness Measurement.....	78
CHAPTER 5	79

DAMAGE TOLERANCE TEST RESULTS AND DISCUSSION	79
5.0 INTRODUCTION	79
5.1 PHYSICAL PROPERTY TESTING	79
5.1.1 Microstructural Analysis	81
5.2 INTERLAMINAR SHEAR STRENGTH (ILSS) TEST.....	84
5.2.1 Variation of ILSS with Temperature	86
5.2.2 Microscopic Examination.....	88
5.3 INSTRUMENTED IMPACT TESTING	91
5.3.1 Effect of Lay-up.....	91
5.3.2 Low Energy Impact Damage	92
5.3.3 Impact Response: Dent Depth	93
5.3.4 Impact Response: Force Based Approach	95
5.3.5 Impact Response: Energy Based Approach.....	102
5.3.6 Impact Response: Strain-Rate Dependency.....	107
5.3.7 Final Damage State.....	109
5.3.7.1 Delamination Mapping	109

5.3.7.2 Thermal Depty Analysis	115
5.3.7.3 Ultrasonic C-Scan Analysis	116
5.3.8 Concluding Remarks	119
5.4 THROUGH PENETRATION IMPACT	121
5.4.1 Results and Discussion	121
5.4.2 Concluding Remarks	126
5.5 COMPRESSION TESTING	127
5.5.1 Compression Testing of Unimpacted Samples	127
5.5.2 Compression after Impact (CAI) Test	130
5.5.3 Evaluation of the Compression Test Results	135
CHAPTER 6	138

ENVIRONMENTAL DURABILITY TEST RESULTS AND DISCUSSION.....	138
6.0 INTRODUCTION	138
6.1 PERCENTAGE WATER UPTAKE	138
6.2 INTERACTION OF WATER WITH MTM 44 RESIN	142
6.3 FTIR SPECTROSCOPY	143
6.3.1 Assignment of IR bands.....	143
Effect of Hydration	146
6.3.2 Degradation Processes in Epoxy Resin	148
6.4 LASER RAMAN SPECTROSCOPY	149
6.4.1 Raman Mapping of Aged Samples	152
6.5 HARDNESS TESTING	158
6.6 INTERLAMINAR SHEAR STRENGTH (ILSS) TEST	159
6.7 DYNAMIC MECHANICAL THERMAL ANALYSIS (DMTA)	164
6.7.1 Determination of T_g	164
6.7.2 Experimental Results	165
6.7.3 Effect of Multi-frequency on DMTA	165
6.7.4 Effect of Reinforcement Architecture on Damping.....	168
6.7.5 Effect of Moisture on the Viscoelastic Response	169
6.7.6 Concluding Remarks	179
6.8 THERMO-HUMID EFFECT ON COMPRESSION STRENGTH	180

6.8.1 Thermo-humid Effect on Compression Strength of Unimpacted Samples	180
6.8.2 Thermo-humid Effect on Compression after Impact Strength	184

CHAPTER 7 **189**

CONCLUSIONS	189
--------------------------	------------

CHAPTER 8 **191**

FUTURE WORK	191
--------------------------	------------

REFERENCE	193
------------------------	------------

APPENDIX	214
-----------------------	------------

Table 19: Optical Micro-Sections of the Compression Moulded Laminates	214
---	-----

Table 20(a): ILSS at 70° C – Laminate S	215
---	-----

Table 20(b): ILSS at 70° C – Laminate M	215
---	-----

Table 20(c): ILSS at 70° C – Laminate L	215
---	-----

Table 21 (a): Force, Energy & Displacement at Damage Initiation	216
---	-----

Table 21 (b): Force, Energy & Displacement at Peak during Low Energy Impact	216
---	-----

Table 22(a): Compression Strength of Dry Unimpacted Samples	217
---	-----

Table 22(b): Compression Strength of Dry 10 Joules Impacted Samples	217
---	-----

Table 22(c): Compression Strength of Dry 20 Joules Impacted Samples	218
---	-----

Table 22(d): Compression Strength of Dry 30 Joules Impacted Samples	218
---	-----

Fig. 118(a): Laminate S after 15 Days of Ageing (% w.c.= 1.369)	219
---	-----

Fig. 118(b): Laminate S after 30 Days of Ageing (% w.c.= 1.09)	219
--	-----

Fig. 118(c): Laminate S after 60 Days of Ageing (% w.c.= 1.118)	220
---	-----

Fig. 119(a): Laminate M after 15 Days of Ageing (% w.c.= 1.201)	220
---	-----

Fig. 119(b): Laminate M after 30 Days of Ageing (% w.c.= 0.969)	221
---	-----

Fig. 119(c): Laminate M after 60 Days of Ageing (% w.c.= 1.046)	221
---	-----

Fig. 120(a): Laminate L after 15 Days of Ageing (% w.c.= 0.971)	222
---	-----

Fig. 120(b): Laminate L after 30 Days of Ageing (% w.c.= 0.913)	222
---	-----

Fig. 120(c): Laminate L after 60 Days of Ageing (% w.c.= 0.959)	223
---	-----

Fig. 121(a): Raman Mapping of Laminate Surface M, after 15 Days of Ageing –	224
---	-----

Fig. 121(b): Raman Mapping of Laminate Surface M, after 30 Days of Ageing –	225
---	-----

Fig. 121(c): Raman Mapping of Laminate Surface M, after 60 Days of Ageing –	226
---	-----

Fig. 122(a): Raman Mapping of Laminate Surface L, after 15 Days of Ageing –	227
Fig. 122(b): Raman Mapping of Laminate Surface L, after 30 Days of Ageing –	228
Fig. 122(c): Raman Mapping of Laminate Surface L, after 60 Days of Ageing –	229
Table 23(a): ILSS after 12hrs of Ageing in 70° C Water– Laminate S	230
Table 23(b): ILSS after 12hrs of Ageing in 70° C Water– Laminate M	230
Table 23(c): ILSS after 12hrs of Ageing in 70° C Water– Laminate L	230
Table 24(a): ILSS after 24hrs of Ageing in 70° C Water– Laminate S	231
Table 24(b): ILSS after 24hrs of Ageing in 70° C Water– Laminate M	231
Table 24(c): ILSS after 24hrs of Ageing in 70° C Water– Laminate L	231
Table 25(a): ILSS after 96hrs of Ageing in 70° C Water– Laminate S	232
Table 25(b): ILSS after 96hrs of Ageing in 70° C Water– Laminate M	232
Table 25(c): ILSS after 96hrs of Ageing in 70° C Water– Laminate L	232
Table 26(a): ILSS after 264hrs of Ageing in 70° C Water– Laminate S	233
Table 26(b): ILSS after 264hrs of Ageing in 70° C Water– Laminate M	233
Table 26(c): ILSS after 264hrs of Ageing in 70° C Water– Laminate L	233
Table 27(a): ILSS after 528hrs of Ageing in 70° C Water– Laminate S	234
Table 27(b): ILSS after 528hrs of Ageing in 70° C Water– Laminate M	234
Table 27(c): ILSS after 528hrs of Ageing in 70° C Water– Laminate L	234
Table 28(a): Compression Strength after 6 Days' Ageing of Unimpacted Samples	235
Table 28(b): Compression Strength after 6 Days' Ageing of 10J Impacted Samples	235
Table 28(c): Compression Strength after 6 Days' Ageing of 20J Impacted Samples	236
Table 28(d): Compression Strength after 6 Days' Ageing of 30J Impacted Samples	236
Table 29(a): Compression Strength after 26 Days' Ageing of Unimpacted Samples	237
Table 29(b): Compression Strength after 26 Days' Ageing of 10J Impacted Samples	237
Table 29(c): Compression Strength after 26 Days' Ageing of 20J Impacted Samples	238
Table 29(d): Compression Strength after 26 Days' Ageing of 30J Impacted Samples	238
Table 30(a): Compression Strength after 96 Days' Ageing of Unimpacted Samples	239
Table 30(b): Compression Strength after 96 Days' Ageing of 10J Impacted Samples	239
Table 30(c): Compression Strength after 96 Days' Ageing of 20J Impacted Samples	240
Table 30(d): Compression Strength after 96 Days' Ageing of 30J Impacted Samples	240
Table 31: Retention in Compression Strength Due to Thermo-Humidity	241

LIST OF FIGURES

Fig. 1: Schematic of Quadriaxial Multi-axial Warp Knitted Fabric	5
Fig. 2: LIBA 'Copcentra MAX 3 CNC' Showing the Orientation of the Ply	7
Fig. 3: Linear and Non-Liner Weft (90°) Layers	8
Fig. 4: Definition of the Orientation of the Yarn Direction.....	9
Fig. 5: Left Handed (A) and Right Handed (B) Quadriaxial Fabric.....	10
Fig. 6: Typical Structure of a MWK Fabric. (a) Chain Stitch; (b) Tricot Stitch	10
Fig. 7: Typical Double Loop Stitch Structure of a MWK Fabric	11
Fig. 8: Schematic Diagram of (a) Lock Stitch and (b) Modified Lock Stitch	11
Fig. 9: Comparison of Mechanical Properties of MWK and UD Prepreg Composites.....	15
Fig. 10: Fractographs of Tensile Specimens.....	16
Fig. 11: Process Cost/ Volume Comparison.....	18
Fig. 12: Schematic of Resin Film Infusion Method	19
Fig. 13: Resin Fibre Interface Showing Contact Angle θ	24
Fig. 14: Effect of Tow Crimp on Compression Strength and Modulus.....	28
Fig. 15: Three Basic Fracture Modes	32
Fig. 16: Interlaminar Shear Testing Modes	33
Fig. 17: Potential Moisture Absorption Curves	40
Fig. 18: Schematic of Stitching in MWK	50
Fig. 19: Isothermal Viscosity Profile of MTM 44	52
Fig. 20: Dynamic Viscosity Profile of MTM 44	52
Fig. 21: Traditional Lay-up Methods.....	53
Fig. 22: Application of Resin Film to the Fabric.....	54
Fig. 23: Laminate Stacking Sequence	55
Fig. 24: Modified Envelop Bagging Arrangement.....	56
Fig. 25: Modified Laminate Cure Cycle.....	57
Fig. 26: Typical C-Scan of a Good Quality Laminate.....	58
Fig. 27: Polished C.S. Viewed under Optical Microscope	58
Fig. 28: Interlaminar Shear Strength Test Arrangement.....	63
Fig. 29: IFWI Testing Unit	64
Fig. 30: Locations of the Test Specimens in the Laminate.....	65
Fig. 31: Photograph of the C-scan Set-up.....	67
Fig. 32: C-Scan of the Unimpacted and Impacted Samples	69

Fig. 33: QMW Compression Anti-buckling Fixture.....	71
Fig. 34: Accelerated Ageing Setup (A) Outside View (B) Inside View	72
Fig. 35: Photograph of DMTA Set up	73
Fig. 36: Main Components of Bending Measurement Unit in DMTA.....	74
Fig. 37: Schematic of Raman Spectroscopy	77
Fig. 38 (a): Resin Flow Through Preform and the Void Formation Mechanism	80
Fig. 38 (b): Distinct Voids Observed in Laminate L	81
Fig. 39: Polished C.S. of Laminate S, M and L.....	82
Fig. 40: Effect of Temperature on ILSS	87
Fig. 41: Optical Micrographs of the ILSS Samples Tested at 70°C	88
Fig. 42: Effect of Stitching Yarn on Crack Propagation	89
Fig. 43: Multiple Shear Failure between the Plies.....	90
Fig. 44: Effect of Lay-Up on the Impact Properties	92
Fig. 45: Effect on Impact Energy on Dent Depth.....	94
Fig. 46(a): Force-Time Plot for the Laminates at 5Joules Impact.....	95
Fig. 46(b): Force-Time Plot for the Laminates at 10Joules Impact.....	96
Fig. 46(c): Force-Time Plot for the Laminates at 20Joules Impact.....	96
Fig. 46(d): Force-Time Plot for the Laminates at 30Joules Impact.....	97
Fig. 47: Impact Force (Damage Initiation) vs. Impact Energy Level.....	98
Fig. 48(a): Average Force-Displacement Results for 5 Joules Impact	99
Fig. 48(b): Average Force-Displacement Results for 10Joules Impact.....	99
Fig. 48(c): Average Force-Displacement Results for 20Joules Impact.....	100
Fig. 48(d): Average Force-Displacement Results for 30Joules Impact.....	100
Fig. 49: Impact Force (Peak) versus Impact Energy Level	101
Fig. 50(a): Average Energy-Displacement Results for 5 Joules Impact	102
Fig. 50(b): Average Energy-Displacement Results for 10Joules Impact	104
Fig. 50(c): Average Energy-Displacement Results for 20Joules Impact	104
Fig. 50(d): Average Energy-Displacement Results for 30Joules Impact	105
Fig. 51: Effect of Impact Energy on Absorbed Energy	106
Fig. 52: Effect of Impact Energy on Elastic Energy.....	106
Fig. 53(a): Force-Time and Energy-Time Plot of Laminate S at 10Joules Impact	107
Fig. 53(b): Force-Time and Energy-Time Plot of Laminate S at 20Joules Impact	108
Fig. 53(c): Force-Time and Energy-Time Plot of Laminate S at 30Joules Impact	108

Fig. 54(a): Delamination Map of a 5J Impact on Laminate S	110
Fig. 54(b): Delamination Map of a 5J Impact on Laminate M.....	110
Fig. 54(c): Delamination Map of a 5J Impact on Laminate L	110
Fig. 55(a): Delamination Map of a 10J Impact on Laminate S	111
Fig. 55(b): Delamination Map of a 10J Impact on Laminate M.....	111
Fig. 55(c): Delamination Map of a 10J Impact on Laminate L	111
Fig. 56(a): Delamination Map of a 20J Impact on Laminate S	112
Fig. 56(b): Delamination Map of a 20J Impact on Laminate M.....	112
Fig. 56(c): Delamination Map of a 20J Impact on Laminate L	112
Fig. 57: Crack Propagation around the Tow.....	113
Fig. 58: Delamination Map of (a) Across 0° and (b) Along 0° Tows	113
Fig. 59(a): Delamination Map of a 30J Impact on Laminate S	114
Fig. 59(b): Delamination Map of a 30J Impact on Laminate M.....	114
Fig. 59(c): Delamination Map of a 30J Impact on Laminate L	114
Fig. 60 (a): Top View of the De-plyed 0° Layer.....	115
Fig. 60 (b): Side View of the Deplied 0° Layer	116
Fig. 61: Effect of Impact Energy on Damage Area	117
Fig. 62: Effect of Absorbed Energy on Damage Area.....	118
Fig. 63: Photograph of the Damaged Surface (Tensile) of Laminate L	122
Fig. 64(a): Force-Displacement, Energy-Displacement History of S.....	123
Fig. 64(b): Force-Displacement, Energy-Displacement History of M	123
Fig. 64(c): Force-Displacement, Energy-Displacement History of L	124
Fig. 65: Energy versus Displacement trace for Through Penetration Impact.....	125
Fig. 66: Energy Absorbed in Thorough Penetration Impact vs. (Thickness x V_f)	126
Fig. 67: End Crushing of the Unimpacted Sample	128
Fig. 68: Compression of the Unimpacted Samples (S, M and L from the top).....	129
Fig. 69: Ultrasonic C-Scans of 10J CAI Sample of L (left) and S (right)	131
Fig. 70: Optical micrographs of CAI samples 10J, 20J, 30J	131
Fig. 71: Compression Strength versus Impact Energy	132
Fig. 72: Effect of Impact Energy on % Retention of Compression Strength	133
Fig. 73: Compression Strength versus Damage Area.....	134
Fig. 74: Compression Strength versus Damage Area.....	135
Fig. 75: % Water Uptake vs. Time (Days ^{1/2}) – Unimpacted Samples.....	139

Fig. 76(a): % Water Uptake vs. Time (Days ^{1/2}) – 10J Impact Samples	141
Fig. 76(b): % Water Uptake vs. Time (Days ^{1/2}) – 20J Impact Samples	141
Fig. 76(c): % Water Uptake vs. Time (Days ^{1/2}) – 30J Impact Samples	142
Fig. 77: FTIR Spectrum of Cured Epoxy	144
Fig. 78: FTIR Spectrum of Composite Laminate	145
Fig. 79: Laminate L after 60 Days of Ageing (% w.c.= 0.959).....	147
Fig. 80: Raman Spectra of the Reinforcement, Matrix and Composite.....	150
Fig. 81: Raman Spectral Shift due to Hydration.....	151
Fig. 82: Optical Microscopic View of Dry Laminate S Showing Micro-Voids.....	153
Fig. 83: Raman Mapping of Laminate Surface S, after 15 Days of Ageing.....	154
Fig. 84: Raman Mapping of Laminate Surface S, after 30 Days of Ageing.....	155
Fig. 85: Raman Mapping of Laminate Surface S, after 60 Days of Ageing.....	156
Fig. 86: Raman Modeling of Laminate Surface S, after 60 Days of Ageing.....	157
Fig. 87: Water Uptake Behaviour of ILSS test Samples	159
Fig. 88: Effect of Water Uptake on the ILSS	160
Fig. 89: Optical Micrographs of the ILSS Samples Tested after 528 hrs of Ageing.....	162
Fig. 90: Typical Force-Displacement curves during ILSS Test	163
Fig.91: Effect of Test Frequency on Storage Modulus.....	166
Fig. 92: Effect of Test Frequency on Loss Modulus	166
Fig. 93: Effect of Test Frequency on Tan δ	167
Fig. 94: Typical DMTA Test Result of Dry Laminate S	170
Fig. 95: Typical DMTA Test Result of Laminate S, Aged for 4 Days (%MC=0.823) ...	170
Fig. 96: Typical DMTA Test Result of Laminate S, Aged for 61 Days (%MC=1.555) .	171
Fig. 97: DMTA Test Result of a Dried Sample (of S) after Aging for 61 Days	172
Fig. 98: Effect of Water Uptake on Storage Modulus of Laminate S	173
Fig. 99: Effect of Water Uptake on Storage Modulus of Laminate M.....	173
Fig. 100: Effect of Water Uptake on Storage Modulus of Laminate L	174
Fig. 101: Effect of Water Uptake on Loss Modulus of Laminate S	175
Fig. 102: Effect of Water Uptake on Loss Modulus of Laminate M.....	175
Fig. 103: Effect of Water Uptake on Loss Modulus of Laminate L.....	176
Fig. 104: Effect of Water Uptake on Tan δ of Laminate S.....	177
Fig. 105: Effect of Water Uptake on Tan δ of Laminate M	177
Fig. 106: Effect of Water Uptake on Tan δ of Laminate L.....	178

Fig. 107: Variation of Tg (Based on Loss Modulus) with Percentage Water Uptake.....	179
Fig. 108: Compression Strength vs. Impact Energy: Laminates S	181
Fig. 109: Compression Strength vs. Impact Energy: Laminates M.....	182
Fig. 110: Compression Strength vs. Impact Energy: Laminates L.....	182
Fig. 111: Effect of Water Uptake on Compression Strength of Unimpacted Samples ...	183
Fig. 112: % Retention of CAI Strength vs. Impact Energy after 6 Days Immersion	185
Fig. 113: % Retention of CAI Strength vs. Impact Energy after 26 Days Immersion	185
Fig. 114: % Retention of CAI Strength vs. Impact Energy after 96 Days Immersion	186
Fig. 115: Compression Strength vs. Water Uptake: 10 Joules Impacted Samples.....	187
Fig. 116: Compression Strength vs. Water Uptake: 20 Joules Impacted Samples.....	187
Fig. 117: Compression Strength vs. Water Uptake: 30 Joules Impacted Samples.....	188

LIST OF TABLES

Table 1: Manufacturing Parameters of Multi-axial Fabrics	8
Table 2: Surface Energies of Various Materials.....	24
Table 3: Properties of T700SC- 12K.....	49
Table 4: Fabrics Used	51
Table 5: Resin Gelation Characteristics of MTM 44.....	53
Table 6: Impact Parameters	66
Table 7: IFWI Drop Parameters	66
Table 8: Initial Setting of the C-Scanner	68
Table 9: DMTA Set-up Parameters	74
Table 10: Summary of Basic Physical Properties.....	83
Table 11: ILSS Test Results at Room Temperature (21°C).....	85
Table 12: Summary of ILSS Test Results at 70°C.....	86
Table 13: Summary of the Compression Test Results.....	132
Table 14: Assignment of FTIR Band.....	146
Table 15: Vibration of the Sorbed Water from FT-IR Study	148
Table 16: Summary of Hardness Test Results.....	158
Table 17: Tan δ Values for the Laminates S, M and L.....	168
Table 18: Summary of the Compression Test Results of 'Wet' Samples	180

GLOSSARY

Non-Crimp Fabrics (NCF)	High performance fabrics produced by laying layers of fibres on top of each other in a particular orientation which are held together by stitching. This particular manufacturing process imparts very little crimp in the fabric
Compression after Impact (CAI)	A widely used technique to determine damage tolerance of composites
Open-Hole Compression (OHC)	Compressive strength of a composite in presence of a hole
Areal Density	The total fabric weight/unit area
Tow	Bundle of fibres
CFRP	Carbon Fibre Reinforced Plastic Composites
Laminates	Flat-plate composites produced for testing
Barely Visible Impact Damage (BVID)	A common technique for determination of damage resistance using low velocity and low energy impact
Multi-Axial Warp Knitting (MWK)	One method of producing non-crimp fabric

Stitch-Bonding	Method of producing high performance fabric by multiple needle stitching. Stitch bonding can be carried out on uncured prepreg and on textile reinforcements
Preform	Reinforcing fabric used for lay-up
Weft-Inserted Warp-Knit Fabrics	Initial development of the Multi-Axial Warp Knitting
Left Handed (A) Fabric	0°/-45°/90°/+45° orientation of a quadaxial NCF fabric
Right Handed (B) Fabric	0°/+45°/90°/-45° orientation of a quadaxial NCF fabric
Warping	The deformation of a flat laminate because of the symmetry of the lay-up
Tricot	A type of stitching method where inter-looping of yarns with adjacent loops are formed while the fabric is knitted
Overstitching	Standard Stitching procedure using a sewing machine, similar to stitch bonding
Tex	The weight in grams of 1000 linear metres of the fibre

CHAPTER 1

INTRODUCTION AND AIM

1.1 INTRODUCTION

Composite materials, fibre reinforced systems in particular, play significant roles in many scientific and engineering endeavours. They have gained their importance primarily because of their unique physical and mechanical characteristics. Today, it is difficult to find any industry that does not utilise the benefits of composite materials. The largest user of composite materials is the transportation industry. The USA alone shipped approximately half a billion kilogram in the year 2000 [1]. Other major users are construction, marine, electrical and the consumer goods industry.

The aerospace industry was one of the first industries to realize the benefits of composite materials. Glass, carbon and aramid fibres are commonly used in various composite aerospace parts. However, carbon fibre composites have overtaken the others because of its performance characteristics.

A primary barrier (which is not always true in the case of the aerospace industry) to the use of composite materials is their high cost. The expensive reinforcing fibres and lack of automation of the fabrication process are the main areas where the cost accrues. However, in the last 30 years because of advancement in fibre production technology and increased use of composites, the price has come down significantly (as low as £6/Kg [2]) and should continue to do so.

Economic development of advanced composite components can, therefore, be characterised as a trade-off between cost and performance. In this trade-off, advanced composites usually provide a significant performance advantage, such as stiffness to weight, or strength to weight and corrosion resistance, when compared to other competitive materials. However, cost is still an issue. As a result of this, advanced composites make their most important successes in the

'High-End' market such as aerospace and sporting goods, where customers are willing to pay for enhanced performance [3].

A second obstacle to new researches in composites with novel reinforcements is the unwillingness of the designers to try them out. Unidirectional prepreg tapes (UDPT) have long been the industrial benchmark, because of the knowledge (physical and mechanical properties) that had already been developed. However, UDPT has several disadvantages – absence of through-the-thickness reinforcement, short shelf life, and the thickness issue (in terms of cost, not suitable for thick primary structures).

In terms of materials properties, Baker et al [4] identified delaminations as the most important type of defect because they can cause large reductions in residual compressive strength and can go undetected. Delaminations can develop during the service life of a product due to: (a) Through thickness stresses developed at free edges, holes, ply terminations or ply drops, bonded or co-cured joint and bolted joints. (b) Effects of moisture and temperature, for example residual thermal stresses from processing and moisture gradients through the thickness of the laminate. (c) Low energy impact damage caused by runway debris, dropped tools etc. Among these low energy impact has been identified as the most dangerous [5] because, the probability of occurrence is high which leads to large reductions in residual compressive strengths and the damage is likely to remain undetected as NDT is costly and time consuming.

The problem of these large reductions in residual strength has led to researches into various types of reinforcements aimed at improving relevant properties. The compression after impact test had been widely adopted to assess the toughness and damage tolerance of a material.

Through the development of 3D textile reinforcements in recent years [6-7], it has been possible to overcome these drawbacks of UDPT. Among all the 3D textile reinforcements, Non-Crimp Fabrics (NCF) have brought together the advantages of textile technology (high deposition rates, unlimited shelf-life, lower cost) and the improvement of through-thickness properties (stitching). Moreover, thick NCF

can be tailor-made for composite parts required to withstand certain magnitudes and directions of load.

Experimental results and economic considerations have shown that NCFs are more than adequate alternatives to traditional prepreg materials for structural applications. NCFs offer obvious processing advantages derived from the elimination or reduction of labour costs associated with lay-up and draping, and the elimination of refrigerated storage. In terms of in-plane mechanical properties, although NCF laminates show lower level of tensile and compressive strength compared to UDPT [8-9], the properties that determine the design allowable ,e.g., compression after impact (CAI), open-hole compression (OHC), are comparable or even improved for NCF-based structures [8-9].

Despite these facts, NCFs are relatively new in the composite industry. Some aspects of NCF technology that affect the final material performance, that have received little or no attention [10] are the processability issues (permeation, compaction, drape behaviour etc.), the NCF manufacturing parameters (stitch type and tension, type of stitching material, areal density, number of layers, inter-tow gap etc.), the composite fabrication variables (manufacturing route, volume fraction, vacuum pressure, resin viscosity etc.) and the effect of exposure to thermo-humid conditions on the overall composite properties.

Based on the lack of a clear understanding of NCF technology as stated above, this particular research project was undertaken to assess the influence of stitch architecture on the low velocity impact performance and subsequent damage tolerance of composites made from such materials. The environmental durability, of the particular carbon-epoxy system used, and the relevance of the above variables has also been evaluated.

1.2 AIM AND OBJECTIVES

The main aim of this project was to assess the influence of stitch density of Multiaxial Warp Knit (MWK) fabric on the damage resistance, damage tolerance and environmental durability of carbon fibre reinforced plastics (CFRP).

To achieve this aim the following objectives were set:

- To assess the influence of stitch density on the production of CFRP through physical property testing.
- To assess the influence of stitch density on the interlaminar shear properties of CFRP.
- To assess the influence of stitch density on the damage resistance due to low energy impact and through penetration impact.
- To assess the influence of stitch density on the residual compressive strength (damage tolerance) of low energy impacted samples.
- To assess the effect of temperature and humidity on the chemical (through FTIR and Raman spectroscopy) and thermal properties (T_g) of CFRP with different stitch density.
- To assess the influence of thermohumid conditions on the residual compressive strength of CFRP with different stitch density.

Having completed each of these objectives further characterisation studies were undertaken to explain the dependencies observed. Finally conclusions were drawn.

CHAPTER 2

BACKGROUND AND MANUFACTURING VARIABLES

2.0 NON CRIMP FABRIC

According to general textile terminology non-crimp fabrics are those which consist of layers of fibres that are without crimp (waviness), although, close examination shows a small degree of crimp. Their manufacturing methods incorporate aspects of both weaving and knitting [11]. Various manufacturing methods are used to produce non-crimp fabric, for example, Multi-Axial Warp Knitting (MWK), Stitch-bonding etc. The NCF used in this particular project were manufactured using MWK and therefore this term is used henceforth to describe these materials.

From the structural geometry point of view a MWK system consists of warp (0°), weft (90°) and bias ($\pm\theta^\circ$) fibres held together by a chain or tricot stitch through the thickness of the fabric (Fig. 1). Therefore, in a single stage, desired fibre orientations with specific layer weights can be produced to replicate a laminate ply lay-up. MWK fabrics are mainly used for structural integrity and strength in different directions [12]. However, when out of plane force is applied, MWK due to lack of interlacement, tend to delaminate.

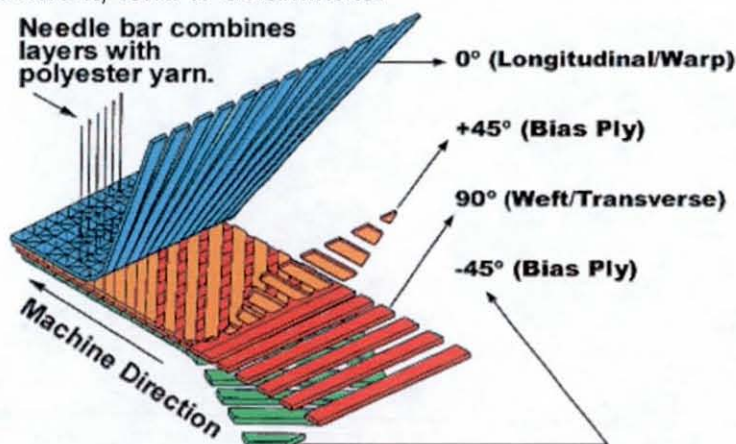


Fig. 1: Schematic of Quadriaxial Multi-axial Warp Knitted Fabric
(Courtesy: TechTextiles International)

Two main machine types used to produce MWK are currently available in the market: LIBA [13] and MALIMO [14] (from Karl Mayer). Recently Hexcel has introduced a new non-crimp multiaxial fabric (NC2) which utilizes lower-cost, high tow-count carbon fibres (24K+) [15]. The company claims their quality to be superior compared to existing NCF technology.

The most publicised application of Multi-axial NCF has been in the NASA ACT Program [16] in USA in collaboration with Boeing (McDonnell Douglas). In the UK, the Aerospace Composites Centre at Cranfield University, in a major collaboration with Airbus, QinetiQ and several others, led an AMCAPS project [17]. Both of these projects were based on LIBA multiaxial fabrics to develop aircraft wing structures.

MWK fabrics, among all other Non-crimp fabrics are attracting interest because of their low production cost (compared to their woven equivalents) [18], high production rate, structural integrity, design flexibility, high tear resistance and overall improved through-the-thickness strength [19]. In the following section the manufacturing technology of Multiaxial Warp Knitted fabrics is discussed in detail. Also Investigated are the various manufacturing parameters.

2.1 MULTI-AXIAL WARP KNITTED FABRIC MANUFACTURING TECHNOLOGY

LIBA Machines are most commonly used for the industrial production of MWK fabrics. A schematic of this process is shown in Fig. 2 [13]. As illustrated, yarns are fed from a creel system (1) and are laid onto a long table according to the desired orientations, through the placement heads (2). The placement heads travel across the table to lay the yarns and finally secure them (yarns) on a chain of needles, the 'transport chain', (3), which travels along the table. The fibres are then cut and the placement heads continue the same cycle. Lay-up arrangements are controlled by the motor-driven placement heads and are programmable. Along with the lay-up of weft and the bias yarns, a chopped strand mat can also be incorporated into the fabric through the use of a chopper

system (4). The chopper cuts glass fibres to produce an individually adjustable fibre mat on the surface of the fabric. Fleeces or mats can also be inserted through the use of two roll carriers (5). The 0° fibres are the last to be inserted and are fed from a warper's beam (6) or a creel system (also in Karl Mayer). All the assembled layers are then stitched together by a warp knitting machine (7). This machine is specially designed with sharp needles that are positioned in such a way that the knitting process does not damage any yarns while forming the knitting loops. However, there are some restriction on the size of yarns used and 'areal weights' for this purpose. The Malimo machine from Mayer utilizes similar lay-up methods; however this type of machine can only produce fabrics up to 4 layers.

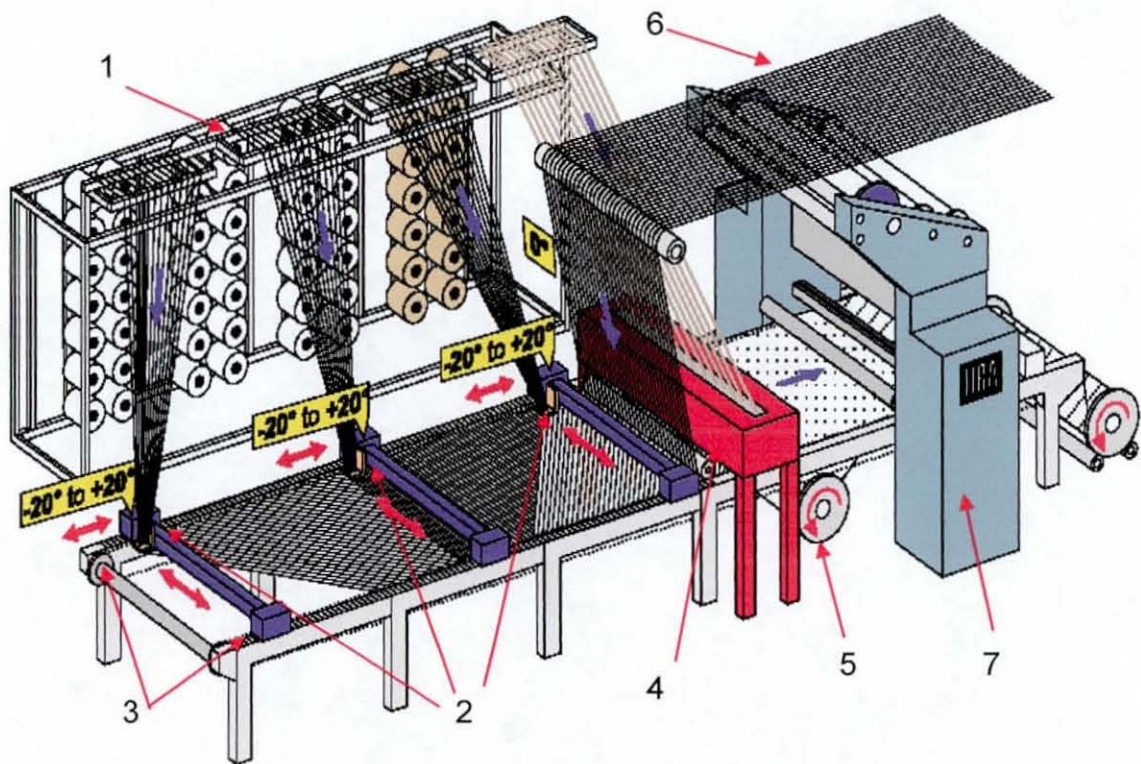


Fig. 2: LIBA 'Copcentra MAX 3 CNC' Showing the Orientation of the Ply [13]

Notations: 1 = Creel System, 2 = Placement Heads, 3 = Transport Chain, 4 = Chopper System, 5 = Two Roll Carriers, 6 = 0° Yarns from Warper's Beam, 7 = Warp Knitting Machine

2.1.1 Manufacturing Variables

According to Ko [20], and different manufacturers' manufacturing parameters, MWK fabrics can be classified according to five basic parameters which are listed in Table 1.

Variables	Levels
Linearity of the bias yarn	Linear, Non-linear
Orientation of the bias yarn (θ°)	-20° to + 20°
Possible No. of Layers	1,2, 3.....up to 7
Stitching geometry	Chain, Tricot, Double Loop
Stitching Mechanism	Impalement, Non-impalement

Table 1: Manufacturing Parameters of Multi-axial Fabrics

In the following sections each of the variables are described in detail. Also described are the capabilities and limitations (in terms of the variables) of the manufacturing techniques that are currently available.

(a) Linearity of Weft and Biased Yarns

Linearity of the fabric is determined by the method of introduction of the bias and the weft yarn. Linear or parallel weft/bias fabrics are produced both by LIBA and Karl Mayer [13-14]. Apart from these parallel weft insertion systems, there is also a slightly crossed weft possible which is produced by the earlier Malimo machines [21] and is conveniently called non-linear. The later principle is carried out in a slightly crossed form, with an angle of deviation with the fed weft/bias yarns, of up to approx. 4° from the normal direction of production, where the angle depends on the number of wefts in the weft inserter [14].

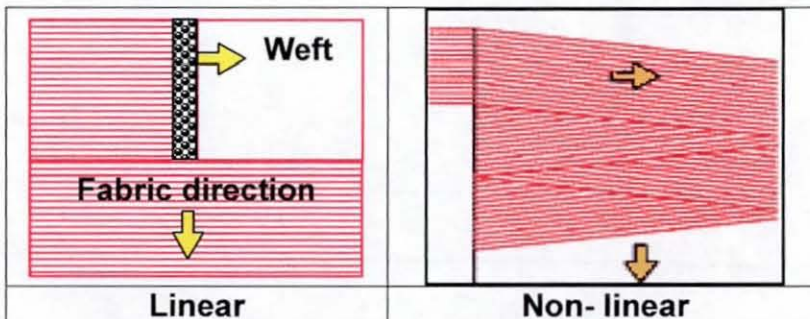


Fig. 3: Linear and Non-Linear Weft (90°) Layers

Fig. 3 shows the visual difference between linear and non-linear weft insertion systems. It can be suggested that the modulus along the direction of the weft/bias yarn will be higher in the case of the linear fabrics compared to the non-linear fabrics. However, in a composite this difference may not be prominent, as load transfer would occur between the adjacent yarns.

(b) Orientation of the Bias Yarn

BS EN 13473-1:2001 [22] specifies the orientation of the yarn directions for MWK fabrics. The orientation of the single thread plies is related to the production direction i.e. the direction of the 0° plies. The \pm angle orientation, designated ' α ' (Fig. 4) in the range between 0° and 90° , is derived from ISO/DIS 1268-1:1997 [22] and is described as either "+" or "-" in relation to 0° (3 in Fig. 4). The orientation is defined as "+", if the threads are oriented in the "+" quadrant and "-" if the threads are laid in the "-" quadrant (Fig. 4).

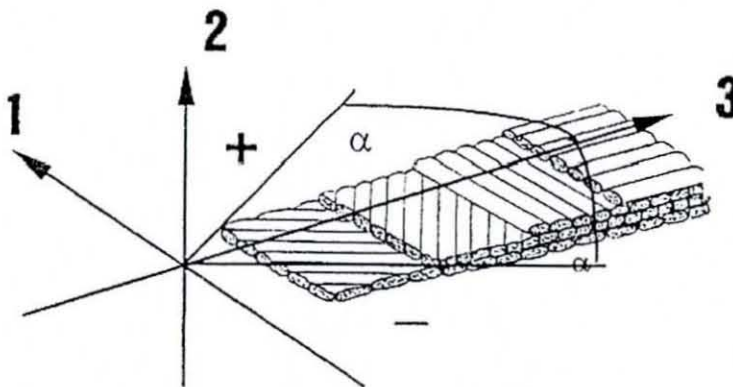


Fig. 4: Definition of the Orientation of the Yarn Direction

In the LIBA's new system any layer can be programmed to be laid at the minimum range of $+20^\circ$ and -20° , while MALIMO's Multiaxial system is only capable of inserting weft/bias yarns at $+45^\circ$ and -45° . In order to avoid confusion, it must be noted that the range described here indicates the value of α . Laying is, therefore, possible between 90° and α . 0° yarns come directly from the warper's beam as shown in Fig. 2.

(c) Number of Layers

The number of axes used is determined by the end use and the requirement for reinforcement in a particular direction. The LIBA machines [13] can assemble up to 7 layers, although in practice this is usually limited to a maximum of 4 (quadriaxials) for most of the common applications. While, for the MALIMO multiaxials the standard is $-45^\circ/90^\circ/45^\circ$ [14]. Depending on the orientation and order multiaxials are divided into Left Handed (A) and Right Handed (B) types. These two types of fabrics are complementary to each other and are used to produce a symmetric lay-up which prevents warping. An example of handed quadraxial fabric is shown in Fig. 5.

A	0°	B	0°
	-45°		$+45^\circ$
	90°		90°
	$+45^\circ$		-45°

Fig. 5: Left Handed (A) and Right Handed (B) Quadraxial Fabric

(d) Stitching Geometry

MWK is produced mainly through two different stitching systems [23]. The first one is a true warp knitting structure, where the number of layers laid is knitted to form a net like structure with 'tricot' stitch. The second one is the 'chain' stitch where the stitching yarns are not interlinked as the previous type. Fig. 6 shows the planar and the cross-sectional views of both types of stitching geometries.

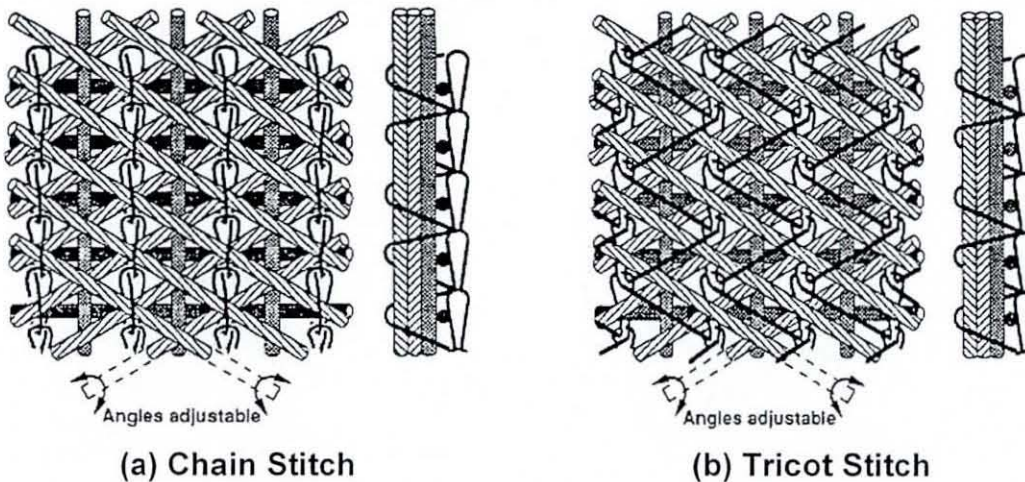


Fig. 6: Typical Structure of a MWK Fabric. (a) Chain Stitch; (b) Tricot Stitch

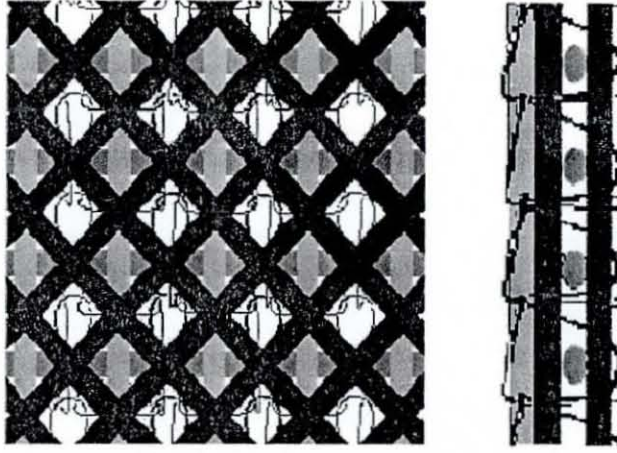


Fig. 7: Typical Double Loop Stitch Structure of a MWK Fabric

In a recent work Rongxing et al [24] investigated the use of double loop pillar stitches (Fig. 7) and compared with the traditional tricot or chain stitches. They found that the energy absorption capability of MWK reinforced composites with these stitches was much better than that of the MWK reinforced composite with the tricot stitch. They concluded that the uniform distribution and the increased number of binding spots of the double loop pillar stitch yarns compared to that of tricot/ chain stitches, considerably improved the through-thickness reinforcement and the energy absorption capability of the MWK reinforced composites.

These types of stitching are often confused by many with 'overstitching' – which is actually a use of sewing technology to stitch through the entire thickness, usually by lock stitching as shown in Fig. 8.

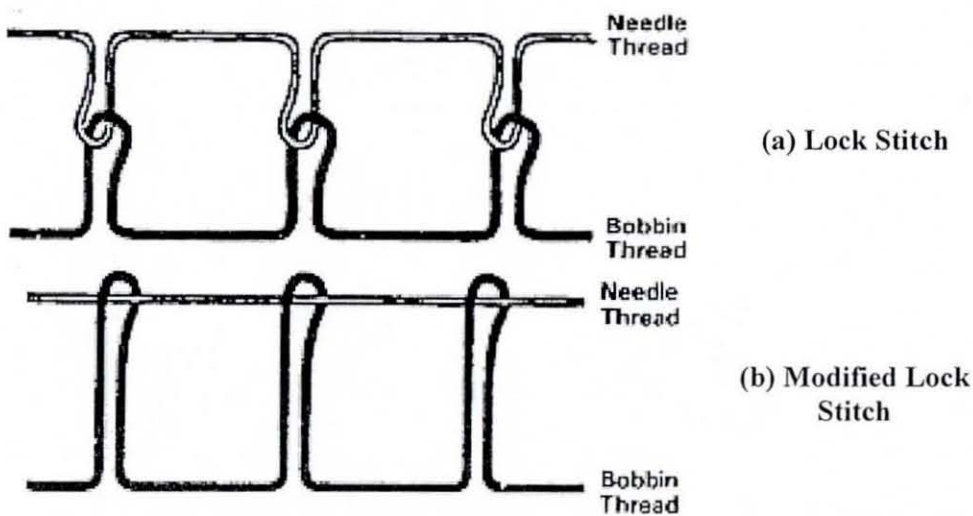


Fig. 8: Schematic Diagram of (a) Lock Stitch and (b) Modified Lock Stitch

There have been a number of papers published by Mouritz and co-workers [25-27] on overstitched fabrics and the mechanical behaviour of the composites made from them. In these papers, the damage resistance was shown to improve as stitching increases the fracture toughness [25]. However, most of them showed a marked decrease in the in-plane mechanical properties. In one particular paper Mouritz et al. [26] indicated that it is not uncommon that overstitching reduces the in-plane properties (compression, tension and shear) by up to 20%. It is still not well understood which mechanisms are responsible for the reductions in the in-plane properties; however, it might be attributed to both the clusters of broken fibres and the fibre distortions due to stitching.

In the case of MWK production with the advanced LIBA machines, layer system works with very low yarn tension [13]. This enables safe processing (least damage to fibres) of sensitive materials like carbon at a high production rate.

(e) Stitching Mechanism

Non-impaled MWK were developed by the Mayer Textile Corporation [20], where formation of the stitches is done without piercing through the stacked layers. This stitching mechanism is carried out by a multiaxial magazine weft insertion mechanism.

Impaled MWK are produced by the LIBA system [13], where linear layers are first laid and then stitched together by knitting needles piercing through the yarn layers. This mechanism unavoidably damages reinforcing fibres (but permits the incorporation of nonwoven mats as in the case of PARAMAX™ fabrics) and degrades the composite tensile properties. However, as mentioned in the earlier section, low stitching yarn tension reduces the magnitude of the damage.

2.1.2 Disadvantages of MWK

The initial cost of production of MWK is high because of the expensive machinery used and a slow rate of production. These reasons, together with the fact that more expensive low-tex fibres are required to get good surface coverage for the low weight fabrics, means that the cost of good quality MWK fabrics can be relatively high.

Extremely heavy weight fabrics can be difficult to impregnate with resin without some automated process and in addition polyester stitching yarns do not bond well to some resin systems [28]. The stitching, therefore, can be a starting point for failure initiation. Moreover, control of the stitching process is difficult for some fabric styles, which can result in bunching of tows, particularly in the 0° direction, subsequently creating resin-rich areas in the laminate. Bibo and Hogg [8] suggested that gaps will have detrimental effects on the mechanical performance, as they cause crimp in adjacent fibre layers which can cause poor compressive properties.

2.1.3 Mechanical Properties of MWK Reinforced Composites

MWK fabrics contain a substantial proportion of relatively straight 'in-plane' yarns. The weight fraction and orientation of the yarns of these fabrics dictate the mechanical performance of the composite. MWK fabric reinforced composites perform considerably better mechanically than the traditional knitted composites. However, this is achieved through the sacrifice of the excellent formability of the knitted composites [29]. Nevertheless, the formability of MWK can be controlled to some extent through the manipulation of the stitch density.

A number of researchers have published their measurements, detailed later in this section, of the tensile, compression, flexural, interlaminar shear, impact and post-impact compression (CAI) properties of MWK reinforced composites. In most cases these composite properties were compared with traditional prepreg laminates or woven composites. However, in most cases the later types did not

have an equivalent amount of in-plane fibres as MWK, and for this reason it is difficult to assess the relative performance of the MWK composites.

Interest in MWK as a preform for structural composites can be dated back to 1988, when Ko and Kutz [30] assessed the tensile and flexural properties of MWK glass-vinyl ester composites and compared them to woven composites.

Wang et al. [31] studied tension, compression, three-point bending and short beam shear of glass-epoxy MWK reinforced composites. They compared experimental results of tension and flexural moduli with Classical Laminate Theory (CLT) predictions, and found good agreements. They, therefore, concluded that MWK composite laminates behave like their prepreg laminate counterparts. Truong et al. [32] echoed Wang et al. [31] views. They found that the experimental stiffness of MWK composites is quite close to the computed results based on CLT and concluded that the effects of stitching on stiffness are limited, and that the stiffness of the fibres and stiffness of unidirectional plies in MWK almost completely translates into laminate stiffness.

Dexter and Hasko [33] showed that MWK fabric, which was still in its infancy, could be considered as an alternative to biaxial woven and unidirectional prepregs. They presented experimental results of composite materials reinforced with four different MWK carbon fabrics and compared them with conventional prepreg tape and woven fabric composites. They produced aerospace quality laminates through resin transfer moulding and found that the tension and compression strength was either comparable or reduced by up to 30% compared to prepreg tape laminates, depending on the type of MWK fabric used. Interestingly they found that the MWK fabric composites exhibited compression after impact strengths up to 80% higher than comparable prepreg tape laminates.

Bibo et al [34] also found a reduction in MWK composites compared to unidirectional prepregs. Their results are shown in the Fig. 9.

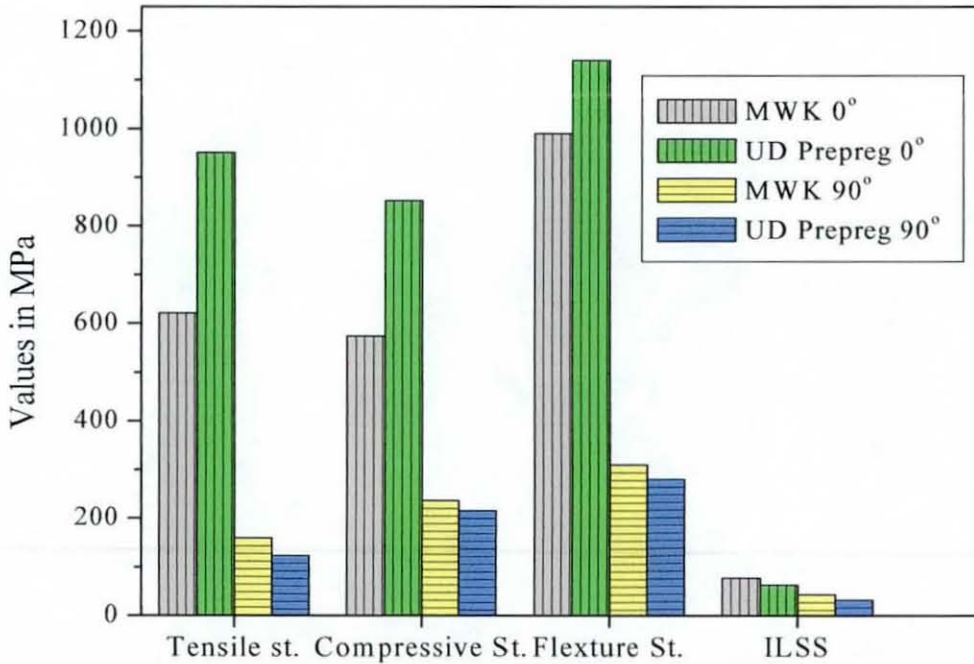


Fig. 9: Comparison of Mechanical Properties of MWK and UD Prepreg Composites [34]

In general, it does appear from Fig. 9 that MWK composites have inferior or at best similar tensile and compressive properties compared with prepreg tape laminates of similar lay-up. Bibo et al [34] suggested that the tensile properties of the laminate are degraded by crimp and fracture of the in-plane fibres during stitching. However, they did not fully investigate the adverse effects of this damage. The crimping of the tows was also suggested to be responsible for MWK composites having lower compressive strengths than prepreg tape laminates with an equivalent amount of in-plane fibres [34]. It is worth noting that the 0° UD prepreps show significantly higher tensile and compressive values compared to MWK in the same direction. These comparisons can not be valid as the laminates did not have the same V_f (60 for UD prepreg against 54 for MWK). Flexural strength values they found also should be treated with caution as ply thickness along different directions were not similar.

Fractographic analysis carried out, by the same authors, of a unidirectional prepreg tape and a MWK laminate subjected to tensile loading are shown in Fig. 10. They claimed that MWK and unidirectional prepreg tape laminates have very similar failure mechanisms. However, they observed that the knit structure in the MWK composite constrains delamination and longitudinal splitting, which was not

observed in the unidirectional prepreg laminates. The same reason can also be attributed to the improved resistance to interply failure (i.e. ILSS) of MWK (Fig. 9). However, the level of improvement in ILSS was claimed to be linked to the mechanical properties of the through-the-thickness yarn; for example, Bibo et al [35] showed that Kevlar knitting yarns produced more impact resistant laminates than polyester yarns.

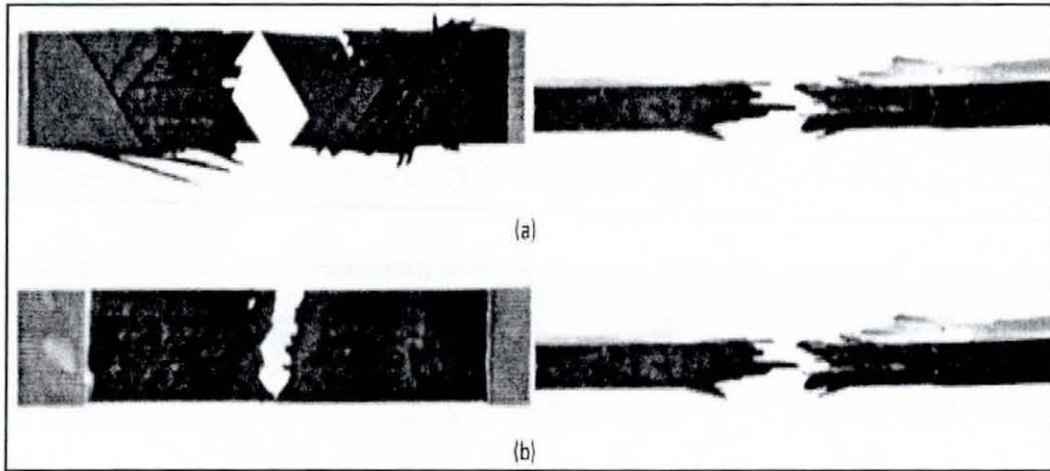


Fig. 10: Fractographs of Tensile Specimens of (a) Unidirectional Prepreg Tape and (b) Non-Crimp Fabric Composites [24]

Some more recent published results on MWK are presented by Kang and Kim [36] who evaluated the tensile, flexural, short beam shear and impact properties of Kevlar MWK fabric reinforced composite laminates and compared them with those of woven laminated composites. They found that MWK possessed up to 52% increased interlaminar shear strength compared with plain woven laminates, in the process retarding delamination growth. They also indicated that MWK composites reduced vertical deformations compared with woven laminates, as the stitch density increased. They showed in a more recent paper [37] that due to the through-the-thickness stitching, the total absorbed impact energy reduces along with the delaminated area. They also showed that the onset of delamination is delayed in MWK composites because of higher impact fracture toughness compared to that for unidirectional or woven composites. Shyr and Pan [38] also found that the threshold load for major damage (perforation) is more for MWK, which they attributed to the fabric structure. Conversely, they showed that during impact, delamination damage in MWK composites is more than for woven and nonwoven composites. They assigned this to the interlaced

structure of the woven fabrics, and the random structure of the nonwoven fabrics, which they claimed restricted the crack propagation. MWK composites, therefore, resist perforation by absorbing more energy through delamination.

Schrauwen and Peijs [39] investigated the effect of matrix ductility and reinforcement architecture on the polyester and vinyl ester infused glass MWK and compared the results with woven composites. They concluded that the penetration energy of the specimens with MWK reinforcement was higher than that of specimens with woven fabrics. However, they did not find any significant difference due to matrix ductility and inferred that impact energy absorption is mainly fibre controlled.

Joffe and Varna [40] while investigating vinyl ester infused MWK composites found that MWK generally showed lower compressive strength compared to similar prepreg materials. Interestingly, they found that MWK composites exhibit almost complete notch insensitivity. They proposed that this is due to the waviness of the fibre bundles in the internal structure. They indicated that this complex internal geometry of MWK composites leads to failures close to internal defects, prior to the failure in the vicinity of the notch, where stress concentration takes place.

Edgren et al. [41] while modelling biaxial carbon MWK reinforced composites loaded in tension indicated that stress concentrations points are caused by 0° fibre bundle waviness. They found that longitudinal cracks form at stress concentrations, caused by the forced straightening of the 0° fibre bundles in tension. Their analysis suggests that the effect of the fibre waviness is strongest where the upper and lower 0° fibre bundles extend out-of-phase. Lomov et al. [42] through experimental investigation of the internal structure of the MWK composites showed a complex pattern of porosities inside the fibrous plies of the preform. They indicated that cracks and channels in the plies occupy a significant volume inside the fabric, subsequently creating resin-rich zones in the composite which plays an important role in damage initiation and propagation. Crimp in the 0° fibre and the resin-rich areas, therefore, plays an important role in dictating the mechanical properties of MWK.

2.2 LIQUID COMPOSITE MOULDING (LCM)

In recent years various LCM methods have established their position due to the popularity of the 2D and 3D dry textile preforms. This particular composite fabrication technique overcame the difficulties that standard manufacturing methods (e.g. prepreg) had as a medium to high volume, cost effective processing route. Rudd et al [43] compared process cost/ volume of various manufacturing methods, and has results reiterating this fact (Fig. 11).

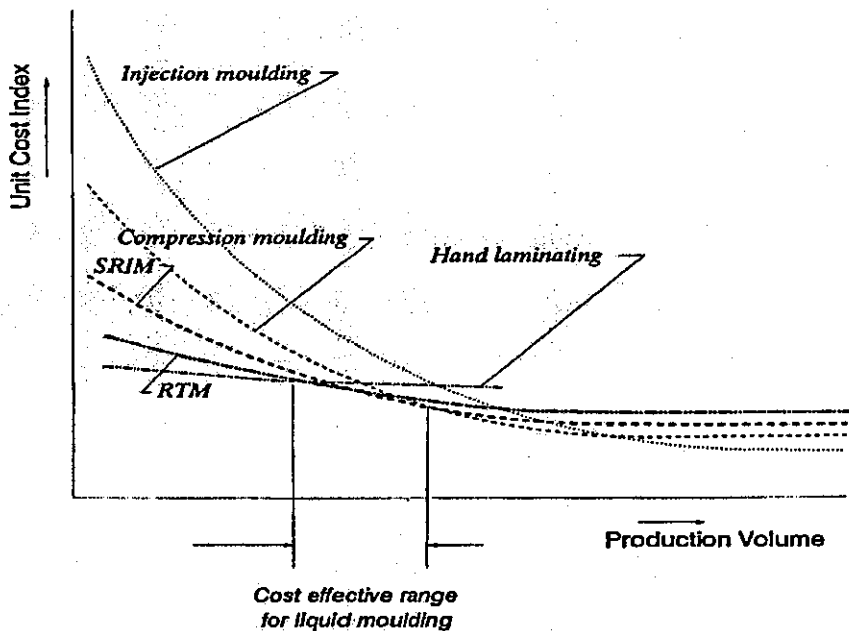


Fig. 11: Process Cost/ Volume Comparison [43]

LCM techniques, sometimes in combination with compression moulding and autoclave vacuum bagging, were developed to achieve high fibre volume fraction ($V_f \geq 45\%$) for medium and large area structures [44]. Moreover, LCM requires light weight, low cost moulds, which cut the initial investment cost. The closed nature of these techniques adds a further advantage in terms of health and safety. LCM also makes it possible to produce complex shapes which are not easy to produce with other moulding methods.

There are a number of LCM processes that are available to the composite industry. They include Structural Reaction Injection Moulding (SRIM), Resin Transfer Moulding (RTM), Vacuum Assisted Resin Transfer Moulding (VARTM),

Seemann Composite Resin Infusion Moulding Process (SCRIMP™) [45], Resin Infusion under Flexible Tooling (RIFT) [44] and RFI [46].

A key issue of all the LCM methods is the achievement of complete impregnation (i.e. free of voids) of the dry preforms, while avoiding fibre distortion due to excessive pressure. These aspects are characterized by resin infusion through a pressure gradient. In many cases the pressure gradient is created by applying a vacuum. However, one main problem with the Vacuum Infusion technology is that it does not have total control over the pressure distribution and therefore the process parameters [47]. A high rate of resin flux can lead to high hydrostatic pressure in the resin which in turn can lead to damage in the reinforcement which in turn can create voids.

2.2.1 Resin Film Infusion (RFI)

In this process a pre-catalysed resin film is used instead of liquid resins (Fig. 12). Once the preform and the films are stacked together, the assembly is enclosed, as in traditional vacuum bagging, and suitable heat and pressure cycles are applied. As a result the resin viscosity first decreases to impregnate the preform and then finally initiates gel and cure. Compared to other processes, RFI has a shorter resin flow path.

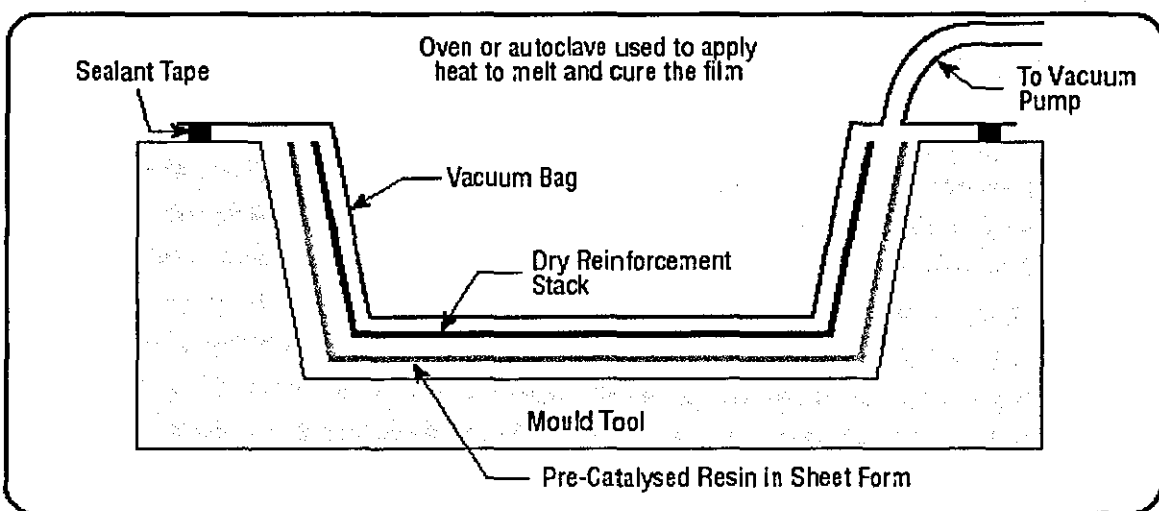


Fig. 12: Schematic of Resin Film Infusion Method [28]

Traditionally, there are two different forms of resin film infusion. Interleaved and thick film forms of this process have both been used in the aircraft and marine industries.

Many variations of the RFI process are available with various trade names – Semipreg, SPRINT, Zpreg, VMS. Their main advantages include the ability to produce high V_f with low void contents, comparable with prepreg, at a lower cost. The resin formulations (due to the solid state of the initial matrix material and elevated temperature cure) are of high quality which results in better mechanical properties. It also helps meet health and safety conditions and contributes to a clean lay-up. While the main disadvantages are that an oven and vacuum bagging system are required to cure the component (though an autoclave system is not always required) the tooling and core materials need to withstand an elevated cure temperature ($\approx 180^\circ\text{C}$). Therefore, this method is not widely used outside the aerospace industry.

2.3 RFI PROCESS VARIABLES AND EFFECTS

The governing theories for resin flow into a dry preform need to be understood in order to understand the process parameters which control RFI. The process variables include fabric variables like permeability and compaction behaviour, and resin parameters like viscosity. The mechanism of void growth is also very important.

2.3.1 Newtonian Flow through a Porous Medium

Laminar flow of fluid through a porous media was first investigated by Darcy in 1856 [48]. He performed experiments in which the pressure above and below a filter (a bed of sand) was monitored, as fluid (water) percolated through it. From this work he defined a constant which related the fluid flow to applied pressure. According to Darcy's Law, one dimensional Newtonian flow through a porous medium can be described as:

$$Q = \frac{K \Delta P}{\eta \Delta L} \quad (a)$$

Where flow rate, Q , is dependent on the pressure gradient ($\Delta P/\Delta L$ is the pressure drop per unit length), permeability (K) and viscosity (η) at a certain time 't'.

Ahn et al [49] suggested that the superficial velocity Q may describe the rate of rise of a fluid meniscus, dy/dt , filling a cylinder of cross-sectional area A , thereby introduced the porosity term in the equation (a).

$$Q = \frac{KA \Delta P}{\eta \Delta L} \quad (b)$$

During vacuum bag curing, assuming linear pressure distribution, $\Delta P/\Delta L$ can be equated with P_t/y (where, P_t is the total pressure at a time 't' and at a distance 'y'). Integrating equation (b) gives,

$$y^2 = \int_0^t \frac{2KA \times P_t}{\eta} dt \quad (c)$$

Further,

$$P_t = P_{\text{mech}} + P_{\text{vac}} + P_{\text{grav}} + P_{\text{cap}} \quad (d)$$

Where,

P_{mech} = Mechanical pressure or autoclave pressure

P_{vac} = Vacuum pressure

P_{grav} = Gravitational pressure

P_{cap} = Capillary pressure

When an autoclave is not used, P_{mech} becomes zero. P_{grav} can also be considered zero, as it does not have a significant effect. P_{cap} varies inversely with the processing pressure and is considered small at high processing pressure. Therefore, for vacuum bag curing the transverse impregnation equation can be written as,

$$y^2 = \int_0^t \frac{2KA \times (P_{vac} + P_{cap})}{\eta} dt \quad (e)$$

Methods to obtain values for the various parameters in equation (e), either theoretical or experimental, are therefore required to solve the equation.

2.3.2 Permeability of Fibrous Preforms

Generally permeability is much higher in the direction along the fibres than in the transverse or through-the-thickness direction. A number of studies [50-52] have been carried out to determine the permeability of fibrous preforms. In general, permeability is a function of the fibre volume fraction, V_f , fibre radius, r_f , and fibre architecture, which is explained by the Kozeny-Carman equation (f) [53]:

$$K = \frac{r_f^2}{4k_0} \times \frac{(1-V_f)^3}{V_f^2} \quad (f)$$

k_0 is the Kozeny constant which varies with the fibre architecture and direction of flow. For flow parallel to the fibres, Gutowski et al [53] suggested $k_0 = 0.7$ (for 4 micron fibre radius), while for the transverse flow they suggested a value of 17.9. However, they suggested a modified expression for the transverse permeability, taking into account the stop-flow phenomenon (as the V_f approaches its theoretical limit, through thickness flow shuts off as the fibres are forced into contact with one another along their entire length):

$$K = \frac{r_f^2}{4k'} \times \frac{\left(\sqrt{\frac{V'_a}{V_f}} - 1 \right)^3}{\left(\sqrt{\frac{V'_a}{V_f}} + 1 \right)} \quad (g)$$

Where V'_a is the fibre volume fraction at which transverse flow is not permitted [i.e. ultimate fibre volume fraction] and k' is the modified Kozeny constant. This equation agrees very closely with the standard Kozeny-Carman equation (f) when

$V_a=1$, but gives much lower permeability when $V_a<1$. From experimentation Gutowski et al. [53] estimated values of V_a to be in the range of 0.76-0.82.

2.3.3 Resin Viscosity during Cure

As explained earlier resin flow rate is also dependent on the resin viscosity, η . In equation (a) all of the parameters except viscosity, η , can be treated as constant [54-55]. During curing the resin viscosity varies greatly. In the RFI process, the resins used are partly reacted; therefore their initial viscosity is relatively high. As a film is heated, the viscosity drops dramatically and reaches a minimum at a temperature that is generally designated as the 'Hold' Temperature (e.g. 130°C in MTM44) [51].

In the cure cycle, this temperature is important as complete wet out can be achieved only at this temperature and any excess resin is squeezed out into the bleeder material. It should also be noted that at this particular temperature resin is most susceptible to void formation. Thus pressure developed at this time in the resin is also critical [43]. Continued heating then leads to the initiation of cure ('Gelation' – It is required that the time for the resin to reach the gel point must be longer than the duration to completely wet the preform) and the resin viscosity increases progressively until the resin solidifies.

2.3.4 Wettability of the Fibres

Surface Tension plays a key role in determining the wettability of reinforcing fibres by a resin matrix during processing [50]. Good wetting is essential for the manufacture of quality composites which also improves mechanical properties. The contact angle between the solid fibre and impregnating liquid resin is the common measure of wettability. A high contact angle is associated with poor wettability.

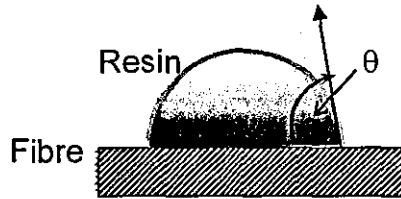


Fig. 13: Resin Fibre Interface Showing Contact Angle θ

The contact angle, θ , depends on the surface chemistry of the fibres as well as the resin. As a ground rule, low energy liquids wet high-energy solids [56]. Table 2 shows surface the energies of some materials.

Materials	Surface Energies (Dyne/cm)
Metal	~ 400-2000
Glass (Clean)	~ 500
Carbon Fibres	~ 50
Kevlar®	44
Polymers	30-45

Table 2: Surface Energies of Various Materials [56]

From the above table it can be inferred that glass will wet out more easily than carbon and Kevlar. Ahn et al [50] suggested that surface tension is very important in void formation and its transport during impregnation and consolidation. For resin matrices with high surface tension, it is difficult to eliminate voids.

Surface tension is also responsible for the capillary pressure (dependent on porosity), which improves impregnation and processability, equation (e). At low processing pressure, capillary pressure due to matrix surface tension becomes even more important [57]. One important aspect when using capillary pressure only is that it does not produce a good quality void-free laminate. In order to avoid voids during consolidation, application of a vacuum is very important when capillary pressure is present [50].

2.3.5 Compaction Behaviour of the Reinforcements

While the preforming techniques – e.g., weaving, knitting, braiding and stitching – orient the fibres into a skeleton of the actual part, the final microstructure of a laminate depends to a great extent on the compaction of the preform. In a review on this particular behaviour, Robitaille and Gauvin [58] presented results from compaction experiments for a wide range of reinforcements. They then fitted the data to the well known power law model, equation (h), which relates fibre volume fraction (V_f) to compaction pressure (P):

$$V_f = AP^B \quad (h)$$

Where, A and B are empirically determined constants for each reinforcement material.

As a RFI process variable, compaction of the reinforcement depends on its geometry [59] (i.e. fabric form and fibre orientations) which subsequently determines its permeability during the processing [60-61]. Visconti et al [62] showed through experimental results that permeability values decrease as the pressure increases – because compaction of the layers increases.

It has also been suggested that compaction pressure is responsible for collapsing and transportation of the bubbles formed during curing, thus reducing voids [63].

CHAPTER 3

CHARACTERISATION OF COMPOSITE MATERIALS

3.1 INTRODUCTION

In order to ascertain how a composite will perform in a structure it is necessary to characterise its behaviour using standard tests. The anisotropy of composites and the use of adhesive bonding lead composites to fracture in different and multiple failure modes, which makes their analysis complex. However, in most cases statistical interpretation of sets of 'coupon' (test laminate) tests is used to generate design data that is either extrapolated or interpolated to the component and loading to which it will be applied. Substructure tests are then needed on parts of the final component with in-service loading and damage scenario. However, coupon test results will only represent the final material behaviour when the features of the final component, for example lay-up, holes, contours etc., are included at the coupon level. It should also be noted that allowable stresses of damaged structures are more important than ultimate undamaged strength in determining the efficiency of a composite structural material.

In this chapter properties measured to characterise the in-plane performance, damage resistance and tolerance and the micro-structural characteristics of composite materials are presented and the literature reviewed. In all cases work particularly relevant to the characterisation of MWK fabrics is emphasised. The characterisation of stitched composites is also included as the disruption and fibre damage caused by stitching is to some extent analogous to MWK fabrics.

3.2 IN-PLANE PROPERTY CHARACTERISATION

In-plane properties refer to those measured in the plane of the fibres; either along them or at an angle to them. Generally five basic properties are measured – tensile strength and modulus, compression strength and modulus, and apparent interlaminar shear strength. In-plane shear strength is also often characterised, so are properties in the presence of holes. The tests can be carried out at room temperature, dry, or at elevated temperatures with different levels of relative humidity, or in the presence of other substances, which may be detrimental to the performance of the composite during its use.

It is important that the tests are carried out in a standardised way which is suitable for the material and that the type of test is relevant to the application of the material in structural use. Various standard test methods are available, for example, ASTM, BS, CRAG, SACMA etc. However, applicability of a test method depends on the dimensions of the repeating unit-cell of the material [64] which become more prominent when considering small sample widths, thickness or gauge lengths. The reason behind this argument is that if the dimensions of the test sample do not extend over several unit-cell lengths the readings obtained will not be averaged out.

In the following sections the compression and interlaminar shear properties are discussed in more details, which are measured in the current study.

3.2.1 Compression Strength and Modulus

The compressive strength of a material in a given situation is determined by the failure process which operates at the lowest stress. Kyriakides et al. [65] recognised that failure is initiated by imperfections (geometric imperfections, such as waviness, voids and cracks) coupled with plastic deformation of the matrix [66]. In composites with good interfacial bonding the matrix fails predominantly by shear. Soutis [67] showed that the multidirectional specimens fail by microbuckling of the 0° fibres similar to the unidirectional specimens. They also found matrix-splitting and delamination occurring with the microbuckling, but they

indicated these to be secondary modes of damage. In a more recent paper Soutis et al. [68] observed that the failure strength of multidirectional laminates containing 0° outer layer was less than that of laminates with $\pm 45^\circ$ outer plies; indicating that the $\pm 45^\circ$ plies provide lateral support to the 0° plies and delay the initiation of fibre microbuckling.

Furthermore, in low V_f unidirectional laminates the fibres buckle in an out-of-phase fashion while in high V_f laminates it happens in an in-phase mode [66]. In the case of multiaxial fabrics the effects of waviness are further enhanced if the adjacent fibre layers have waviness which is in-phase. This particular situation reduces the stability that might otherwise be offered by the adjacent layers.

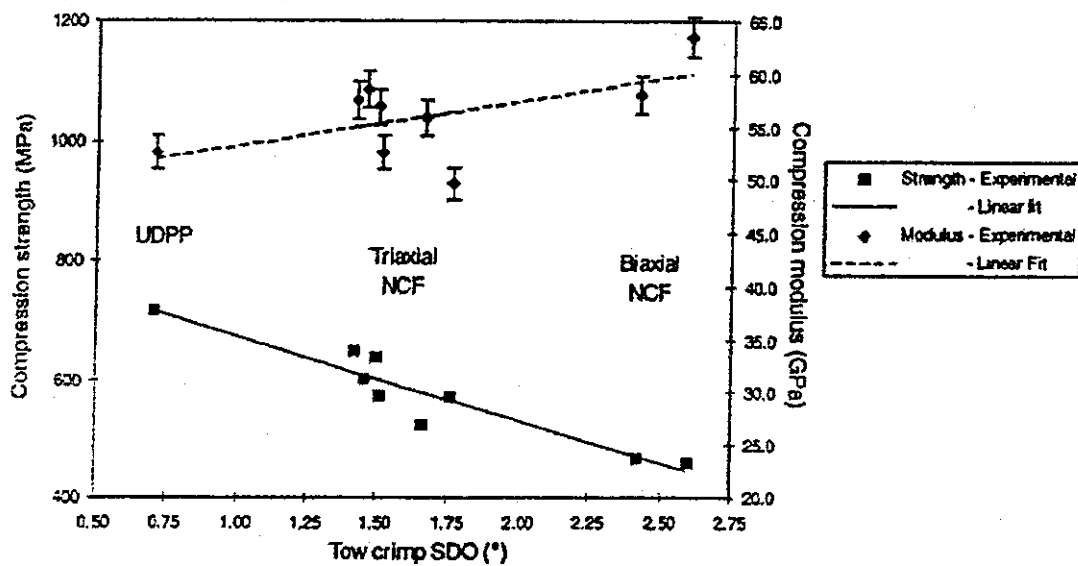


Fig. 14: Effect of Tow Crimp on Compression Strength and Modulus [69]

When comparing the effect of tow crimp on compression strength Miller [69] observed a linear relationship between standard deviation of tow orientation and compression strength for prepreg tape and non-crimp fabric composites (Fig. 14). However, his work did not show the same trend for compression modulus, although there was some indication of decreasing modulus with increasing tow crimp when considering just the tri-axial non-axial data.

Drapier and Wisnom [70] characterised MWK composites and found a very strong correlation between the compressive strength and the tow crimp level and

the size of resin-rich pockets in the composite. They showed that stiffness of MWK depends on the fibres, whereas MWK strength is mainly dependent on parameters controlling the 0° tow buckling. They suggested that the MWK compressive strength will be improved when the crimp level is limited (through increasing the 0° tow tension during lay-up), the resin has high mechanical characteristics (especially a high modulus), tows are spread (low stitching tension) and the overall fibre content is increased.

It is crucial when measuring compressive property that the samples be stabilised from global buckling [71]. Use of either an anti-buckling fixture to constrain the sample, a gauge length which is too short to buckle, or a self supporting shape (sides of which are sufficiently constrained and too short to buckle) are all methods of solution. A specimen geometry optimization study by Joffe and Varna [40] led to research concerning notch sensitivity of MWK. They performed compression testing on specimens with circular centre holes and symmetric sharp edge notches and found MWK composite to be notch insensitive. They proposed that this behaviour of MWK composite is due to its irregular and uneven internal structure which leads to failures close to an internal defect, prior to the failure in vicinity of the notch, where stress concentration takes place.

3.2.2 Interlaminar Shear Strength (ILSS)

For a given resin the interlaminar shear behaviour depends on the stress concentration effects associated with the presence of fibres and voids and on the strength of the interfacial bond [72]. Although increasing the fibre/matrix bond strength increases interlaminar shear strength this only applies up to the point at which failure occurs in the resin rather than at the interface. The fibre surface treatment also favours interfacial failures – reducing the notch sensitivity of the composite.

Fibre volume fraction, V_f , also affects the ILSS. As the V_f reduces, the additional resin tends to accumulate in the interlaminar region [73]. Miller [69] showed that apparent interlaminar shear strength decreases with an increase in free resin volume fraction and also with the thickness of the resin layers. An increase in V_f

increases the ILSS up to a point from where the strength was observed to drop suddenly [72]. This sudden load drop can be attributed to the stress concentration of the fibres as the resin layer thickness reduces. For laminates with brittle resin, the stress concentration effect leads to interlaminar shear strength in the composite which is lower than that of the neat resin. For tougher systems the shear strength of the composite and neat resin is approximately the same as local stress concentrations are relaxed by local deformation [72].

Drapier and Wisnom [74] used a bi-dimensional FE model of a bi-axial MWK and verified that, under pure shear loading, the overall response is largely controlled by the resin response and the highest strains develop in the resin-rich areas. They concluded that in order to improve the shear behaviour of the MWK fabrics it is necessary to limit the development of high shear strains by reducing the resin pockets in the intralaminar and interlaminar regions. Other suggestions made were the use of resin with a high yield stress and a high modulus, and by limiting overall stitch tension to avoid shear strain localisation. The latter suggestion was made because under low tension the tows can spread and form homogeneous fibre structures.

The effect of fibre waviness on ILSS can also be considered, as there is a possibility that wavy fibres will bridge the interlaminar region and will have to be broken or pulled out to cause failure [75].

3.3 FRACTURE CHARACTERISATION

3.3.1 Introduction

Carbon/epoxy composite structures are highly sensitive to damage from low velocity impact loads which may occur in-service, e.g. dropped tools, runway debris. Different failure mechanisms have been observed under this type of loading, such as broken fibres, micro-cracking of the resin matrix, debonding and delamination. Among these forms the most critical is often delamination. Imperfections created during manufacture, such as air entrapment or dry patches (resin-devoid areas) may give rise to delaminations which can spread to

undamaged areas of a structure under compressive in-plane load. Delaminations also initiates in areas of stress concentration.

Understanding the mechanisms of delamination initiation and growth are typically addressed in two types of tests: firstly, interlaminar fracture tests, which are aimed at measuring the strain energy release rate in a number of loading modes or a combination of modes. Secondly, impact tests in which the response of a material to impact is observed in terms of how load is transferred to the material and the resulting delamination extents. The latter test is typically followed by measuring the residual strength of the material under compressive loading.

3.3.2 Mechanism of Interlaminar Fracture

The failure processes occurring in fracturing composites are complex. The critical strain energy release rate is representative of the matrix toughness and is influenced by the fibres, interface and microstructure. It is also dependent on the mode of the interlaminar stress. There are three basic interlaminar failure modes [76], opening or peel (mode I), shear (mode II), tearing (mode III) or a combination of modes (Fig. 15). During impact the failure process includes mode I and mode II delamination initiation and growth, matrix cracking, fibre debonding and laminate flexure [77].

The generation of delamination is associated both with the interlaminar stresses, determined by the geometry of the sample and the magnitude of the load, and by the interlaminar strength – dictated by material properties. Thus to improve the resistance to delamination, interlaminar stresses must be reduced or interlaminar strength increased. The MWK fabric, by virtue of the through-thickness stitching, may enhance the interlaminar toughness (through fibre bridging [78] etc.) of the composite and correspondingly minimise the composites susceptibility to delamination damage development and subsequent propagation under load. The MWK's lower fundamental mechanical properties (tension, compression etc.) may therefore be compensated for by reduced damage sensitivity.

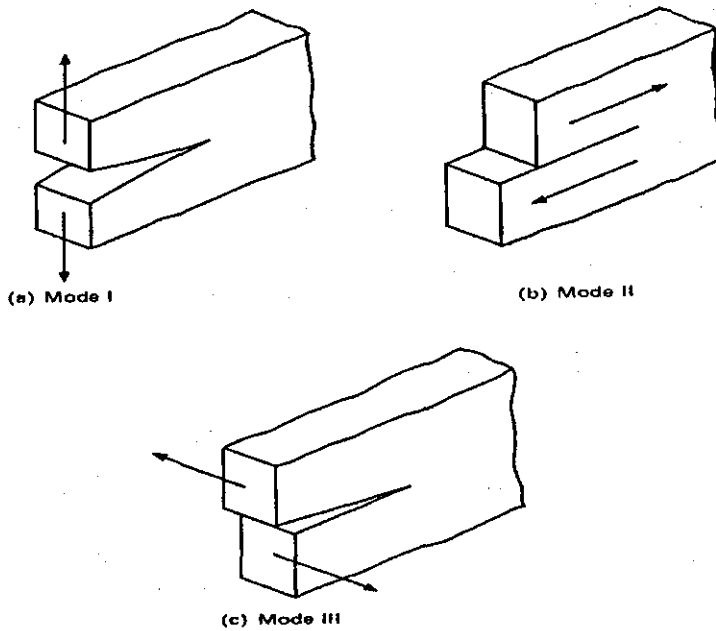
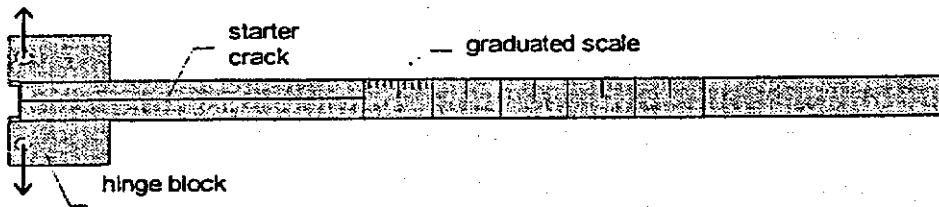


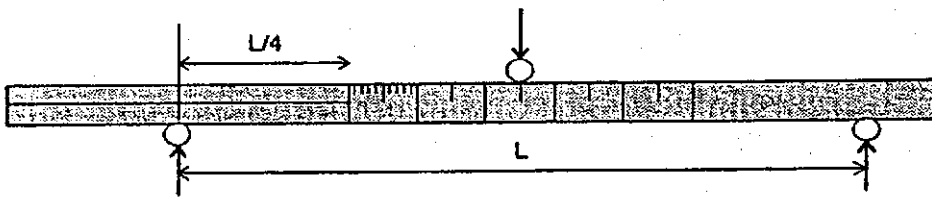
Fig. 15: Three Basic Fracture Modes

The generation of mode I strain energy release rate data is performed on a double cantilever beam (DCB) test sample [ESIS][79]. This consists of a narrow beam with a starter crack running a known length into the sample at the laminate mid-plane. Load is introduced, as shown in Fig.16a, through hinges or hinge blocks bonded to the cracked end. The crack is then propagated by pulling apart the hinges at a constant rate during the test. The resulting force/cross head displacement curve, together with information on the location of the crack tip at intervals during the test allows the strain energy release rate for crack growth to be calculated for that material system and between that interfaces.

The mode II [79] test measures the strain energy release rate for crack growth in shear loading as illustrated in Fig. 16b. The test configuration is called End Notched Flexure (ENF) and uses the same specimen as the mode I DCB test but is loaded in three-point bending with the crack tip half way between the mid-span and one knife edge. In this case the crack propagation tends to be unstable and the point of non-linearity on the load displacement curve, the 5% offset point and/or the maximum load achieved, tend to be used to characterise the mode II strain energy release rate for the material system.



(a) Mode I (crack opening)



(b) Mode II (crack shear)

Fig. 16: Interlaminar Shear Testing Modes

(a) Effect of Constituent Properties

As well as propagating in neat resin interlaminar cracks interact with the fibre surface via an interface. The strength of this interface is often controlled by sizing [80] on the fibre surface. As long as the interfacial bond strength is stronger than the resin itself, the crack will tend to propagate only in the matrix.

The role of the fibre properties on composite fracture is related primarily to its effect on the compliance of the composite [34]. An applied load will result in a given opening or shear displacement depending on its stiffness and hence stress level at the crack tip.

The effect of resin toughness [34] in relation to the toughness obtained for the composite is related primarily to the constraint, by fibres, of the zone of plastic deformation which surrounds the crack tip. For tough matrices the neat resin plastic zone is larger than the resin layer between the plies [81]. This reduces the degree of load redistribution away from the crack tip, and thus allows the critical strain or stress condition for local failure at the crack tip to be achieved earlier.

For resins where the plastic zone ahead of the crack tip is less than or equal to the height of the resin layer between plies, neat resin and composite toughness will be similar.

For brittle resins crack growth is more difficult when the crack tip is loaded in shear. The reason for this is related to the shape of the plastic zone which surrounds the crack tip [81].

(b) Effect of Fibre Architecture

The architecture of the textile preform, or the fibre orientation, and the level of structural integrity determine the fibre volume fraction (which depends on the fibre packing density) and subsequently the translation of the fibre properties to the composite structure. MWK fabric with its near zero crimp and through thickness stitching has a failure mechanism which is quite different from the traditional unidirectional prepreg materials [66]. MWK fabrics fail through a combination of matrix micro-cracking, fibre matrix debonding, fibre breakage, stress redistribution and delamination [77]. Because of the stitching, the failure process proceeds gradually compared to the sudden catastrophic mode exhibited by the unidirectional prepreg composites. Occasional damage to the tows by the stitching process of MWK may reduce the in-plane properties of the composite; however, the interlaminar shear strength is expected to be high because of the stitching. The failure mechanism may change significantly with the fibre type and matrix toughness as well as arrangement of the fibres [76].

3.4 IMPACT AND DAMAGE TOLERANCE CHARACTERISTICS

3.4.1 Theoretical Aspect

The instrumented falling weight impact machine is generally used to characterise the impact properties of composite materials. In these machines, the level of impact energy is varied by varying the drop height of the impactor, which changes the impact velocity simultaneously. Alternatively, the mass of the impactor may be varied, while keeping the velocity constant. The following equations [82] of motions are utilised to define the relationships between force, F , velocity, v , displacement, x , and energy, E at a time, t .

$$F = Mg - f = M \frac{dv}{dt} \quad (a)$$

$$v = v_0 + gt - \frac{1}{M} \int_0^t f dt \quad (b)$$

$$x = v_0 t + \frac{1}{2} gt^2 - \frac{1}{M} \int_0^t \int_0^t f dt dt \quad (c)$$

$$E = v_0 \int_0^t f dt + g \int_0^t f t dt - \frac{1}{2M} \left[\int_0^t f dt \right]^2 \quad (d)$$

Where, v_0 = Velocity at the point of impact,

M = Mass of the impactor

g = Acceleration due to gravity (9.81 m/s²)

f = Force

The force value is recorded directly through a force transducer [83], attached to the impactor, during the impact. It is possible to calculate the energy absorption and displacement using the equations (a) – (d).

3.4.2 Impact Characteristics

The damage created during an impact event is dependent both on the magnitude of the blow and the constraint of the target. A thin skin with a large span between supports will be relatively free to deflect and the damage introduced is primarily due to flexure – large tensile forces on the back face of the material and some localised shear buckling close to the front face adjacent to the impact site [66]. The deflection of the laminate, if sufficiently large, causes transverse cracks between fibres close to the tensile back face of the skin and with increasing deflection these grow and nucleate delaminations where the cracks meet a ply boundary. These delaminations extend in the direction of the lower ply to an extent dependent on the deflection and interlaminar fracture properties of the ply interface [76]. The mode of the delamination growth is a mixture of mode I and II. Further deflection may cause tensile fibre fracture starting at or close to the back face followed by perforation of the laminate. In cross section the damage is conical with the largest delaminations close to the back face [34].

For rigid targets, contact damage dominates the failure process with fibre fracture and delaminations generated by shearing of material away from the striker as it indents the surface plies. These delaminations may be conical or may exhibit the largest delamination on the impacted surface [66].

3.4.3 Effect of Material Properties and Fibre Architecture

Delamination and matrix cracking are sensitive to matrix toughness and relative resin layer thickness, whereas fibre breakage is sensitive to the properties of the fibres [84]. Experimental results indicate that matrix properties govern the threshold for damage initiation. Damage area however is governed by a combination of matrix properties and fibre strain to failure. Penetration resistance at large impact energies is dominated by fibre properties [34].

While comparing laminates manufactured with high strain and standard carbon fibres of the same modulus, manufactured with the same matrix system, Cantwell et al. [85] showed that fibres with a higher strain to failure exhibit smaller damage

areas for the same incident impact energy. The scenario was explained by greater transfer of strain from the matrix to the fibre and the fibre's property to withstand it. Similarly tougher matrices should behave in a similar way [39]. Neat resin with better tensile properties should also exhibit improved damage tolerance. Williams et al. [86] suggested that there must be sufficient resin between the fibres in the laminate to permit plastic deformation of the resin to ensure better damage tolerance.

Fibre architecture plays an equally important role as the constituent properties. It has been well established [87] in unidirectional prepreg tape that both the onset and extent of damage is determined by the difference in angle between the adjacent plies (due to fibre bridging). Hitchen et al [88] studied the effect of stacking sequence, of a carbon/toughened epoxy system, on impact damage and concluded that panels containing 45° surface plies gave higher peak energies (in falling wt. Impact test) than panel containing 0° surface plies. They also concluded that stacking sequence influenced both the shape and size of the delamination area and that increasing the number of dissimilar interfaces reduces the energy available for delamination propagation. Strait et al. [89] in their work showed that stacking sequence and reinforcement form can have significant effects on impact resistance particularly at higher impact energies. Their results demonstrated that energy at maximum load is highly dependent on stacking sequence. However, they found no major effects of stacking sequence or reinforcement form on the energy required for the onset of damage in the laminates.

Enhanced suppression of delamination damage in MWK laminates may be expected on the basis that all the most likely planes of fracture, between layers of differing fibre orientation, are bridged by the through thickness stitching yarn, providing some crack tip shielding or crack face closure [8].

3.4.4 Post Impact Mechanical Characteristics

In order to quantify the effect that impact damage has on the laminate, mechanical testing is required. As stated earlier the damage from an impact may consist of various amounts of fibre failure, matrix cracks and delaminations. Damage dominated by fibre failures results in load redistribution that can affect both the tensile and compressive residual strength. Damage causing matrix failure results in load redistribution and primarily affects compressive residual strength [90].

The stacking sequence is also important while considering post impact characteristics. Cantwell and Morton [91] in their review quoted a number of references showing that composites having $\pm 45^\circ$ surface plies offer improved residual strengths. The reason they stated was that $\pm 45^\circ$ plies placed on the outer surface protected the load bearing 0° plies against damage caused by impact. The effect of stitching on post-impact tension and compression strengths was presented by Poe et al. [6], which showed that stitching improved the post impact tensile and compressive properties. However, compression strength ratio improved far more than the tension strength ratio (i.e. Ratio of post-impact strength to undamaged strength). Dickinson et al. [92] in their review of trans-laminar-reinforced composite (defined as a composite laminate with up to 5% volume of fibrous reinforcement oriented in a translaminar or through-thickness direction) pointed out substantial improvement in compression-after-impact response along with considerable increase in fracture toughness in Mode I (double cantilever beam) and Mode II (end notch flexure). Through-thickness reinforcement is also shown to restrict size and growth of impact damage and edge delamination.

In the case of the MWK, as it is a stitched preform, one should expect similar results. Experimental results of Bibo et al. [34] tend to support this expectation. Dexter and Hasko [33] also found MWK fabric composites, made from Liba and Mayer multiaxial warp-knitting machines, exhibiting compression after impact strengths up to 80% higher than the strength of comparable prepreg tape laminates.

3.5 ENVIRONMENTAL EFFECTS

Since carbon fibres are inert to moisture and temperature, the matrix and fibre/matrix interface components of the carbon fibre composite are of the greatest concern when considering the effects of moisture and temperature on these materials. The potential effects of each condition are very similar in nature: interfacial degradation, matrix property degradation, the building up of residual intralaminar stresses due to expansion and swelling, and changes in fracture toughness and ductility. The presence of moisture may also result in a decrease in glass transition temperature. Under load, visco-elastic effects (e.g. creep, relaxation) may also become important. The extent to which any of these effects are realized may vary significantly between composite material systems, even those of the same general type (e.g. carbon/epoxy). However, the literature available [e.g. 93-96] provides some insight as to what one may expect to find and the various ways in which the effects of temperature and moisture manifest themselves. Such literature limited to carbon fibre composites is investigated in more detail below.

3.5.1. Influence of Moisture Absorption

Moisture absorption characteristics comprise an important aspect of moisture/durability studies. Such information can generally be used to obtain some insight into how and why the material is influenced by moisture. For instance, in Fig. 17, Curves A to D represents four typical, reversible, moisture absorption behaviour. Curve C is indicative of significant interfacial degradation, Curve D is indicative of material leaching, and curve LF is classical Fickian moisture absorption [95].

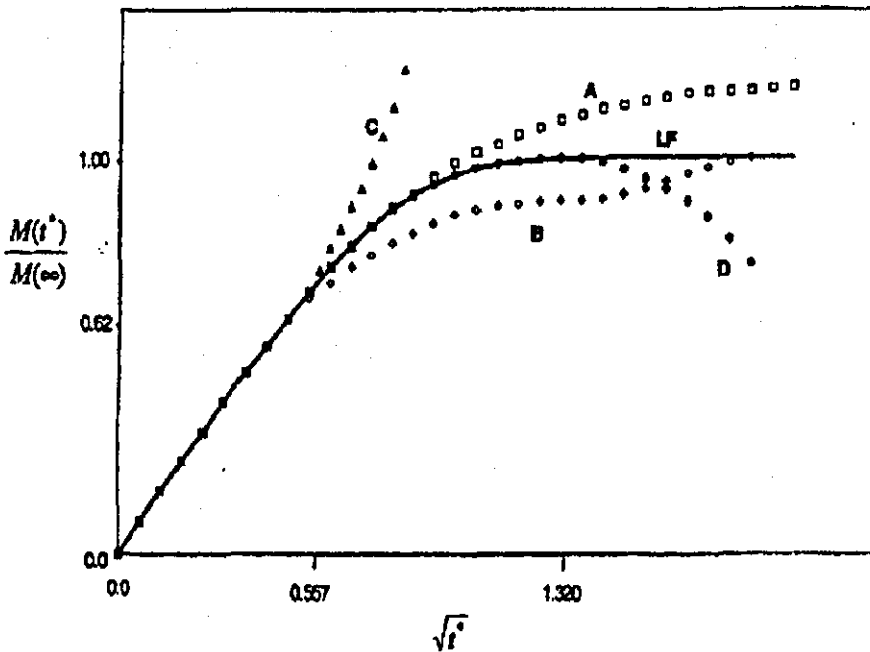


Fig. 17: Potential Moisture Absorption Curves [93]

Such characteristic features of moisture absorption are dependent on the composite system, fluid, exposure condition and time. Fluid absorption that follows along curve A or curve B is typically thought to occur as a result of the competing rate processes of water diffusion and polymer relaxation [96]. Such absorption behaviour may also be a result of the combination of two distinct absorption mechanisms which result in two physical states – bound water and free water [97-98].

External factors can also influence composite moisture absorption. Wong and Broutman [99] showed applied tensile stress increases equilibrium water content while the diffusion mechanism remains unaltered. Damage due to applied stress and/or moisture diffusion and temperature also plays a major role in composite absorption behaviour. Some studies have reported increased diffusion rate but unchanged saturation concentration [100], while others reported unchanged diffusion rate but increased saturation concentration [101]. Roy et al. [102] developed a damage mechanics based model to predict moisture absorption behaviour as a function of transverse and longitudinal cracking.

Other factors that influence diffusion and/or saturation concentration are temperature, fluid acidity, and exposure duration [95]. Rao et al. [103] suggested that angle of fibre orientation to the diffusion direction also has significant effect on the diffusion coefficient. They found that diffusion gets impeded as the fibre orientation to the diffusion path increased.

All these factors become important in considering a composite's durability in immersed conditions. The general theory of diffusion is described in the following section.

3.5.2 Theory of Diffusion

Fluid diffusion into solid materials involves the displacement of the fluid molecules from regions of high concentration to regions of lower concentration [104]. For steady-state one-dimensional diffusion, Fick's law applies [105]:

$$q_x = -D_x \frac{\partial c}{\partial x} \quad (i)$$

Where, q_x is the flux of the material in question in direction x , D_x the diffusion coefficient and $\partial c/\partial x$ the rate of change of the concentration of the diffusing material.

If the flux of the diffusing material varies with diffusion length, the liquid accumulates in the material and the concentration at each point varies with time. For transient three-dimensional diffusion, Fick's second law applies [106]:

$$\frac{\partial c}{\partial t} = \frac{\partial}{\partial x} \left(D_x \frac{\partial c}{\partial x} \right) + \frac{\partial}{\partial y} \left(D_y \frac{\partial c}{\partial y} \right) + \frac{\partial}{\partial z} \left(D_z \frac{\partial c}{\partial z} \right) \quad (ii)$$

Where, the coefficient of diffusion D_x is related to the temperature by the Arrhenius equation (in the same way as the kinetic reaction constant):

$$D = A e^{-\frac{E_a}{RT}} \quad (iii)$$

Where E_a is the activation energy required before diffusion could occur, A is the frequency factor, R is the gas constant and T is the absolute temperature.

The maximum moisture content M_m is practically a constant when the material is immersed in a liquid, and is a maximum when the liquid is immersed in distilled water. In humid air, M_m depends on the relative humidity Φ as follows [107]:

$$M_m = a(\phi)^b \quad (\text{iv})$$

Where, a and b are experimental constants which vary with the material.

The moisture distribution within a laminate can be calculated by analytical or numerical methods, assuming that diffusion depends only on concentration, and that the coefficient of mass diffusion depends only on temperature (and not on moisture content or stress level) [108]. If these assumptions hold the diffusion coefficient can be expressed as a function of temperature by the Arrhenius equation:

$$D = D_0 e^{-\frac{A}{T}} \quad (\text{v})$$

Where, D_0 and A are constants of the material.

The diffusion coefficient will also vary with direction if the material is orthotropic, and the coefficients parallel and perpendicular to the fibres can be expressed as a function of the matrix and fibre coefficients [107]:

$$D_0 = (1 - \nu_f) D_m + \nu_f D_f \quad (\text{vi})$$

and

$$D_{\perp} = \left(1 - \sqrt{\frac{\nu_f}{\pi}} \right) D_m + \left[\pi - \frac{4}{\sqrt{1 - B^*}} \arctan \left(\frac{\sqrt{1 - B^*}}{1 + \sqrt{B^*}} \right) \right] \frac{D_m}{B} \quad (\text{vii})$$

Where,

$$B^* = \frac{4 \left(\frac{D_m}{D_f} - 1 \right)^2 v_f}{\pi} \quad (\text{viii})$$

v_f is the fraction of the volume occupied by the fibres and the subscripts 'f' and 'm' refer to the fibres and the matrix, respectively. In general, the coefficient of diffusion of the fibres is negligible compared to that of matrix and the above formulae can be simplified.

Experimental Determination:

The diffusion coefficient D and the maximum moisture content M_m can be determined experimentally [107]. For experimental determination of one-dimensional diffusion, the specimen must first be oven dried, till there is no more weight loss. Weighing the dry sample will give the unconditioned weight W_{dry} . This is followed by wet-conditioning. During this process the weight is determined periodically and the moisture content reported as a function of the square root of the time. The curve will tend to the value M_m asymptotically if Fick's law is being obeyed. The initial part of the curve has a constant slope:

$$\frac{dM}{d\sqrt{t}} = \frac{4M_m}{h\sqrt{t}} \sqrt{D} \quad (\text{ix})$$

Implying:

$$D = \pi \left(\frac{h}{4M_m} \right)^2 \left[\frac{M(t_2) - M(t_1)}{\sqrt{t_2} - \sqrt{t_1}} \right]^2 \quad (\text{x})$$

Thus, once the moisture content at times t_1 , t_2 and saturation have been determined the diffusion coefficient can be calculated.

3.5.3 Influence of Moisture on Static Strength/Stiffness

The mechanical response of CFRP laminates subjected to moisture absorption is largely determined by the matrix and the interfacial properties since carbon fibres are insensitive to moisture (as opposed to glass fibres which are known to degrade in the presence of moisture [95]). The known possible effects of moisture include the formation of residual stresses due to sorption (generally compressive) [109-110], polymer and interfacial degradation, and polymer plasticization. Combined, these effects can act to enhance or degrade the fracture toughness of the material. Moreover, the plasticization can result in a decreased glass transition temperature [111] which may affect how the composite behaves in elevated temperature environments after ageing.

Interlaminar shear strength degradation has been reported for carbon/epoxy systems by Zhang and Mason [112]. Bradley and Grant [113] found that for a graphite/epoxy system, the reduction in transverse strength due to water saturation is similar to the observed change in interfacial shear strength. The interfacial strength was measured using a micro-indentation technique. The authors consequently hypothesized that for their graphite/epoxy material system, the degradation of the composite system was primarily interfacial in nature rather than due to changes in the matrix.

Zhuang and Wightman [114] studied the effect of moisture on interfacial shear strength using single fibre fragmentation testing. Samples were stored in a 100% relative humidity environment at either 23°C or 75°C prior to testing. Their results indicate that exposure to humidity does cause interfacial shear strength reduction, which they attributed to moisture induced matrix plasticization and subsequent decrease in matrix T_g . The reduction, however, was shown insensitive to aging temperature, which is debatable. They conducted a parallel study, to distinguish between the effect of temperature and humidity, by aging the specimens at the same temperature in dry condition and found no reduction in interfacial strength.

3.5.4 The Influence of Temperature

The potential effects of temperature are very similar to the effects of moisture. Carbon fibres tend to be unaffected up to temperatures of 600°C. Therefore, in CFRP, the effects of temperature are dependent on changes in the matrix and interfacial regions.

Takeda and Ogihara [115] studied the microscopic failure processes of two graphite/epoxy crossply composite laminates at room temperature and at 80°C. One of the systems consisted of a toughened epoxy while the other consisted of a conventional epoxy. Experimentally, they found that in the toughened epoxy composite system the crack density decreased with temperature, while the first delamination onset strain increased with temperature. However, the amount of delamination decreased with temperature. The amount and rate of delamination also increased with thicker 90° layers. From SEM images of failure surfaces they found that little or no additional interfacial debonding took place at elevated temperature compared to the room temperature. They found completely opposite behaviour shown by the conventional epoxy composite system.

Detassis et al. [116] used fragmentation testing on single-fibre model composites to study the interfacial shear strength of carbon/epoxy composites as a function of temperature. The study considered both sized and de-sized fibres (Besfight HTA-7-3000), and the epoxy had a low T_g specification ($T_g = 39^\circ\text{C}$). While interfacial shear strength values were found to decrease with temperature in single fibre composites, sized and de-sized, the values of the sized single-fibre composites were generally much higher than that of the de-sized single fibre. Moreover, in the desized single fibre composite interfacial shear strength values were very similar to matrix shear strength values. The higher interfacial strength values for the sized single fibre composites were hypothesized to be as a result of superior interphase (region where properties of fibre, interface, and matrix combine) properties as compared to the bulk matrix. A similar study by Wimolkiatisak and Bell [117] showed similar results.

Zhuang and Wightman [114] also studied the effect of temperature on interfacial shear strength in carbon epoxy composites using single fibre fragmentation

testing. In considering the effect of temperatures below T_g (144°C in this case), the interfacial shear strengths of three different types of fibres in epoxy were found to decrease with temperature. It was suggested that an explanation for this was the interphase region exhibits a lower T_g and modulus than the bulk matrix, and that a sharp decrease in interfacial shear strength, seen around 80°C, coincided with the degradation of this interphase region. This hypothesis is somewhat in contrast to that put forth by Detassis et al. [116].

Im et al. [118] used Carbon-Epoxy orthotropic laminated plates with two-interfaces $[0_6/90_6]_s$ and $[0_4/90_4]_s$ for their experiments in the temperature range of -30° to 120°C. They found that as the temperature of a CFRP laminate increased, the delamination area due to high velocity impact-induced damage decreased linearly. Furthermore, they found that the critical delamination energy increased as the temperature increased. They concluded that delamination is generated easily as the energy required to cause damage reduces as the temperature decreases. Another observation they made was that the thicker laminates were less susceptible to impact damage in the temperature range they used.

3.5.5 Moisture and Temperature Interaction

The work done to date in examining the effect of the combination of moisture and temperature on the durability and damage of carbon fibre polymer matrix composites has been limited. Potter and Purslow [119] and Purslow [120] investigated compression strength behaviour of notched $[\pm 45^\circ/0^\circ]_{ns}$ Carbon fibre-epoxy composites under various environmental conditions. They found that under hot-wet conditions the samples failed by out-of-plane micro-buckling of the 0° ply. This was said to be because the elevated temperature and increased moisture content reduced the fibre-matrix bond strength. Any weakening in the fibre-matrix interface resulted in less lateral support for the fibres and a premature failure of the laminates due to out-of-plane buckling.

Karasek et al. [121-122] performed a study on the influence of moisture and temperature on the impact resistance of graphite/epoxy composites. They found that damage initiation energy decreased with temperature due to reduced matrix

properties with temperature. They also found that moisture individually had no effect on damage initiation energy or subsequent energy absorption at ambient temperatures. However, the influence of moisture at elevated temperatures was significant and was thought to depend on the matrix behaviour and wet glass transition temperature of the matrix. Their results also showed that the damage initiation energy of a composite made from unmodified epoxy increased with moisture at elevated temperature, while toughened epoxy showed inverse characteristics.

In examining the nature of the damage, the authors found that moisture exposure in general does result in a decrease in the number of delaminations and matrix cracks after impact, indicating that the energy absorption per unit area of damage is higher in the wet state than in the dry state. This result is consistent with the idea that the strain energy release rate increases with moisture. On the other hand, they also found that the number of delaminations and matrix cracks increased with temperature (when dry), which again is consistent with a reduction in strain energy release rate with temperature. When they considered thermohumid effect at elevated temperature, they found that the number of delaminations and matrix cracks decreased. These changes in behaviour were generally attributed to plasticization and increased ductility in the matrix, as well as degradation of properties.

Harper and Abd Aziz [123] investigated the thermohumid effect on the compression after impact (CAI) properties of glass, carbon and hybrid fibre reinforced laminates. They exposed the impacted samples to thermohumid conditions of 60°C and 95% relative humidity for periods up to eighty days, but found very small reduction in CAI strength. They attributed this effect to short exposure time.

Imielińska et al. [124] worked on epoxy glass-aramid hybrid composites, which they aged first then impacted. They found that the impact damage area was slightly less extensive in wet samples and suggested it to be the result of the propagation of interfacial damage present in wet samples prior to impact, that absorbed impact energy and inhibited the delamination formation.

A number of studies have been performed to determine how hygrothermal environments affect the strain energy release rates of carbon/epoxy composites. A review of these is given by Asp [125]. The combined results of the studies point to an ambiguity as to the effects of moisture and temperature on strain energy release rates, implying that each carbon/epoxy system must be examined individually.

CHAPTER 4

EXPERIMENTAL

4.1 MATERIALS

4.1.1 Reinforcements

Three different carbon MWK fabrics with different stitch architectures were produced by Formax Ltd. according to the specification given to them. All the preforms used were quadaxial (4 ply orientations) made from Toray's T700SC carbon fibres. The fibres were sized (by the manufacturer) to make them compatible with epoxy resin. The properties of the fibres are listed in Table 3.

Designation	Number of Filaments	Tensile Strength (MPa)	Tensile Modulus (Gpa)	Elongation (%)	Mass per Unit Length tex(g/1000m)	Density (g/cm ³)
T700SC – 12K	12000	4900	230	2.1	800	1.8

Table 3: Properties of T700SC- 12K [126]

Tricot stitching was used to produce the MWK. Both the 'A' (0/-45/90/+45) and the 'B' (0/+45/90/-45) hands were produced to ensure that no warping occurred during laminate manufacturing. The stitch architecture in MWK has two variables: stitch pitch and gauge [127], which is illustrated in Fig. 18. 'Stitch Gauge' refers to the number of stitches per unit length in the weft direction (across the width of the fabric) and the 'Stitch Pitch' is the number of stitches per unit length in the warp direction (along the length of the fabric).

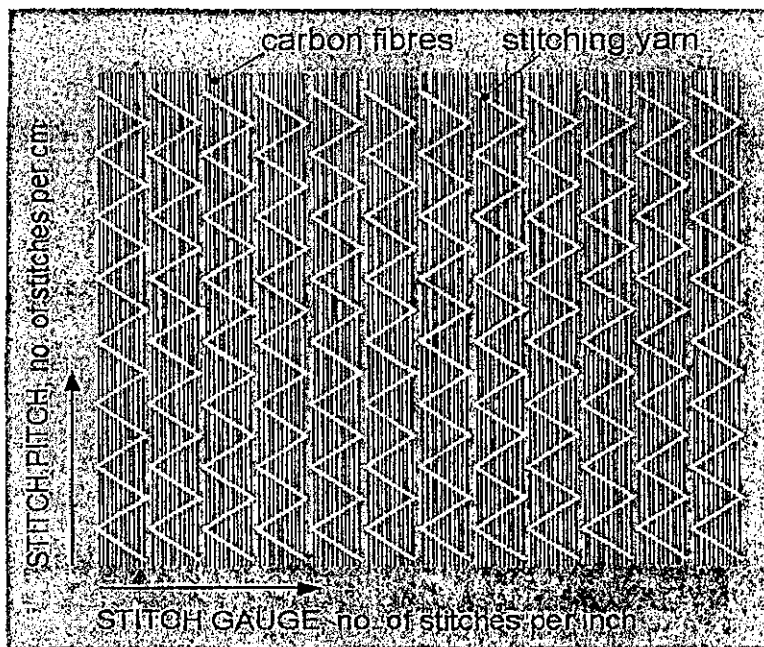


Fig. 18: Schematic of Stitching in MWK

The basic differences between the stitch architectures used are listed in Table 4, in the following page.

4.1.2 Matrix Material

The resin film selected was a modified epoxy resin film MTM 44, produced by the Advanced Composites Group. The interest in this particular resin film was based on the fact that it was used in the CASCADE project run by QinetiQ and the fact that the long term performance of this resin had to be investigated.

MTM 44 is a high performance 180°C cure, 340g/m², epoxy matrix specially developed for the aerospace and industrial markets. The isothermal viscosity profile, dynamic viscosity profile and the gelation properties as provided by the Advanced Composites Group are presented in Figs. 19, 20 and Table 5 respectively [128]. The viscosity data were recorded using a Bohlin CVO-50 rheometer, using parallel 25mm diameter plates, in the oscillation mode. The temperature ramp rate was 2°C/min for the dynamic viscosity profile. The isothermal viscosity profile provides information on the heat of reaction at a particular temperature, while the dynamic viscosity profile shows the extent of reaction, i.e., degree of cure as a function of time at a particular heating rate.

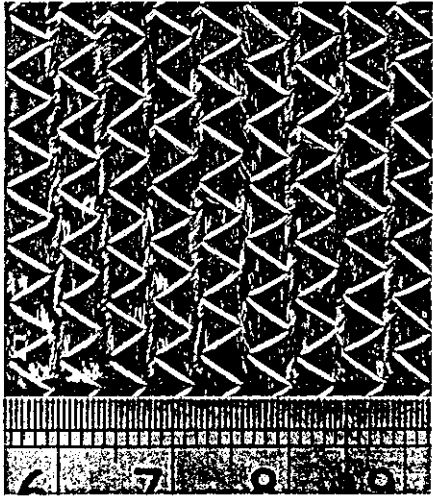
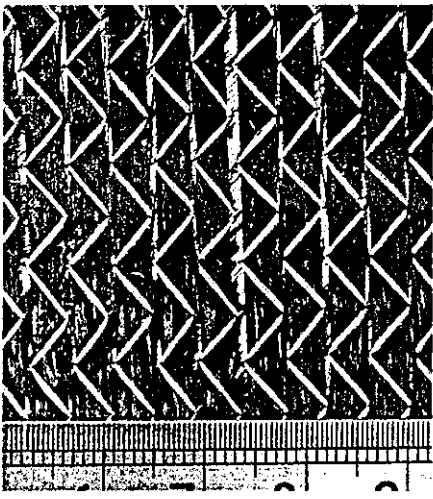
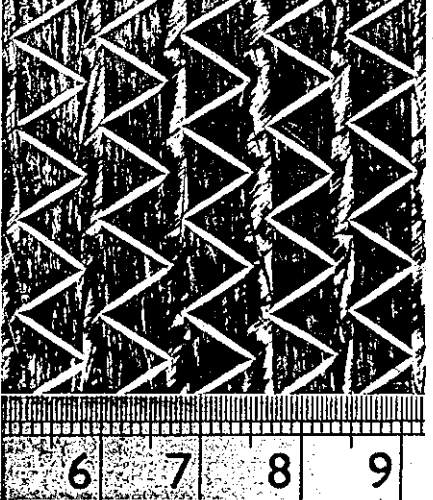
Fabric No.	Fabric Appearance	Fabric Designation	Fabric Characteristics
Fabric 1		S [6gg@4cpcm]*	Fabric with standard stitch pitch and stitch gauge (465 linear stitch metres/ metre ²)
Fabric 2		M [6gg@2cpcm]	Half stitch pitch density and standard stitch gauge (310 linear stitch metres/ metre ²) 67% of std.
Fabric 3		L [3gg@2cpcm]	Half stitch pitch and stitch gauge density (232 linear stitch metres/ metre ²) 50% of std.

Table 4: Fabrics Used

Where gg = stitch gauge, cpcm = courses per cm (i.e. stitch/ cm).

* In the case of '6gg@4cpcm' the fabric has 6 stitches per inch (2.54 cm) in the weft and 4 stitches per cm in the warp direction. The length of the stitch is therefore 2.5mm.

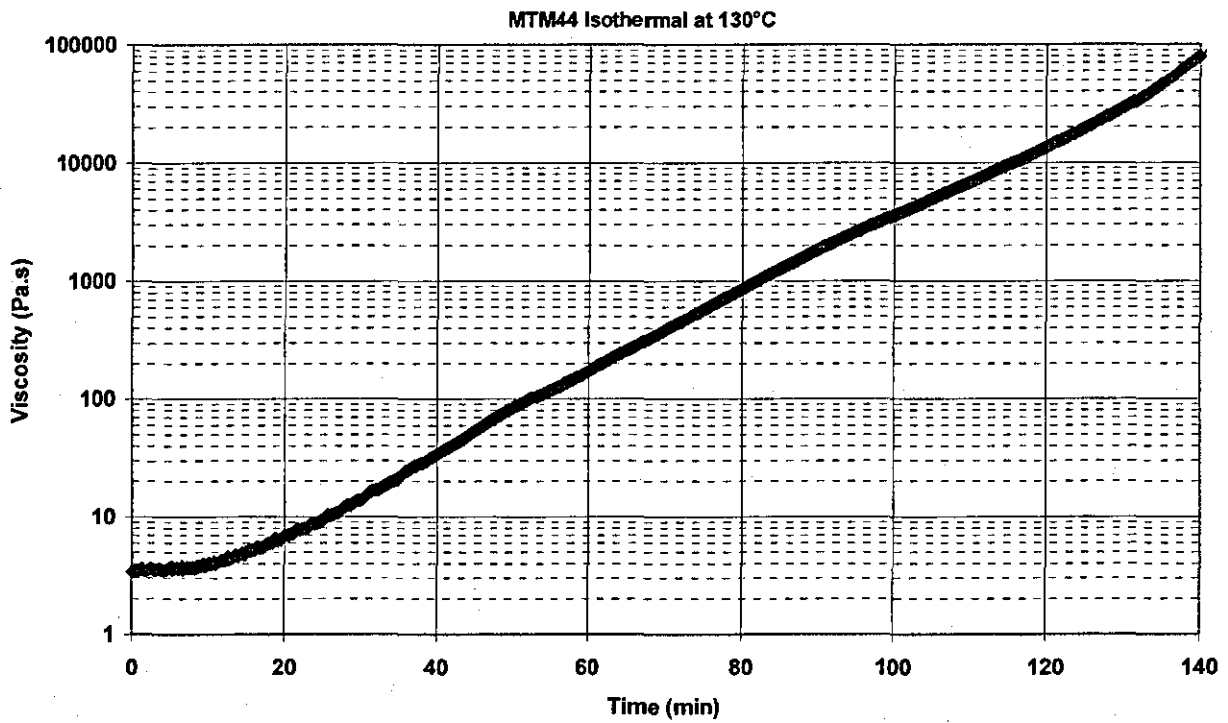


Fig. 19: Isothermal Viscosity Profile of MTM 44

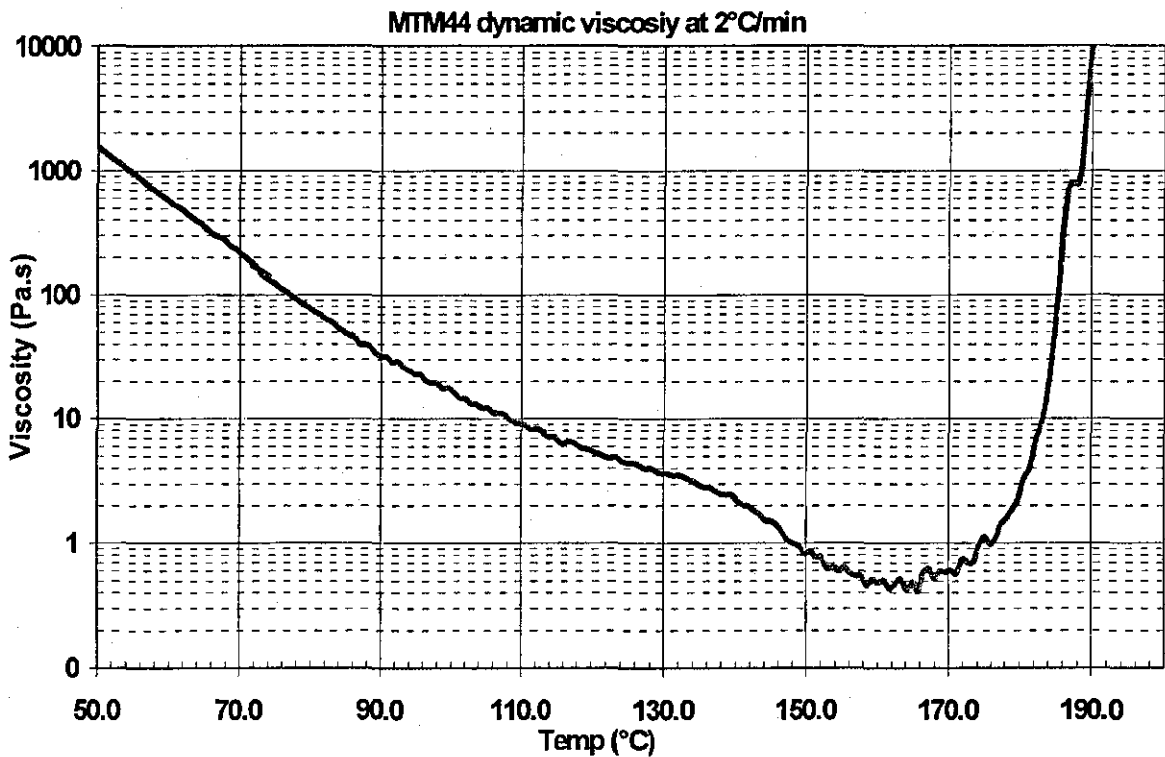


Fig. 20: Dynamic Viscosity Profile of MTM 44

The gelation data was measured using a pin-pricking method, where the resin film is put on a heated plate and a pin is pricked manually at some time interval to find out the gel time. The data for the gel time for the corresponding temperatures are listed in Table 5.

Curing Temperature (°C)	Gel Time (min.)
130	110
150	50
180	25

Table 5: Resin Gelation Characteristics of MTM 44

4.2 LAMINATE MANUFACTURE

The laminates were manufactured by stacking MWK fabrics with resin films (interspersed) and using a Resin Film Infusion (RFI) process. There are two traditional lay-up methods (Fig. 21) for the dry fabrics and the resin films in RFI: one is the 'block method' where the dry fabrics and all the resin films are laid separately in blocks, while the second is the 'interspersed (interleaved or semi-preg) method' [57] where resin films are interspersed between the dry fabrics.

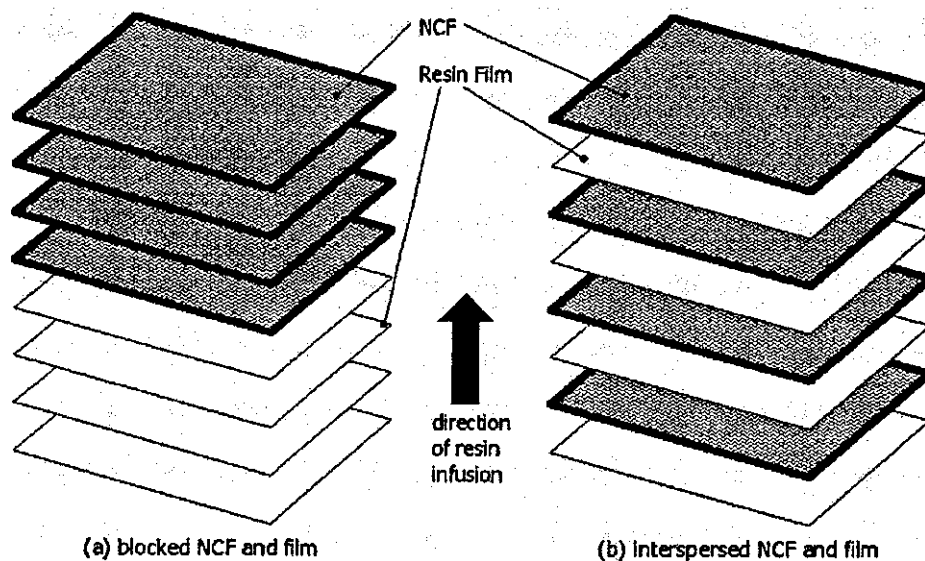


Fig. 21: Traditional Lay-up Methods [129]

It has been found [129] that for thin laminates (up to 4 mm) the block method could yield good quality laminates, however, for thicker laminates, for better resin migration, the interspersed method should be used.

The frozen resin film, supported on a backing paper, was supplied on a roll. Typical thaw time for a full 25m roll of MTM44 from storage at -18°C (0°F) was between 4 to 6 hours [51]. After the initial thawing of the roll, small pieces of resin film were cut into suitable length and were refrozen (not a recommended practice but used because of shortage of space). Before lay-up, the required number of pieces were removed from the freezer and allowed to thaw for ten minutes. Thawing is very important as the presence of moisture (as a result of condensation) within a curing laminate may generate voids and thereby degrade the quality and aesthetic appearance of the structure produced. The level of degradation varies depending, to a large extent, on the specific processing route selected [51].

The fabrics were cut, by a sharp CSM wheel cutter, into the required size. The thawed resin film was then laid on the face of the fabrics. One end of the film was put on the fabric first, held down, and then the rest of the film was rolled on to the fabric as shown in the Fig. 22. This procedure reduced the possibility of air getting entrapped between the resin and the fabric.

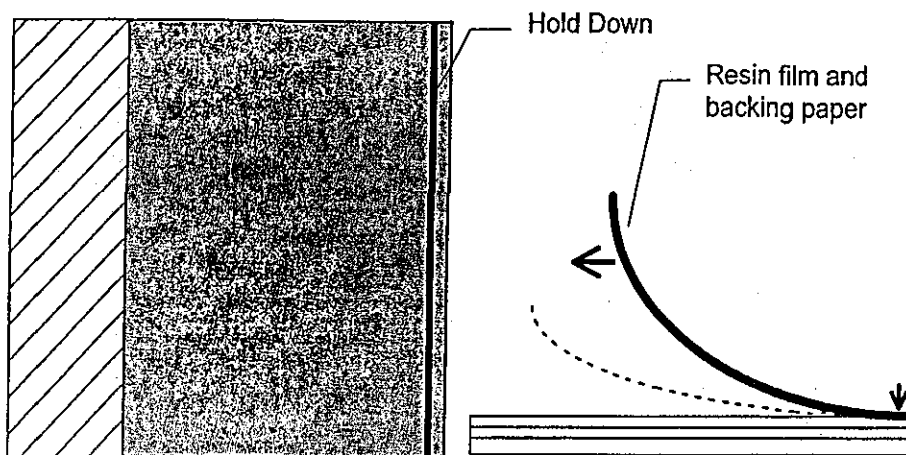


Fig. 22: Application of Resin Film to the Fabric [130]

The lay-up sequence used to produce laminates for this project is shown in Fig. 23. It consisted of 5 resin layers interleaved between 4 MWK fabrics so as to

yield volume fractions of approximately 55%. The right-hand column of the Fig. 23 shows the exact orientations of the fibres.

Resin	
Left Handed (A) Fabric	+45°
	90°
	-45°
	0°
Resin	
Left Handed (A) Fabric	+45°
	90°
	-45°
	0°
Resin	
Right Handed (B) Fabric	0°
	-45°
	90°
	+45°
Resin	
Right Handed (B) Fabric	0°
	-45°
	90°
	+45°
Resin	

Fig. 23: Laminate Stacking Sequence

The Advanced Composites Group Ltd. suggested an autoclave cure cycle [51], which consisted of a two stage curing process: an initial curing at 130°C for 3hrs followed by a post-curing at 180°C for 2hrs. They also suggested an alternative single stage curing [51] at 180°C for 2hrs.

However, Rudd et al. [43] suggested the possible use of compression moulding. Initially this approach was followed, with a positive mould, to cure the resin. Trials were carried out with the two curing cycles mentioned above. Although compression moulding achieved high volume fraction of 65%, it was accompanied by high void fractions (up to 13%) and crimping of the reinforcements [appendix].

Therefore, a modified envelop bagging was finally adopted (Fig. 24), with a modified two stage curing process (Fig. 25), in order to achieve the desired and reproducible quality.

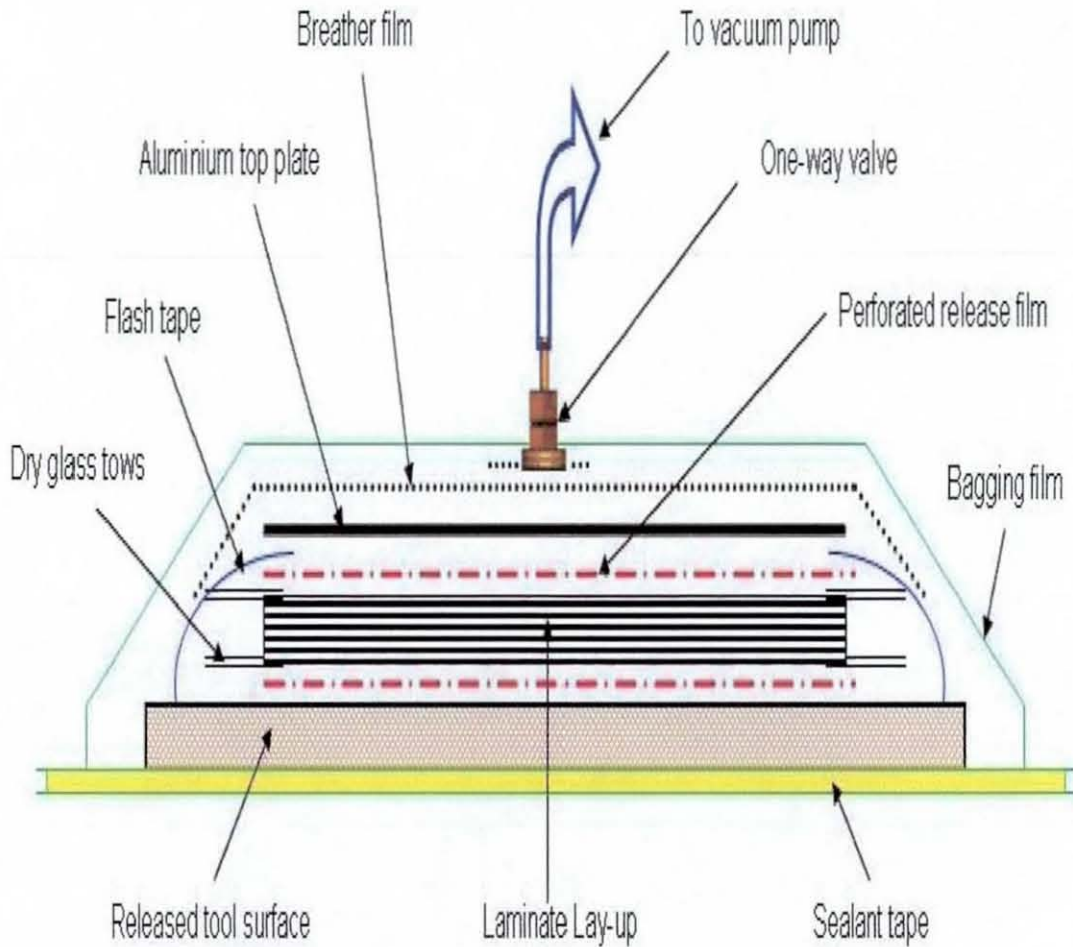


Fig. 24: Modified Envelop Bagging Arrangement

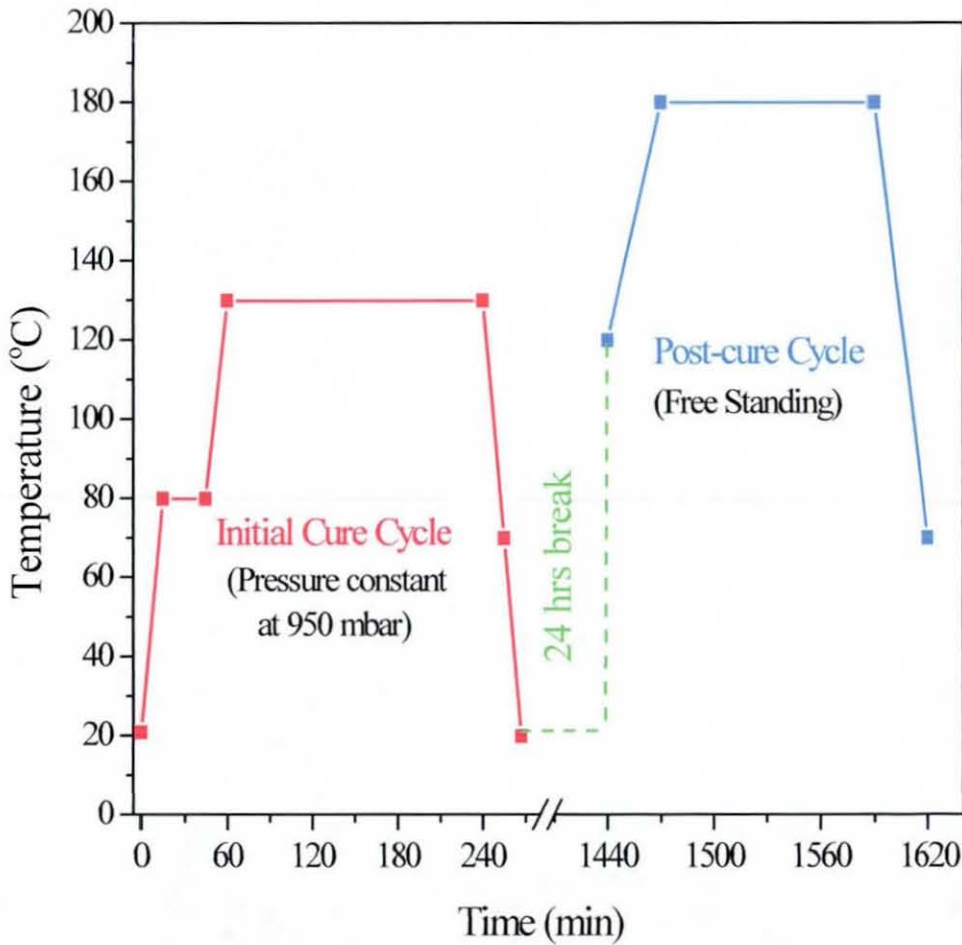


Fig. 25: Modified Laminate Cure Cycle

After the initial optimization process, a total of forty-five laminates were produced, i.e. fifteen laminates per stitch architecture type. All these laminates were subjected to quality control checking: visual checks for surface quality and c-scanning for internal defects. Thirty-nine of them passed the quality standards, of which twenty-four (eight/ stitch type) were used exclusively for damage tolerance testing. The rest were used for other characterization purposes.

4.2.1 Examination of Cured Laminates

All the cured laminates were routinely subjected to a non-destructive C-Scan, prior to any further testing. A typical C-Scan is shown in Fig. 26. Any laminate containing flaws or defects was rejected. Acceptable laminates were cut through the middle with a dry diamond tipped circular saw. Two small samples from the centre were then polished on 600 and 1200 grit silicon carbide paper and examined for voids using an optical microscope (Fig. 27).

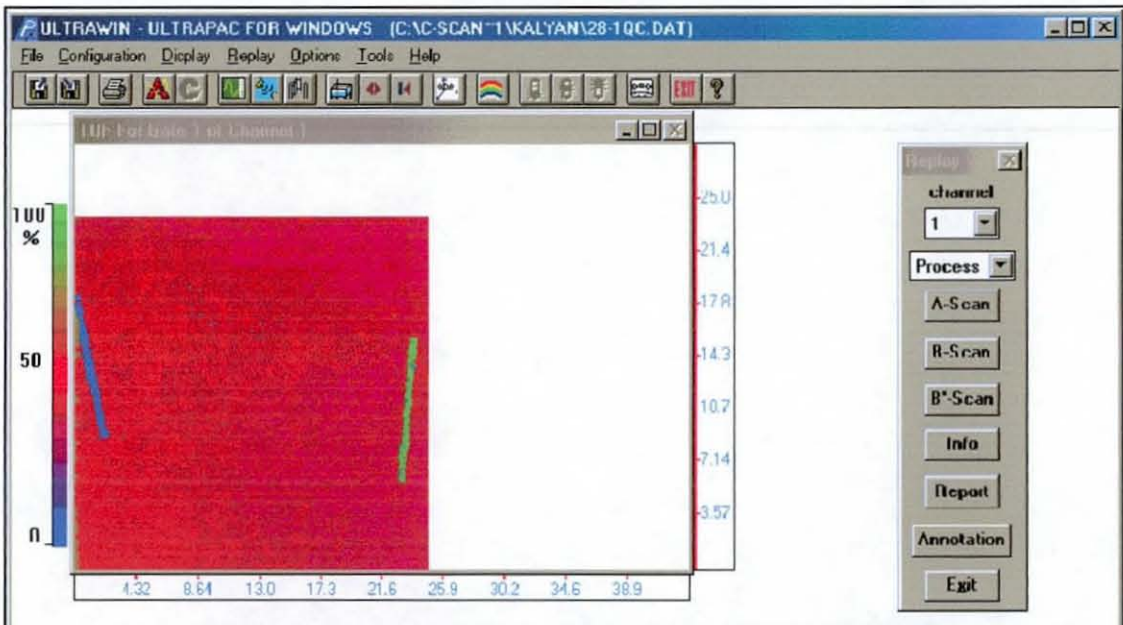


Fig. 26: Typical C-Scan of a Good Quality Laminate

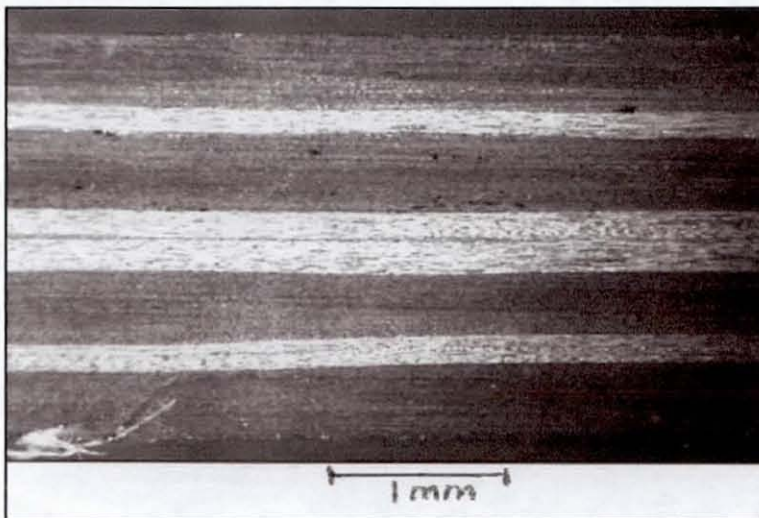


Fig. 27: Polished C.S. Viewed under Optical Microscope

4.3 PHYSICAL PROPERTY TESTING

4.3.1 Density Measurement

The density measurement was carried out according to ASTM D792-00 [131] by the displacement method based on Archimedes' principle. The samples were first conditioned at room temperature then were degreased with acetone. All the samples were weighed in air to an accuracy of 0.1mg. Each specimen was then suspended from the balance by a string, immersed completely in water and weighed. Care was taken, so that no bubble adhered to the string or the specimen. The measurement was taken quickly in order to minimize any absorption of water by the specimen and the string. Also the same length of string was used so that the depth remained constant for all the immersed specimens. The density of the composite was calculated as:

$$D_c = \frac{A}{A - B} \times 0.9975$$

Where,

D_c = Density of Composite (g/cm³)

A = Weight of specimen in air (g)

B = Apparent weight of specimen completely immersed in water (g)

Density of water = 0.9975 g/cm³.

4.3.2 Determination of Fibre Volume Fraction

There are several recommended methods for the determination of fibre volume fraction. CRAG standard test methods [132] give a range of methods without preference. However, thickness measurement and resin removal (acid digestion) are widely used. The former method gives an estimation of the fibre volume fraction and therefore, is not suitable for void content calculations.

All the cured laminates were conditioned at room temperature and a quick estimation of the fibre volume fractions was obtained from the thickness of the composites using the following equation. Ten measurements were taken with a

micrometer from a 5 cm² area and then an average was calculated and used as the thickness of the composite.

$$V_f = \frac{N \times M_f}{t \times \rho_f}$$

Where,

V_f = Fibre volume Fraction

N = Number of fabric plies in the laminate

M_f = Blanket fibre weight (g/m²)

t = Cured laminate thickness (m)

ρ_f = Fibre density (1.80×10^6 g/m³)

The acid digestion method was also carried out on a sample of each of the laminates. These results were subsequently used to determine the corresponding void content. The procedure [132] was carried out in three stages.

Firstly, the test sample of 1 cm² size was placed in a tall beaker containing 20ml of conc. sulphuric acid. The beaker was then heated on a hot plate, inside a fume cupboard, till the acid fumes evolved. In order to make sure that the oxidation process was complete, the mixture was stirred slowly with a glass rod to check whether all the fibres were dispersed in the acid solution. The beaker was then removed from the heat and 30ml (100 volume) of hydrogen peroxide was added dropwise down the side of the beaker. Recommended safety procedures were carried out while handling the chemicals. The solution was then left for 10 minutes to allow the reaction to complete. Additional peroxide was then added to make the solution colourless, which indicates the completion of the decomposition of the resin.

The second step involved filtering the fibres from the solution. The content of the beaker was filtered through a sintered glass crucible (no. 3 porosity) into a flask, connected to an air suction system. The beaker was rinsed with deionised water and the content was also filtered to collect all the fibres. More deionised water was then poured through the glass crucible to make sure that the filtered fibres were washed thoroughly.

Thirdly, the crucible was dried in a vacuum oven at 120° C for 3 hours and then cooled in a desiccator. The dried fibre weight was then calculated using the following formula:

$$\text{Dried fibre weight} = (\text{Weight of fibre} + \text{glass crucible}) - (\text{weight of glass crucible})$$

The fibre volume fraction was calculated using the formula:

$$V_f = \frac{W_f \times \rho_c}{W_c \times \rho_f}$$

Where,

W_f = Weight of dry fibre (g)

W_c = Weight of composite before acid digestion (g)

ρ_f = Fibre density (1.80×10^6 g/m³)

ρ_c = Composite density measured by the displacement method (g/m³)

4.3.3 Determination of Void Content

The void contents of the specimens were determined according to ASTM D2734-94 [133], assuming the density of the resin to be the same in the composite as it is in a large cast mass. This assumption overestimates the value of resin density, as the curing and the reorientation of the resin molecules actually reduce the resin density in the composite. Void content is therefore underestimated.

The void content was calculated as:

$$V_p = 100 - D_c \left(\frac{r}{D_r} + \frac{f}{D_f} \right)$$

Where,

V_P = Void content % (in volume)

D_C = Measured composite density (g/cm^3)

D_r = Resin density (g/cm^3)

D_f = Fibre density (g/cm^3)

r = weight percentage of resin (%)

f = weight percentage of fibre (%)

4.4 STATIC MECHANICAL TESTING

4.4.1 Interlaminar Shear Strength

ILSS is not particularly suitable for comparing materials of different lay-ups, as the resulting strength depends on the local fibre architecture at the ply interface and can not reasonably be considered to be a true material property. Since in this research materials of the same fibre and resin type, lay-up and nominal fibre volume fraction are considered, the difference in shear strength will be due to differences in fibre architecture. Samples were tested according to the CRAG test protocol [132].

The thickness of each laminate was measured at five points along its length. The width of the sample was set to five times the mean thickness calculated. The length was set to (width + 10) mm. The span between the rollers was set to five times the thickness, for each of the three types of laminate, using a vernier calliper. The laminates were tested at room temperature (21°C) on a 50 kN Lloyds L10000 hydraulic test machine with a 2.5 kN load cell. Samples were loaded at 5 mm/min in displacement control with the controller set to record the peak load for each sample. This speed was selected in accordance with the CRAG standard, which requires samples to fail between 15-45 seconds. The support and loading roller diameters were 6mm and 10mm respectively (Fig. 28). Five samples were tested for each reinforcement type.

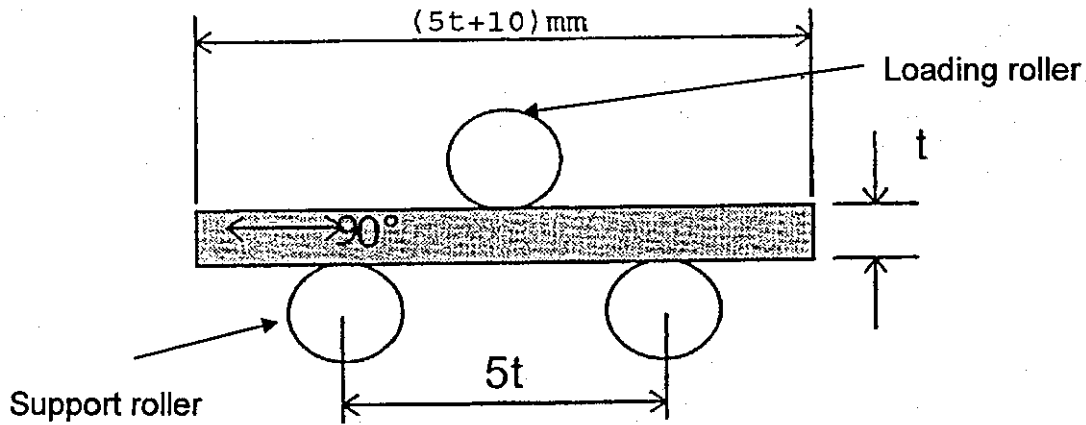


Fig. 28: Interlaminar Shear Strength Test Arrangement

The ILSS was calculated using:

$$ILSS = \frac{3P_{\max}}{4Wt} \quad (\text{MN/m}^2)$$

Where,

P_{\max} = Maximum Load (N)

W = Specimen width (mm)

t = Specimen thickness (mm)

4.5 DAMAGE TOLERANCE TESTING AND ASSESSMENT

4.5.1 Instrumented Low Energy Impact

Impact tests were performed using an Instrumented Falling Weight Impact (IFWI) Tester, Rosand (Model 5). The machine is capable of using variable mass and geometry impactors and has a second-strike prevention facility for non-penetration energy impacts. The impact carriage unit works under gravity (Fig. 29) and falls, along guiding rods, onto the specimen.

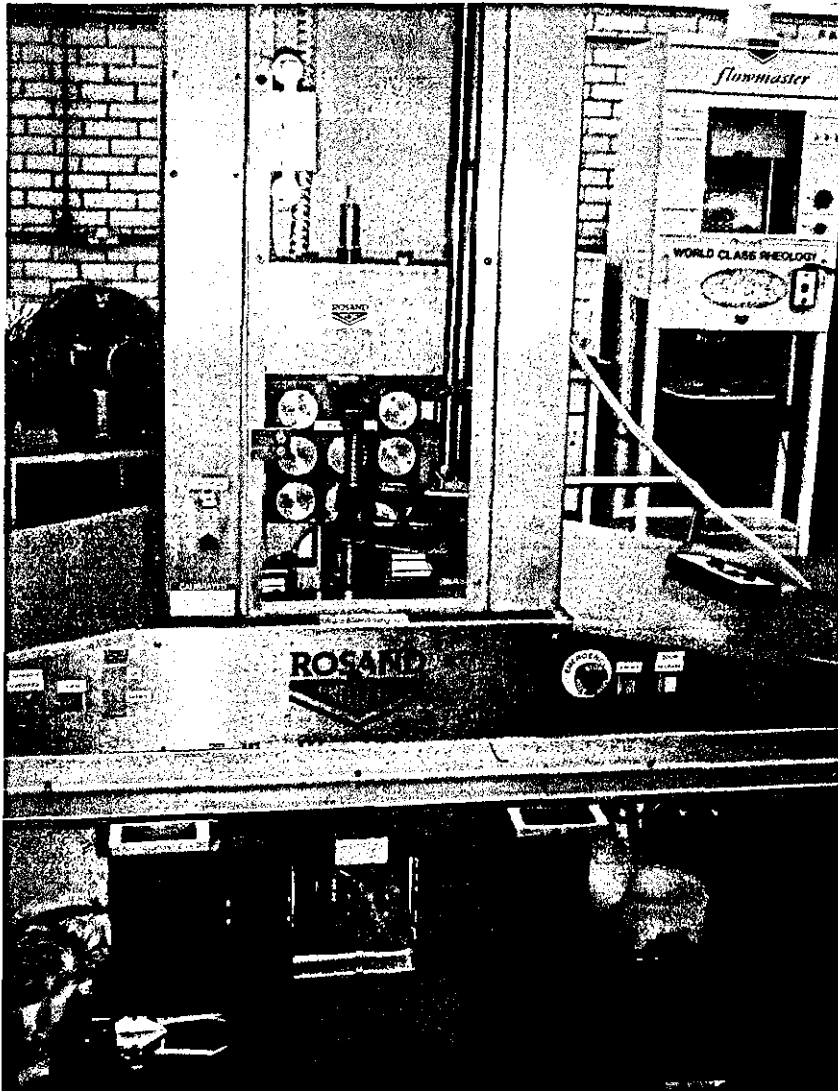


Fig. 29: IFWI Testing Unit

A Kistler piezo-electric load cell, which was logged at a 20ms sweep time, recorded the impact force during the event. This information was then automatically converted by the software to acceleration, velocity and displacement data, as described in the literature review. The initial impact velocity was recorded by an optical actuation switch, which was 'zeroed' according to the thickness of the sample before impact. The optical actuation switch was activated by a 'flag' which was attached to the impactor carriage. 'Zero' position was defined manually by lowering the impactor while it just touched the impact sample. The same system was also used to trigger the load cell data capture [134].

The IFWI testing unit had two different impact carriage units and for this work a variable 10.3 kg impact carriage unit was used. This unit itself had a mass of 2.3 kg, plus a provision of attaching eight 1 kg floating masses. The pneumatic second-strike prevention unit was able to catch this impactor unit.

Pneumatic clamping and simple support units were available on the Rosand. The clamping unit had a smooth and an emery paper-backed face. The impact sample rested on a conventional anvil, while the clamping unit secured the sample from the top. After the impact test, the impactor unit was automatically lifted by an electrically powered winch.

The layout in Fig. 30 shows the locations of the test specimens. Samples were cut using a dry diamond tipped circular saw and were then polished on a vertically mounted automatic finisher (abrasive band machine) with 600 grit silicon carbide paper.

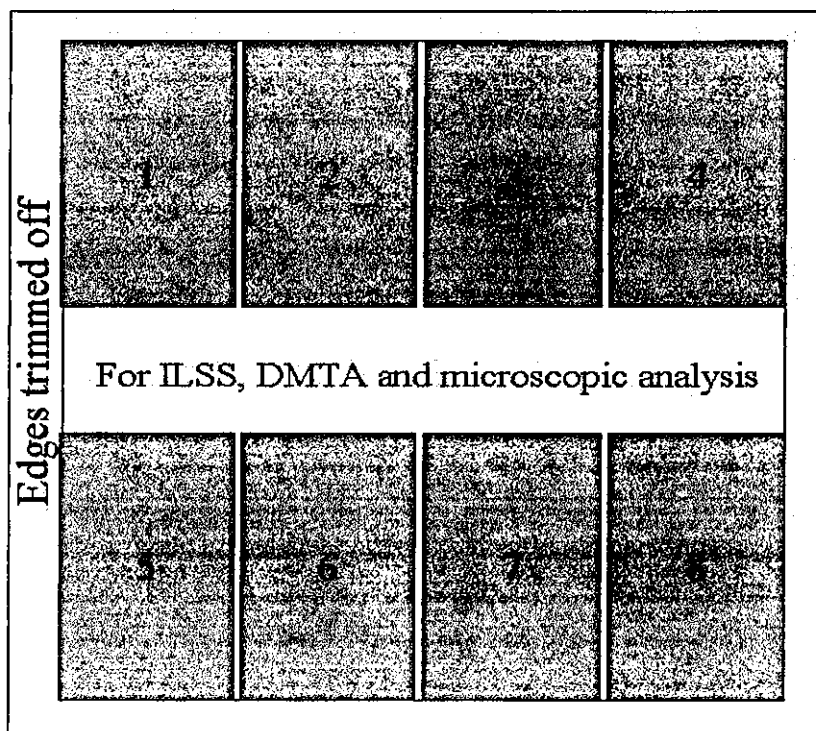


Fig. 30: Locations of the Test Specimens in the Laminate

Details of the impact test conditions are given in Table 6. All samples were impacted onto the top face of the laminate. Unfiltered data using a 10kN load scale were set to ensure full and accurate data capture. Data acquisition was performed using Rosand software running on an IBM PC. The velocity-time,

force-time, energy-time, deflection-time and force-deflection traces were recorded and analysed.

Parameter	Laminate Details
Sample size (mm)	110 by 65
Support Conditions	Clamped with emery paper backing
Support Span (cm)	6 (diameter)
Drop Weight (kg)	4.3
Impact Energies, (J)	10, 20 and 30
Indenter Diameter (cm)	1

Table 6: Impact Parameters

4.5.2 Instrumented Through Penetration Impact

This test procedure is different from the impacting process used for the compression after impact tests. BS EN ISO 6603-2:2000 [135] was used for all through penetration impact tests. The procedure was the same as for the low velocity impact except that the specimens were impacted with a set velocity of $4.4(\pm 0.2)$ m/s. A specimen size 70mm x70mm was selected so that they fitted the rig and were securely held by the clamp rings. The diameter of the hemispherical indenter used was 10 mm. The striker mass was 10.3 kg. The load scale (10kN), filter (1000Hz) and sweep time (20 ms) were selected to ensure full and accurate data capture. The test parameters used are tabulated below:

Impact Velocity (m/s)	Impact Energy (J)	Striker Mass (kg)	Test Chamber Temperature (°C)
4.4	98.736	10.3	21.5

Table 7: IFWI Drop Parameters

The velocity-time, force-time, energy-time, deflection-time and force-deflection traces were recorded and analysed.

4.5.3 Impact Damage Assessment

The fracture states and degree of delamination damage were determined non-destructively and destructively. There are a number of methods available [136] for the assessment. The non-destructive assessments used included: visual inspection and Ultrasonic C-scanning, while destructive assessment methods used were thermal deply and optical microscopy.

Determination of Impact Damage Mode by Visual Inspection

The impacted face and the tensile face of all the samples were inspected visually. Local shear cracks on the impacted surface were noted and the tensile crack lengths were measured. The permanent indentation on the impacted surface was measured using a displacement dial gauge accurate to 0.01mm.

Determination of Impact Damage Area by Ultrasonic C-Scan

Ultrasonic C-Scan was used to accurately measure the global delamination zone of all the impact specimens. As this method is non-destructive, all the impacted samples were scanned.

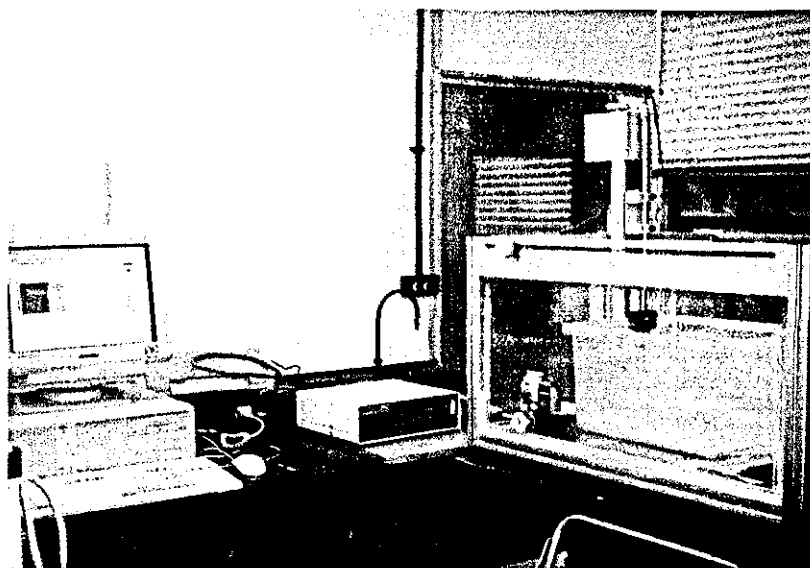


Fig. 31: Photograph of the C-scan Set-up

Fig. 31 shows a photograph of the set-up; a glass sheet was placed at the bottom of the container of water to reflect the incident ultrasound. Four small rectangular steel blocks were placed on top of the glass and above them were placed the

impacted samples to be scanned. The reason for using the steel blocks was that some of the impacted samples had fibre failure on the tensile face, which caused difficulty when placing the samples horizontally. As the C-scan was very sensitive, care was taken to ensure that the height of the transmitter above the test specimen, amplifier gain etc. were kept constant.

A Physical Acoustics® Ultra Pac window-based-software controlled scanning machine with a single probe, mounted perpendicular to the samples, was used for the scanning. The scanner plotted attenuation versus axial position of a specimen resulting in a two dimensional plot. A CRAG [132] standard describes the procedural guidelines for this method. The following C-scan settings were used initially for the specimens:

Pulse Echo		Digitizer Set-up	
Pulser Voltage (v)	400	Delay (μ s)	3
Damping (Ω)	251	Width (μ s)	32
Filter (MHz)	5	Wave Average	5
Attenuation (dB)	0	Sampling Rate(MHz)	32
Gain (dB)	54.5	Scale(v)	1
Water Path velocity (in/ μ s)	0.0584	Display Mode	Full
		Trigger Mode	Internal(-)
Gate Set-Up		Scanner Set-up	
Synchronization	First		
Synchronization Thresholds (%)	Echo	X-Direction Speed	10.0
Detection	20	Y-Direction Speed	1.0
Detection Thresholds (%)	Peak	Bidirectional Point	
Gate Start (μ s)	15	Acquisition	
Gate Width (μ s)	18.9		
	6.2		

Table 8: Initial Setting of the C-Scanner

A comparison of the unimpacted, 10J, 20J and 30J samples (Laminate M) using the above setting is shown in the Fig. 32.

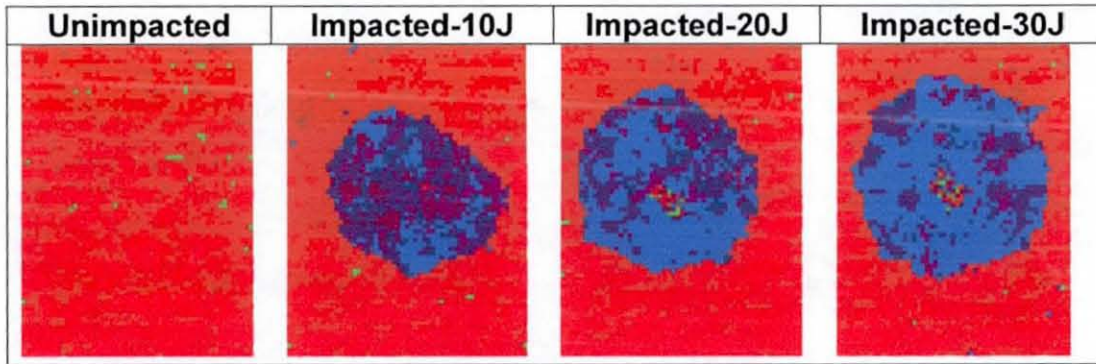


Fig. 32: C-Scan of the Unimpacted and Impacted Samples

The damage areas, shown in the C-scan images, were measured using the software: Image-Pro® Plus, version 4.5.0.19, running on Windows 2000. Initial calibration was performed to obtain the area in square centimetres. The damage area was then selected and the software calculated the area in cm^2 .

Thermal Depley Analysis

Due to limited availability, only one sample from each impact level was chosen for thermal depley analysis. This method uses a penetrant injected into the damage area of the sample, which is then heated to a high enough temperature to burn-off the resin. This procedure allows individual plies to be removed one by one. Pavier and Clarke [137] experimented with gold chloride, sodium sulphate, calcium oxide, potassium dichromate and magnesium sulphate as penetrants. Based on their findings, calcium oxide was used for this experiment as it is cheap but effective.

A 2 mm hole was drilled through the centre of the impact, followed by four 0.5mm holes 1 cm away from the initial hole. Calcium oxide (CaO) was dissolved in water and injected with a hypodermic needle through the holes. The sample was then put in a beaker containing the CaO solution and left for 24 hrs. Occasional stirring was carried out. The samples were then placed in a vented Carbolite Furnace, at 500°C for two hours. CaO left a light yellow residue on the delaminated area which was then analysed visually.

Optical Microscopic Analysis

In this destructive analysis, the impacted samples were cut through the middle of the impacted samples with a diamond tipped rotary wheel. The cut pieces were then polished on silicon carbide paper (240, 600, 1200 progressively). A fluorescent green highlighter pen was then used to highlight the delamination and matrix cracks. Then an optical microscope was used to take a micrograph of the damaged area, in low magnification. From each micrograph a map was drawn by hand to show the delamination of the respective impact samples.

4.6 COMPRESSION STRENGTH TESTING

The unimpacted and impacted samples were tested in compression on a Dartec servo-hydraulic machine with 9610 control unit. The machine had bi-directional wedge grips with a 100kN load cell. Workshop 96 software was used to communicate with the control unit. The Toolkit96 data acquisition system was used to manually operate the load and cross head displacement. The samples were supported in a QMW miniature test anti-buckling fixture (Fig. 33) and loaded in stroke control at a cross-head speed rate of 0.2mm/min.

Initially it was found difficult to achieve reliable failure of the unimpacted samples – the samples crushed at either end, rather than failing in the gap area between the top support and the edge support (Fig. 33). The end-crushing problem was reduced to a large extent by adjusting the gap between the supporting edges of the anti-buckling guide according to the sample thickness. The maximum compression strength value was measured from the maximum load recorded in the load-time trace.

The compression strengths of the impacted and unimpacted samples were calculated using:

$$\sigma_{\max} = \frac{1000P}{wt}$$

Where,

σ_{\max} = Maximum Compression Strength(MPa)

P = Maximum Load (KN)

w = Original Width (mm)

t = Original Thickness (mm)

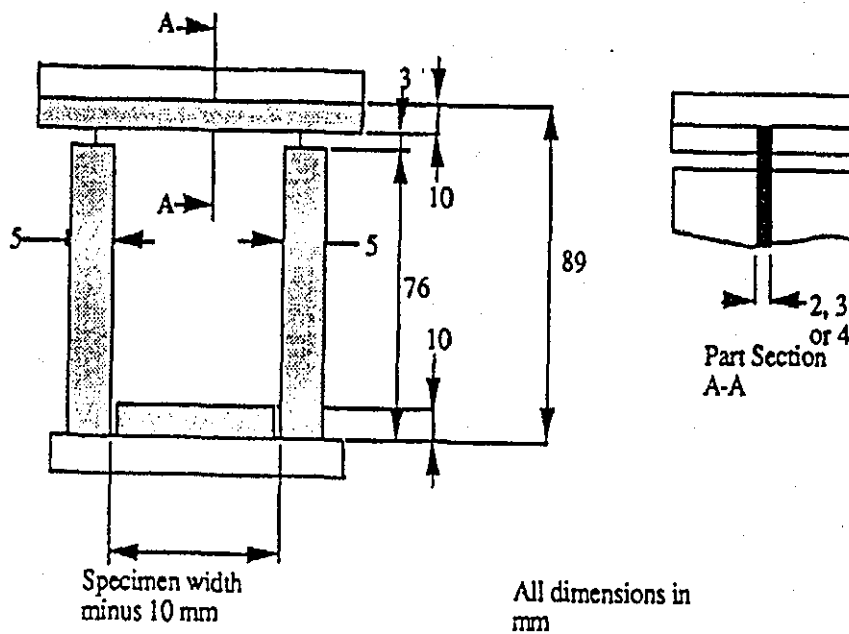


Fig. 33: QMW Compression Anti-buckling Fixture [71]

4.7 THERMO-HUMID EFFECT TESTING AND ASSESSMENT

4.7.1 Accelerated Ageing in Water

Initially all the samples were dried in an air circulated oven at 21°C [138]. Periodical weighing was carried out to check the weight loss due to evaporation of the moisture from the samples. Once the weight reached a steady state, samples were considered dry.

Accelerated ageing of the dried samples was achieved by completely submersing them in water at a temperature of 70°C [139]. A Grant Instrument's water bath (max. temp. 80°C) along with a custom built rack was used for this purpose. The photograph in Fig. 34 shows the set up. During ageing the samples were initially taken out of the bath every 24 hours, wiped dry with tissue paper and weighed. As the rate of water absorption decreased the samples were weighed less frequently.



Fig. 34: Accelerated Ageing Setup (A) Outside View (B) Inside View

Percentage weight gain due to diffusion was calculated using the following:

$$\% \text{Weight Gain} = \frac{W - W_d}{W} \times 100$$

Where,

W = Moist Weight of the specimen

W_d = Dry Weight of the specimen

4.7.2 Dynamic Mechanical Thermal Analysis

A Rheometric Scientific Dynamic Mechanical Analyser MKII was used to determine the glass-transition temperature (T_g) of the specimens. The instrument consists of four main parts [140] shown in the Fig. 35: (i) the mechanical spectrometer head with a dismountable low-temperature furnace, (ii) the thermal analyzer, (iii) the temperature programmer and (iv) an IBM-compatible computer with a plotter.

A cut away view of the mechanical spectrometer head [140] is shown in Fig.36. The test sample was clamped rigidly at both ends of the dual cantilever and its central point vibrated sinusoidally through a drive shaft. The drive shaft is supported on light metal diaphragms which allow only longitudinal motion. The stress experienced by the sample via the ceramic drive shaft is proportional to the current supplied to the vibrator. The strain is proportional to the sample displacement and is monitored by non-loading eddy current transducers and the metal target on the drive shaft.

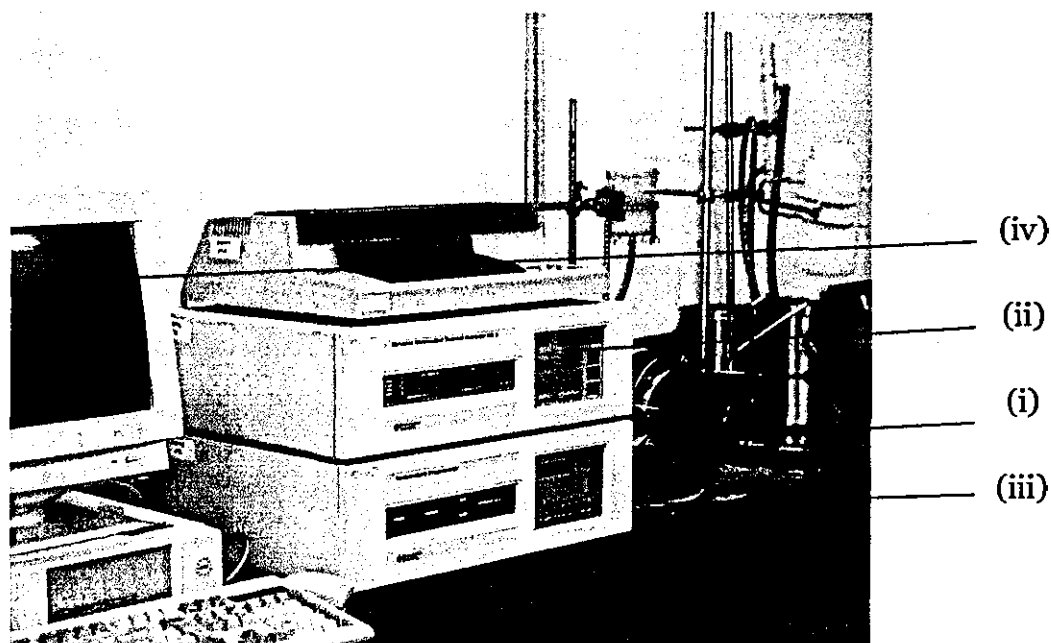


Fig. 35: Photograph of DMTA Set up

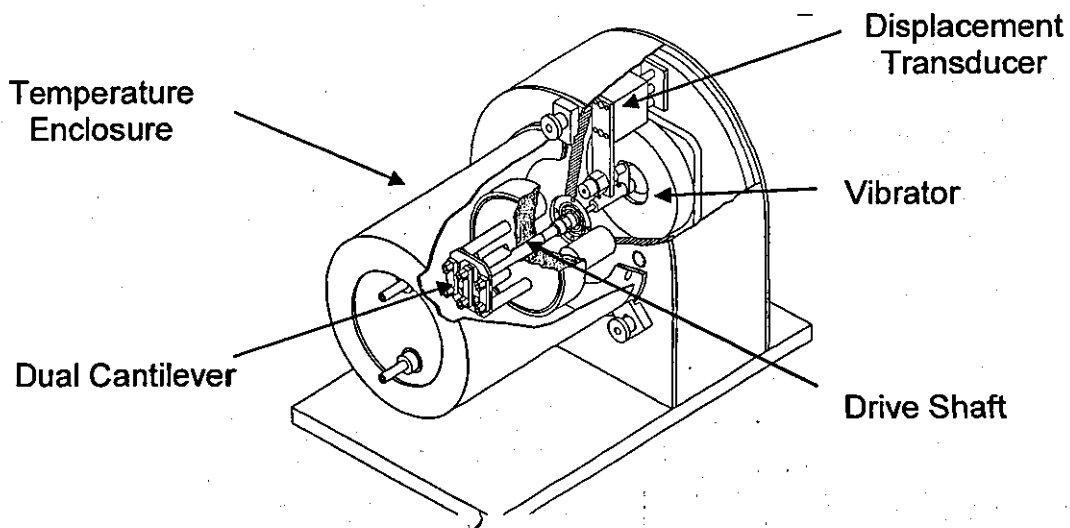


Fig. 36: Main Components of Bending Measurement Unit in DMTA

The temperature programmer controls the temperature ramping. As the temperature is raised the DMTA senses any changes in the molecular mobility in the specimen. The specimens soften as it passes through the glass transition temperature and is recorded as the peak of the loss component of the modulus.

The samples were mounted on the dual cantilever, in the bending mode, with a specified torque (10cNm). The sample was then heated inside the mechanical head with a temperature ramping of 4°C/min. The test parameters used are tabulated below:

Frequency (Hz)	Strain Rate	Torque (cNm)	Temperature Range(°C)	Temperature Ramping(°C/min)
1	64 x 4	10	25-260	4

Table 9: DMTA Set-up Parameters

The information obtained consisted of plots of log storage modulus (E'), log loss modulus (E'') and loss factor ($\tan \delta$) against temperature. The temperature corresponding to the peak of the loss modulus is considered as the T_g of the specimen tested. The test samples were aged according to the method described in section 4.7.1. They were weighed regularly and were tested at 1, 3.5, 17, 30 and 61 days interval.

4.7.3 Raman and Infra-red (IR) Spectroscopy

Raman spectroscopy uses a monochromatic laser which when irradiated into a specimen causes light scattering. Most of the scattered light has the same frequency or colour as the laser, but a very tiny amount experiences a frequency shift, which is characteristic of the chemical bonds or molecules present in the material. This inelastic scattering of light is called the Raman Effect [141]. The analysis of the scattered frequencies gives information on the material's chemical composition, state, aggregation, and even factors like stress, orientation, or temperature to cite some. As the laser beam can be focused to a small diameter, Raman spectroscopy can be used to analyse materials of 1 μ m diameter. With the latest developments it is now possible to map a sample for functional groups.

In Infra-red spectroscopy, functional groups absorb IR when dipole vibrates naturally at the same frequency [142]. The pattern of vibration of a molecule is unique which allows identification of the molecular structure. The FTIR technique employs a moving mirror to produce an optical transformation of the IR signal, and a Fourier analysis is conducted to determine the relation between the intensity and frequency. Concentration of the absorbing species is proportional to the area under the peak, according to Lambert-Beer Law [142].

Because of their different selection rules, Raman and IR spectroscopies are considered complementary to each other. Raman scattering occurs when the electric field of light induces a dipole moment by changing the polarizability of the molecules. While IR spectroscopy requires an intrinsic dipole moment of charge to exist, along with a molecular vibration [143].

The intensity of a band in Raman spectroscopy is linearly related to the concentration of the species. Contrarily in IR, the concentration of the absorbing species is proportional to the logarithm of the ratio of the incident and transmitted intensities [143].

Instrument Details: FTIR

The molecular structures of the samples were examined as KBr discs (13mm diameter and 0.5-1mm thickness) containing ~3 mg of the scrubbing of the composite in ~300 mg of KBr. The spectra were obtained on a Unicam Mattson 3000 FTIR spectrometer in the mid-infrared range, from 600 to 4000cm⁻¹. 64 scans with a resolution of 4.00cm⁻¹ per data point were collected and averaged. The same numbers of scans were averaged to record the background.

Instrument Details: Raman Spectroscopy

Raman Spectra were obtained using a 632.817 nm (red) He-Ne laser with a full power (i.e. 100% Filter) of ~17 mW. The laser beam was focused through an objective on to the test sample with laser beam intensity of ~10 mW at the sample. A highly sensitive (2000x800 pixels of 15 microns) charge coupled device (CCD) camera was used to collect Raman Spectra. The specimens were placed onto the stage of an Olympus high stability BX40 microscope (with x10, x50, x100 objectives) connected to a black and white camera.

The diameter of the laser spot (i.e. sampling area) can be calculated using the following formula. The depth of the sampling volume, as quoted by the manufacture, is likely to be between 1.6-2 μm.

$$Diameter (\mu m) = \frac{1.22 \times \text{Laser Wavelength}}{\text{Numerical Aperture of Objective} \times 1000}$$

A 600 gr/mm grating was used, which gave a spectral resolution of 1.3 cm⁻¹ per data point. Hole aperture and Slit used were 300 and 200 μm respectively. Single spectrums were acquired using a x10 objective with acquisition time of 10 seconds and 100% Filter. A x50 objective with acquisition time of 1second and 50% Filter were used for mapped image acquisitions.

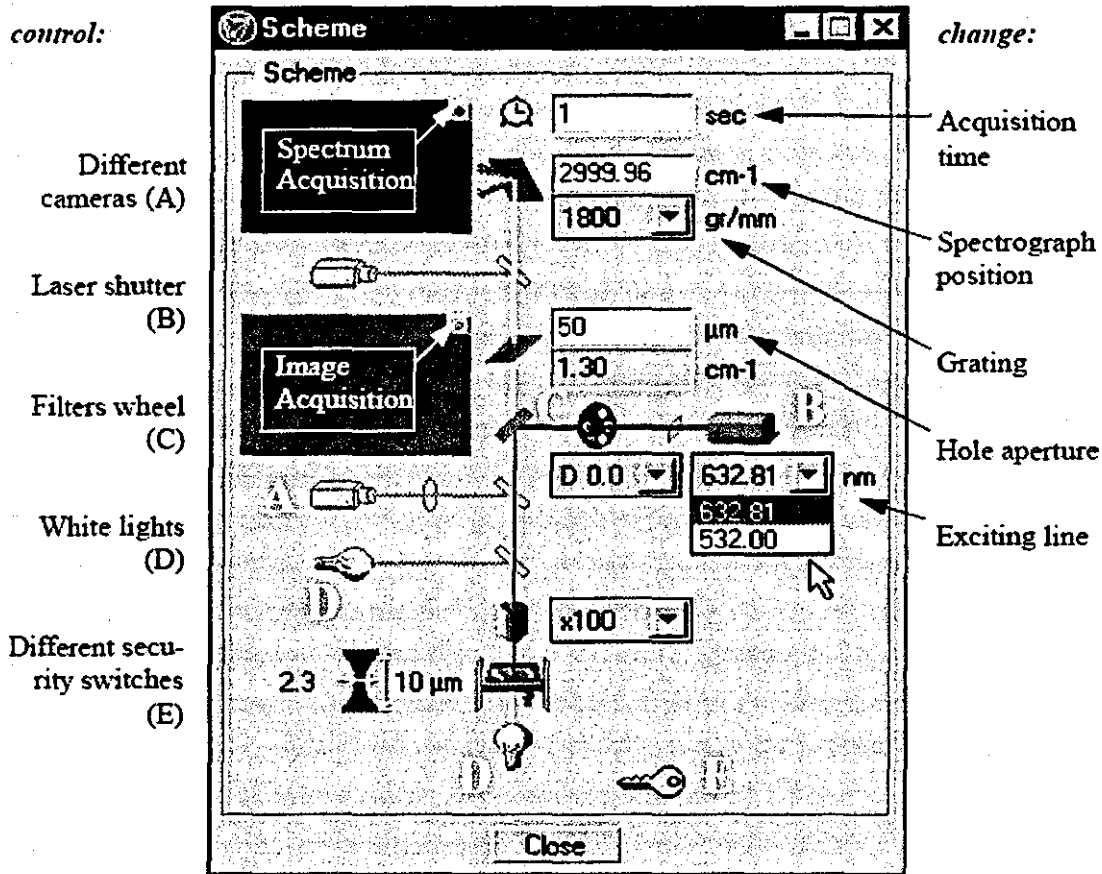


Fig. 37: Schematic of Raman Spectroscopy [144]

All the test samples for FTIR and Raman Spectroscopy were aged according to the method described in section 4.7.1. They were weighed regularly and were tested at 1, 30 and 61 days interval.

4.7.4 Inter-laminar Shear Strength (ILSS) Analysis

For the elevated temperature ILSS testing, a Hounsfield Tensile testing machine with a heating unit was used. Tests were carried out at 70°C with a load cell of 10kN. Samples were loaded at 4 mm/min in displacement control in accordance with the CRAG standard [132]. Five samples of each reinforcement type were tested. Details of ILSS calculations are given in section 4.4.1. The test samples were aged according to the method described in section 4.7.1. They were weighed regularly and were tested at 0.5, 1, 4, 11 and 22 days interval.

4.7.5 Damage Tolerance Analysis

The compressive strength of unimpacted and impacted aged samples was tested as detailed in section 4.6. The test samples were aged according to the method described in section 4.7.1. They were weighed regularly and were tested at 7, 30 and 90 day intervals.

4.7.6 Hardness Measurement

Vickers micro-hardness was measured on both dry and aged samples using a "Mitutoyo AVK-C2" automatic digital micro-hardness tester with a 5Kgf indenting load ($F=49.03\text{N}$) and 10 seconds dwelling time. The load was chosen in order to make large indentations covering both the matrix and a reasonable amount of fibres, so as to get an average hardness value for the composite. The measurements were done at room temperature at all four edges and at the centre of the samples. These five readings were then averaged to get the hardness number (HV). The hardness number (HV) is obtained by dividing F by the area, A (mm^2), of contact between the indenter and specimen. This area is calculated from the diagonal length, d (mm), of the indentation when the indenter is removed. The test samples were aged according to the method described in section 4.7.1. They were weighed regularly and were tested at 1, 30 and 61 day intervals.

CHAPTER 5

DAMAGE TOLERANCE TEST RESULTS AND DISCUSSION

5.0 INTRODUCTION

In this chapter the dry test results are grouped under the heading of physical property testing, static mechanical testing and, damage resistance and tolerance testing. For each type of testing and assessment carried out, a summary of the results is presented. Graphs are plotted to manifest the influence of non-crimp fabric's stitch architecture on the damage tolerance of CFRP. Discussions follow the results, which are compared and contrasted with the existing literatures.

5.1 PHYSICAL PROPERTY TESTING

After moulding, the physical properties of the laminates were examined. The testing included density measurement, determination of fibre volume fraction from thickness, and determination of void content. The results are presented in the Table 10. The main physical property that determines many of the subsequent mechanical properties tested is the percentage void content. The average void contents found for laminates S, M and L were 2.15%, 2.5% and 2.8% respectively. These results correspond well with the microscopic evaluation, where laminate L showed largest void size and distribution compared to laminates S and M. It is generally accepted that the void content of more than 2% can cause a reduction in structural performance ,i.e. lower transverse and through-thickness tensile, flexural, shear and compression strengths, particularly when exposed to hot/ wet service environment conditions for long periods. Large voids of sufficient size may also act as delamination initiation points and result in premature failure of the component.

The propensity of L to form larger void content could be explained by the void formation mechanism proposed by Rudd et al. [43]. Their proposed mechanism for resin flow and void formation is presented in the Fig. 38 (a). They suggested that in a liquid composite moulding, the resin impregnation is achieved through a macro-flow (i.e. a transverse flow around the fibre bundles, shown with blue arrow) and a micro-flow (i.e. the fibre bundle wetting). Though no permeability measurements were carried out, the architectures of the reinforcements show clearly (Table 4) that L has the largest gap between the fibre bundles. It could therefore be assumed that, given the same moulding conditions, the macro-flow during moulding of laminate L would be higher than the micro-flow, compared to that in S and M. This particular condition would lead to more void formation in L, as shown in Fig. 38(b).

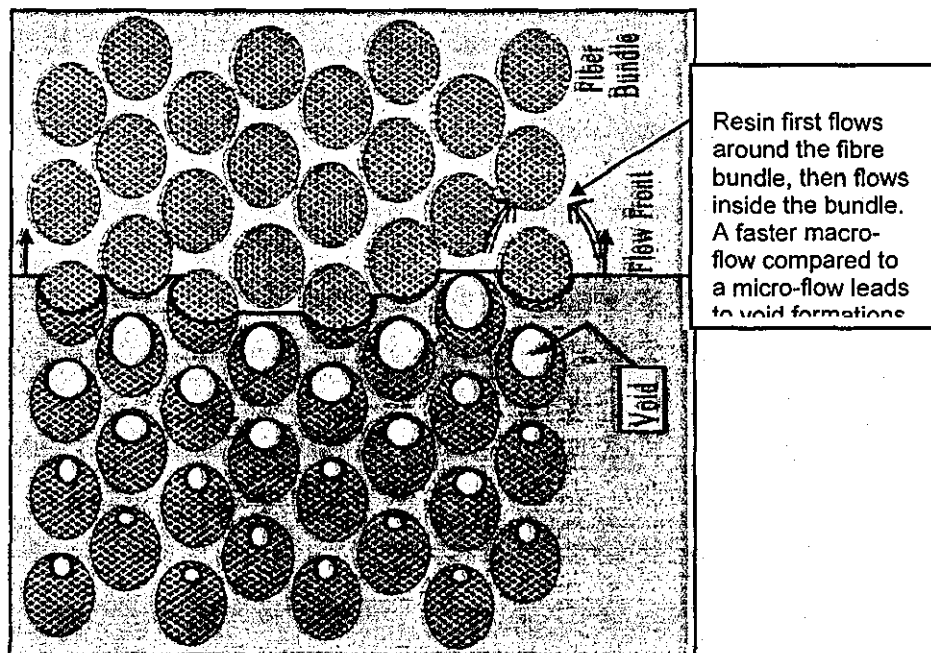


Fig. 38 (a): Resin Flow through Preform and the Void Formation Mechanism



—| 0.55 mm

Fig. 38 (b): Distinct Voids Observed in Laminate L

5.1.1 Microstructural Analysis

The microsections of all three laminates are shown in Fig. 39. The images are obtained by cutting the laminates perpendicular to the 0° fibre tows. The figure shows two important features of the laminates, tow waviness and resin-rich areas, varying due to the difference in the stitch architecture.

Although quantitative measurements were not carried out, the qualitative analysis clearly shows larger degree of tow waviness in laminate L, indicating that low stitch density leads to large degree of tow waviness. The Fig. 39 also showed that resin-rich areas around the stitching yarn are of similar size in all the laminates. Laminate S, therefore, contains greater resin-rich area per unit area along the thickness, because of its higher stitch density. On the other hand, due to the large gap in the 0° tow of fabric L, compared to M and S, laminate L contains more resin-rich area in that ply. The resultant overall distributions of resin-rich areas in the laminates are, therefore, different in laminates S, M and L. As resin-rich areas are potential locations for the initiation of failure, distribution of resin rich area plays an important role in deciding the mechanical properties, especially when composite parts are exposed to hot/ wet service environment conditions for long periods.

It is shown, while discussing the mechanical test results later in this chapter (section 5.2 and 5.5), that resin-rich areas and tow waviness decide the crack propagation behaviour and compete against each other.

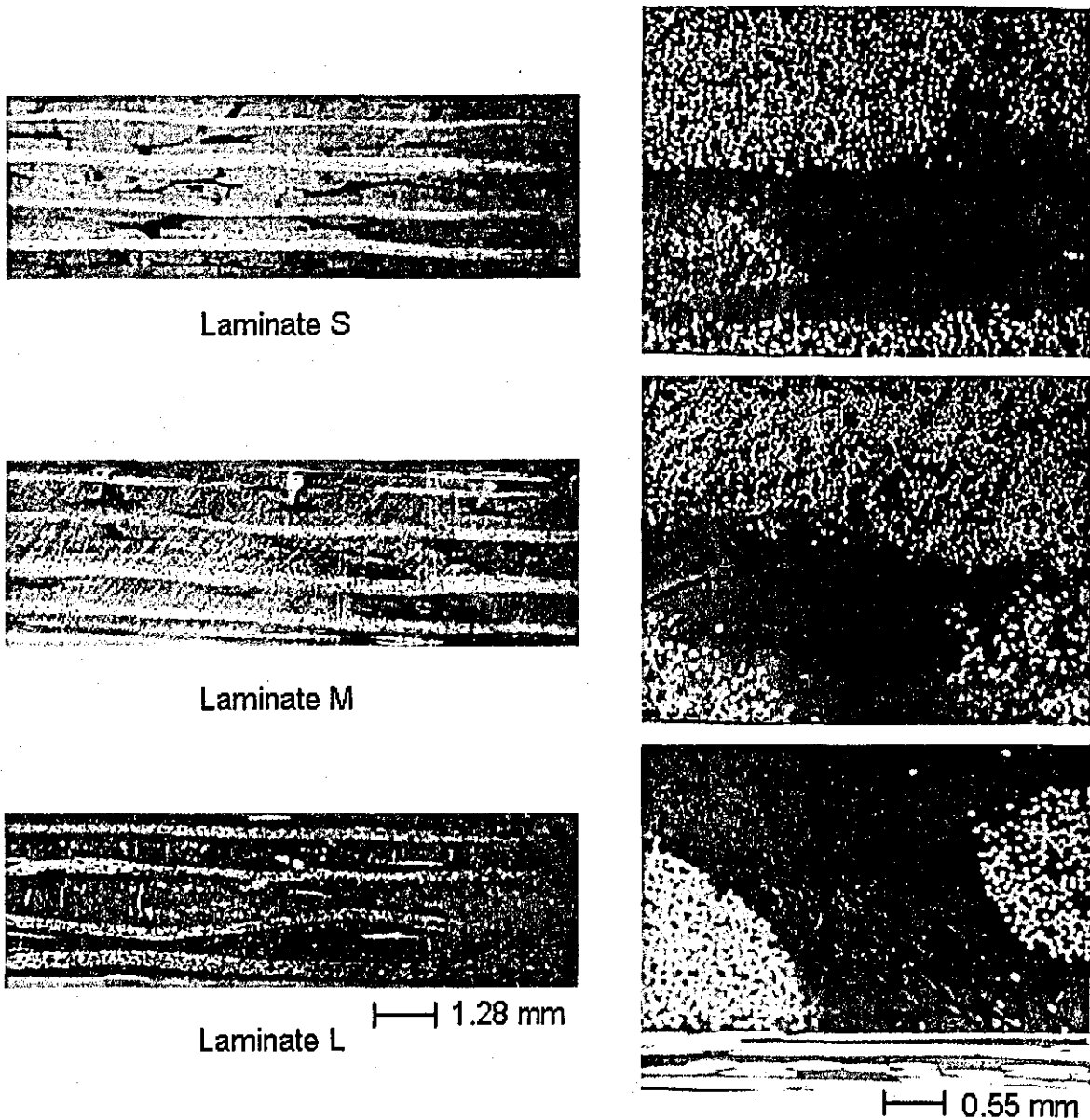


Fig. 39: Polished C.S. of Laminate S, M and L.

Showing the Extent of 90° Tow Waviness (Left) and Resin-Rich Area around Stitching Yarn (Right)

Sample Code	Electrical Balance Reading in Air(gm)	Analog Balance Reading in Air(gm)	Analog Balance Reading in Water(gm)	Fibre wt. after Acid Digestion (gm)	Fibre Wt. Fraction	Resin Wt. Fraction	Density (gm/cc)	Void % in composite	Thickness	FVF from Thickness
S1	2.5392	2.5335	0.9080	1.8903	74.4447	25.5553	1.555	2.0302	3.26	0.556
S2	2.4136	2.4074	0.8248	1.6683	69.1208	30.8792	1.517	2.0249	3.34	0.539
S3	2.6159	2.6116	0.9144	1.8993	72.6060	27.3940	1.535	2.4527	3.34	0.529
S4	2.4234	2.4195	0.8413	1.7235	71.1191	28.8809	1.529	2.1499	3.26	0.545
S5	2.4325	2.4260	0.8500	1.7345	71.3065	28.6935	1.535	1.8341	3.26	0.549
S6	2.6345	2.6293	0.9750	2.0905	79.3509	20.6491	1.585	2.3662	3.28	0.539
S7	2.5673	2.5610	0.9358	1.9820	77.2017	22.7983	1.572	2.2135	3.34	0.556
S8	2.7535	2.7501	0.9256	1.8546	67.3543	32.6457	1.504	2.1417	3.32	0.539
M1	2.5423	2.5365	0.9363	2.0140	79.2196	20.7804	1.581	2.5672	3.24	0.549
M2	2.3430	2.3387	0.8362	1.7628	75.2369	24.7631	1.553	2.5186	3.3	0.539
M3	2.6432	2.6381	0.9138	1.9003	71.8939	28.1061	1.526	2.6943	3.24	0.549
M4	2.5844	2.5790	0.9198	1.9432	75.1896	24.8104	1.550	2.6335	3.2	0.556
M5	2.2633	2.2572	0.8140	1.7432	77.0203	22.9797	1.560	2.8620	3.26	0.545
M6	2.3436	2.3399	0.8407	1.7532	74.8080	25.1920	1.557	2.0590	3.34	0.532
M7	2.3780	2.3738	0.8414	1.7645	74.2010	25.7990	1.545	2.5190	3.4	0.523
M8	2.2647	2.2602	0.7815	1.5964	70.4906	29.5094	1.525	2.1619	3.38	0.526
L1	2.3460	2.3400	0.7906	1.6226	69.1645	30.8355	1.506	2.7465	3.2	0.545
L2	2.5330	2.5282	0.9454	2.0714	81.7765	18.2235	1.593	3.0077	3.3	0.532
L3	2.7342	2.7303	0.9452	1.9820	72.4892	27.5108	1.526	2.9887	3.36	0.532
L4	2.3582	2.3539	0.8127	1.7069	72.3815	27.6185	1.523	3.0789	3.26	0.545
L5	2.4264	2.4228	0.8975	1.9334	79.6818	20.3182	1.584	2.5785	3.24	0.545
L6	2.4972	2.4920	0.9300	2.0230	81.0107	18.9893	1.591	2.7676	3.3	0.542
L7	2.5124	2.5059	0.8432	1.7094	68.0385	31.9615	1.503	2.4543	3.2	0.532
L8	2.4524	2.4481	0.9009	1.9443	79.2815	20.7185	1.578	2.7701	3.3	0.535

Table 10: Summary of Basic Physical Properties

5.2 INTERLAMINAR SHEAR STRENGTH (ILSS) TEST

During low energy impact, the energy absorbed can create a damage zone which consists of matrix cracking, fibre breakage, fibre debonding and delamination [145]. Transverse impact loading, therefore, can cause cracks and delaminations in composites when the interlaminar strength is low. It is possible to modify the delamination failure mode by through-thickness reinforcement (stitching) or through the use of toughened matrix [146]. In the current study the former parameter has been varied, therefore, the effect of stitch density on ILSS was examined.

Delamination growth has been characterised extensively by using the strain-energy release rate (G) in Mode I and II loading conditions [147] to measure the interlaminar fracture toughness of composite materials. The short-beam-shear test has also been used extensively for evaluating the apparent interlaminar shear strength of composite laminates because of its simplicity. The latter method has been used in this study. ILSS behaviour was of interest for two major reasons:

- To check the fabrication quality as several authors have already shown that this method is very sensitive to the fibre/matrix interface quality [148],
- To investigate the degradation of the laminate properties after thermo-humid ageing [149].

In Table 11 a summary of the ILSS results of the dry laminates for the three reinforcement types is presented. The load values were read directly from the maximum load value on the load-extension curve. Thickness and widths were measured using a digital vernier calliper. For each of the laminates five samples were tested and the average of those results is included in the table in the Appendix. Finally the results of the five laminates are averaged and standard deviation calculated. The results showed similar average ILSS value and scatter for all three reinforcement types. Hence, it was concluded that the laminates were of acceptable quality and there is no variation in ILSS due to stitch density.

Laminate	ILSS (MPa)		
	S	M	L
1	40.31	41.58	37.86
2	40.34	37.40	40.15
3	37.19	37.12	39.87
4	38.34	37.20	38.01
5	38.43	39.77	36.70
Average	38.92	38.61	38.52
Std. Dev.	1.37	1.99	1.46

Table 11: ILSS Test Results at Room Temperature (21°C)

Backhouse [150], in his study of various stitch architecture of NCF, found that increasing the stitch pitch (lengthwise) and using medium stitch tension favoured ILSS. However, he also conceded that the apparent effect was small in relation to the experimental scatter. His latter view has been reinforced by the results presented in this study. Here results showed that a reduction of stitch density, by 50% in both length and width direction, did not produce any significant variation of ILSS.

A finite element investigation of the ILSS behaviour of a much simpler bidirectional NCF carried out by Drapier and Wisnom [74], suggested that, ILSS is controlled mainly by resin behaviour and partly by strain developed in the resin pockets. They concluded that to improve the NCF shear behaviour the fabric has to be manufactured in a way to limit the development of high shear strains. Their suggestion included the use of toughened resin, reducing the thickness of the resin layers and limiting stitching tension. Stitching tension is very important because it causes bunching of tows which increases the likelihood of resin pocket. In this study none of the factors mentioned earlier were varied, which accounts for the fact that there was little difference in ILSS between the laminates S, M and L.

Fracture mechanics based interlaminar testing, mode I, was carried out in QinetiQ, by Foreman [151] on S, M and L laminates made from a different epoxy resin system. His results showed similar crack initiation energy, G_{Ic} and Mode I strain energy release rate for all the laminates. He, however, found that the initial slope of r-curve for the high stitch density, laminate S, is higher. In the SEM image of the corresponding fracture surface he found a rougher appearance,

suggesting resistance to crack propagation. Backhouse [150] carried out an investigation on nine different triaxial NCFs and reported that crack initiation energy for all the stitch architectures were similar. He also found that strain energy release rate for crack propagation tended to increase with stitch density. As delaminations do not always progress between plies, carbon fibre tows and polyester stitching yarns bridge delamination cracks and creates more crack fronts, resulting in increased strain energy release rate for crack propagation. The results found in the current study, therefore could be confirmed by both the above studies.

5.2.1 Variation of ILSS with Temperature

BS EN ISO 14130:1998 [152] suggests conducting the ILSS test in the same atmosphere as that used for conditioning. Dry testing at 70°C (accelerated ageing temperature) was therefore carried out to set the baseline ILSS values for the aged samples of the laminates S, M and L. A summary of the test results is shown in Table 12. Detailed results are included in the Appendix, where V_f was calculated using the equation mentioned in the CRAG standard [132]. Average and standard deviations of load, thickness, width and ILSS were then calculated for each of the laminate type. The standard deviation of V_f for all the samples of laminates S, M and L is ± 0.0094 , which is within tolerance limit. It is, therefore, possible to compare the results achieved from different laminates.

Laminate	ILSS (MPa)	
	Average	Std. Dev.
S	35.73	2.83
M	35.02	3.14
L	35.11	2.44

Table 12: Summary of ILSS Test Results at 70°C

Comparison between the ILSS results at room temperature (21° C) and at 70° C for the laminates are shown in the Fig. 40. The average values of ILSS at 70° C show very little difference between the laminates S, M and L, despite the differences in stitch densities. The results also showed similar scatter.

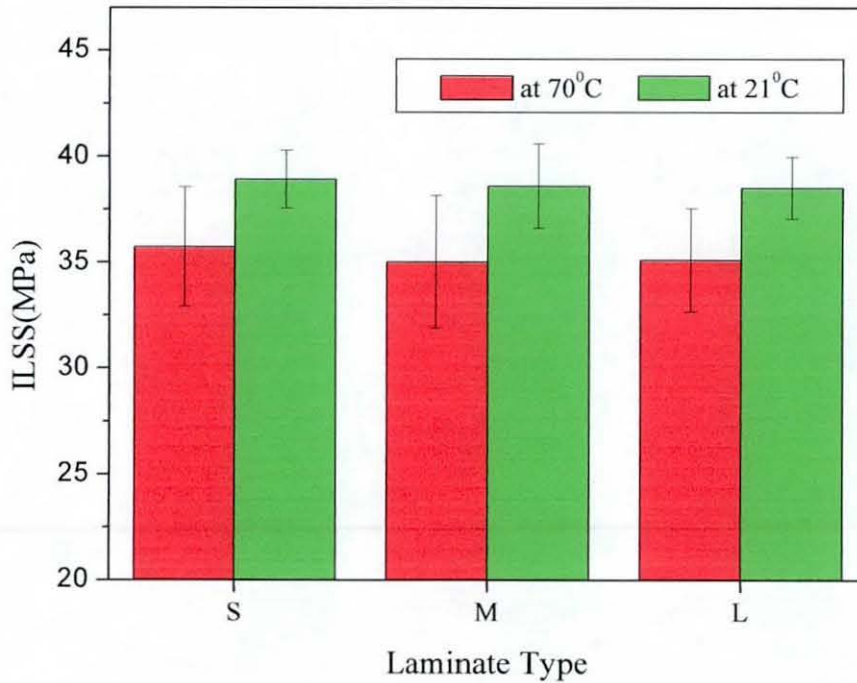


Fig. 40: Effect of Temperature on ILSS

The ILSS at 70°C showed 8.2%, 9.3% and 8.8% reductions for laminates S, M and L respectively. The reduction seems quite large considering that the T_g of the dry composites are above 200° C and that the samples were tested at 70° C inside an oven for a duration of only 10 minutes. The results could be attributed to the mismatch of thermal expansion coefficients between the carbon fibres and epoxy matrix governing the interphasial stress transfer characteristics.

5.2.2 Microscopic Examination

The fractography shown in Fig. 41 presents damage distributions through the laminate thickness. The most predominant type of interlaminar failure observed was a network of interconnecting delamination through transverse matrix cracks. The delamination occurred at the interface between matrix and reinforcement fibres while matrix cracks were prevalent in the resin-rich areas surrounding the stitching yarns. The whole damage area had a characteristic 'top-hat' shape [153] as in the case of impact damage.

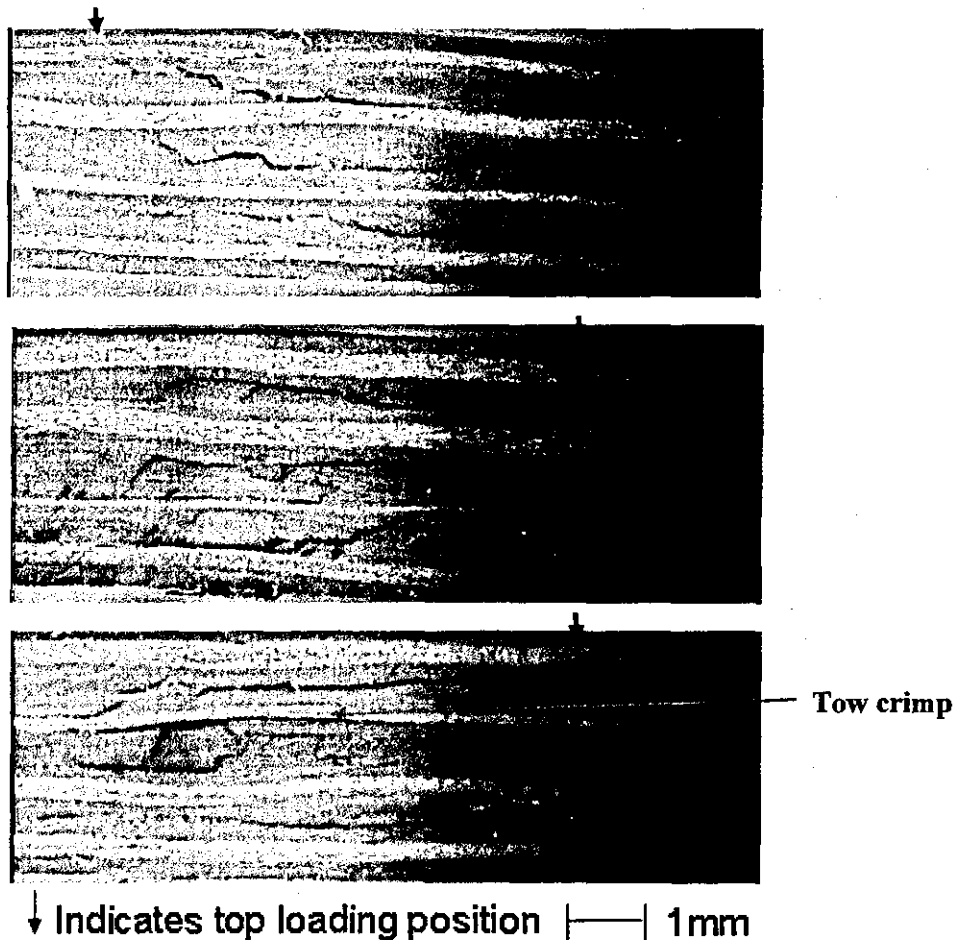


Fig. 41: Optical Micrographs of the ILSS Samples Tested at 70°C (From Top: S, M, L)

Fig. 42 illustrates that the stitch material contributes to the behaviour of the interlaminar crack propagation. The micrograph shows how a crack stops at the stitching yarn at (a) or deviates after encountering the stitching yarn at (b). It could therefore be suggested that the polyester knitting yarns, and subsequently the stitch density, do play a role in deciding the extent of fracture.

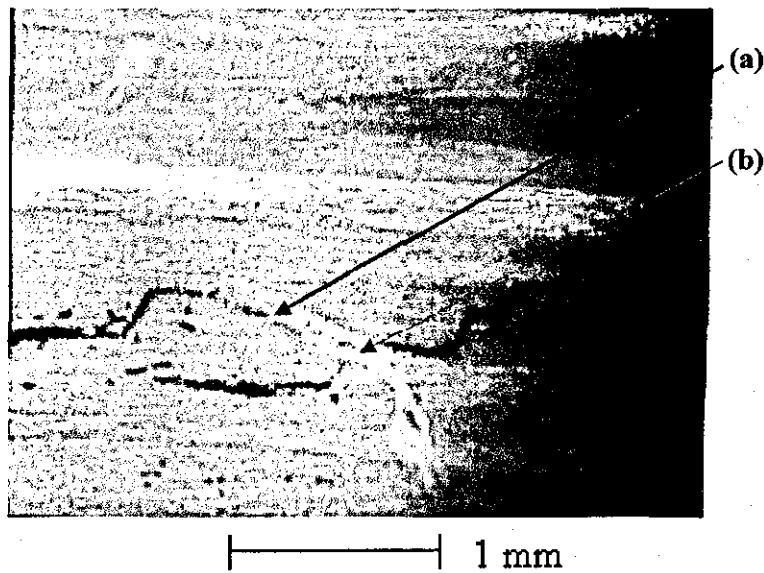


Fig. 42: Effect of Stitching Yarn on Crack Propagation

A second factor that can be considered while interpreting the ILSS value is the tow crimp. Pearce et al. [154] suggested that in woven fabric reinforced composites, the crimped fibres bridge the shear failure surface, thereby increasing the shear strength. This particular situation also provides a degree of mechanical 'keying' between the layers of fibres and would thus be expected to increase the ILSS value. It has been shown in section 5.1 that tow crimp varies inversely with the stitch density, which indicates that laminate L should have better ILSS properties. A third factor contributing to the ILSS value is the void content. Laminate L consistently showed higher void content, as discussed earlier, which should lead to a decrease in ILSS Yoshida et al. [155]. These latter two factors may have negated the useful properties rendered by the stitching yarns on the ILSS, which may have resulted in no improvement in ILSS due to increasing stitch density.

One disadvantage of MWK observed during the ILSS testing is that the ply interfaces have the lowest resistance to crack propagation, which is evident from Fig. 43. As stitching is present only in the plies, rather than through the thickness of the laminate, the laminate's resistance to delamination is also dependent on the strength of the interface between the fibre and the matrix.

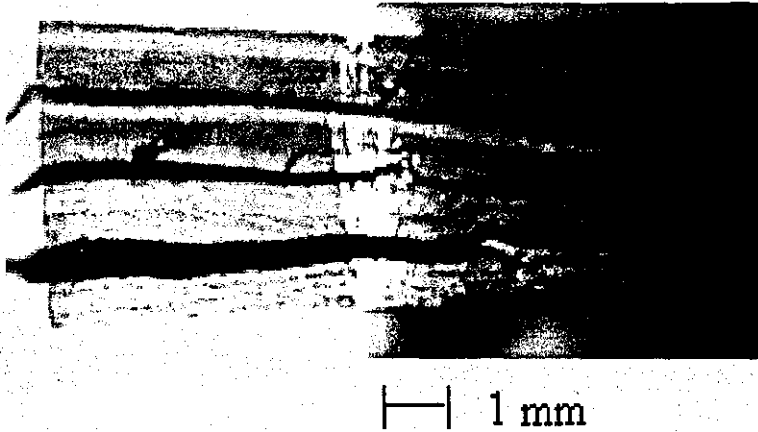


Fig. 43: Multiple Shear Failure between the Plies

5.3 INSTRUMENTED IMPACT TESTING

In this section the results of impact tests and subsequent assessment of damage will be presented and discussed. All the impacted samples were subsequently tested in compression, except of those which were sectioned for microscopy. Initial work was carried out to determine the effect of lay-up on damage resistance. This was followed by impacting laminate S, M and L with 5, 10, 20 and 30 Joules of incident impact energy. Ultrasonic C-scanning was carried out on all the samples to measure the damage area, while delamination mapping and thermal depleting were carried out on three samples because of the destructive nature of the testing. Through penetration impact testing was carried out on a different set of laminates S, M and L.

5.3.1 Effect of Lay-up

Initially the effect of lay-up on the damage resistance was examined. Due to the quasi-isotropic nature of the reinforcements, it was only possible to have two lay-up conditions: either 0° or 45° , on the outer face of the laminates. This aspect of the impact resistance was not investigated in detail; therefore, only laminates of S were moulded and tested for impact properties. Through penetration impact testing was carried out with a 26.2kg weight, which was dropped at 3 m/s speed.

Fig. 44 shows the effect of lay-up on the impact properties. The force-displacement traces were filtered at 1 kHz. The problem faced with a filtered result is that, it is not possible to determine the damage initiation energy. However, damage initiation is matrix and interface dependent and therefore, has little or no dependence on the stacking sequence [5].

Peak force, reached during impact and the energy at peak force are strongly dependent on the stacking sequence. The results in Fig. 44 show that the lay-up sequence has a definite effect on the impact resistance. Peak force reached during impact, for the laminate with 45° orientation on the outer faces was found to be higher than that with 0° orientation. Better impact resistance of laminate with outer 45° orientation may be contributed by two factors. Firstly, the zigzag

stitching pattern (refer to fabric photo in Table 4) which is on the 0° face provides crack bridging and thus inhibits the propagation of fractures. Secondly, because of the stitching, the 0° face is more crimped, which offers further crack bridging [69]. Both these contribution becomes ineffective for laminate with outer 0° orientation.

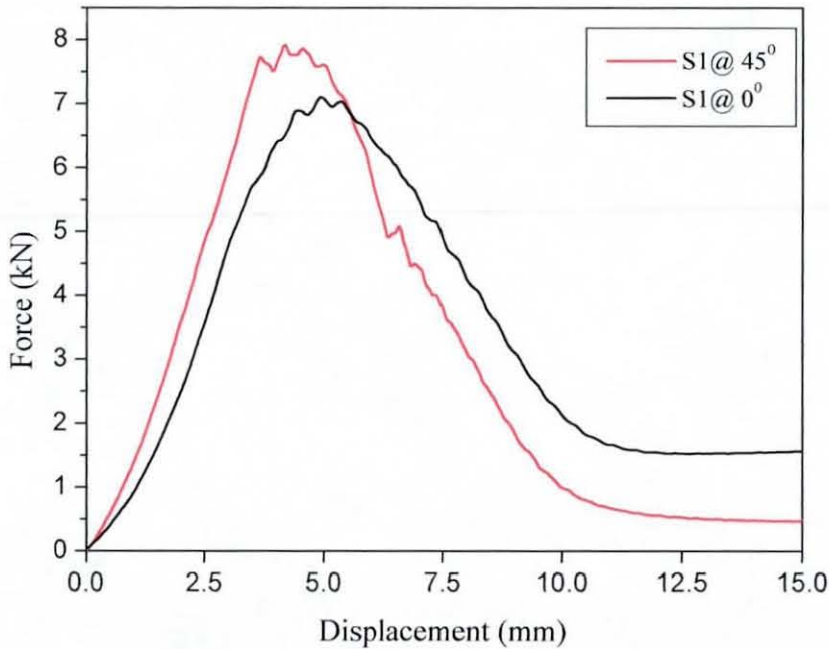


Fig. 44: Effect of Lay-Up on the Impact Properties

Based on these results, all the laminates were produced with the 45° orientation on the outer face of the laminates.

5.3.2 Low Energy Impact Damage

In this work, the main consideration when choosing the impact test conditions was the following CAI (QMW) test. For a CAI test delamination damage should be the major failure mode. The use of miniaturised CAI test geometry and the smaller clamping unit (60mm diameter) of the Rosand Impact Tester with a 10mm diameter hemispherical indenter ensured that delamination damage is initiated at low incident impact energies. This testing geometry was therefore adopted, which is mentioned in section 4.5.1.

The laminates S, M and L were impacted with incident kinetic energies of 5, 10, 20 and 30 Joules. The 5J impact showed very little indentation, while the 10J and 20J impacts showed slight indentation on the impacted face and protrusion on the back face. However, the 30 Joules impact caused visible fibre breakage on the back face at the impact point.

The results of the impact on S, M and L at the damage initiation point and at peak are included in the Appendix. The tables contain the average values of force, energy and displacement experienced by the samples for each impact energy level. Respective standard deviation values are also included.

The following presentation of results is based on two approaches: force based and energy based. The 'force based approach' is suitable for onset of damage, whereas the 'energy based approach' gives more information about the extent of damage.

5.3.3 Impact Response: Dent Depth

Dent depth is used to classify barely visible impact damage (BVID) energy levels. BVID is defined as the energy which causes an impact dent which is just on the verge of being detected [156]. It is often used for design and certification purposes. Some authors [157] have shown that this approach has significant problems because of large variations. Wardle and Lagace [158] found that thin laminates of less than 2.4mm thickness did not show any trend correlating the internal damage. Despite these problems this approach is still widely used and useful for comparing material performances. Furthermore, Caprino and Lopresto [159] proposed a general indentation law, correlating indentation depth and impact energy. They suggested that for a given fibre/resin system, the indentation depth is substantially independent of fibre architecture and orientations, laminate thickness and resin content, and uniquely varies as a function of the ratio of the impact energy to the penetration energy. The results they presented suggest that even the resin and fibre type has a secondary effect on the relationship between indentation depth and non-dimensional energy (i.e. impact energy/penetration energy).

Fig. 45 shows the plots of dent depth against impact energy for laminates S, M and L. From the figure, it is evident that indentation increases with increasing impact energy. The rate of increase is asymptotic, as shown by the solid lines drawn to illustrate the general trends. The result found in the current study is contrary to Foreman and Meeks's findings [156] of the same reinforcements. He suggests that stitch density is directly proportional to the ability of the laminates to resist the formation of impact dent. However, the current results are supported by the delamination maps and photographs of the damaged samples (section 5.3.7). 5J and 10J dent depths of the laminates show very little difference, which is not significant. 20J and 30J impacted samples of the laminates show extensive fibre damage on the compression face, which tend to recover after the impact event. The recovery of these damaged areas indicates that laminate L, with the low stitch density, recovers more than the laminates M and S which is reflected in the dent depth trend.

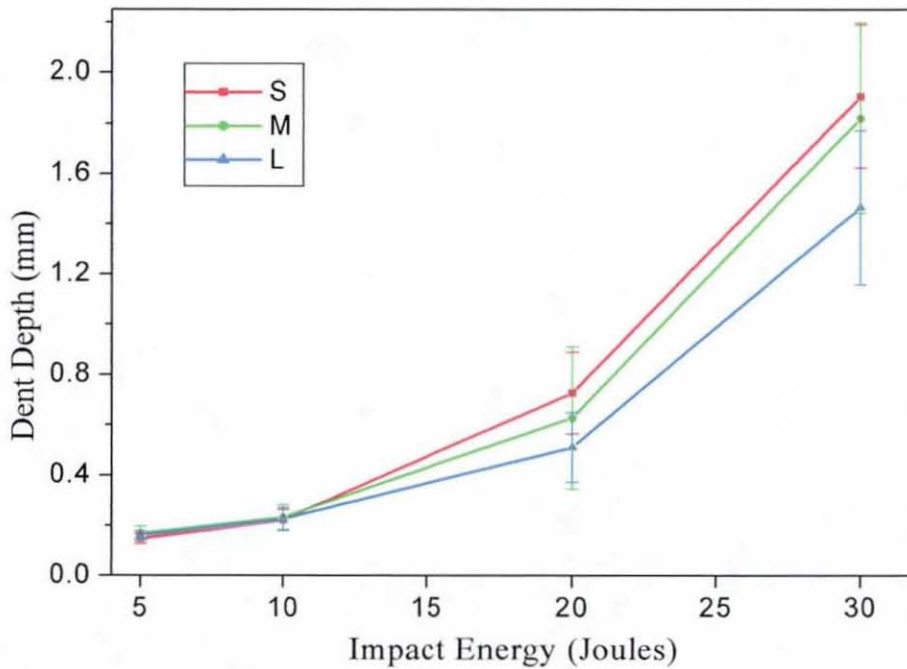


Fig. 45: Effect on Impact Energy on Dent Depth

5.3.4 Impact Response: Force Based Approach

Fig. 46(a)-(d) show typical force-time traces of laminates S, M and L for incident impact energies of 5, 10, 20 and 30 Joules. The force drop at F_i is associated with the initiation of delamination damage. This delamination damage is thought to have been initiated by bending induced shear stresses which are at a maximum at the neutral axis [5]. The presence of isolated delamination close to the neutral axis in all the 5J impacted laminates, shown in the delamination mapping in Fig. 54(a)-(c) also supports this hypothesis.

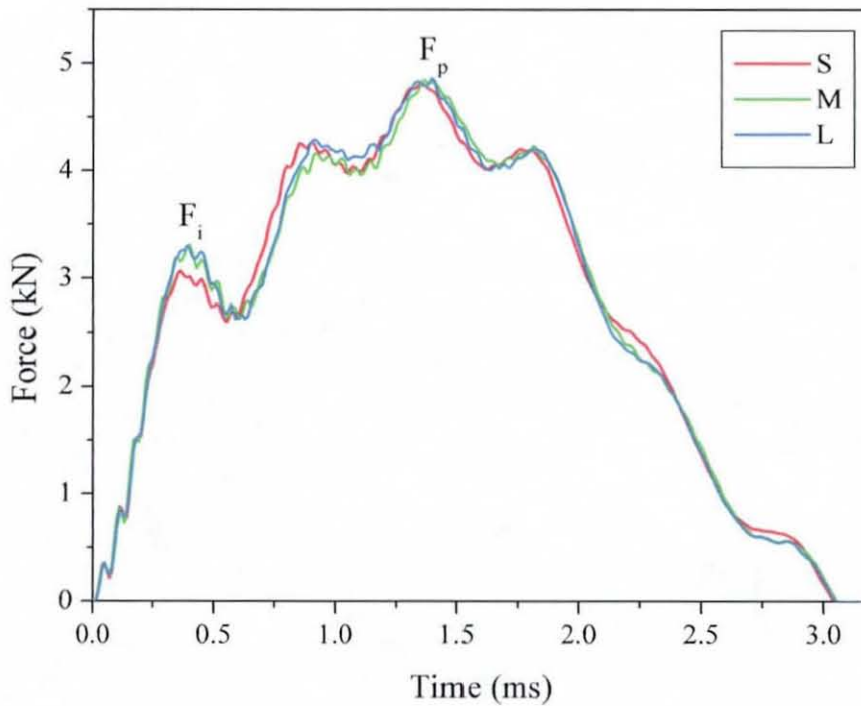


Fig. 46(a): Force-Time Plot for the Laminates at 5Joules Impact

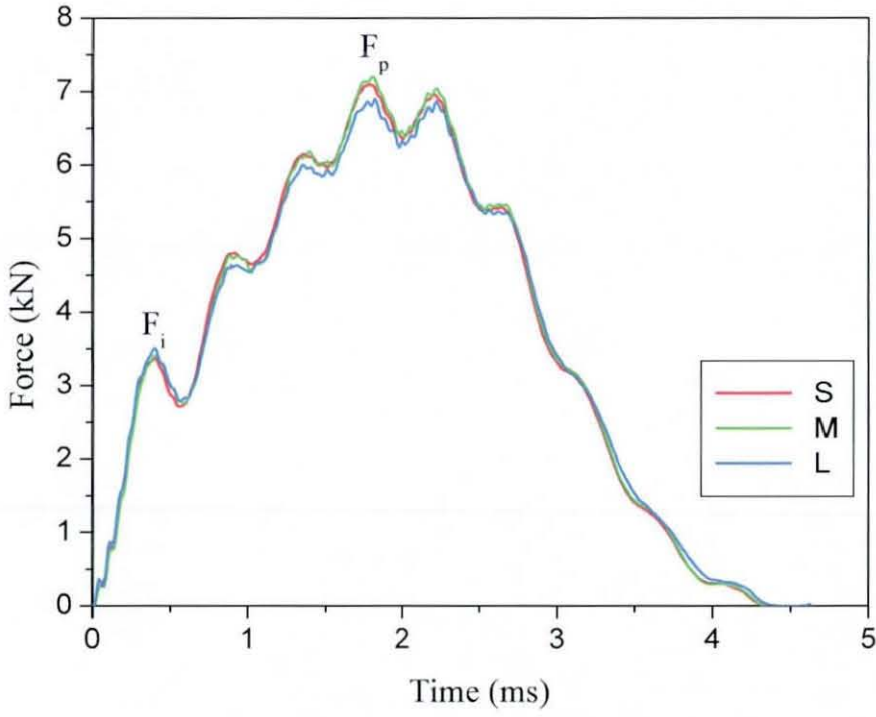


Fig. 46(b): Force-Time Plot for the Laminates at 10Joules Impact

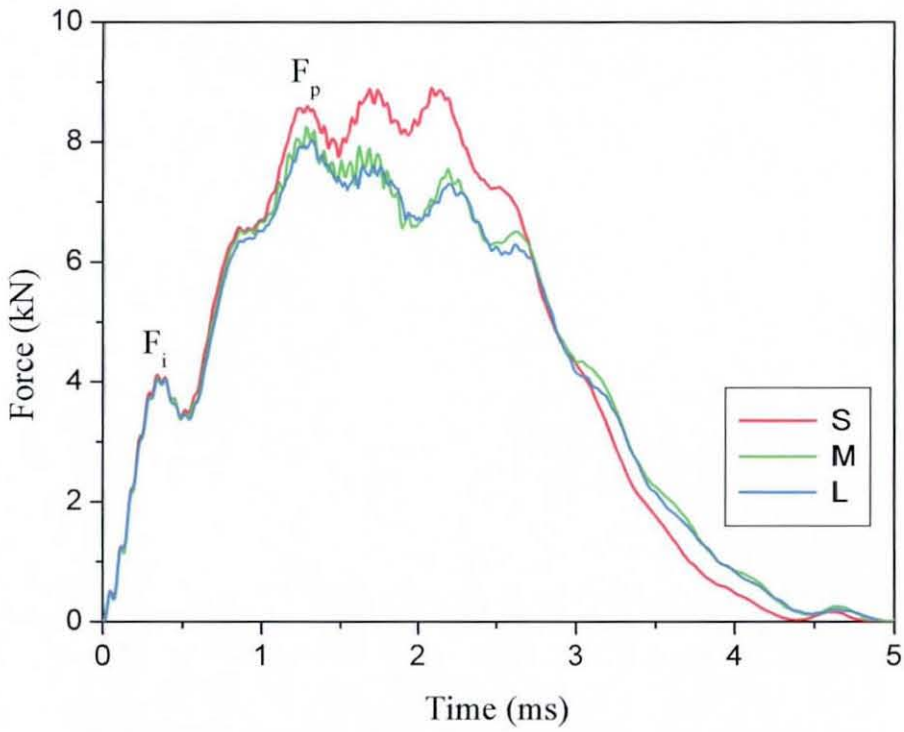


Fig. 46(c): Force-Time Plot for the Laminates at 20Joules Impact

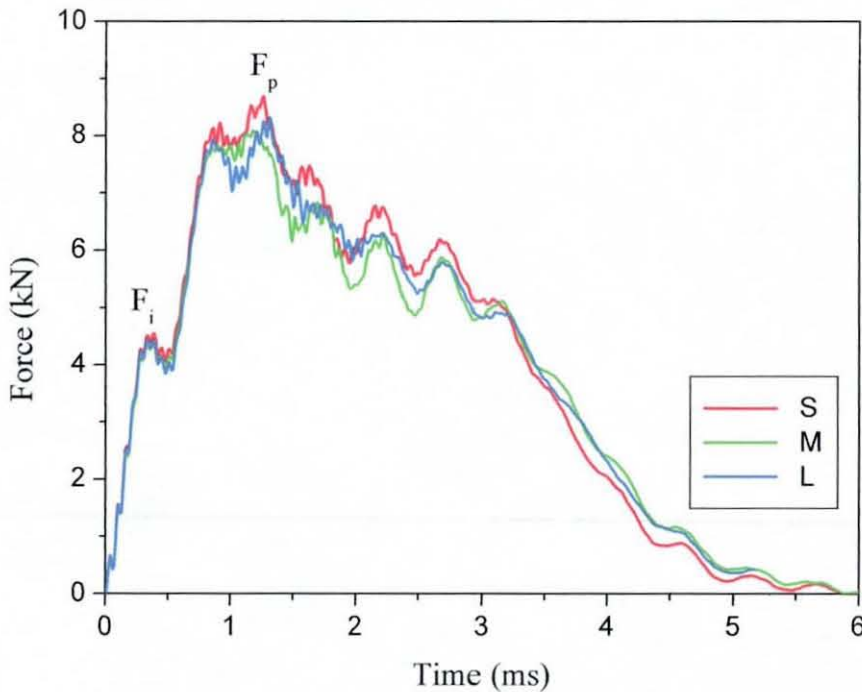


Fig. 46(d): Force-Time Plot for the Laminates at 30Joules Impact

Cantwell and Morton [160] suggested that delamination damage follows after the initiation of tensile cracks on the impacted surface (pine tree shape), due to contact stress, or on the back face (reverse pine tree shape), due to bending induced tensile stress. These tensile cracks were not observed during the delamination mapping of 5J impacted samples. However, in the delamination map of 10J impacted samples, the tensile cracks appear in the pine tree shape. Fractographic evidence found in the current study, suggests that damage initiation may have been caused by bending induced shear stress rather than bending induced tensile stresses.

Having established the damage initiation mode, the effect of the stitch density on the damage initiation was evaluated. The value of F_i , of laminate S, M and L, shows (Fig. 47) very little difference, suggesting that stitch density may not have played any role in the damage initiation.

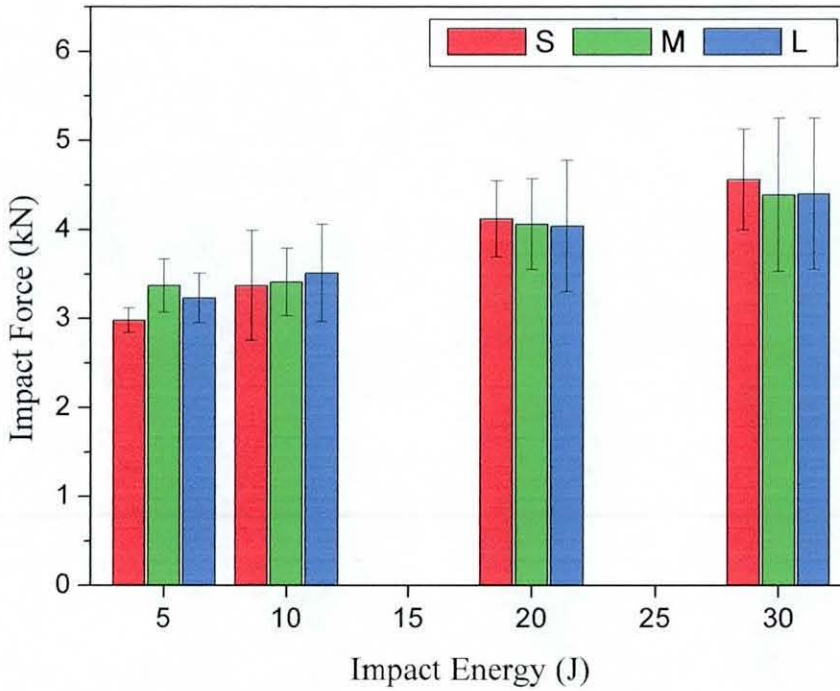


Fig. 47: Impact Force (Damage Initiation) vs. Impact Energy Level

In order to compare the impact events with other static or dynamic events, the time scale was eliminated and the force was plotted as a function of indenter displacement in Fig. 48(a)-(d). Comparison of the force-displacement response exhibited by laminates S, M and L showed that the force necessary to create a specific initial displacement was similar for each of the laminate types. However, it appeared that laminate S was slightly stiffer, with a higher maximum force and lower maximum displacement (in the case of 10, 20 and 30 Joules Impact). It was also noted for all three laminates that both elastic and permanent displacements predictably increased with impact energy.

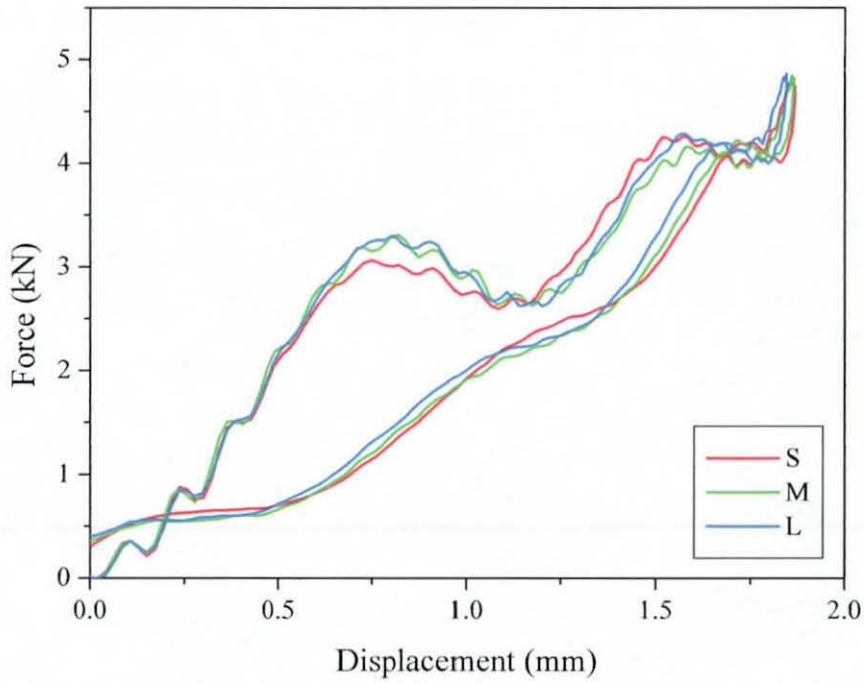


Fig. 48(a): Average Force-Displacement Results for 5 Joules Impact

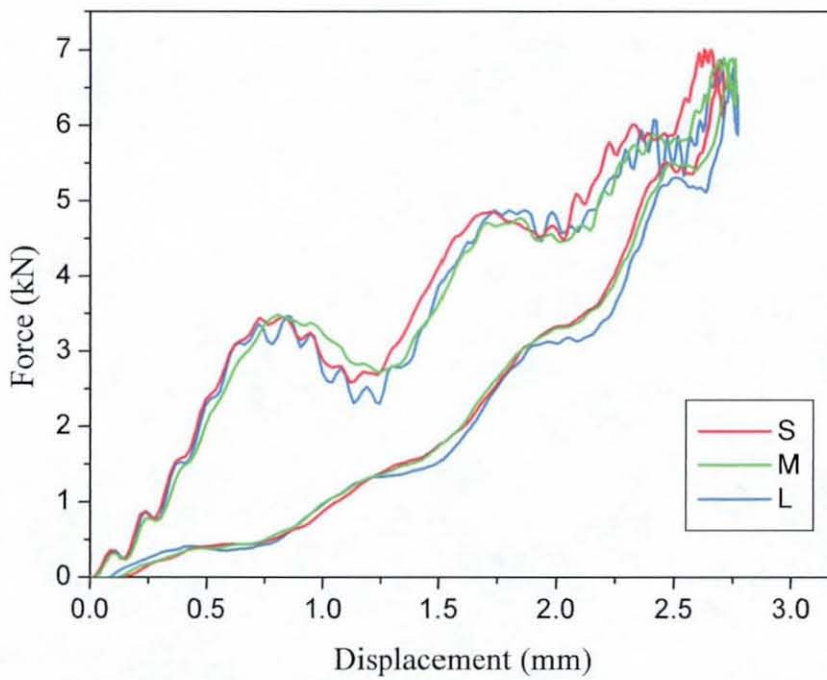


Fig. 48(b): Average Force-Displacement Results for 10 Joules Impact

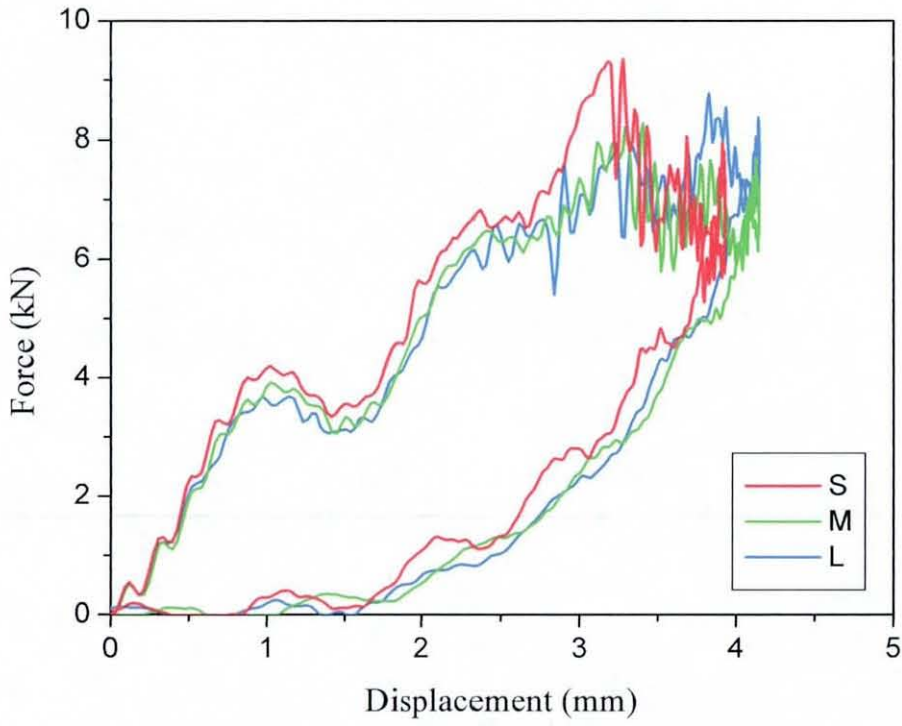


Fig. 48(c): Average Force-Displacement Results for 20Joules Impact

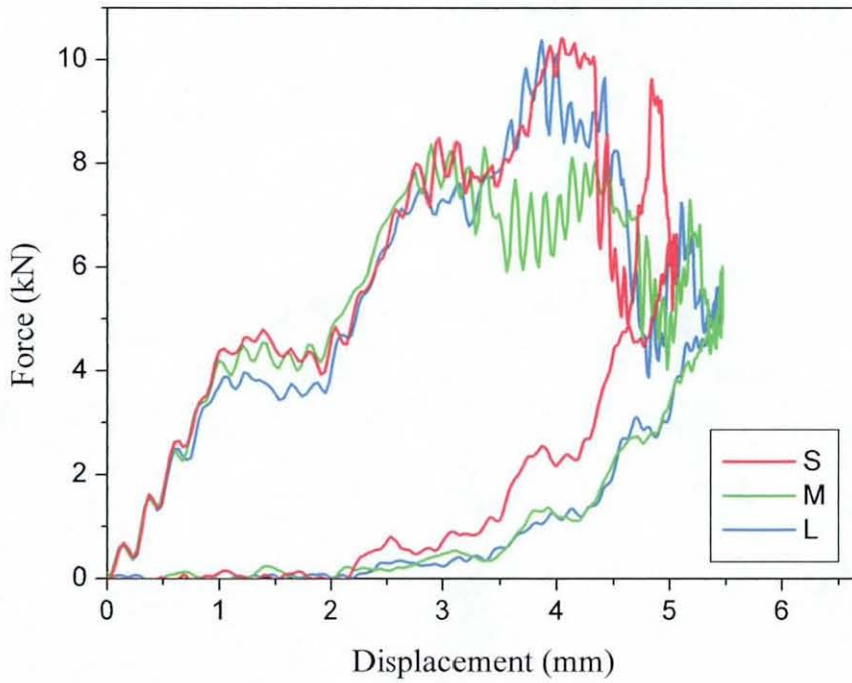


Fig. 48(d): Average Force-Displacement Results for 30Joules Impact

Fig. 49 shows force at peak plotted against incident impact energy. The peak force initially increases with increasing impact energy and then appears to become relatively constant. The difference in peak force for 20 and 30J impact energy for S, M and L shows no significant difference. The reason may be that the incident energy was high enough for damage initiation. However, maximum force is of secondary importance to onset of damage.

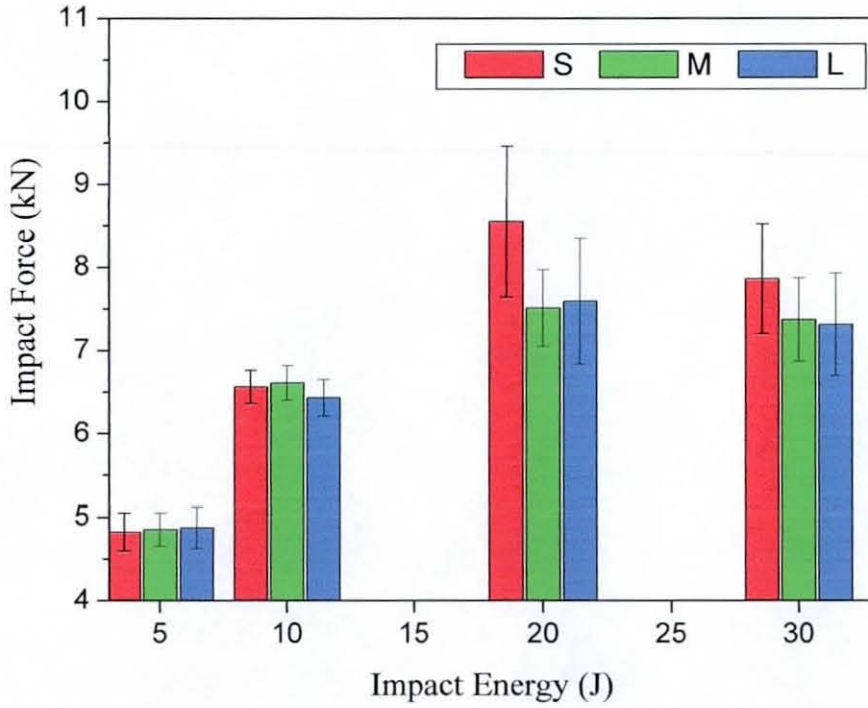


Fig. 49: Impact Force (Peak) versus Impact Energy Level

5.3.5 Impact Response: Energy Based Approach

The energy-displacement curves, Fig. 50(a)-(d) reveal additional information. These curves are created by integrating the Force-Displacement results presented in Fig. 48(a)-(d).

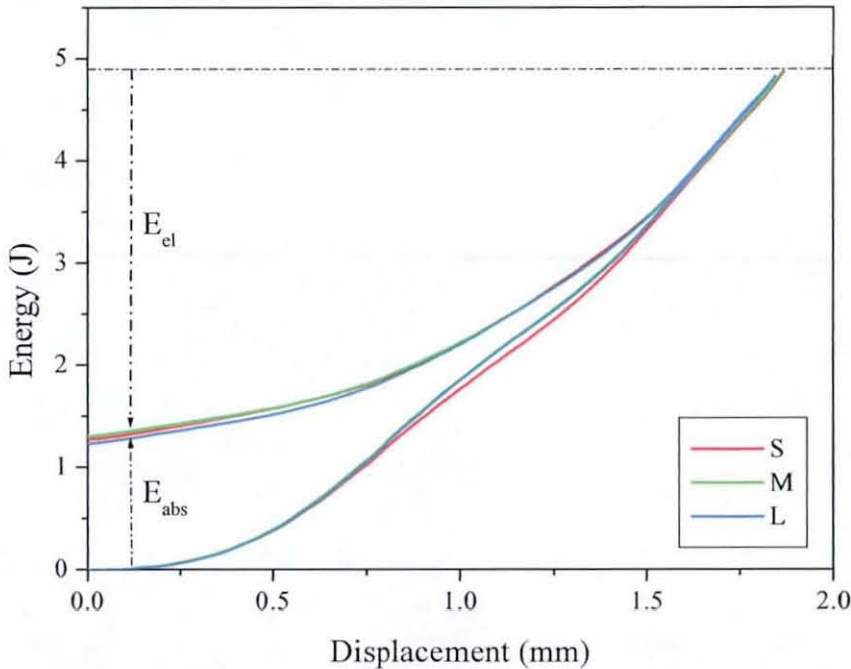


Fig. 50(a): Average Energy-Displacement Results for 5 Joules Impact

It is worth noting that not all of the incident kinetic energy was used during the impact event. A fraction of the energy was lost probably due to friction between the guide rods and the weight or may have been dissipated acoustically and thermally during the impact [161].

Analyzing the shape of the energy-displacement curve for the 5J impact shows very little difference between S, M and L. Here, large parts of the impacting energy were stored elastically, E_{el} . Approximately 1.25J of the impact energy was absorbed, E_{abs} , which caused the delamination seen in the delamination map.

As the incident impact energy was increased to 10, 20 and 30 joules, a definite trend for S was observed. The loading part of the curves in Fig. 50(b)-(d) indicates that laminate S is stiffer than laminate M and L at displacements from 1.25 mm up to the maximum displacement. Interestingly, there was very little

difference between M and L in that respect. At the maximum displacement, all the impacting energy is transferred from the impactor to the target sample, which is stored elastically by bending or absorbed by the creation of damage as mentioned earlier. Upon unloading, the stored elastic energy is used to accelerate the rebounding impactor [162].

For S the maximum displacement for both the 10J and 20J impact show a similar trend. It bends less than M and L (very little difference between M and L), showing its better stiffness characteristics. At the same time, S absorbs more energy and the resultant effect is evident in the delamination map (Figs. 55-56), where S was seen to withstand more damage. The energy-displacement trend for the 30J impact shows a higher elastic energy for S compared with M and L. This result could be explained though the delamination map where S shows more recovery, due to fibre breakage, compared to M and L.

This result links directly with the higher stitch density of S. More through-thickness stitching yarns in S arrest crack propagations, which in turn, increases the crack density. From the delamination mappings (Figs. 56 and 59) of 20J and 30J it can be inferred that stitch density directly influences the damage extent.

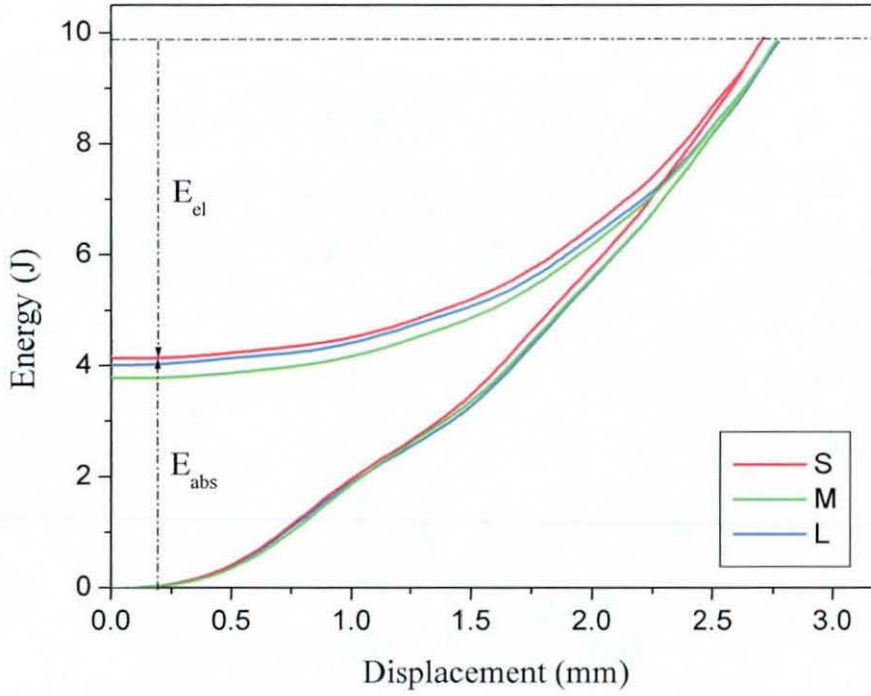


Fig. 50(b): Average Energy-Displacement Results for 10Joules Impact

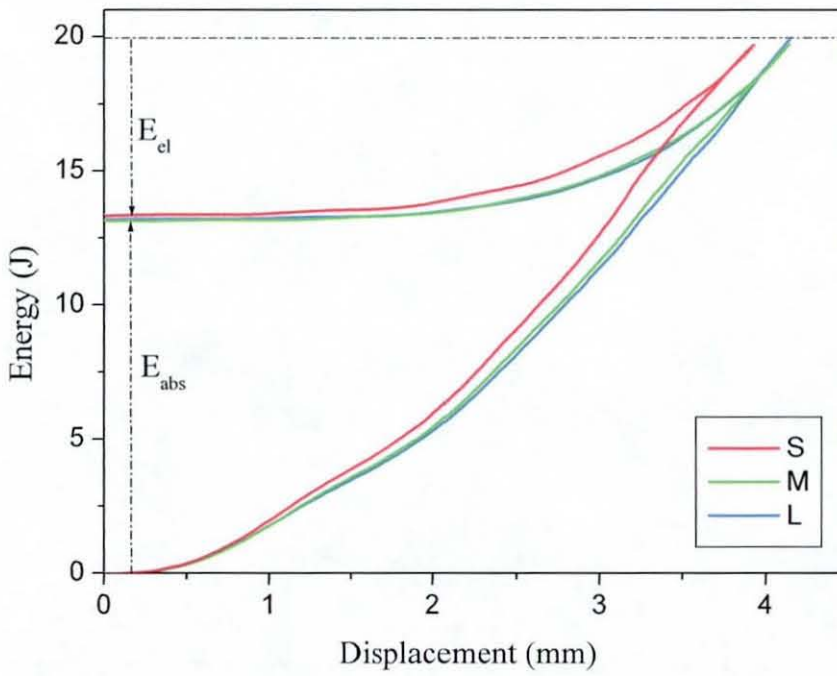


Fig. 50(c): Average Energy-Displacement Results for 20Joules Impact

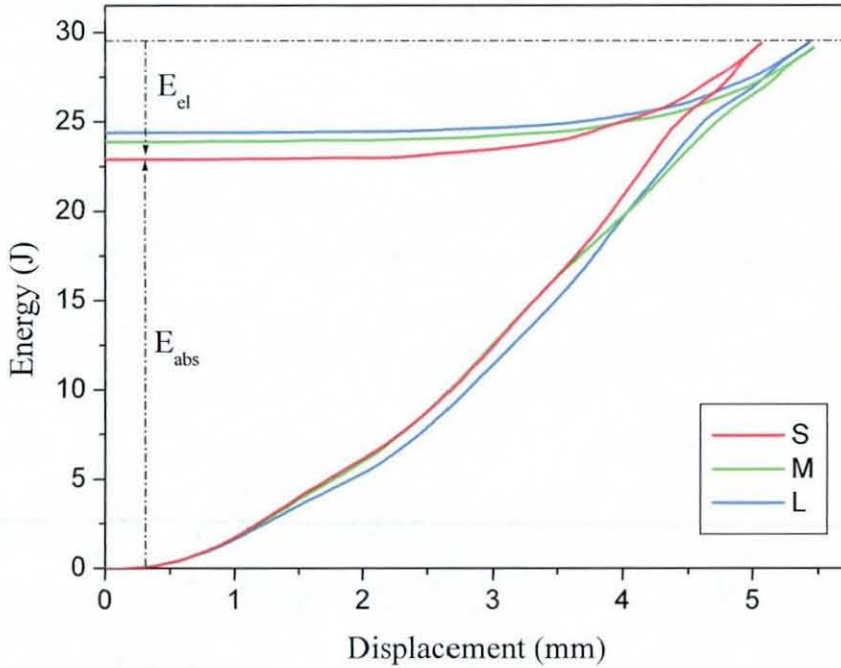


Fig. 50(d): Average Energy-Displacement Results for 30Joules Impact

The curves for absorbed energy, E_{abs} , against incident impact energy (Fig. 51) for S, M and L shows very little difference. Dorey's [163] proposed equation, which states that the absorbed energy is proportional to the thickness of the specimen, may be valid in this case. In the current study the thickness variations, shown in Table 10, between the laminates were within the standard deviation.

The curves for elastic energy, E_{el} , against incident impact energy for S, M and L are plotted in Fig. 52. Laminate S retains more elastic energy compared to laminate M and L at 30J incident impact energy level. The result could be attributed to the higher stiffness of laminate S.

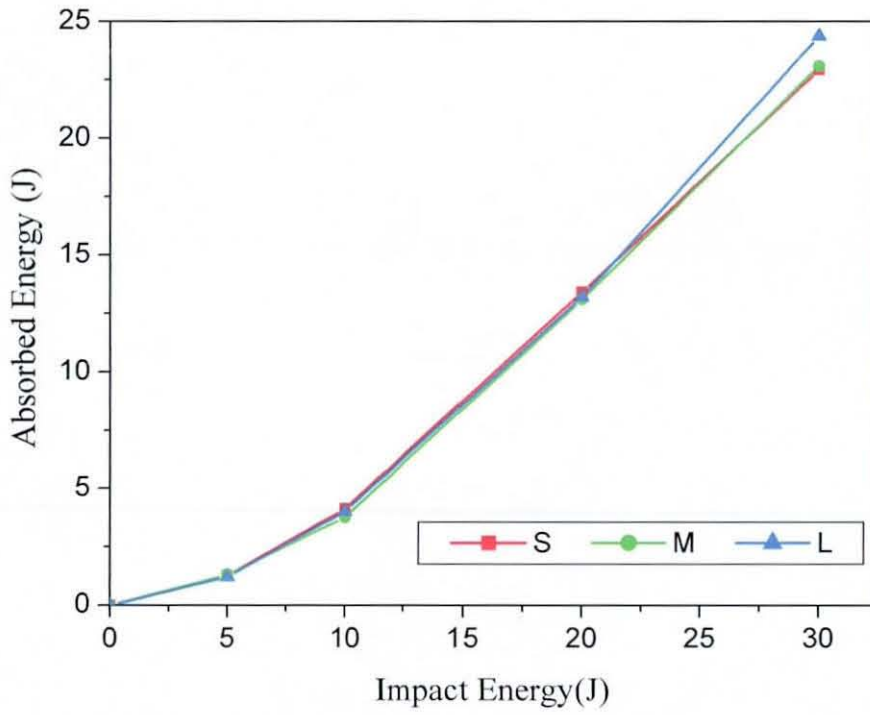


Fig. 51: Effect of Impact Energy on Absorbed Energy

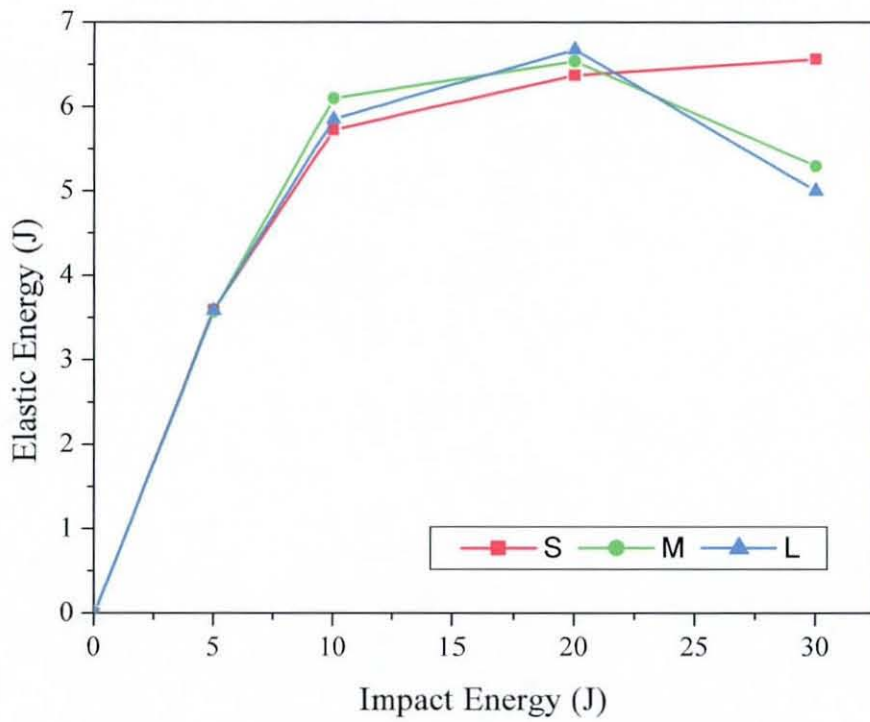


Fig. 52: Effect of Impact Energy on Elastic Energy

5.3.6 Impact Response: Strain-Rate Dependency

The strain-rate dependency is a characteristic of composite and polymeric materials. The strain-rate dependence of the tested composites is important because the strain energy accumulated in the material is related to it. The viscoelasticity describes the strain-rate dependency of polymeric material. Composite materials have several failure modes and the strain rate sensitivity can result in a change from one failure mode to the other. Fig. 53(a)-(c) show the results of force-time and energy-time plots for laminate S at 10J, 20J and 30J respectively. The data were filtered at 1 kHz and the mean was plotted. The results show a lag of the energy-time plot (shown by green dotted lines) with respect to the force-time trace. These results emphasize the importance of including material viscoelasticity, along with other parameters, in the analysis concerning the prediction of the mechanical response of laminated composites under impact loading.

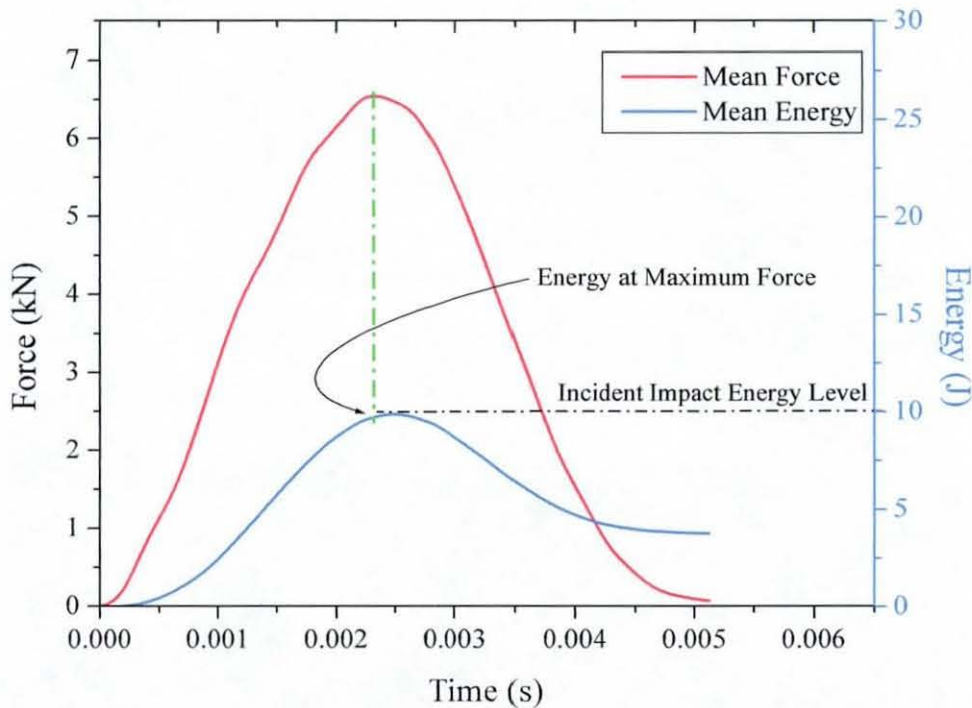


Fig. 53(a): Force-Time and Energy-Time Plot of Laminate S at 10Joules Impact

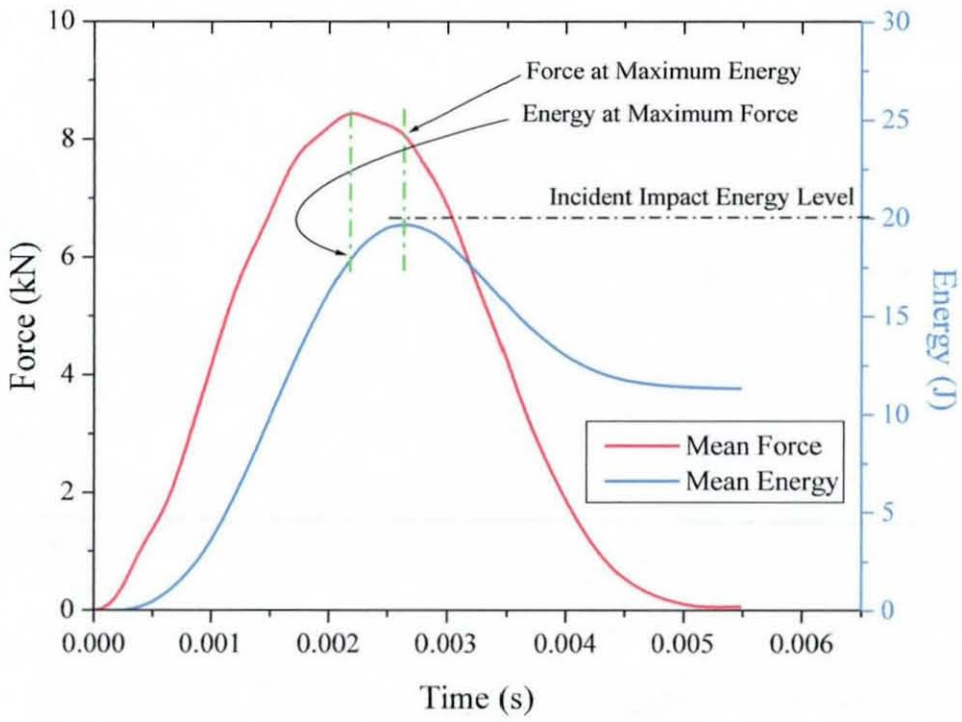


Fig. 53(b): Force-Time and Energy-Time Plot of Laminate S at 20Joules Impact

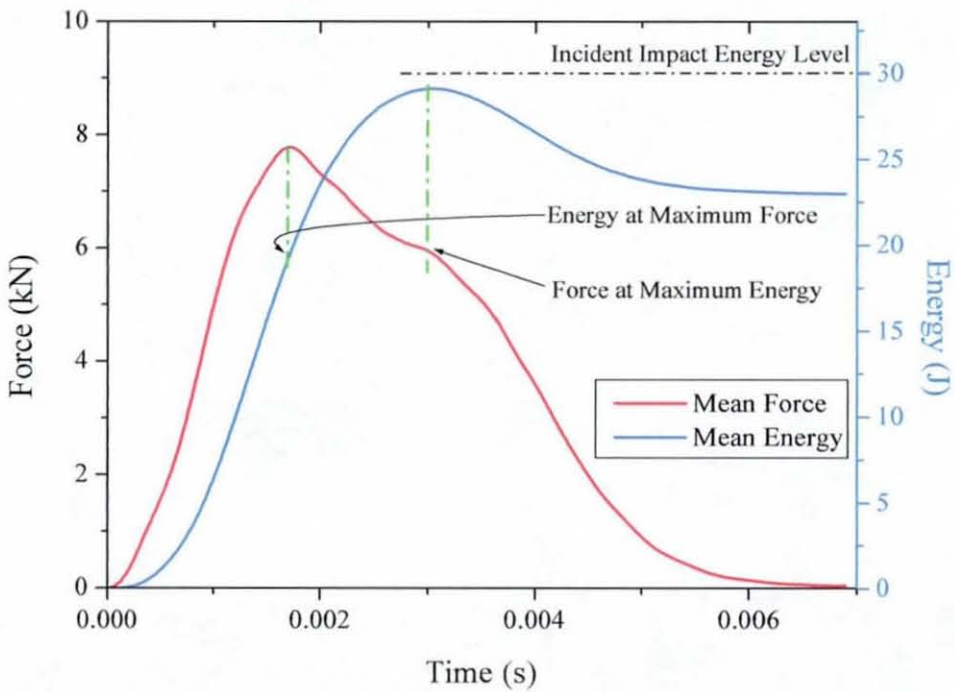


Fig. 53(c): Force-Time and Energy-Time Plot of Laminate S at 30Joules Impact

5.3.7 Final Damage State

Final damage state after impact is important as it determines the residual strength of the damaged structure. In the literature review section, it was stated that both the lateral extent and through thickness distribution of damage can effect the residual strength (Chapter 3). For CFRP, both destructive (including photographs and schematic diagrams recording the damage state) and non-destructive methods (C-scan) are used to assess the damage extent. In the following subsections results from both these methods are discussed.

5.3.7.1 Delamination Mapping

Delamination mapping was carried out by sectioning the impact point into two halves across the 0° fibres. The Figs. 54-56 and 59 show the maps for 5 and 10 Joules, and actual micrographs of laminates S, M and L after 20 and 30Joules impact respectively.

The mappings for 5J show delaminations within the fabric at dissimilar faces and between the fabric plies on the tensile side. 10J delamination mappings show a similar trend. While the extent of damage increases, a cone-shape pattern becomes evident and damage also occurs on the compressive side.

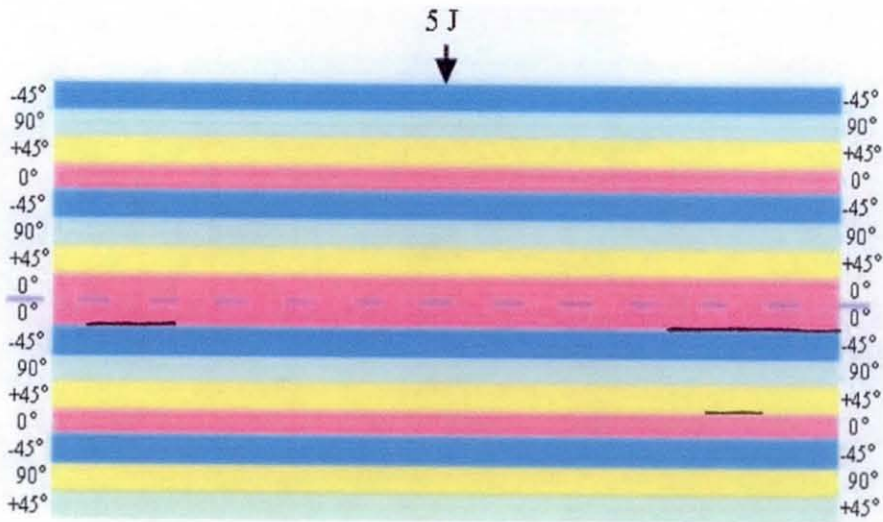


Fig. 54(a): Delamination Map of a 5J Impact on Laminate S

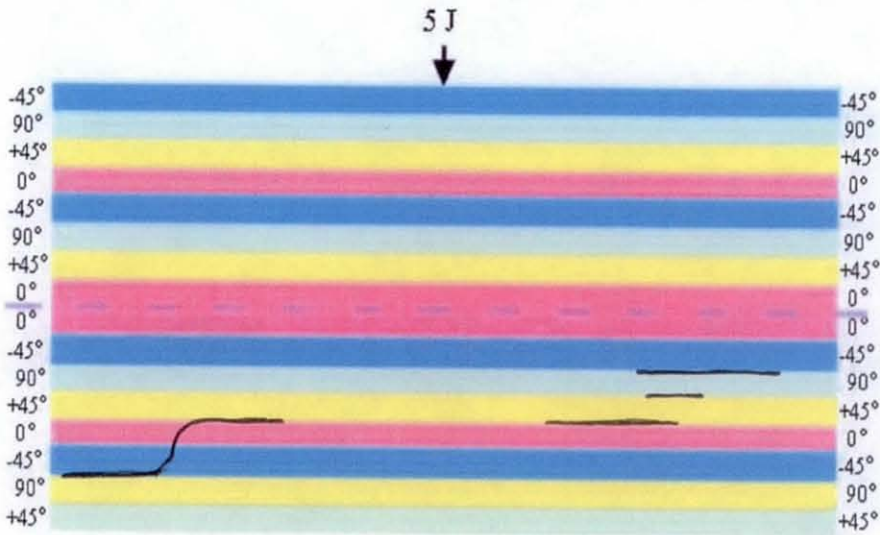


Fig. 54(b): Delamination Map of a 5J Impact on Laminate M

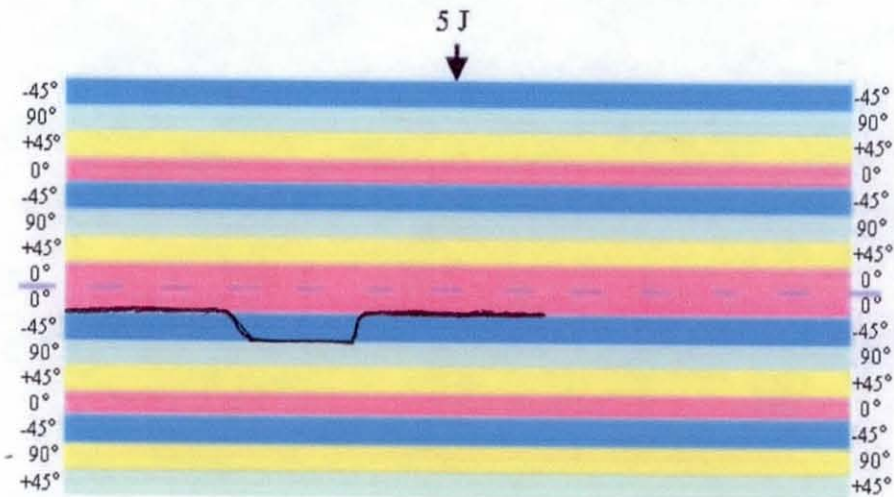


Fig. 54(c): Delamination Map of a 5J Impact on Laminate L

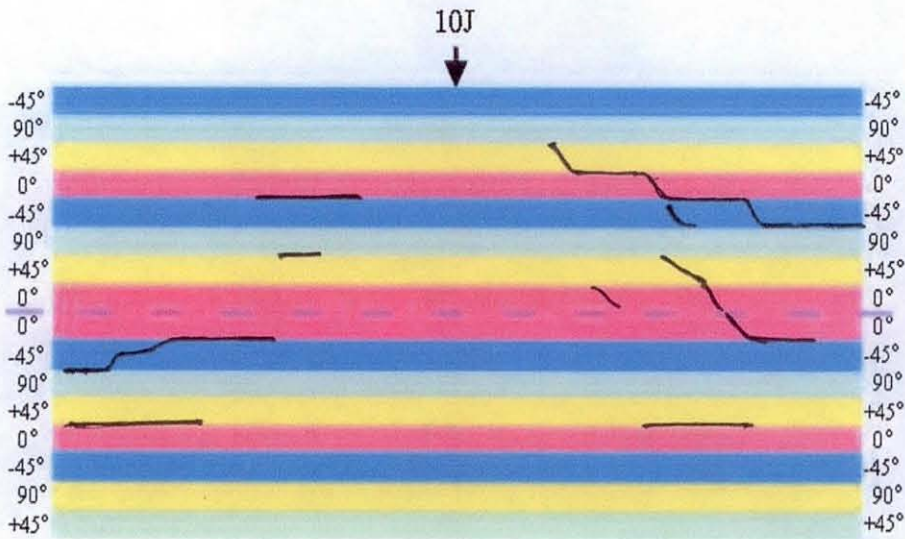


Fig. 55(a): Delamination Map of a 10J Impact on Laminate S

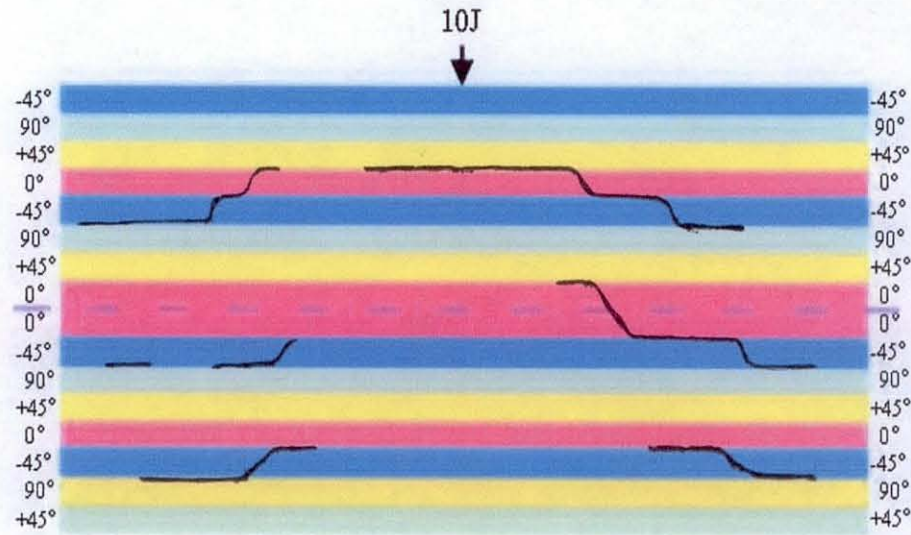


Fig. 55(b): Delamination Map of a 10J Impact on Laminate M

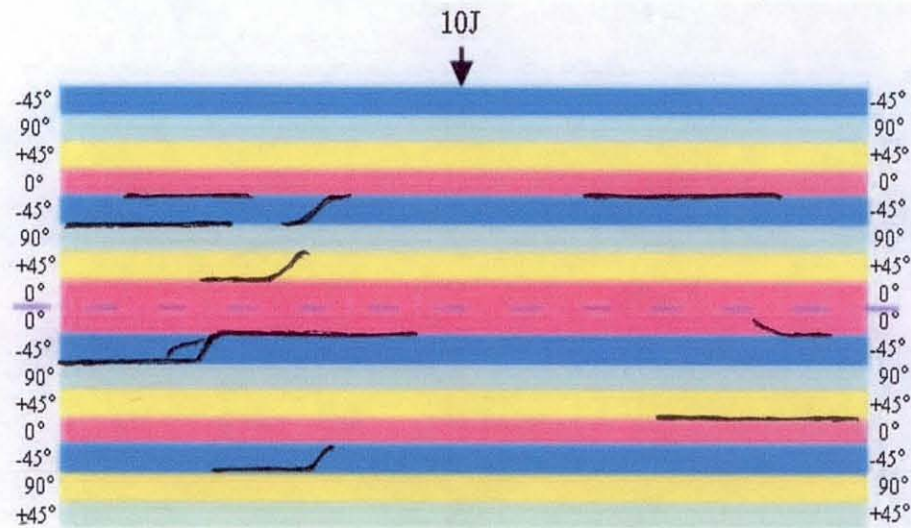


Fig. 55(c): Delamination Map of a 10J Impact on Laminate L

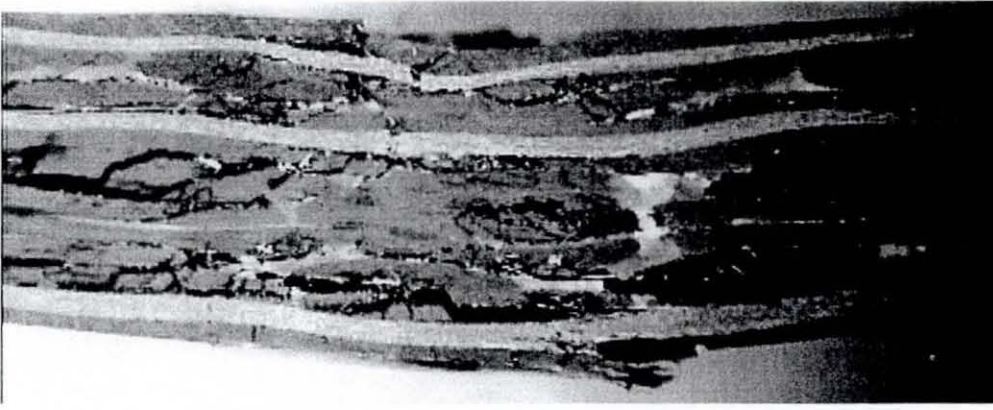


Fig. 56(a): Delamination Map of a 20J Impact on Laminate S

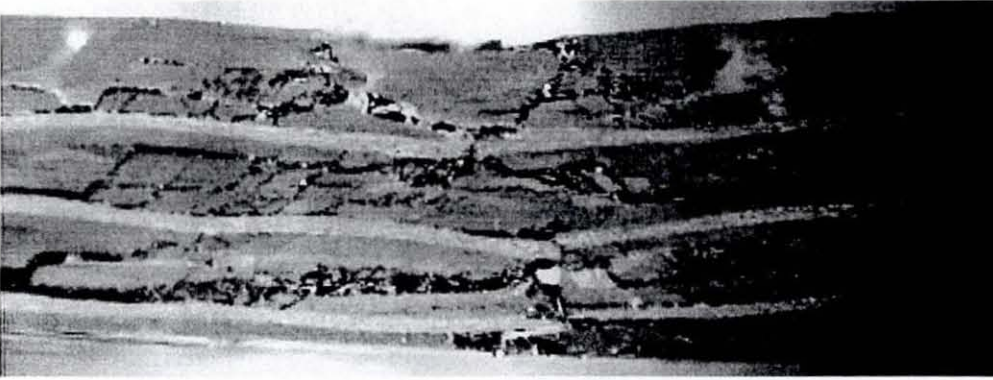


Fig. 56(b): Delamination Map of a 20J Impact on Laminate M

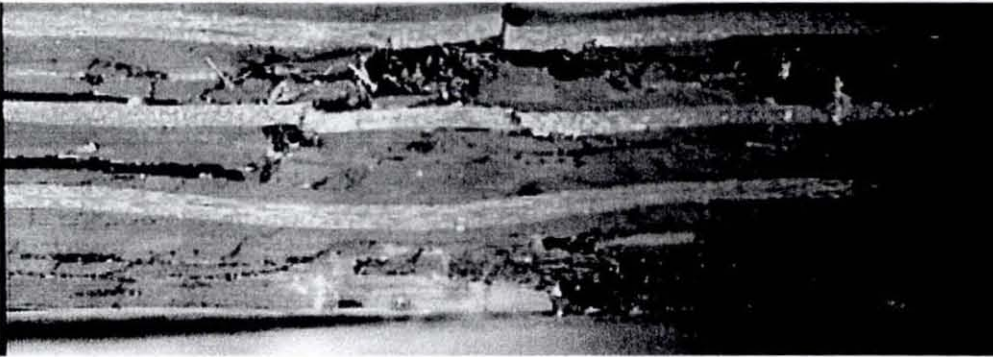


Fig. 56(c): Delamination Map of a 20J Impact on Laminate L

In the photographs, Fig. 56(a)-(c), of the 20J impact samples, more extensive damage was evident. The density of the transverse cracks was found to be more in S and M compared to L. Stitching yarns were shown to reduce or stop the propagation of the delamination, however, the crack density increased in the process. Transverse cracks, shown in Fig. 57, were also influenced by the local fibre architecture: cracks seem to have deflected around the periphery of the tow bundles rather than passing through them.

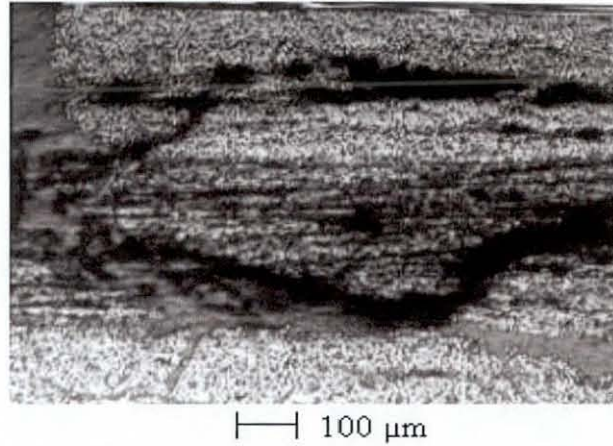


Fig. 57: Crack Propagation around the Tow

The origin of the delamination in a particular ply seen in Fig 56(a)-(c) only gives an indication of the likely position. The Fig. 58(a)-(b) showing the delamination mapping along and across 0° fibres, for a 20J impact sample of laminate S, show a rather peanut shape, recorded by number of other researchers [123, 160].

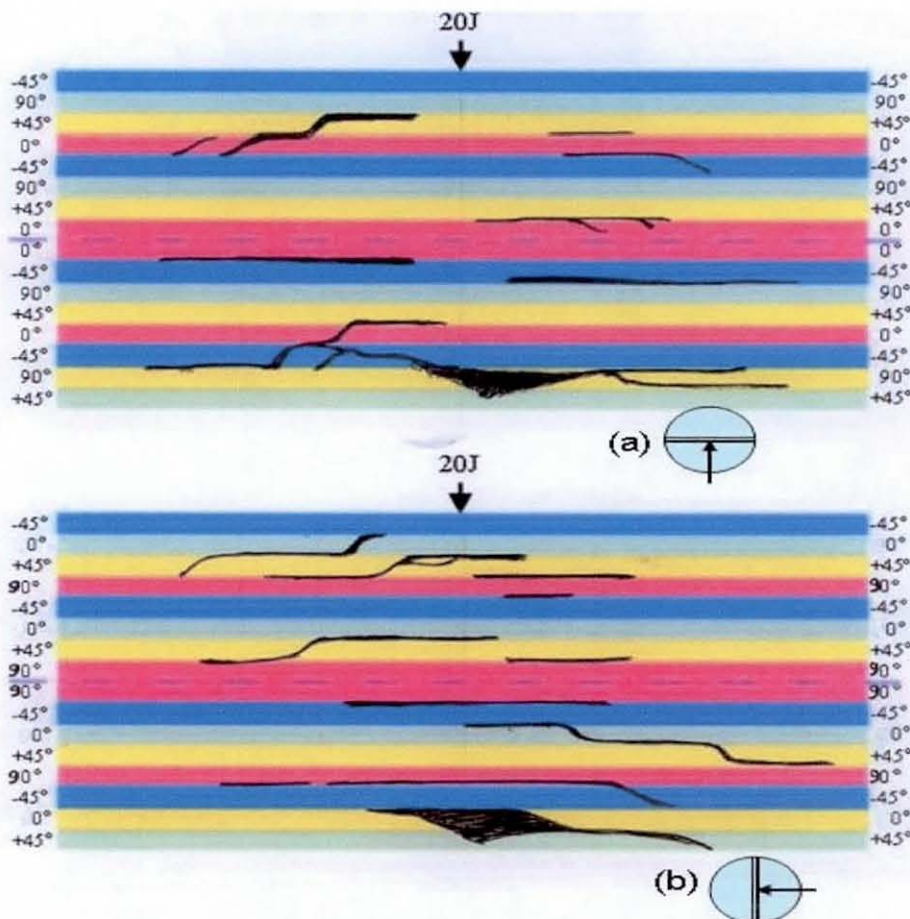


Fig. 58: Delamination Map of (a) Across 0° and (b) Along 0° Tows

A further observation of interest is that the delaminations were never observed at the neutral axis, even though at this position the interlaminar shear stress is higher than layers further from the centre. The reason for this is that the laminates were made symmetric; the 0° fibres from both the fabric plies in the middle got fused together during the compaction, and act as a single ply.

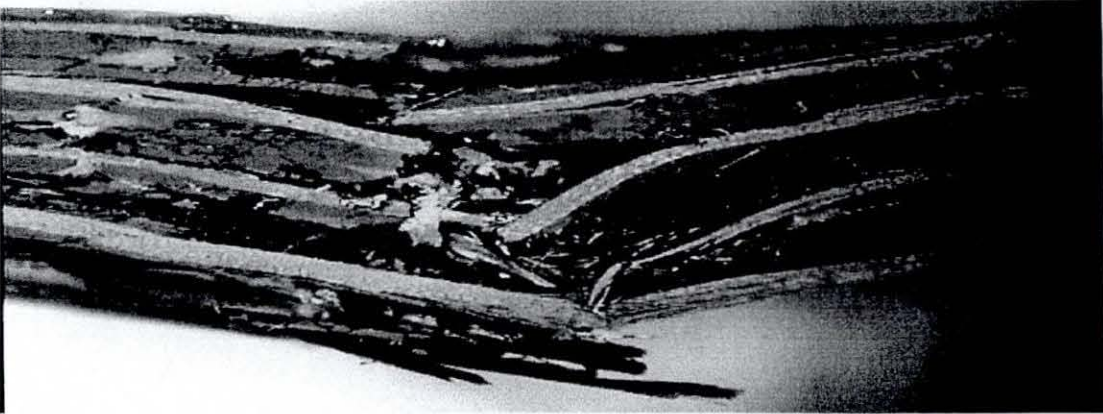


Fig. 59(a): Delamination Map of a 30J Impact on Laminate S



Fig. 59(b): Delamination Map of a 30J Impact on Laminate M

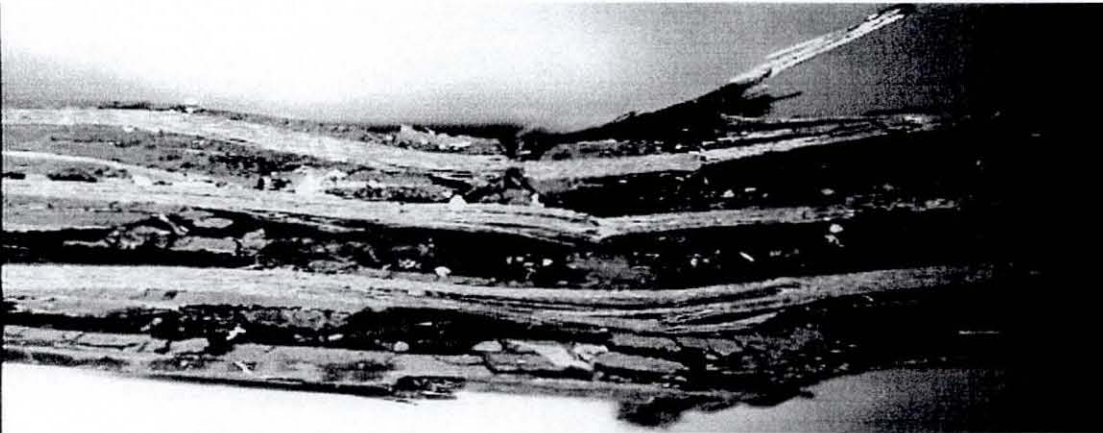


Fig. 59(c): Delamination Map of a 30J Impact on Laminate L

In the photographs of the 30J impact samples, extensive damage is displayed. The C-Scan results shown in Fig. 32 did not show any major increase in the delamination area (which in a way was restricted by a limited clamping area). However, the absorbed energy data presented in Fig. 51 shows a doubling of energy absorption. This extra energy was evidently used in breaking the fibre tows. Laminate S showed the largest amount of fibre breakage along with displacement, while M and L showed reduced levels of each, with L showing the lowest amount. Laminates L and M shows more matrix damage, larger cracks, which thus reduce energy available for fibre breakage.

5.3.7.2 Thermal Deply Analysis

Due to limited material availability, only one sample each (of laminate S) after 10J, 20J and 30J impact were chosen for thermal deply analysis. The results for 10J and 20J were not successful as the light yellow residue, left after the resin burn-off, was very little and was difficult to quantify. The reason for this problem was thought to be related to the lower extent of damage in the samples, leading to restricted pathways for calcium oxide to percolate and settle in the damaged area.

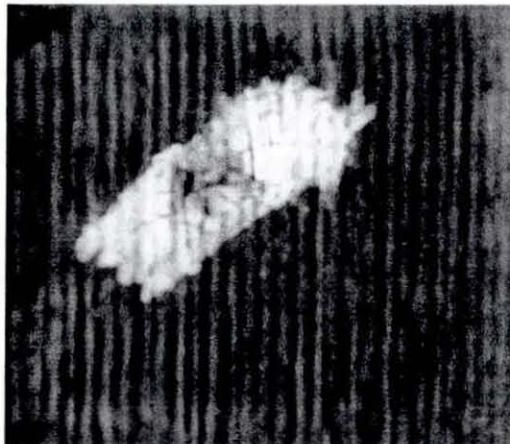


Fig. 60 (a): Top View of the De-plyed 0° Layer

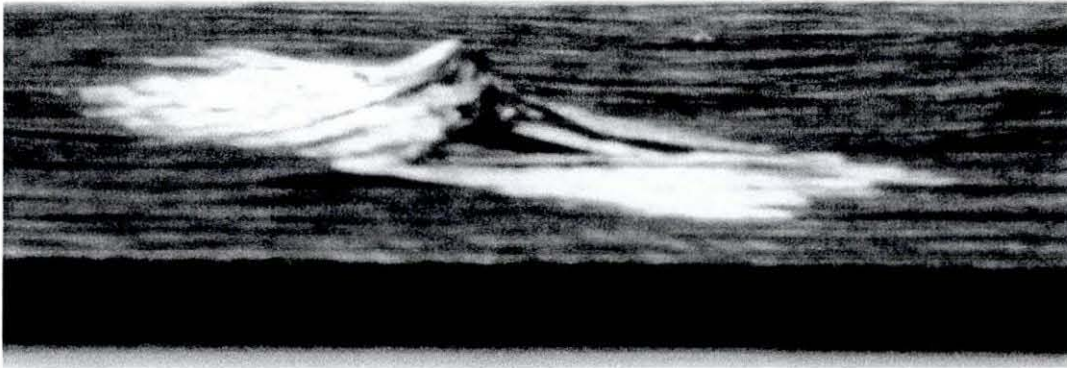


Fig. 60 (b): Side View of the Deploded 0° Layer

A better result was obtained for the 30J impacted sample. After partial resin burn-out, a sharp blade was used to separate the plies out from the tensile face of the impacted sample. Figs. (a)-(b) show the top and side views of the stained surface showing the first 0° layer from the tensile face. A golden marker was used to mark out the light yellow stain initially present. The overall damage area found through this process was still significantly lower than that found in the C-scan image.

It, therefore, was concluded that calcium oxide was not very effective as a staining agent for the laminate used in the current study. Calcium oxide did not impregnate the damaged areas well, which may be due to its large particle size. However, this method still was found to be suitable for the measurement of length of fibre breakages in the current study but was not investigated further.

5.3.7.3 Ultrasonic C-Scan Analysis

The damage area for all impacted samples was assessed using non-destructive ultrasonic C-Scanning. After the initial calibration of the instrument it was possible to acquire an image of the in-plane extent of the damage. The resolution of the C-scanner used was low and therefore, it was not possible to find the exact location, in the lay-up, of the damage as is believed to be the case for newer models of ultrasonic C-scanners. Despite the disadvantage of this damage detection technique, the images produced were used to complement the results.

The damage area of all the samples were subsequently quantified using image analysis software – Image-Pro® Plus. After the initial length calibration and manual selection of the damaged area, the software calculated the damage area in cm^2 . The damage areas of each laminate, for 10J, 20J and 30J incident impact energy levels, were averaged and standard deviations were calculated for further analysis of the results. The 5J impacted samples were excluded from damage area analysis, as the extent of damage was very small in these samples.

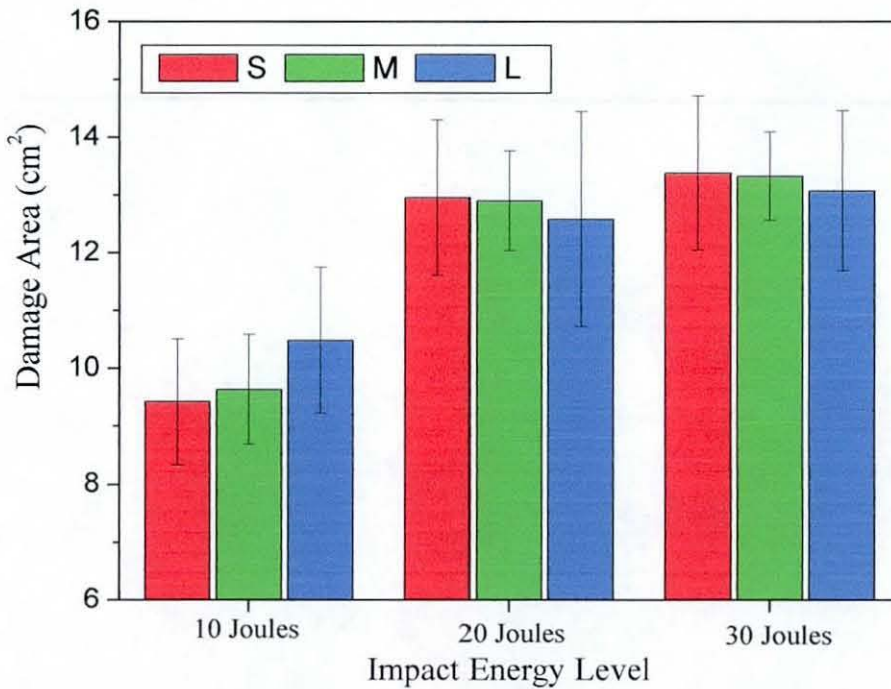


Fig. 61: Effect of Impact Energy on Damage Area

Fig. 61 shows a plot of damage area as a function of incident impact energy. It is evident from the figure that damage area does not increase significantly with incident impact energy, beyond the 20J impact energy. The primary reason for this is that the small clamping area acts as limiting factor. However, Fig. 51 in section 5.3.5, clearly showed increase in absorbed energy after 20J, indicating that damage in the material is still increasing in the through-thickness direction, mainly through fibre breakage. The 2D nature of the C-scan image, therefore, gives a fallacious picture of the true state of damage in the case of the 30J incident impact.

The overall trend in Fig. 61 therefore, shows the effect of stitch density on the in-plane damage. Higher stitch density, Laminate S, was shown to limit the in-plane damage area during lower energy impacts. However, at higher impact energy levels this effect was not significant.

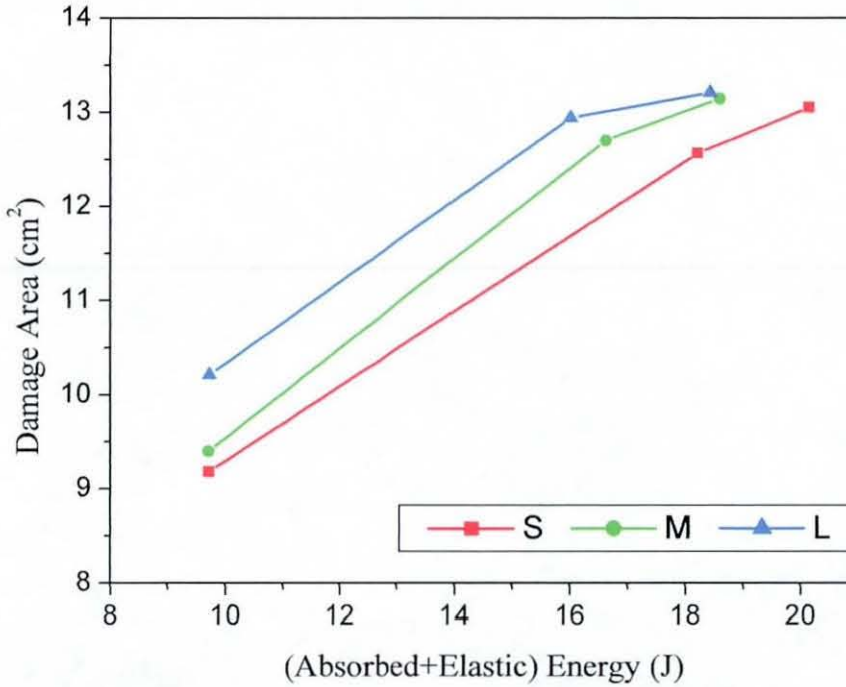


Fig. 62: Effect of Absorbed Energy on Damage Area (Avg. Values)

Fig. 62 gives more insight into the effect of stitch density. Data points at the left of the Fig. 62 show that for similar total absorbed energy (absorbed and elastic), laminate S limits the damage area to a minimum compared with laminate M and L. Data points in the far right of the same figure show that for similar damage areas laminate S was able to absorb higher energy. These results show that higher stitch density leads to higher damage resistance. This outcome was supported by the delamination mapping where it was observed that the stitching yarns were reducing or stopping the propagation of the delamination.

Analysing all the results of damage analysis it seems that there is more damage when width-wise stitch density is reduced, that is, between laminate M and L, rather than between laminates S and M. The reason is due either to the reinforcement architecture, mentioned earlier in Table 4, or the geometry of the

test samples. This latter reason could be supported by the results found in a QinetiQ based study [151] on the same reinforcements, using a 100mm diameter clamping. They carried out impact testing with the Boeing standard (for CAI) and found contrary results to those presented here.

5.3.8 Concluding Remarks

The fracture mechanisms in the MWK appear to be a combination of shear/transverse and delamination fracture, which is the same as that of traditional prepregs. However, a closer inspection, through delamination mapping, reveals that the intricate nature of the cracking pattern in the MWK laminates was directly influenced by the complex fibre structure. The fractures that occurred inside a ply were subjected to obstacles caused by the stitching yarns, which caused the fractures to divert or stop. The ripple appearance of the fracture surface can also be attributed to the *tow nesting* and the gap between the tows (evident from the photographs of the fabrics shown in the Table 4).

Furthermore, one might expect delamination between the plies as there are no stitches. However, according to previous studies [8] the most likely plane of fracture would occur between plies of dissimilar fibre orientation. This hypothesis seems to be effective in MKW, as there were no delaminations found in the $0^\circ/0^\circ$ interface, despite being in the highest shear stress zone, while delaminations were found in $0^\circ/45^\circ$ interfaces.

The results found are in agreement with the reported results on damage characterisation by Zhou and Greaves [164]. The dominant failure modes during low velocity impact are the initiation and propagation of delamination. Generally, the first fracture event during an impact is the formation of matrix cracks within the plies, caused by through-thickness shear stresses generated by the out-of-plane impact forces. Delaminations are usually initiated by opening forces at matrix cracks. Delamination growth is mainly driven by interlaminar shear stresses (mode II) induced by the bending of the laminate during the impact event. Finally, fibre fracture can be a significant energy absorbing mechanism at higher impact energy level and is generated by the high through-thickness forces

generated during impact (in the case of 30J impact). Fibres can either fail in tension generated during impact, or by shear-out during penetration of the impactor.

However, the relative proportions of the different damage modes are controlled by a variety of material parameters such as impactor conditions (shape, energy, mass and velocity) [165], material properties (matrix toughness, fibre surface treatment, moisture content, fibre stiffness and strength), stacking sequence and laminate geometry.

The effects of the stitching density found in this study were that less delamination occurred at high stitch density at lower impact level, and less fibre fracture occurred for low stitch density at higher impact level.

5.4 THROUGH PENETRATION IMPACT

This section deals with the through penetration properties of laminates S, M and L subjected to low-velocity, high-energy impact. Caprino and Lopresto [166] have shown that, for a given fibre type, the penetration energy is substantially influenced by the total fibre volume and impactor diameter, whereas other factors, such as resin type and content, fibre architecture, stacking sequence and orientations, play secondary roles. Bibo et al. [84] also suggested that through penetration energy depends on fibre volume fractions. Their claim was based on the results of three MWK glass fabric reinforced composites along with other prepreg materials. They plotted their results on a master curve (consisting of a range of materials and produced by Babic et al. [167]) with absorbed energy against thickness $\times V_f$ and found that the energy absorbed by the MWK was within the experimental error. Subsequently they concluded that stitch density along with other related fabric architecture of MWK did not have any effect on energy absorption during through penetration.

5.4.1 Results and Discussion

Through penetration impact was carried out on nine samples of each of the three laminates. They were impacted with a velocity of 4.4 (± 0.2) m/s – according to BS EN ISO 6603-2:2000 [135]. The striker mass was 10.2 kg. Emery paper was used on the top clamp for better grip. All the laminates were tested both at the front and the back faces (according to lay-up) in order to eliminate any effect of surface irregularity. A photograph of the damaged surface of laminate L is shown in Fig. 63. The force-displacement and energy-displacement of all nine samples for laminates S, M and L were averaged and plotted in the Fig. 64 (a)-(c).

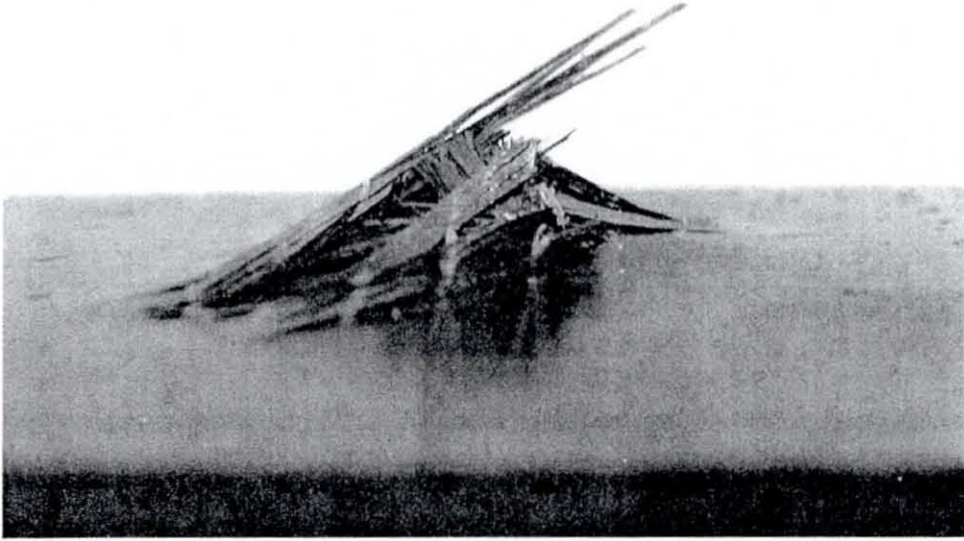


Fig. 63: Photograph of the Damaged Surface (Tensile) of Laminate L

Using Belingardi and Vadori [168] suggestion the experimental definition of the perforation energy (E_p) was read at the penetrated point, where the force–time curve is nearly constant and the energy increases with a constant slop. They also suggested that two perforation failure zones for a specimen can be observed through-the-thickness: region I, fibre shear-out and fibre breakage; and region II, tensile fibre failure and delamination.

The force-displacement traces in Fig. 64 (a)-(c) show three significant drops in force at F_1 , F_2 and F_m contrary to two suggested by Belingardi and Vadori [168]. However, their conclusion was based on prepreg and woven fabrics and the impact conditions they had used were also different. In the current study, it is evident from Fig. 64 (a)-(c) that after the drops of force at F_1 and F_2 the corresponding energy absorption rates increase, clearly indicating some form of damage in the impacted samples. From the traces it would not be possible to identify the exact mode of failure, however, it could be speculated that the force drop at F_1 is associated with fibre shear out and matrix cracking, followed by delaminations and fibre tensile failure in two stages at F_2 and F_m .

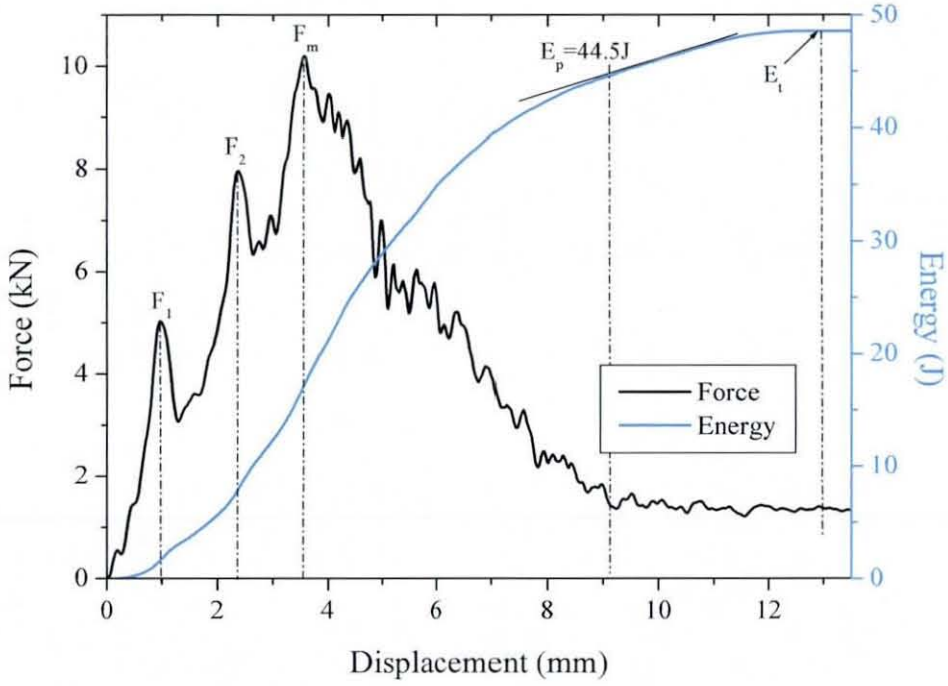


Fig. 64(a): Force-Displacement, Energy-Displacement History of S

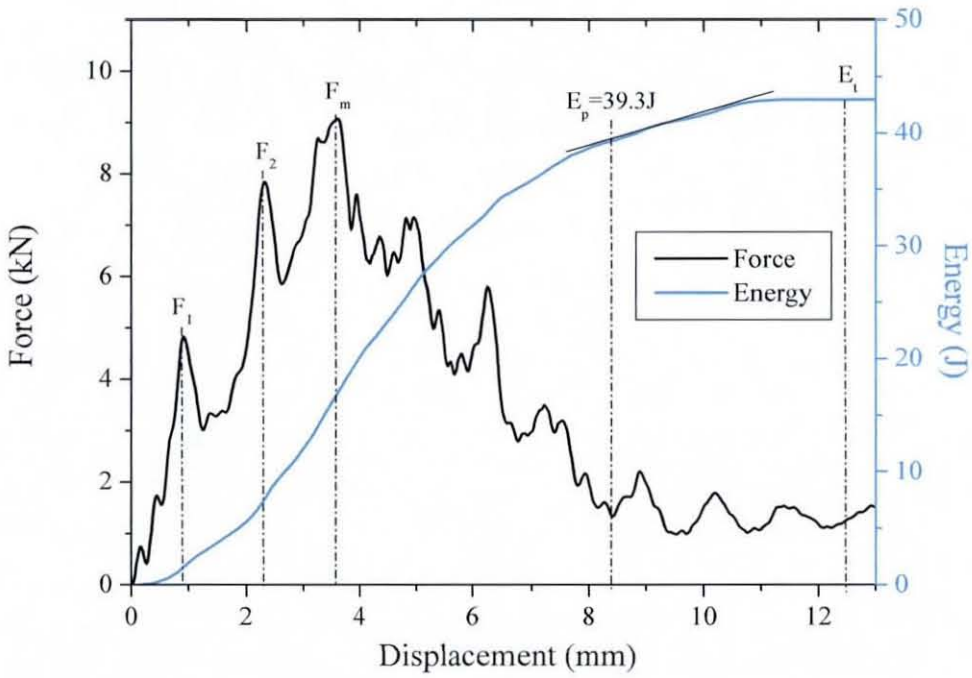


Fig. 64(b): Force-Displacement, Energy-Displacement History of M

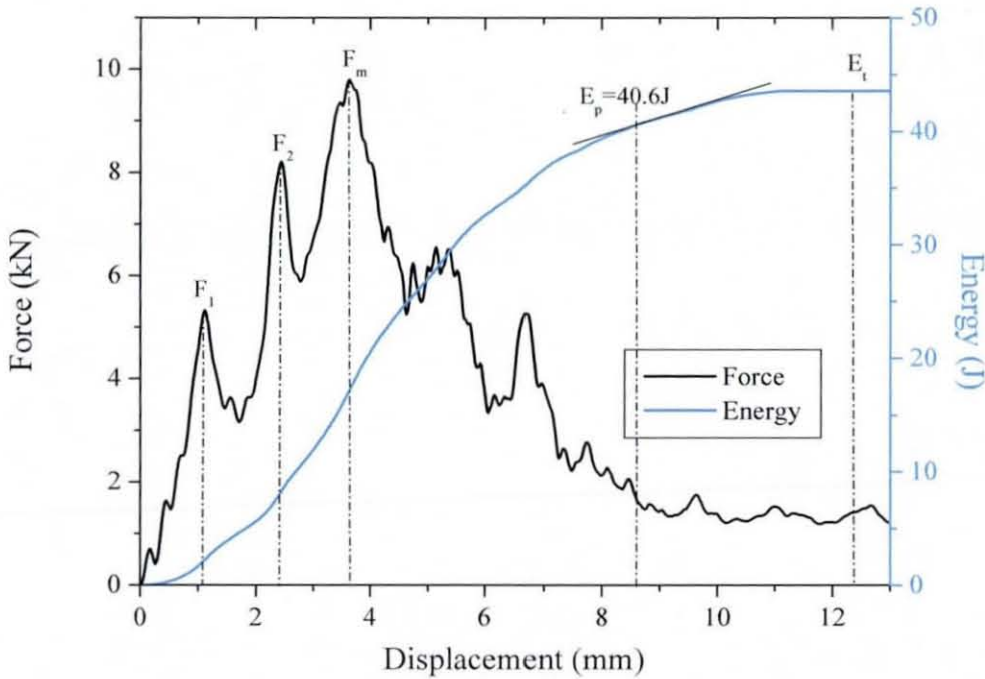


Fig. 64(c): Force-Displacement, Energy-Displacement History of L

The experimental perforation energy (E_p) was measured according to the definition given by Belingardi and Vadori. It is apparent from the values that laminate S performs the best under through penetration impact. The E_p value for S was 13.2% and 9.6% more than that of M and L. These results show that S performed better than laminates M and L. The standard deviation had a maximum value of 2.03J indicating no statistical difference between M and L. Therefore, it could be suggested that stitch density does have some effect, of secondary order, on the through penetration impact properties, as suggested by Caprino and Lopresto [166].

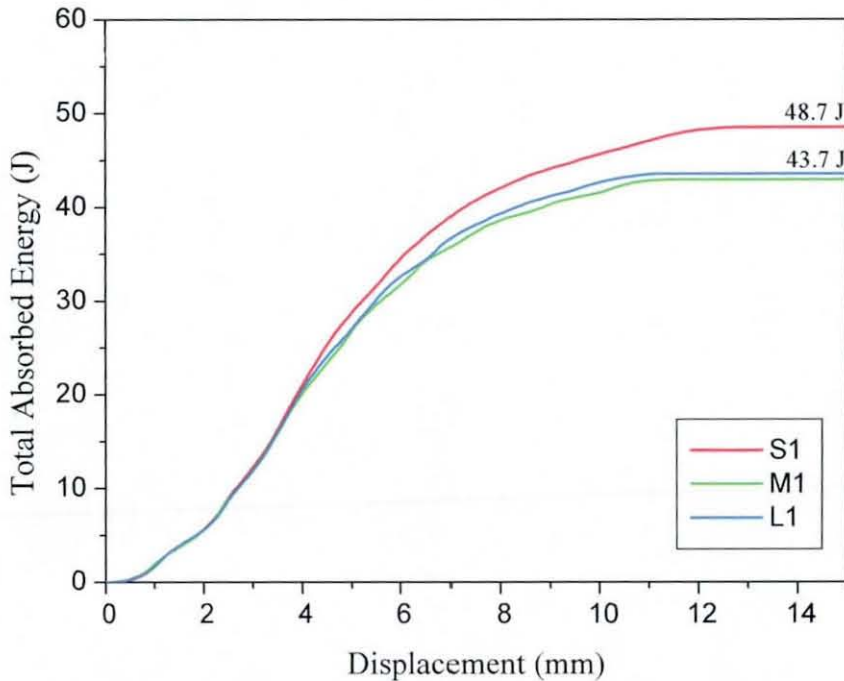


Fig. 65: Energy versus Displacement trace for Through Penetration Impact (Avg. Values)

Fig. 65 shows the comparison of the energy-displacement traces of all the laminates. It is interesting to observe that the absorbed energy values for all three laminates remain constant up to a displacement of 4 mm. The final absorbed energy values show that laminate S absorbed the highest energy, followed by laminates L and M. The high stitch density of S, therefore, comes into play as the damage grows during the impact event.

One other observation that needs explanation is that, as the indenter did not rebound during through penetration impact, the energy-time curve continued going up (Fig. 65) unlike the low energy impacts. This was due to friction on the edges of the perforation hole against the lateral surface of the indenter as shown by Shyr and Pan [38]. The total absorbed energy, E_t , for S, again shows a value approximately 12% more than for M and L, suggesting that high stitch density has an effect in resisting perforation. However, the relationship between perforated energy and thickness was not easily found in the penetration cases.

Finally the absorbed energy for laminate S, M and L are plotted on the master curve produce by Babic et al. [167] and shown in Fig. 66. The values of the

absorbed energy of the current study seem to be less than those reported by Babic et al. This is due to the fact that the geometry and test condition used in their case is different from the current study. However, the assumptions taken into consideration by the authors still hold (that the number of fibres within a given cross-sectional area of the material governs both impact strength and toughness) and in that respect it can be concluded that higher stitch density does have an effect in through penetration impact.

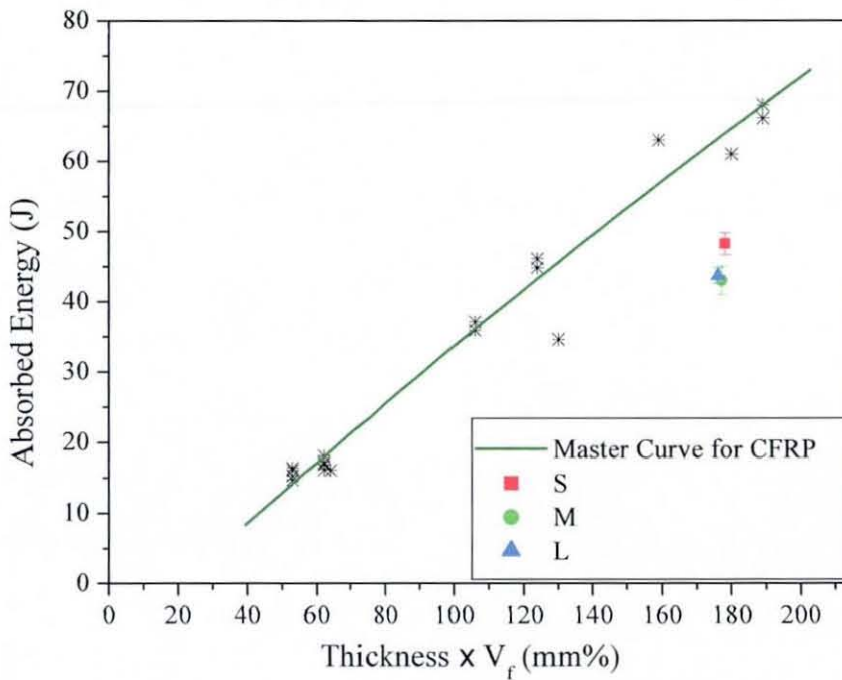


Fig. 66: Energy Absorbed in Thorough Penetration Impact vs. (Thickness x V_f) Compared with data from Hogg [169]

5.4.2 Concluding Remarks

The ability of a MWK carbon fibre composite to absorb energy in a through-penetration impact can be increased by increasing the stitch density. This behaviour is contrary to the case of absorbed energy during non-penetrating low velocity impact as shown earlier (Fig. 51). It, therefore, can be concluded that high stitch density in MWK would probably give better performance during high energy incident impact conditions.

5.5 COMPRESSION TESTING

In this section the results of the compression tests on dry undamaged and impacted samples will be presented and discussed. The compression tests were carried out using the QMW miniature anti-buckling guide described in section 4.4.4. Four samples of laminates S, M and L were tested unimpacted and samples impacted with 10, 20 and 30 joules incident impact energy. Two 5 joules impacted samples were also tested in compression.

5.5.1 Compression Testing of Unimpacted Samples

A measure of the unimpacted compression strength provides the base-line strength for the compression after impact samples. The compression testing was carried out in the miniature anti-buckling guide, as pure compression testing would yield different results. However, miniature testing had its own drawbacks. Two types of failure were noticed for unimpacted samples. Firstly, some of the samples failed through end-crushing i.e. they tended to crush at either ends. One such end-crushed sample is shown in Fig. 67. Some trials with the samples revealed that it was due to the weakness of the anti-buckling guide – after every compression test the gap to hold the sample widened. Consequently the gaps in the anti-buckling guide were set every time before an experiment according to the sample thickness. Occasionally end crushing still occurred and in such cases the result was ignored. The likely reason for this event was probably stress concentration, due to unparallel ends. The force, instead of being distributed evenly across the full width of the sample, became concentrated at a raised portion of the sample causing the end crushing.

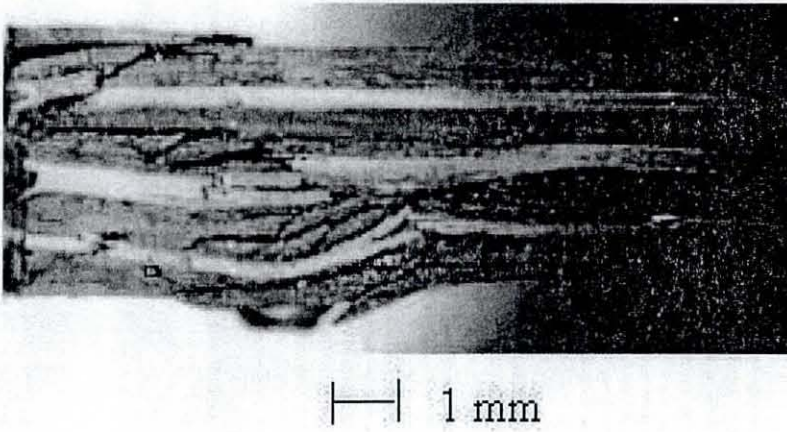


Fig. 67: End Crushing of the Unimpacted Sample

The second type of failure noticed was in the free end region of the test samples, i.e. between the top loading block and the top of the side supports of the anti-buckling guide (Fig. 33). Photographs of such failed samples of laminates S, M and L are shown in Fig. 68. This type of compression failure was characterized by local buckling; fibre kinking was also evident. Most of the sample failures were accompanied by a loud cracking sound. However, in few a cases progressive failure was also noticed. All these types of failures were considered acceptable and were averaged to calculate the compression strength of the unimpacted samples for each laminate.

Both end crushing and buckling failure of the unimpacted samples have been reported by Prichard and Hogg [170] and Harper et al. [123]. For the latter type of failure they suggested that this was due to a concentration of local deformations. They also suggested that failures occurred at the onset of buckling. Both the claims appear reasonable, however, in the current study it could not be confirmed as the strain in the unsupported region was not monitored.

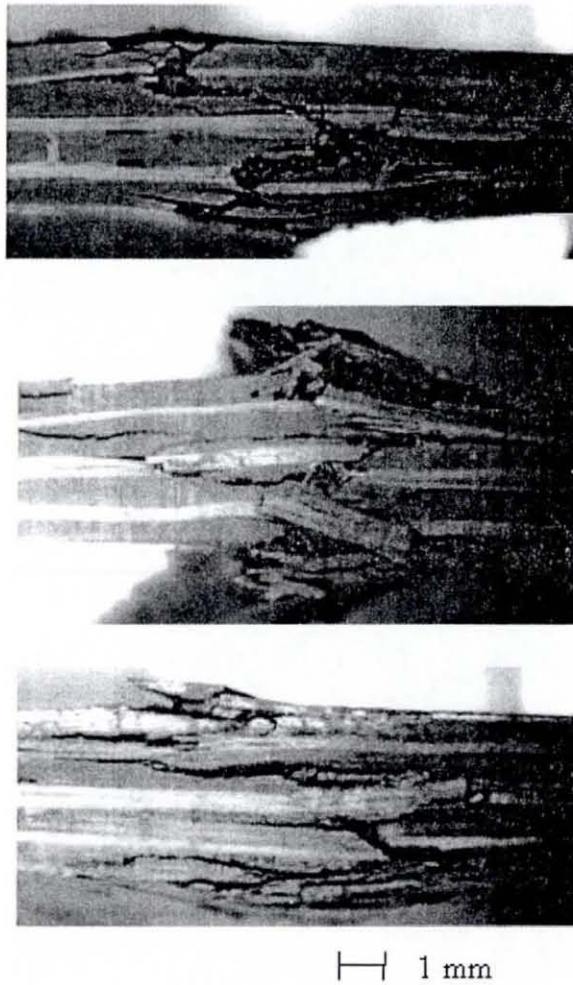


Fig. 68: Compression of the Unimpacted Samples (S, M and L from the top)

The average compression strength of the dry unimpacted laminates of S, M and L were found to be 280, 265 and 233 MPa respectively (Table 13), while the standard deviation varied from $\pm 4\%$ up to $\pm 22\%$ for all the laminates. The detailed strength result for each of the samples can be found in the Appendix. Foreman [151], using BS14126-inplane compression testing method on the laminates S, M and L, found that there was a slight reduction in the compressive modulus and strength with the reduction of stitch density. However, the compression strength values he found were higher compared to the compression results found in the current study using the QMW fixtures. Furthermore, the results he found for all three fabrics were all within one standard deviation.

In this work, the QMW miniature compression test yielded a decrease in compressive strength with reduction in stitch density, similar to the trend presented in Foreman's work. Nevertheless, it should be noted that the standard

deviation in the current work was very high and the trend shown by the compression strength could not be confirmed. Larsson [171] claimed better compressive properties with stitch density while Suh et al. [172], Mattheij et al. [173], and Mouritz [26] showed degradations of compressive properties with stitch density. All these references deal with over stitching but could be applicable to the present study.

5.5.2 Compression after Impact (CAI) Test

Compression after impact gives the measure of 'damage tolerance' of a composite material. This established concept is primarily based on the behaviour of unidirectional prepreg laminates. This damage mechanism is predominantly delamination, which is also the case for MWK laminates. CAI test results, therefore, should indicate any difference in the damage tolerance property of laminates S, M and L, consequently the effect of stitch density.

CAI testing was carried out on mainly 10, 20 and 30 joules impacted samples and two 5 joules impacted samples. Contrary to the problems faced during the compression testing of unimpacted samples, the impacted samples failed within the anti-buckling guide. Some photographs of CAI specimens after failure are shown in Fig. 70 in order to compare the extent and mode of damage.

The impacted samples failed in compression due to sideways propagation of delaminations, which was always perpendicular to the compression loading direction. Ultrasonic C-scans shown in Fig. 69 of a 10 joules sample of laminate S indicates that after CAI test shows clearly that delamination damage grew perpendicular to the compression loading direction. Very little extension of damage was observed in the loading direction, which is similar to the finding reported by Prichard and Hogg [170] for prepregs.

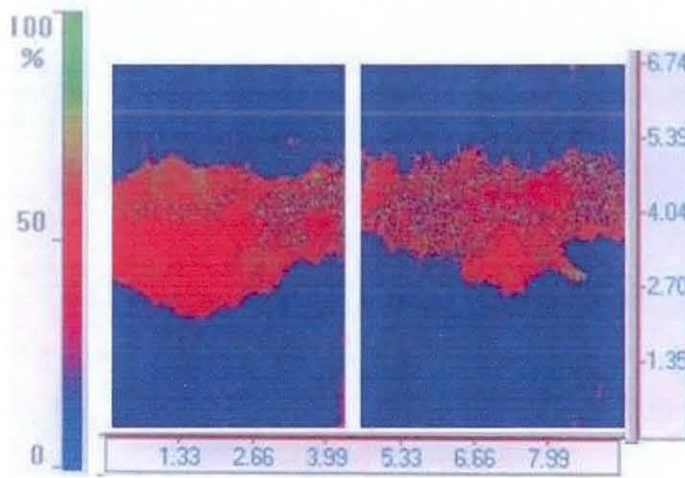


Fig. 69: Ultrasonic C-Scans of 10J CAI Sample of L (left) and S (right)

Closer examination revealed that the CAI samples failed in two modes under axial compression. The failures observed through the thickness of the samples were either a V-notched type (Fig. 70), where delamination buckling occurred on both sides of the sample, or a shear type, where the samples failed at around 45° to the axial loading direction. Samples of laminate S failed predominantly through V-notched type failure, with 75% of the 10 joules impacted samples and 100% of the 20 and 30 joules impacted samples failing in this way. Samples of laminates M and L showed similar trends to each other but unlike S failed primarily in shear. 50% of 10 joules impacted samples of both M and L failed in shear, while all the samples of 20 and 30 joules failed in shear.

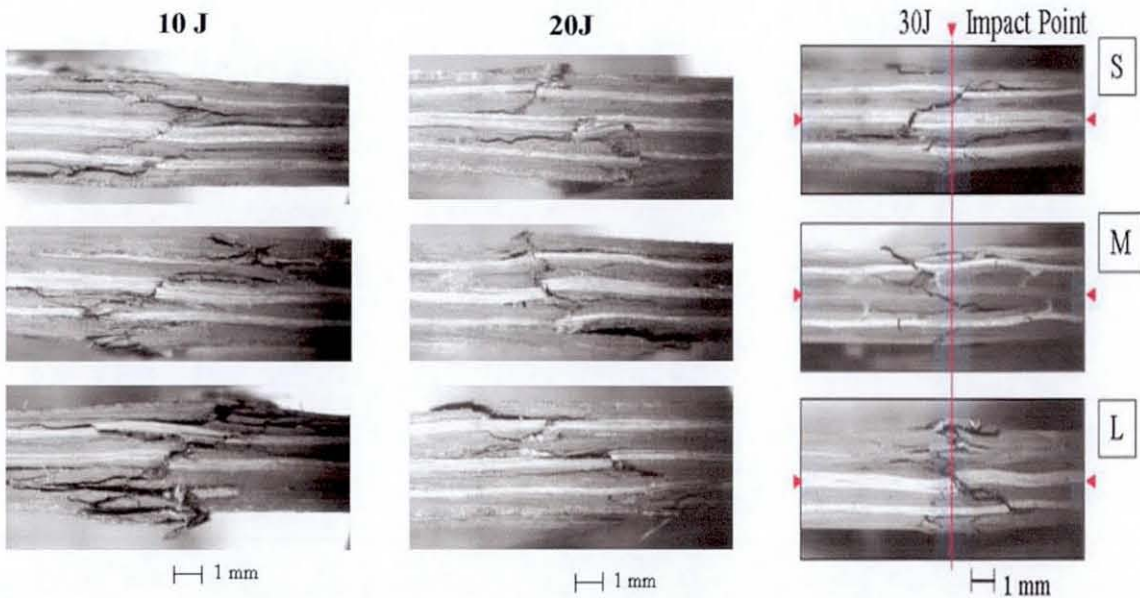


Fig. 70: Optical micrographs of CAI samples 10J, 20J, 30J

A summary of the results for the dry unimpacted and CAI samples are presented in the Table 13. The results of 5 joules impacted samples are not included as only two samples were tested. Detailed results of the other CAI samples are included in the Appendix.

Impact level	Compression Strength (MPa)		
	Laminate S	Laminate M	Laminate L
Unimpacted	280 (± 10)	265 (± 18)	233 (± 15)
10 Joules	167 (± 4)	169 (± 7)	168 (± 22)
20 Joules	157 (± 10)	144 (± 10)	148 (± 11)
30 Joules	140 (± 13)	120 (± 7)	125 (± 6)

Table 13: Summary of the Compression Test Results

A graphical representation of the compression strength results of unimpacted and impacted samples is shown in Fig. 71. The CAI results of laminates S, M and L show a downward trend with the impact energy: CAI strength dropped dramatically as the impact energy increased to 10 Joules, then gradually with increase of impact energy. The laminate S showed the best compressive strength when unimpacted and after being impacted at higher energy levels (20 and 30 joules).

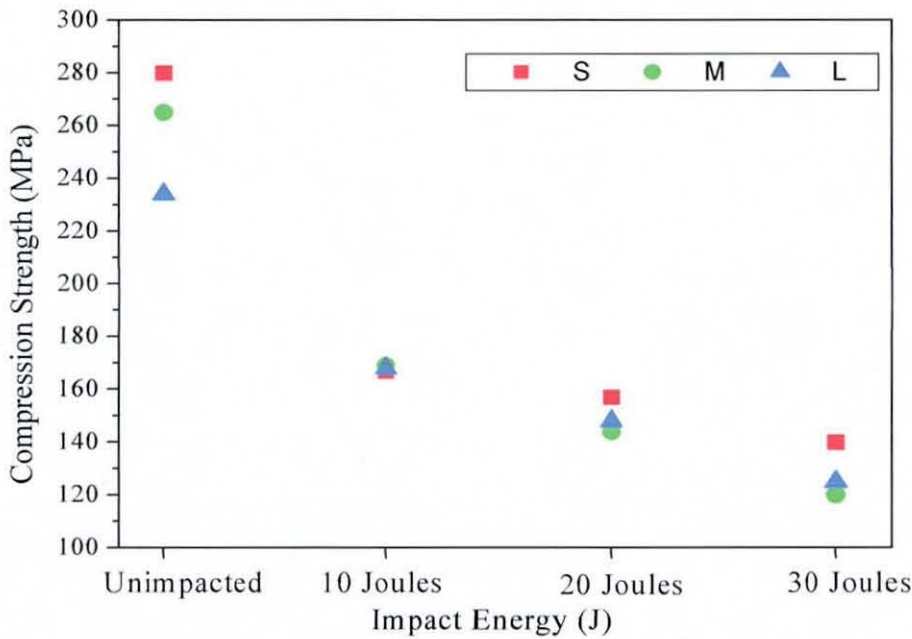


Fig. 71: Compression Strength versus Impact Energy

The behaviour of laminate L appears interesting. Despite having lower stitch density than laminate M, laminate L consistently showed a marginally better compression after impact strength value following 20 and 30 joules impact. These results are consistent with the damage area measurement found for laminates M and L after 20 and 30 joules impact, presented in section 5.3.7.3, where the overall damage area of L was lower than M at these impact levels.

This result, however, gets complicated when %retention in compression strength is plotted against impact energy level (Fig. 72). In this case the percentage retention of compression strength of laminate S is lowest compared to M and L at 10Joules impact energy level. As the impact energy level increases the strength retention percentages of the laminates continue to fall, but less so for laminate S compared to laminates M and L.

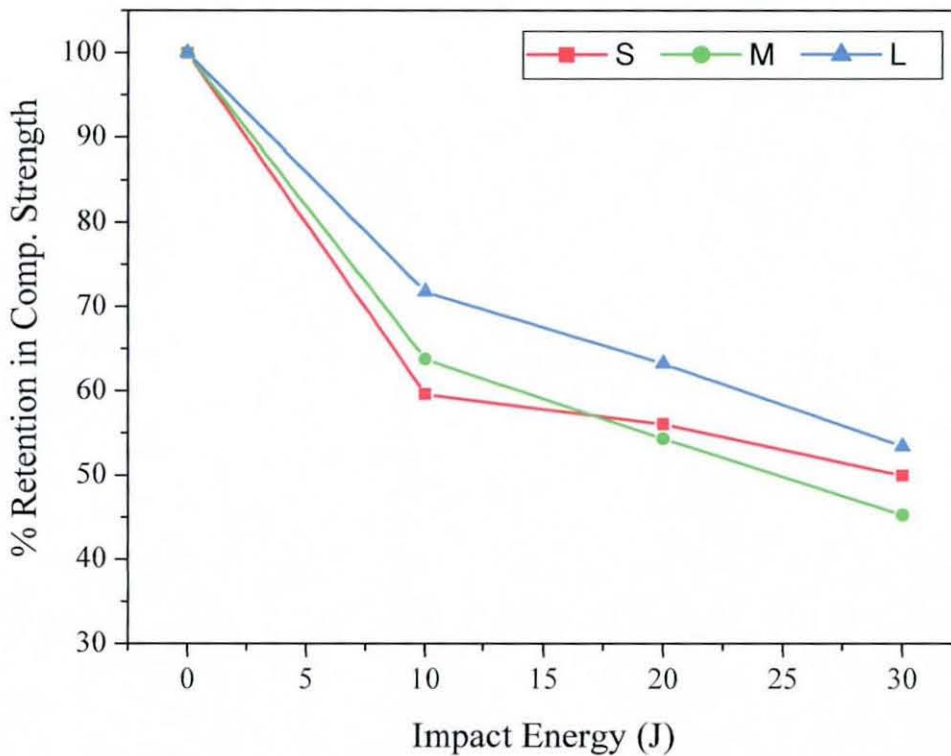


Fig. 72: Effect of Impact Energy on % Retention of Compression Strength

In section 5.3.7.3 it was reported that there were variations in the size of damage area for the same impact energy level. These variations led to high standard deviations in CAI strength results. In order to gain a better understanding of the

CAI results, all the CAI strength values were plotted against corresponding damage area as shown in Fig. 73. Linear fit lines of the results for each laminate were plotted, which indicate that there is a clear correlation between CAI and damage area. Though the data points are clustered they show a decrease in the CAI value with increase in damage area. However, there is no apparent correlation with the stitch density.

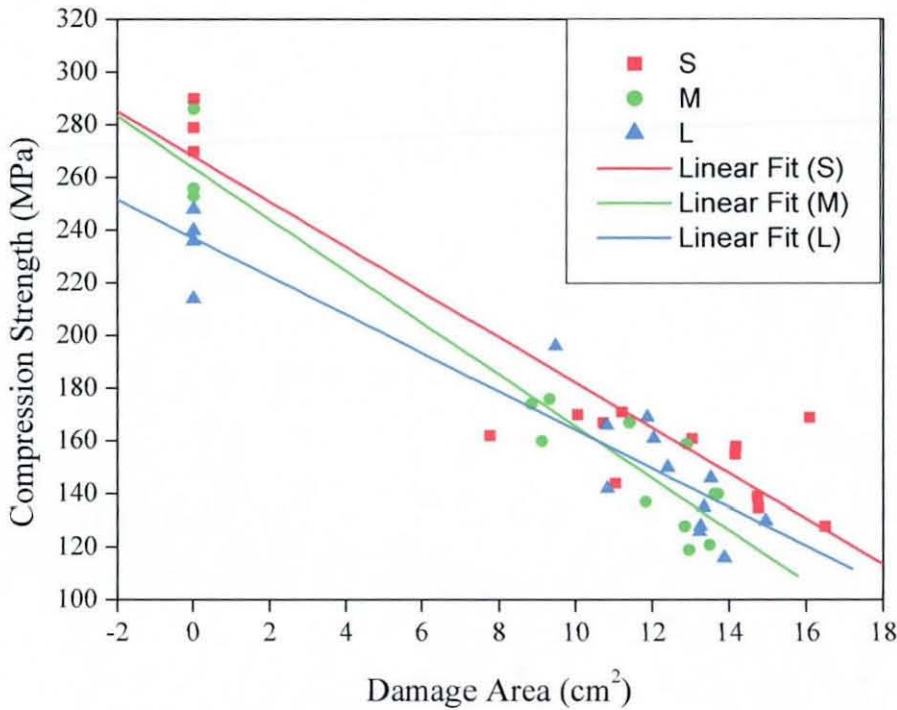


Fig. 73: Compression Strength versus Damage Area

Fig. 74 shows the compressive strength data excluding the undamaged laminates. The variations between CAI and damage area are shown by plotting all the CAI data and fitting them linearly for S, M and L. The trends show that stitch density has some effect on the residual compressive strength. Laminate S appear to have higher compressive strength, particularly after large impact. The compressive strengths of laminates M and L, though lower than S, show little difference after large impact. These trends correspond to the overall stitching density of the laminates.

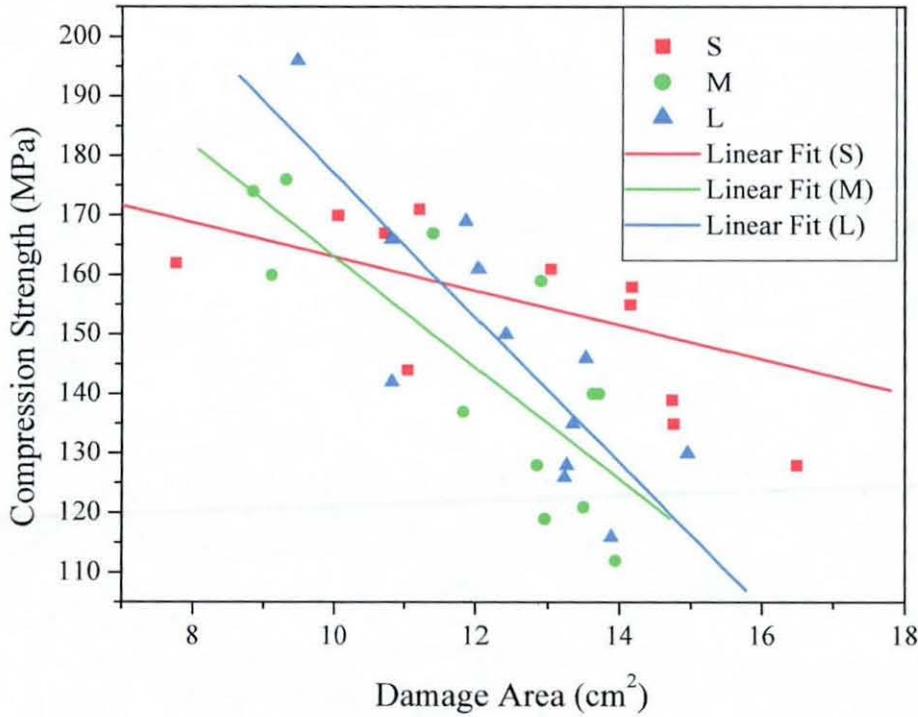


Fig 74: Compression Strength versus Damage Area

5.5.3 Evaluation of the Compression Test Results

Compressive properties are mainly controlled by fibre micro-buckling, which is influenced by a number of factors: fibre/matrix interface strength, matrix stiffness, fibre stiffness, matrix toughness and fibre waviness are often quoted. Among all these factors only fibre waviness was different in laminates S, M and L (Fig. 39) However, another factor that may have had an effect on the compression and CAI is the stitch density. Stitching yarn provides a bridging effect which stabilizes a composite structure through the inhibition of the local sub-laminate buckling tendency. Propagation of delamination is suppressed by stitching yarn through crack closure. Stitch density also dictates the waviness of the fibre layers.

During the compression of unimpacted samples the above two factors were relevant. The highest unimpacted compression strength was displayed by laminate S, which had the highest stitch density in both warp and weft direction. As the failure of the samples was perpendicular to the direction of the applied

load, the weft-wise stitch density was more responsible for the crack closure before a sample subsequently failed. Mode I results reported by Foreman [151] for these three types of fabric also showed laminate S to have better resistance. The intermediate and lowest compression strength values, displayed by laminates M and L respectively, also relates directly with the stitch density where L has half the stitch density of M in the weft-wise direction.

During low energy impact (up to 10 Joules) delamination occurred between the fabric layers (where there was no stitch) and between the plies (where stitching was present). Because of this, there are two competing mechanisms occurring simultaneously during CAI [174]

Firstly, crack closure by stitching which relates to Mode I fracture toughness. As stated earlier, stitches ran parallel to the direction of load application and the delamination propagation was perpendicular to them, therefore, crack closure if any through Mode I should be related more to weft-direction stitch density.

Secondly, crack propagation between the crimped plies which relates more with Mode II fracture toughness. In this case the presence of an increased crimp in the 0° fibre tows caused by stitching may hinder the delamination propagation. Exhaustive research by Backhouse [150] showed that, with the increase in warp stitch density the crimp on the 0° fibre tows decreases. This finding suggests that overall crimp of the laminates used in the current study will be of the order $L > M > S$, which is also shown in the current study. Laminate S should, therefore, have the least resistance to delamination propagation between the fabric plies. The largest initial reduction in compression strength, of the 10J impact samples, shown by laminate S (Fig. 72) therefore indicates that the second type of crack propagation was dominant initially. However, similar CAI value for S, M and L (Fig. 71) indicates that both types of crack propagation are competing in laminate S, and could be supported by the delamination mapping presented in section 5.3.7.1. Similar reason could be attributed to the behaviour of laminate M and L for this impact level (i.e. 10J).

It is, therefore, not possible in this study to predict accurately the local effect of stitching density. If the stitches do not fail, delamination may continue to grow by

mode II, however if they do fail, the resulting mode I failure may also contribute to the growth of the delamination.

During impact at energy levels higher than 10 Joules, the samples were damaged to a great extent. A mixed mode of crack propagation is therefore expected. The evidence of Mode I type fracture is reflected by the lower gradient for laminate S (Fig. 74) compared to laminates M and L. The slightly better CAI strength of L compared to M in Fig. 71 could be attributed to mode II type of fracture because of the higher crimp in L compared to M (because of lower stitch density in L).

The overall effect of stitch density is evident from the photographs of the failed samples (Fig. 70). As stated earlier, laminate S tended to fail in a jagged 'V-shape' way, while laminates M and L failed predominantly in shear. The latter type of failure can be attributed to higher curvature (crimp) in the laminates due to lower stitch density. Similar findings were also reported by Zhou and Greaves [164] for CAI testing of laminated containing woven fabrics. The higher stitch density in S led to multiple delaminations, which led to sub-laminate failure. The adjacent shear bands, therefore, formed a jagged pattern.

CHAPTER 6

Environmental Durability Test Results and Discussion

6.0 INTRODUCTION

This chapter deals with the results and discussion of environmental durability testing. Same test laminates, as mentioned in the earlier chapter are used. The physical properties are therefore not repeated in this chapter. The effect of thermohumid ageing is explained through ILSS, Dynamic Mechanical Thermal Analysis (DMTA) and damage tolerance testing. Further characterization was carried out using Infrared Spectroscopy and laser Raman Spectroscopy to explain the matrix behaviour and its relationship with the mechanical behaviour of respective laminates of varying stitch density.

6.1 PERCENTAGE WATER UPTAKE

Exposure to aqueous environments can cause irreversible changes in the chemical and physical properties of fibre-reinforced polymer composites. The level of degradation increases as the moisture content increases, leading to a reduction on the load carrying capacity of the structure. Reductions in stiffness and strength, and changes in thermo-mechanical behaviour can often be linked directly to the amount of moisture absorbed. The extent and rate of moisture absorbed by the composite material depends on a number of factors including temperature, relative humidity and moisture equilibrium levels, area of exposed surface, diffusivity, fibre content and fibre treatment [107]. The two main types of basic moisture conditioning according to BS EN ISO 62:1999 are [175]:

Non-equilibrium conditioning: where a test specimen is exposed to a conditioning environment for a specified time; and

Equilibrium conditioning: where a specimen is exposed, until it reaches equilibrium with the conditioning environment.

Literatures presented in earlier chapter, involves both exposure to hot and humid environment; and water immersion at elevated temperature. CRAG test method 901 [132] suggested a temperature of 70°C for a 180°C cure system, which had been used for the water immersion. The requirement of BS EN ISO 62 could not be strictly followed as the same samples were tested for compression after impact testing which required a smaller rectangular sample (instead of larger square samples).

Fig. 75 shows the experimental results for percentage water uptake for a period of 96 days plotted against time in days^{1/2}. The results for all S, M and L are plotted in the same graph. Initially ageing started with 12 samples for each reinforcement types, 4 of them were taken out from the ageing environment after 7 days and tested for compression strength. Similarly 4 more were taken out at the end of 30 days for testing. The average of the 4 samples that were aged for 96 days has been included in the graph, so that actual trend is noted.

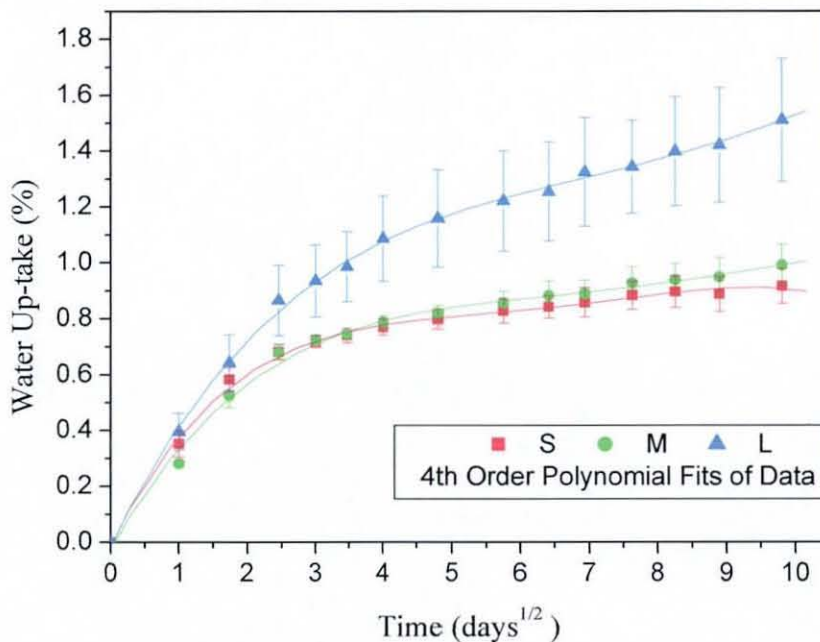


Fig. 75: % Water Uptake vs. Time (Days^{1/2}) – Unimpacted Samples

The rate of water uptake, shown in Fig. 75, is fairly rapid in the early stages of conditioning and decreases with time. The absorption mechanism shows non-Fickian diffusion, as suggested by Springer [107]. The deviation from the Fickian behaviour is least for S, followed by M and L with the most pronounced non-Fickian behaviour.

The water uptake percentage for S, M and L are 0.918%, 0.992% and 1.511% respectively after 96 days. Laminates with high stitch density (S) showed the lowest water uptake, followed by M which was 8% higher and finally L with 64.6% more water uptake. The samples from laminate L still showing an upward trend of water uptake, while that of M showing a less pronounced trend. Interestingly, the water uptake of S was nearing equilibrium by the same time duration. The diffusion coefficient for S calculated, using the Formula (x) stated in Chapter 3, is $4.02 \times 10^{-6} \text{ mm}^2/\text{sec}$.

The water absorption curves for laminates L and M, Fig. 75, could be the result of combined effect of water diffusion and polymer relaxation due to elevated temperature. This assumption could be supported by the conclusion drawn by Suh et al. [96]. Zhou and Lucas [176] suggested that such absorption behaviour may also be a result of the combination of two distinct absorption mechanisms which result in two physical states – bound water and free water.

A look into the microstructure Fig. 39 of S, M and L clearly suggests that L contains voids of larger size and more overall void content than S and M, which may have led to more free water in L. Slightly more water uptake of M, could be attributed to diffusion of water through the surface defects, which was more in M compared to S.

Moisture absorption characteristics of the 10J, 20J and 30J impacted samples of S, M and L are presented in the Fig. 76(a)-(c). The curves follow the same trend as that of unimpacted samples. However, the difference in percentage water uptake values between S, M and L decreases as the impact energy increases. This is due to the fact that, with the increase in impact energy there is more fibre breakage on the tensile face of the impacted samples, creating more open area for water to ingress into the samples.

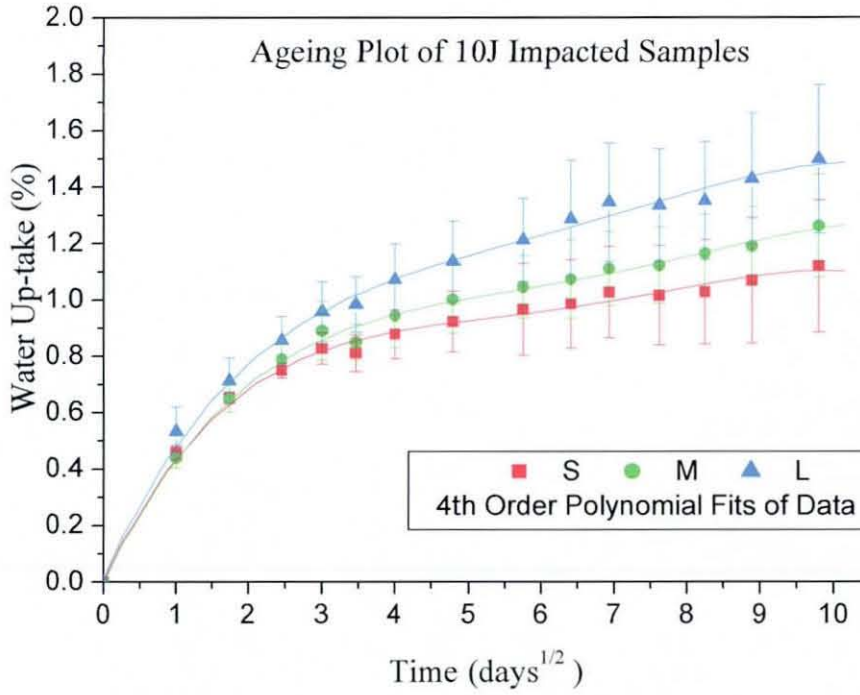


Fig. 76(a): % Water Uptake vs. Time (Days^{1/2}) – 10J Impact Samples

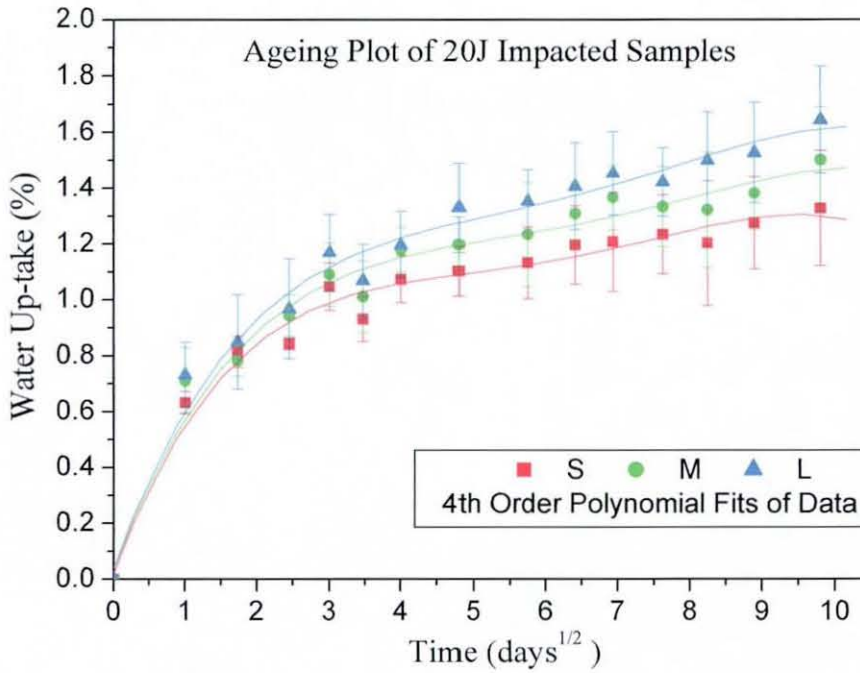


Fig. 76(b): % Water Uptake vs. Time (Days^{1/2}) – 20J Impact Samples

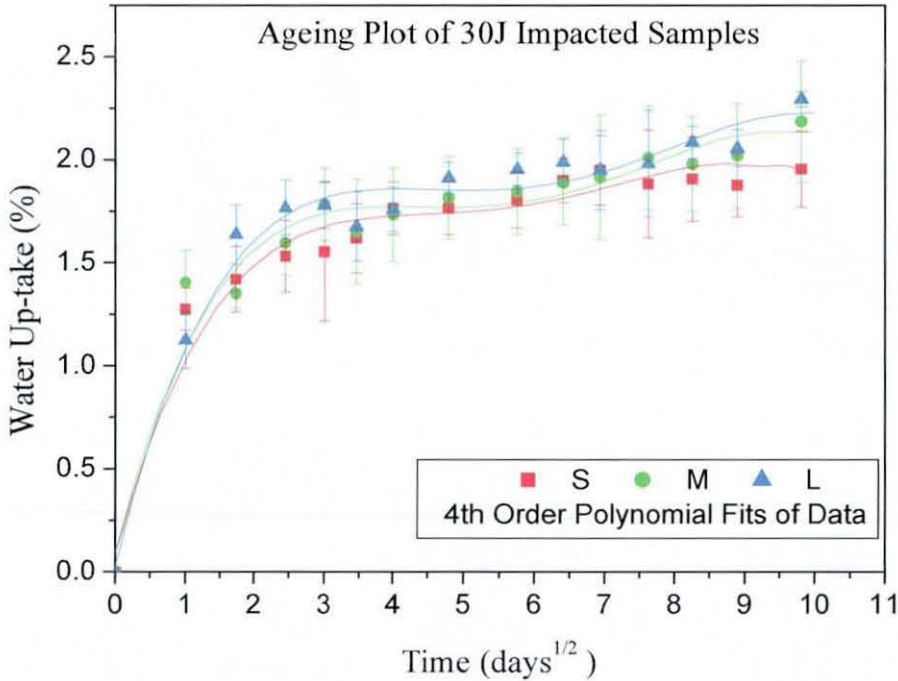


Fig. 76(c): % Water Uptake vs. Time (Days^{1/2}) – 30J Impact Samples

6.2 INTERACTION OF WATER WITH MTM 44 RESIN

The formulations of most of the modified aerospace epoxy resins are highly complex and companies manufacturing them are highly secretive about them. The composition of the MTM 44 [128] resin film used in this particular study includes tetra-functional epoxy resin and two types of aromatic polyamines. Due to this high epoxy functionality, the cured resin is highly cross-linked.

The intrinsic moisture sensitivity of cured epoxy resins is traceable directly to the molecular structure. The presence of polar and hydrogen bonding groups, hydroxyls and tertiary nitrogen, as in this case, provides the chemical basis for moisture sensitivity, while the available free volume and network structure represent the physical basis. FTIR and Raman spectroscopy was therefore carried out, on the 'wet' laminates (DMTA sample size) to recognize the significance of the molecular structure on water uptake.

6.3 FTIR SPECTROSCOPY

FTIR spectroscopy studies in the $4000\text{-}400\text{ cm}^{-1}$ have been used by a number of researchers to reveal the occurrence of reversible hydrogen bonding interactions between the absorbed water and the polymer network [142, 177-178]. Although FTIR produces quality spectra of the epoxy resin, it is necessary to assign the structural origin of the numerous infrared bands in order to use them effectively. In the following section major IR bands are assigned.

6.3.1 Assignment of IR bands

Initially a FTIR spectral measurement was carried out on a cured epoxy ground sample and a composite ground sample using a non-absorbing KBr palette. The corresponding spectra are shown in Fig. 77 and 78. In order to interpret the spectra, it is necessary to have some insight into the structural origin of the numerous infrared bands in order to use them effectively. Unfortunately, the complexity of the molecules involved made complete band assignments impossible and only major bands are assigned and presented in Table 14.

Fig. 77 and 78 show a broad band between 3100 cm^{-1} and 3700 cm^{-1} . This broad band can be assigned to a combination of bands, as a band due to only one kind of vibration would have a very sharp peak. There are several possibilities of assignment of this group. One such possibility is the assignment to the O-H stretch in hydrogen-bonded O-H groups, while another possibility is the assignment to the O-H stretch in non-hydrogen bonded O-H group. The characteristics of these two kinds of bands are different: for the hydrogen bonded O-H stretch, the hydrogen bond is relatively weaker than the covalent bond and the band appears at a lower frequency. As the amount of water is very small in the dried samples, these hydrogen bonds are largely established by C-OH groups of alcohols.

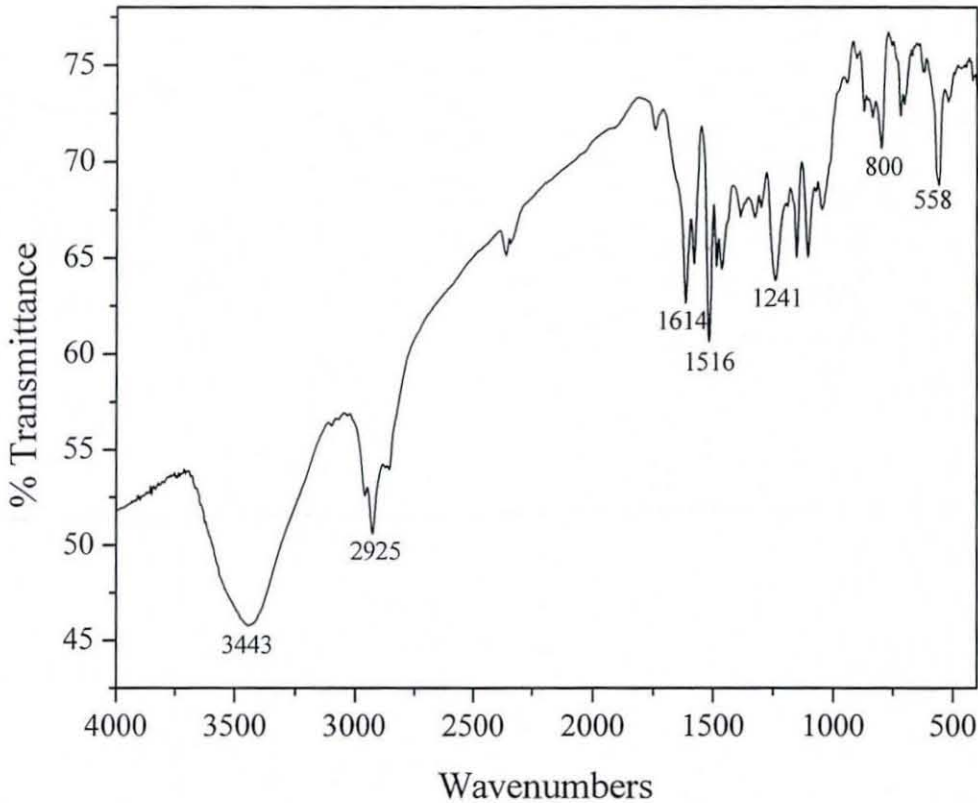


Fig. 77: FTIR Spectrum of Cured Epoxy

Furthermore, primary and secondary amines also have the characteristic N-H stretching absorptions in the $3300\text{-}3500\text{ cm}^{-1}$ range of the IR spectrum. These amine absorption bands are generally sharper and less intense than hydroxyl bands. Primary amines show a pair of bands at about 3350 and 3450 cm^{-1} , and secondary amines show a single band at 3350 cm^{-1} [179]. Tertiary amines show no absorption in this region because they have no N-H bonds. All these functional groups are a possibility; as during cure, amino groups form chemical bonds by opening the epoxy ring to produce hydroxyl groups and secondary/tertiary amine groups.

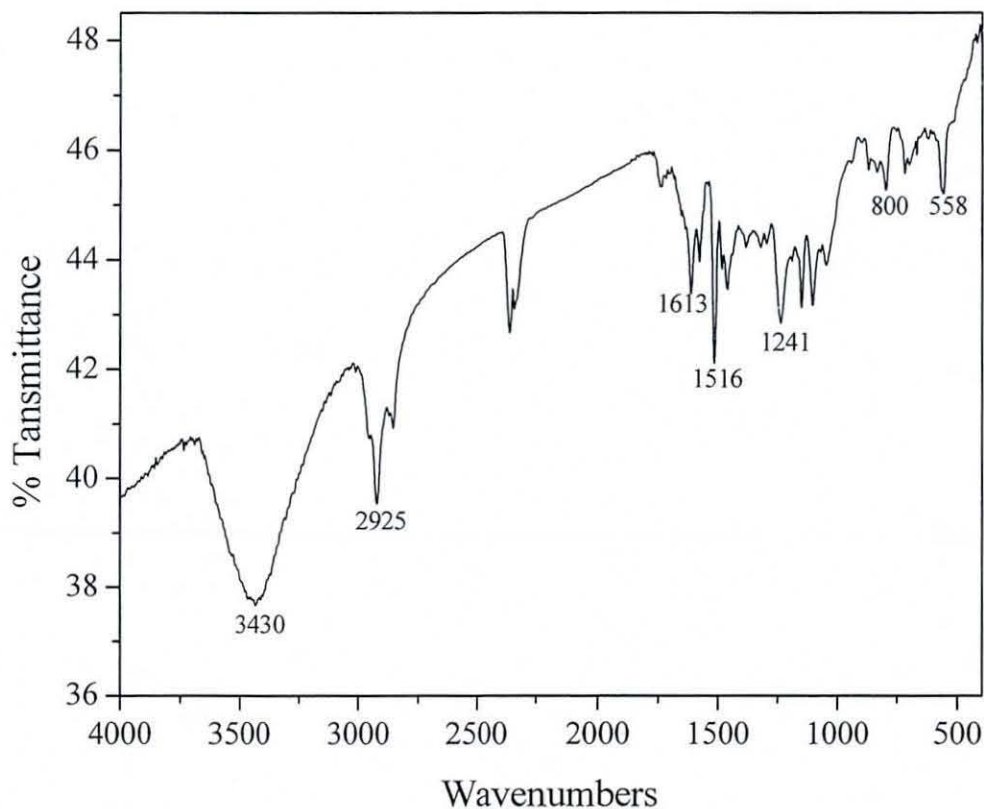


Fig. 78: FTIR Spectrum of Composite Laminate

The region between 2750 -3100 cm^{-1} shows a well-identified group of bands which are due to C-H stretch ($\nu_{\text{C-H}}$) in the alkyl groups.

The last group consists of the set of more compact bands that appear below 1650 cm^{-1} . Most of the important components of this group are assigned in Table 14, following standard assignments [142-143]. The intense band around 1250 cm^{-1} is assigned to $\nu(\text{C-O-C})$ mode that appears in aromatic ethers.

Wave Number (cm ⁻¹)	Characteristics	Assignment
3434	strong	$\nu(\text{OH})$
2954 2923 2854	weak strong weak	$\nu(\text{CH}), \nu(\text{CH}_2)$
1612 1579 1516	strong weak strong	$\nu(\text{C}=\text{C})$ Phenyl Ring
1461	strong	$\nu(\text{C}=\text{C})$ Phenyl Ring + $\delta_{\text{as}}(\text{CH}_3)$
1298	weak	$\nu(\text{C}-\text{O}), \nu(\text{C}-\text{C}),$
1242	strong	$\nu(\text{Ar}-\text{O}-\text{Ar})$
1152	strong	$\nu_{\text{S}}(\text{SO}_2)$
1106	strong	$\nu(\text{Ar}-\text{S})$
800	strong	$\nu(\text{Si}-\text{C})$
718	strong	$\delta(\text{SO}_2)$
557	strong	$\delta(\text{SO}_2)$

Table 14: Assignment of FTIR Band [142-143]

Effect of Hydration

One spectrum after hydration is shown in Fig. 79. This laminate (L) was aged for 60 days at 70° C in water. The bands found consist of full bands due to H₂O and differential bands due to the modification of absorption bands induced by the addition of water molecules. In the spectra, the bands due to water molecules are identified [143] as the broad band at 3400 cm⁻¹, stretch band (ν) O-H (as), and the sharp band at 3645 cm⁻¹, $\nu(\text{OH})$ (sym). The broad band may be due to hydrogen bonding formed either between water molecules and hydroxyl groups or between water molecules and nitrogen atoms on the amine groups or to both of them. The band at 3645 cm⁻¹ is the O-H stretch band due to OH groups of H₂O molecules that do not establish hydrogen bonds.

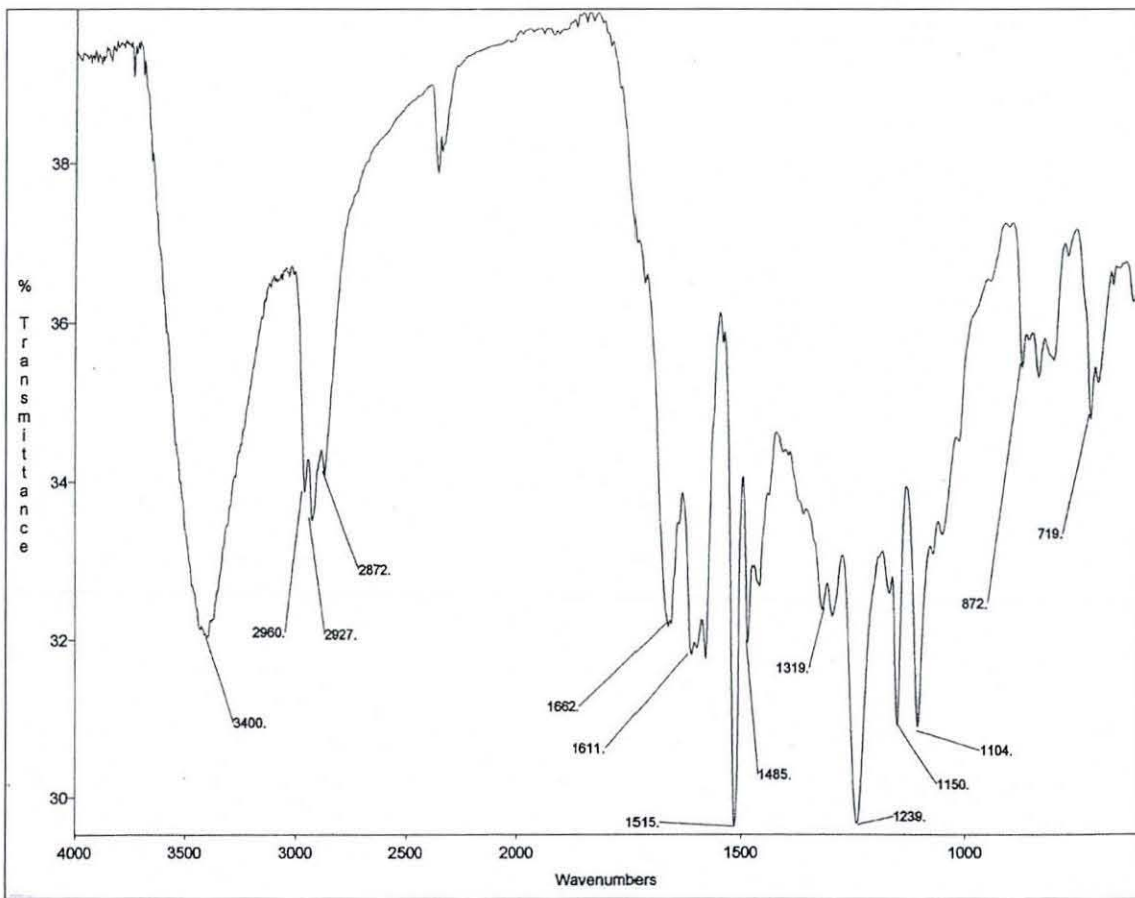


Fig. 79: Laminate L after 60 Days of Ageing (% w.c.= 0.959)

The bending band (δ) of H_2O , which is known to be much less sensitive to hydrogen bonds than the O-H stretch band (ν), is composed of a peak (or shoulder) at 1610cm^{-1} which can be assigned to H_2O molecules that establish no hydrogen bonds. The band at 1640cm^{-1} can be assigned to bending vibrations in H_2O molecules with hydrogen bonds. In liquid water, this band falls close to this value [143]. Assuming that the integrated intensity of this bending mode does not necessarily indicate whether the H_2O molecules establish hydrogen bonds or not, Ngono et al. [180] concluded that only some of the free alcohol groups establish a hydrogen bond with a H_2O molecule embedded in the resin.

6.3.2 Degradation Processes in Epoxy Resin

An understanding of the reversible and irreversible effects of water is critical to the design of reliable composites. FTIR is useful as spectra can be obtained on the same or similar samples as a function of exposure time. The hydrolytic attack on a composite laminate brings about breaks in a polymer chain and creates new end groups. The small spectral differences observed give an indication of the extent of hydrogen bonding and unbounded water in the micro-voids.

Sample	% Water Content	$\nu(\text{OH})$ -Band	$\delta(\text{OH})$ -Band
Dry		3446	1640(weak)
S-15 Days	1.369%	3430	1662
S-30 Days	1.090%	3435	1659
S-60 Days	1.118%	3431	1660
M-15 Days	1.201%	3434	1662
M-30 Days	0.969%	3434	1660
M-60 Days	1.046%	3429	1662
L-15 Days	0.971%	3433	1655
L-30 Days	0.913%	3436	1658
L-60 Days	0.959%	3400	1662

Table 15: Vibration of the Sorbed Water from FT-IR Study
(See Appendix for spectra)

In general, the formation of hydrogen bonds (increase in bond length) affects the vibrational spectra of the groups involved by decreasing the frequency of stretching modes and increasing the frequency of bending modes [142]. These interactions increase the IR intensities as well.

The vibration of the sorbed water found from the FTIR studies of the laminate samples S, M and L aged for 15, 30 and 60 days in 70°C water, compared with dry results, are presented in Table 15. As expected, compared with the dry $\nu(\text{OH})$ and $\delta(\text{OH})$ bands, the 'wet' frequency of the stretching mode decreases while

'wet' frequency of bending mode increases, indicative of the formation of hydrogen bonds. However, no correlation (between S, M and L) is evident from the frequency shift pattern of $\nu(\text{OH})$ and $\delta(\text{OH})$ that hydrogen bonding increases with increase in % water uptake, possibly because the % water uptake value is of a laminate sample (including free water in the voids), while the frequency bands are from ground samples from parts of that laminate.

Overall, FTIR results reveal that polar groups in the cross-linked network are one of the major factors that control the sorption and diffusion of water in epoxy resins. Two possible hydrogen bond configurations are identified from the literature: N-HO and O-HO interactions. Evidence of O-HO bonds exists in the FTIR spectra. However, presence of N-HO can not be confirmed, leading to the assumption of the presence of tertiary amines in the resin film. The diffusion of water molecules into epoxy resins can be attributed to two factors. Firstly, the availability of micro-voids (evident from Raman analysis in the next section) and secondly, the attractive forces between the water molecules and the epoxy resin matrix. The second factor concerns the chemical nature of the water towards the polymer and the FTIR results verify this argument. It, therefore, can be proposed that sorption and transport of water in the epoxy in its glassy state is controlled predominantly by features like cross-link density and by the concentration of possible sorption sites.

6.4 LASER RAMAN SPECTROSCOPY

Although both IR and Raman spectroscopy provide information on vibrational frequencies of various functional groups, with the latest Raman spectroscopy it is possible to obtain spectra of a very small area of a sample and subsequently, a spectral mapping of a particular area of the sample.

Initially Raman Spectra were obtained for cured epoxy, polyester stitching yarn, carbon fibres and dry composite (Fig. 80) using the 632.817 nm (red) He-Ne laser with a full power of ~17 mW. The laser beam was focused through a x10 objective to give an approximate spot size of 3 μm diameter on test sample. A

highly sensitive (2000x800 pixels of 15 microns) charge coupled device (CCD) camera was used to collect Raman Spectra. The specimens were placed onto the stage of an Olympus high stability BX40 microscope connected to a black and white camera.

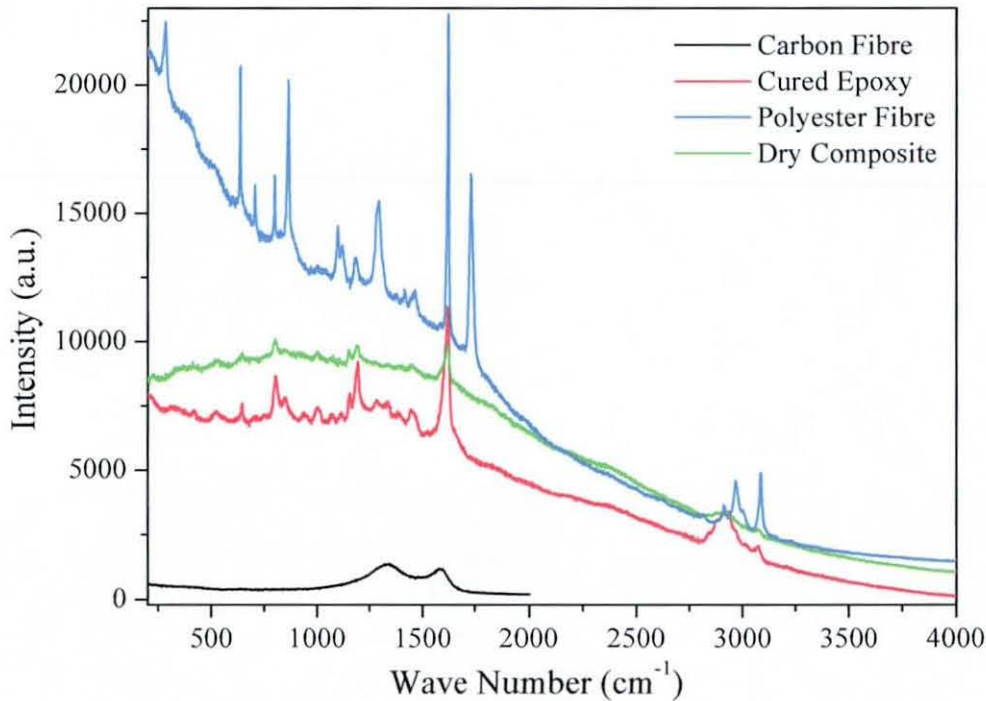


Fig. 80: Raman Spectra of the Reinforcement, Matrix and Composite

The identification of the origin of the Raman band as a result of adsorbed H₂O on the laminate surface and the assignment of any transition was carried out through the comparison of dry and wet (aged for 5 days) composite samples (Fig. 81). The relative intensity change, the shift and broadening of Raman band have been proven to be excellent indications to the extent and strength of hydrogen bonding [181].

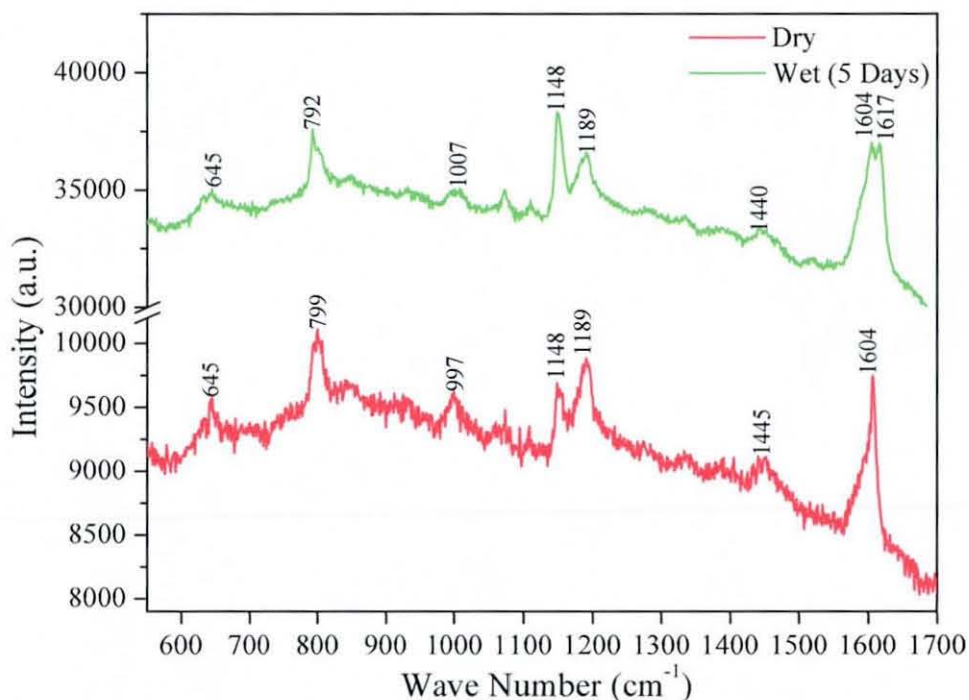


Fig. 81: Raman Spectral Shift due to Hydration

Raman band at 1604 cm^{-1} was ascribed to the stretching mode of phenyl rings earlier (Table 14), which is evident in the dry composite. As the hydrogen bonding increased due to ageing in water (hydrogen bonded phenyl ring associated with $\text{OH} \rightarrow \text{O}=\text{C}$ interaction), a shoulder was clearly observed at 1617 cm^{-1} . The broadening of the peak for $\delta(\text{OH})$, increase in the relative intensity of the hydrogen bonded (wet sample) to the non-bonded phenyl ring (dry sample) and the band shift to a higher wave number all indicate to an increase in the extent of hydrogen bonding in the wet sample.

No peak for $\nu(\text{OH})$ at the frequency range $3100\text{--}3650 \text{ cm}^{-1}$ was noticed. The reasons for this could be either the acquisition time was too low for a better detection or the laser power ($\sim 10 \text{ mW}$) at the sample was too high which caused overheating/ degradation [182].

6.4.1 Raman Mapping of Aged Samples

In this section optical micrographs of laminate S after aging durations of 15 days, 30 days and 60 days are presented, along with corresponding 2D Raman spectral mapping. Optical micrographs, when compared with the dry sample image (Fig. 82), show water attack on micro voids which sometimes led to micro-cracks on the surface. For longer thermohumid ageing duration, leaching of the resin was also observed (Fig. 85).

Figs. 83-85 show Raman maps after the aforementioned ageing durations for laminate S. The maps for laminates M and L are included in the Appendix.

The map imaging in LabSpec [144] works in two ways. Firstly, cursor intensity (Fig. 83-85) – the intensity of the Red (R), Green (G) and Blue (B) components relates directly to the integrated intensity (i.e., area under the spectrum) between the cursors. The intensity scale shown in these figures is graded colour scale which is created by mixing particular contributions of cursor R at different intensities. As it was known that the dry composite had the stretching mode of phenyl rings peak at $\sim 1600\text{cm}^{-1}$, the red cursor was used to plot an image of the intensity of this peak. The intensity is based purely on the intensity between this cursor. When the cursor was extended to the range $400\text{-}1700\text{ cm}^{-1}$, very little change in the colour distribution was observed. It was suggested [197] that it doesn't work well if there are overlapping bands, for example having two species, both with a band at 1600cm^{-1} , using cursors it is not possible to distinguish the two components. Furthermore, setting the cursor over a wide region ($400\text{-}1700\text{ cm}^{-1}$) could be misleading as it simply produces an image of "total spectral intensity", and there is no real chemical distinction between different components.

The colour intensity maps of laminate S after ageing durations of 15, 30 and 60 days show the intensity of cursor R for the band at 1600cm^{-1} . It has been reported [181] that the relative intensity changes of the Raman band have been proven to be excellent indications of the extent and strength of hydrogen bonding. An increase in the intensity (yellow colour) shown in the mapped spectral images relates to increase in hydration and subsequent hydrogen bond formation in and around the defects that existed before ageing. However, it was felt during the

analysis that an acquisition time of 1 second was too little for a good quality spectra acquisition. It is, therefore, recommended that an acquisition time of at least 50 second to be used for future analysis along this line.

The other map imaging technique in LabSpec is modelling. Modelling uses a least squares fitting algorithm to correlate where a particular spectrum occurs within the map data. Through this technique it is possible to generate an image that is based upon an entire spectrum, rather than just intensity in a chosen region. Modelling therefore overcomes the problem of having lots of overlapping bands and distinguishes various components. Fig. 86 shows one such modelling carried out on the 60 day aged sample, with the dry composite Raman spectrum as the reference. As mentioned earlier, with a better spectral map (using long acquisition time) it is possible to model the concentration of hydrogen bonding in a mapped area.

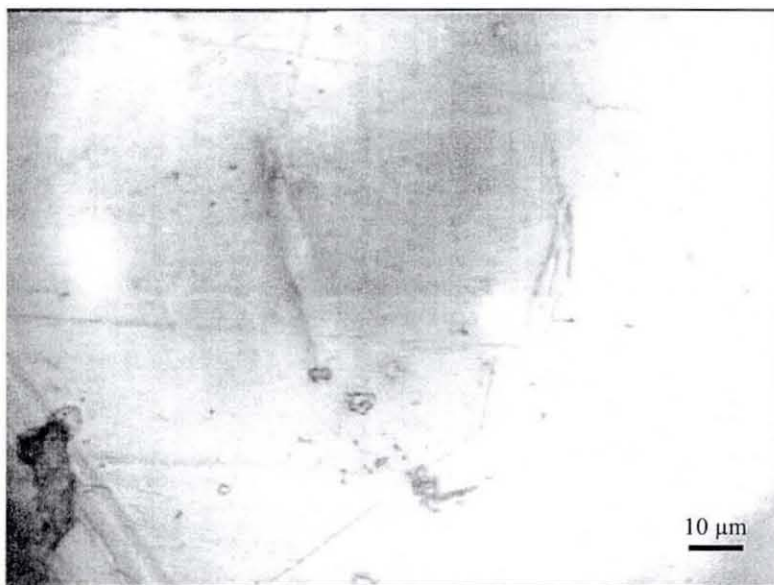


Fig. 82: Optical Microscopic View of Dry Laminate S Showing Micro-Voids

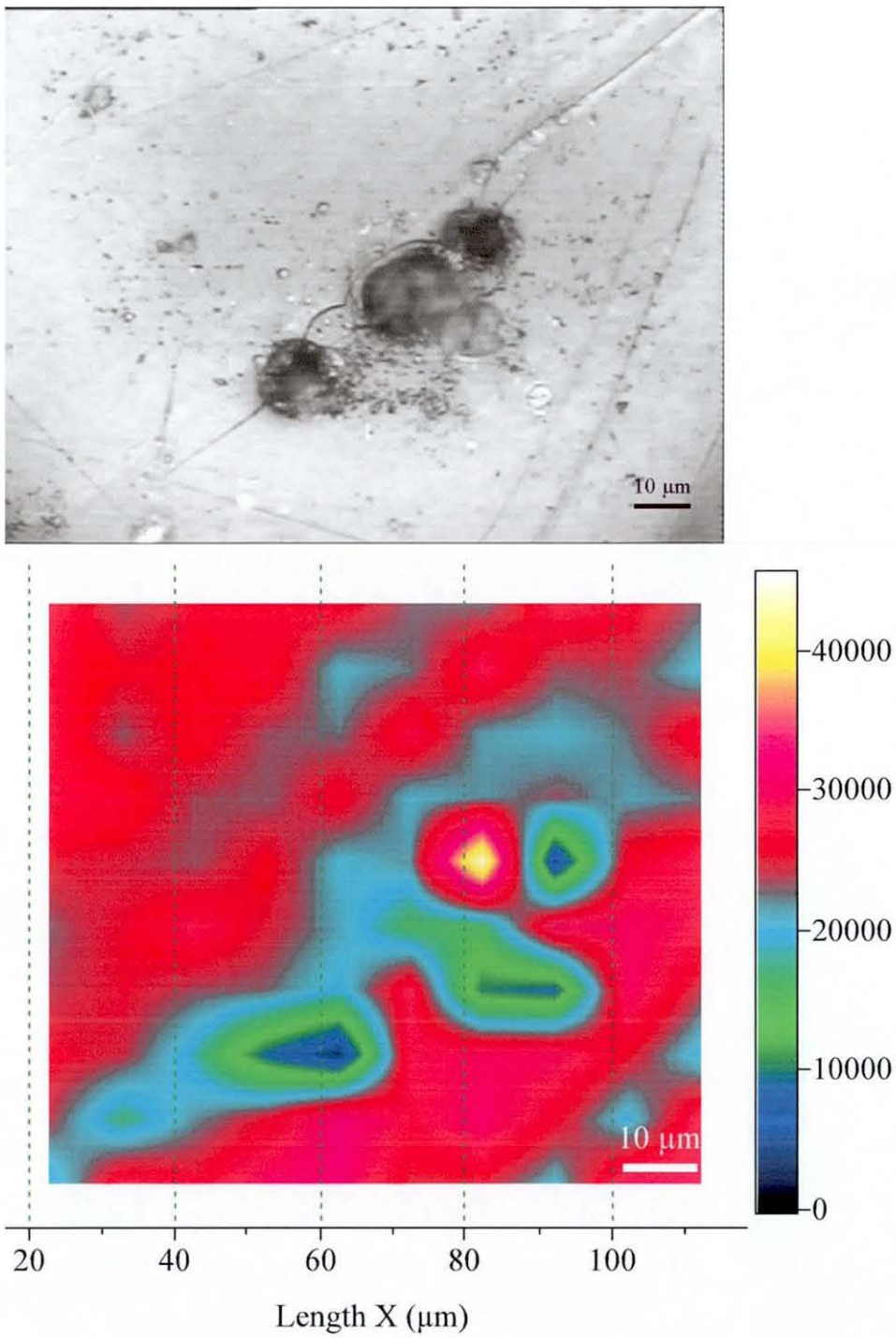


Fig. 83: Raman Mapping of Laminate Surface S, after 15 Days of Ageing – Optical Microscope Image of the Mapped Sample (Top) and Spatial Distribution Plot of the Intensity Values (Bottom), Map Size: 10×10 Points

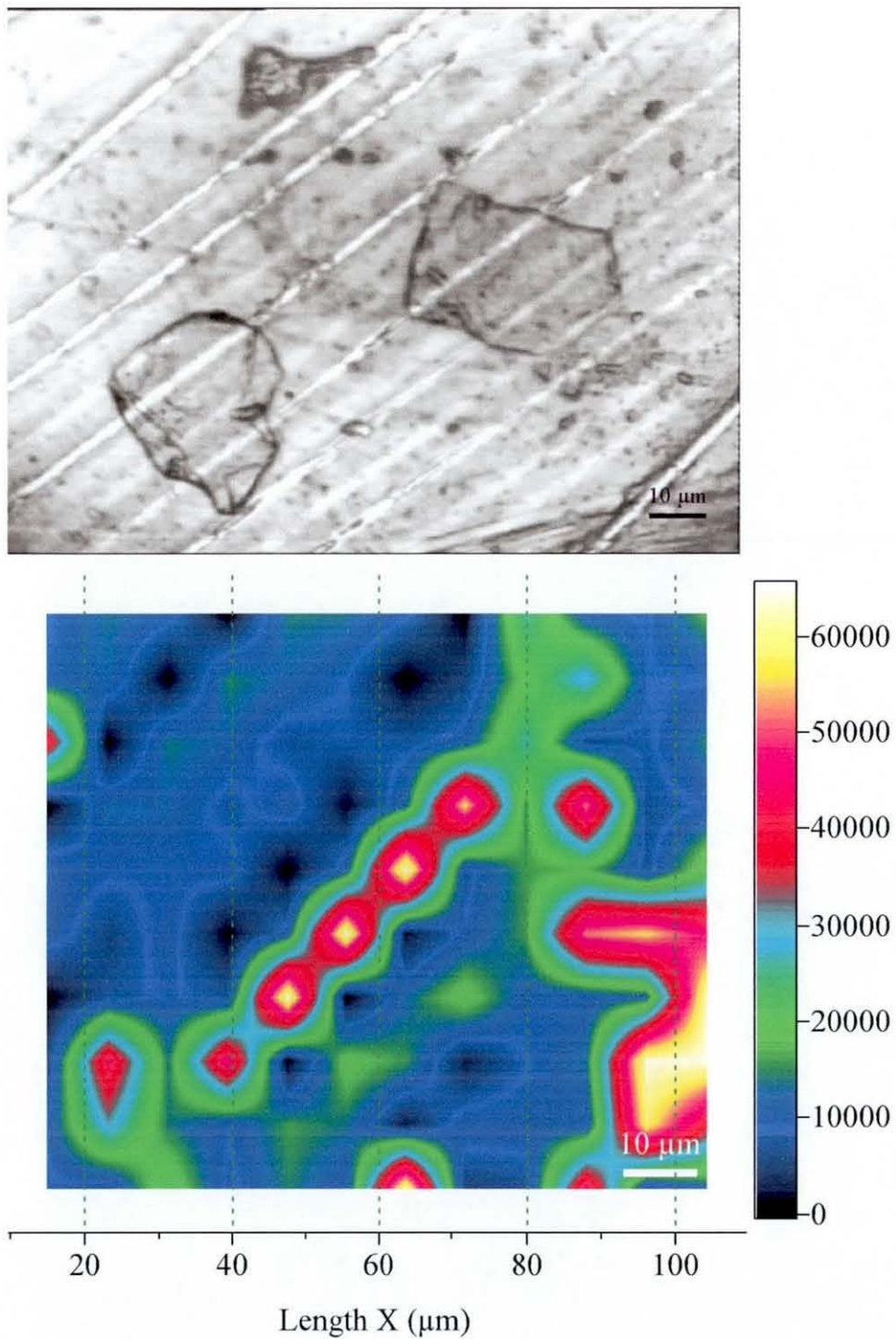


Fig. 84: Raman Mapping of Laminate Surface S, after 30 Days of Ageing – Optical Microscope Image of the Mapped Sample (Top) and Spatial Distribution Plot of the Intensity Values (Bottom), Map Size: 10×10 Points

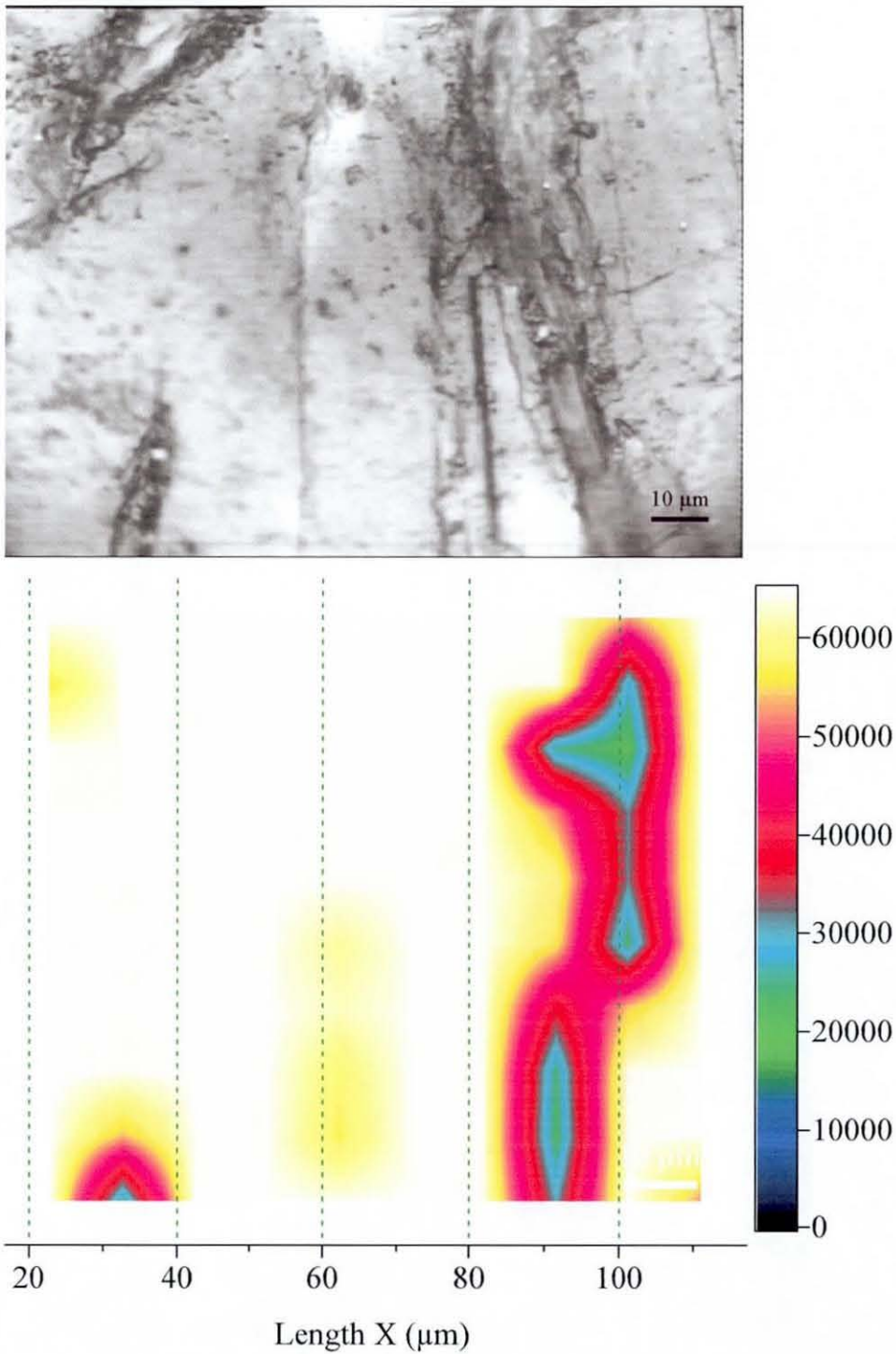


Fig. 85: Raman Mapping of Laminate Surface S, after 60 Days of Ageing – Optical Microscope Image of the Mapped Sample (Top) and Spatial Distribution Plot of the Intensity Values (Bottom), Map Size: 10×10 Points

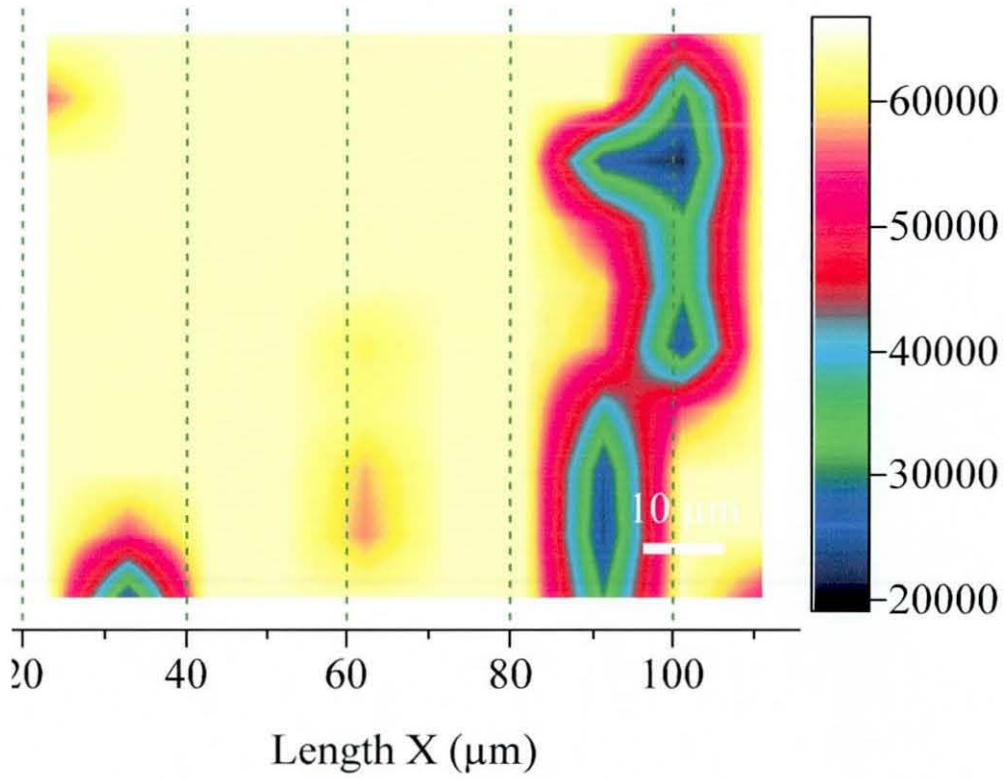


Fig. 86: Raman Modeling of Laminate Surface S, after 60 Days of Ageing w.r.t. Dry Laminate Concentration

6.5 HARDNESS TESTING

Hardness testing was carried out on a separate set of ILSS samples. One sample each of laminates S, M and L were aged in deionised water at 70°C for durations of 12hrs, 96hrs, 264hrs and 528hrs respectively. Table 16 shows a summary of the average hardness test results for all three laminates. Average hardness numbers were calculated from five readings, for each sample, taken at room temperature at some distance from the four edges and at the centre of the samples.

As reinforced plastics materials are inherently heterogeneous, a large scatter of the individual readings was observed. The average Vickers Hardness Number of the laminates after the various ageing durations did not show any significant degradation, indicating that the resin retains most of its hardness property after the thermohumid ageing duration of 528hrs.

Time	Hardness Number (HV)		
	S	M	L
Dry	44.7(±3.6)	45.6(±4.1)	43.8(±4.3)
12 Hours	42.2(±6.6)	43.3(±5.3)	46.1(±7.5)
96 Hours	43.4(±8.5)	44.1(±9.7)	46.8(±7.0)
264 Hours	40.9(±2.9)	42.5(±3.3)	48.9(±3.1)
528 Hours	41.6(±3.7)	41.9(±4.6)	48.9(±5.0)

Table 16: Summary of Hardness Test Results

6.6 INTERLAMINAR SHEAR STRENGTH (ILSS) TEST

All polymer matrix materials absorb water to some extent and with time this affects (and usually reduces) the interlaminar shear strength and other related mechanical properties [183]. It is now well established that the fibre-matrix interface is responsible for the shear strength of composite (Chapter 3). Moisture reduces the bond strength between fibre and matrix through hydrolysis and bond breakage [184]. In certain cases osmotic cracking may appear at the interface which also degrades the ILSS properties [185].

The effect of water uptake on ILSS for samples of laminates S, M and L was tested. Accelerated ageing was carried out through immersion in deionised water at 70°C for a maximum of 528 hours. The maximum % water uptake was approximately 1.5% (Fig. 87), which corresponded to a similar water uptake in the larger samples (unimpacted) used for percentage water uptake testing.

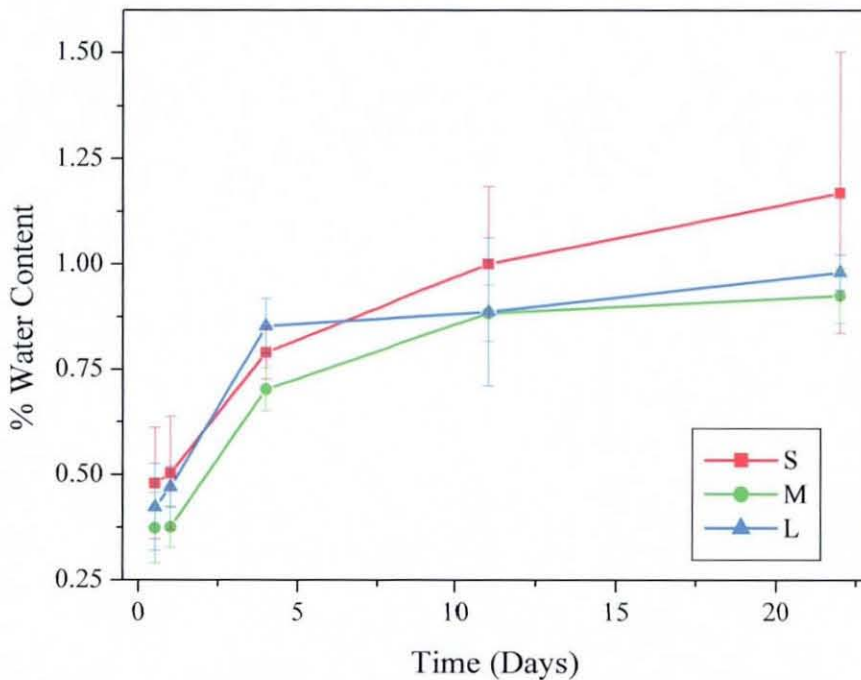


Fig. 87: Water Uptake Behaviour of ILSS test Samples

The data points in the Fig. 87 represent % water contents of different sets of samples and therefore do not show the ageing trend of the laminates. Moreover, the samples were of small dimensions and any interpretation of the ageing trend

would be erroneous. The higher water content of samples S could be attributed to a few samples containing higher void contents and thus leading to large standard deviations.

After ageing for 12, 24, 96, 264 and 528 hours, five samples from each of laminates S, M and L were tested for ILSS. The testing was carried out inside an oven running at 70°C. Detailed ILSS results are included in the Appendix.

Fig. 88 shows the results for ILSS, before and after ageing, of all three laminates. Linear fits of the results show that the loss in apparent interlaminar shear strength varies with the specimen weight gain and there is very little difference between the laminates.

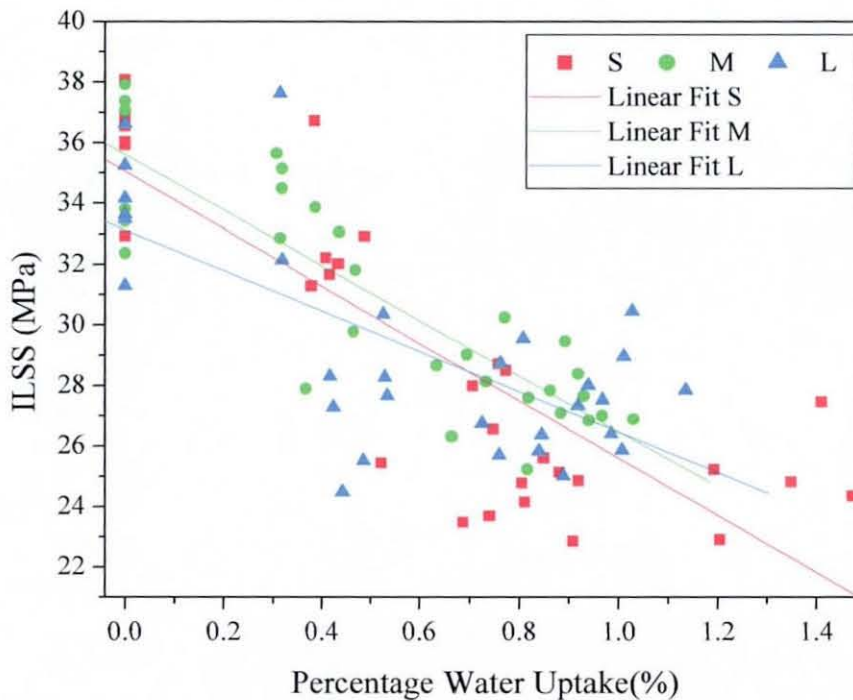


Fig. 88: Effect of Water Uptake on the ILSS

Further investigation shows that the degradation in ILSS up to 0.6% water content was severe whilst further increase in % water content resulted in a smaller reduction in ILSS value, indicating more of an asymptotic relationship than a linear one. The reduction in ILSS after 528hrs of ageing for laminates S, M

and L are approximately 27%, 22% and 20%. These results correspond well with the percentage water uptake values shown in Fig. 87. The higher water uptake by samples of S led to higher degradation in ILSS.

It is interesting to note that in the range of 0.75–1% water content, for a particular value of % water content, the laminates L and M show better ILSS value than S. The inferior ILSS of S could be attributed to high stitch density causing high stress concentration in the resin, added to the stress concentration due to hydrothermal ageing. Mouritz et al. [186] also showed that under short-beam loading, the stitches become sites of stress concentration which contributes to the reduction in interlaminar shear strength.

Individual ILSS values did not always decrease with the percentage water uptake; rather it increased in some cases (Fig. 88). A couple of reasons had been identified in order to explain the results. Firstly, the increase or decrease of ILSS could be attributed to the scatter of the experimental results rather than to any significant effect of moisture. The scatter of the experimental results could be due to the size and distribution of voids and resin-rich areas affecting the interfacial bond between the fibre and the matrix. Secondly, as the testing was carried out at 70°C, some of the free water may have evaporated during the testing, which did not have an effect on the decrease in ILSS properties. Baley et al [149] mentioned other researchers' work, where it was found that the loss in mechanical properties may be partly reversible if water is removed by drying. They indicated that degradation of the mechanical property after ageing is brought about by cracking of the matrix, interface debonding or delaminations.

The micrographs of the ILSS test samples, after 528 hrs of thermohumid ageing, are shown in Fig. 89, which present damage distributions through the laminate thickness. The most predominant type of interlaminar failure observed was a network of interconnecting delamination through transverse matrix cracks, similar to that observed for the dry laminates. It was concluded from the results that the fracture behaviour did not change significantly during the ageing period.

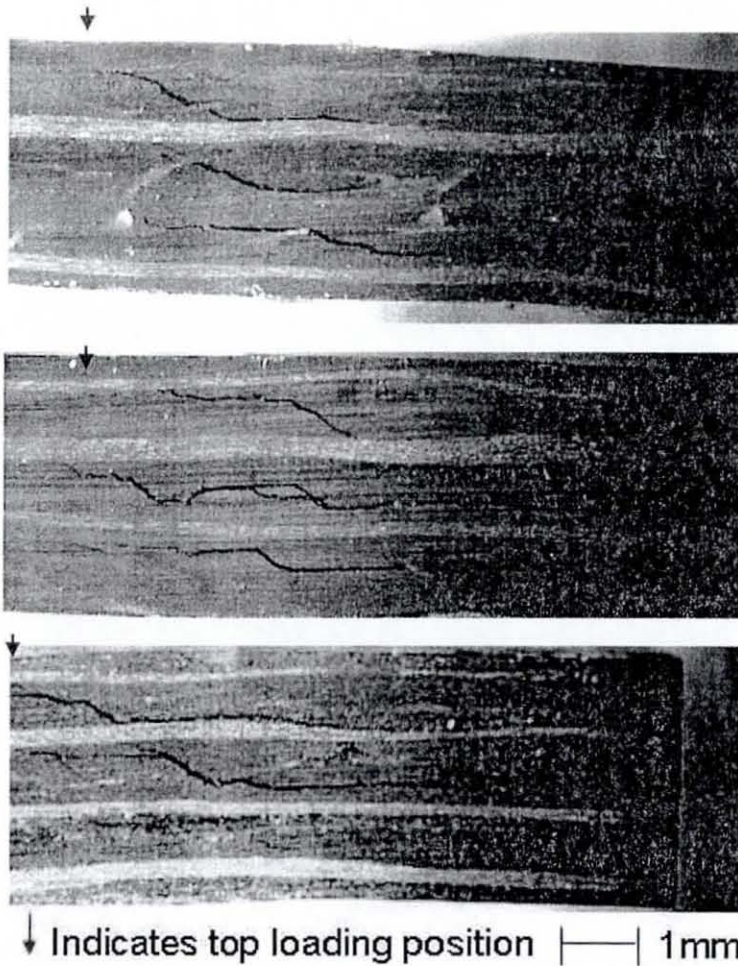


Fig. 89: Optical Micrographs of the ILSS Samples Tested after 528 hrs of Ageing
(From Top: S, M and L)

Fig. 90 shows the comparison of force-displacement trace of dry and 528 hrs aged samples of laminate S during ILSS testing. The maximum values of force in the figure indicate degradation in the ILSS properties for the aged sample. These results are supported by the chemical analysis of the samples, where it was shown that the interfacial bonds between the fibre and matrix were replaced with hydrogen bonding between matrix and water molecules thus weakening the interfacial bonding. The force-displacement trace of the aged sample shows lower strength and less plastic deformation.

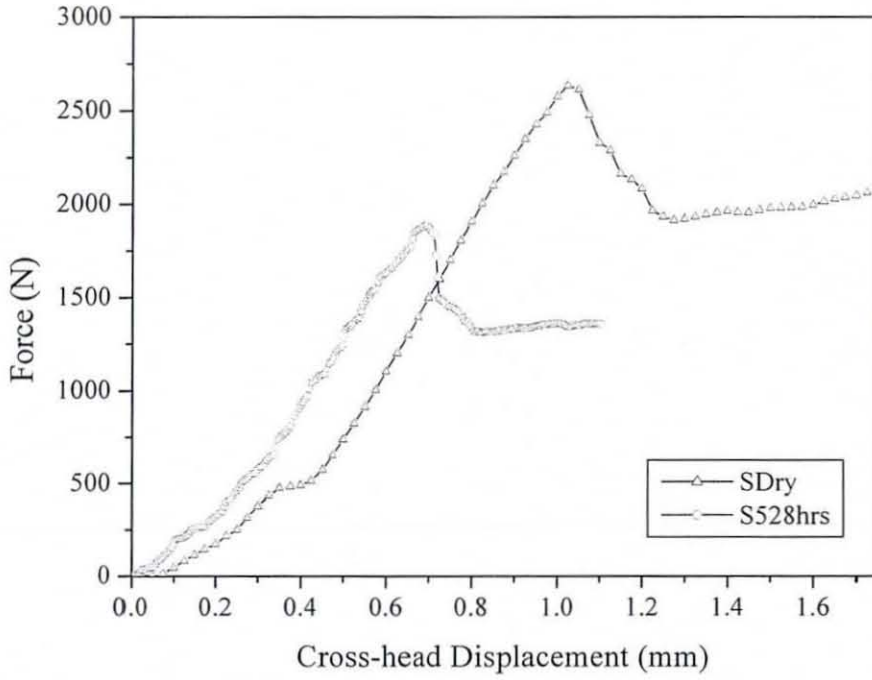


Fig. 90: Typical Force-Displacement Curves during ILSS Test (For Dry and Aged Samples, After 528 Hrs Immersion at 70°C)

6.7 DYNAMIC MECHANICAL THERMAL ANALYSIS (DMTA)

An important property that is being investigated by these dynamic experiments is viscoelasticity - which is a characteristic of polymeric materials and polymer based composites. The dynamic storage modulus and $\tan \delta$ (damping) are two important linear viscoelastic parameters. The storage modulus corresponds to the stiffness of material under dynamic loading. The damping mechanisms in fibre composites can be considered in two categories: low-strain and high-strain damping [187]. Low-strain damping is a domain of the polymeric matrix, which obeys linear viscoelastic relations, while high-strains induce microcracks and contribute to damping by friction [188].

In the case of low-strain damping, DMTA instruments are highly sensitive in detecting changes in internal molecular mobility. Any physico-chemical property change in a composite, due to the degradation of bond strength at the fibre-matrix interfaces should therefore be reflected by the $\tan \delta$ value [189].

6.7.1 Determination of T_g

Dynamic mechanical data are usually determined in a temperature range including the glass transition temperature (T_g). T_g can be determined with significant levels of sensitivity through DMTA by monitoring changes in the storage modulus (E'), loss modulus (E'') or $\tan \delta$, as a function of temperature [190]. However these three indicators give different values, T_g can either be defined as the temperature where the maximum loss tangent or the maximum loss modulus is observed, or as the inflexion point at which a significant drop of the storage modulus occurs. However, the respective peaks (or points) usually occur at different temperatures resulting in a broad transition region. Typically, it has been observed that the E' inflexion point occurs at the lower temperature, followed by the E'' peak and finally by the $\tan \delta$ peak (Section 6.7.3). T_g also changes with the test and the temperature ramping. An increase in the heating rate is known to shift T_g to a higher temperature, whereas an increase in test frequency for a constant heating rate also increases T_g [191].

Sometimes, apart from the glass transition secondary transitions can also be observed. It is well known that the glass transition temperature is associated with conformational crank-shaft movements of the main chain of the polymer, whereas the secondary transitions are associated with movements of the side groups.

6.7.2 Experimental Results

Dynamic mechanical thermal analysis was performed in dual cantilever bending mode using a Rheometric Scientific MK II analyser. Initially the effect of frequency on T_g , was analysed, which is presented in section 6.7.3. Secondly, dry samples of laminates S, M and L were analysed, at a frequency of 1 Hz over a temperature range of 25–260°C with a heating rate of 4°C min⁻¹, to measure their damping properties, which is included in section 6.7.4. Finally, samples of the three laminates were exposed in 70°C water for 61 days and the effect of moisture absorption on the viscoelastic properties, such as the glass transition temperature was determined and is presented in section 6.7.5. The results for the dry laminates were considered as the baseline value for the aged samples.

6.7.3 Effect of Multi-frequency on DMTA

Frequency affects the vibration performance of polymers and, thus, the matrix of polymer composites. For optimal design and analysis it becomes indispensable to determine the actual material properties over the range of operational temperatures and frequencies.

Three samples of laminate S were tested using frequencies of 0.1, 1 and 10 Hz in Multi-frequency Mode. As the same resin system was used for all laminates (S, M and L) only samples from S were tested. The effect of frequency on storage modulus, loss modulus and Tan δ are presented in Figs. 91-93 respectively. As pointed out earlier, determination of T_g from each of these graphs yielded different values. The results found correspond to the conclusion of Li et al. [191] that for higher frequency at a constant heating rate the value of T_g increases.

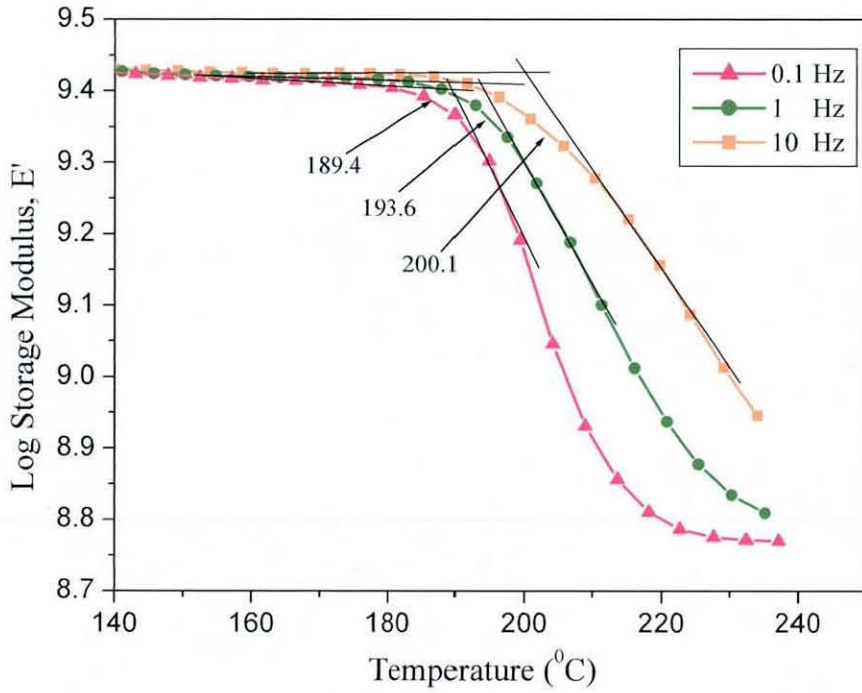


Fig. 91: Effect of Test Frequency on Storage Modulus

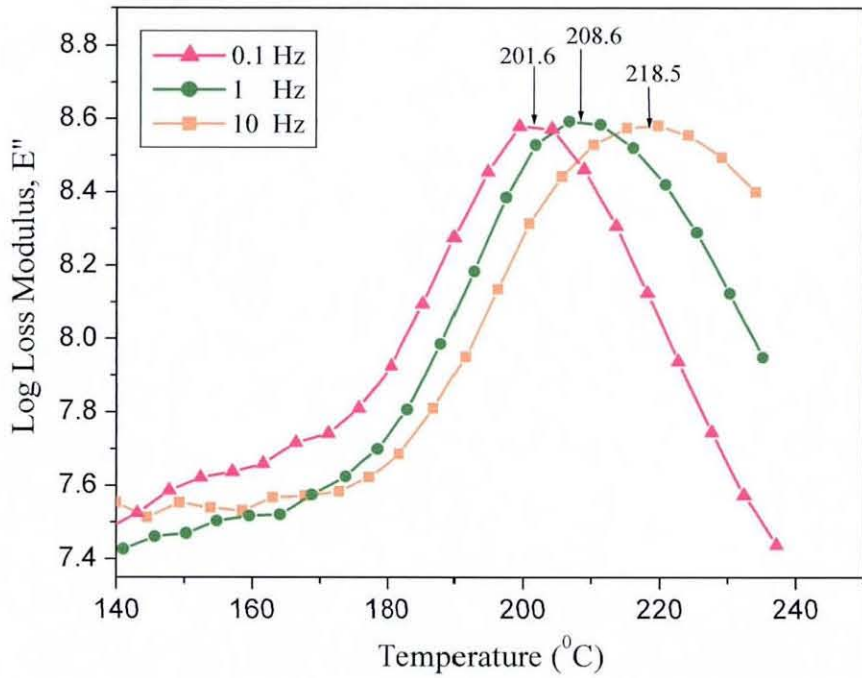


Fig. 92: Effect of Test Frequency on Loss Modulus

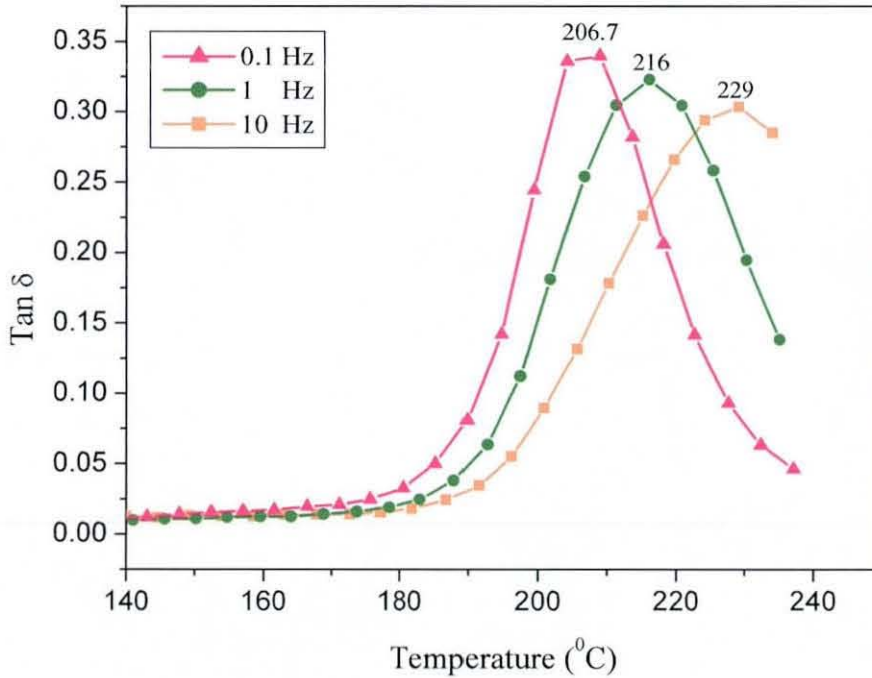


Fig. 93: Effect of Test Frequency on Tan δ

In general, at low frequencies polymeric materials flow more, acting in a similar fashion to flow at elevated temperature, thus showing greater damping (Tan δ value in Fig. 93). As the frequency increases the material behaves more elastically. Absolute values of loss modulus trends, shown in Fig. 92, show no difference with increase in frequency, indicating that the viscous property remains constant. Consequently as the storage modulus increases, with the increase in frequency, the Tan δ value decreases.

The damping of carbon fibre reinforced polymeric composites is derived mainly from the matrix and the fibre–matrix interface response. The decrease in Tan δ value of the composite material with increase in frequency is related to restrictions of chain motions of the polymer at higher frequencies. The same effect is also responsible for an increase in storage modulus with frequency. The results also indicate that the T_g value variation due to frequency, when calculated from the Tan δ is more than that of storage modulus, suggesting that damping (Tan δ value) is considerably more sensitive to changes in frequency than the storage modulus.

6.7.4 Effect of Reinforcement Architecture on Damping

The damping properties of the polymeric matrix are significantly higher than the carbon fibres. Therefore, most of the composite damping is a result of the matrix damping and the fibre-matrix interface response. An ideal interface plays the role of transferring loads and does not contribute to damping. He and Liu [192] in their study indicated that the effective damping of the composite depends on several factors: fibre volume fraction, the relative shear rigidity of fibre to matrix, and a dimensionless parameter composed of interface viscosity, fibre radius, vibration frequency and shear modulus of matrix.

It is possible to tailor damping properties in fibre-reinforced composite materials with respect to constituent properties, fibre volume fraction and ply orientation angles [188]. A properly designed structure can provide significant damping and may further improve the dynamic performance and fatigue endurance. However, increased damping results in decrease in stiffness and strength.

Sample	S		M		L	
	Tan δ	Temp(°C)	Tan δ	Temp(°C)	Tan δ	Temp(°C)
1	0.323	203-211	0.344	201-211	0.355	204-215
2	0.316	201-207	0.35	201-211	0.339	205-214
3	0.333	200-208	0.335	201-210	0.344	205-214
Avg	0.324		0.343		0.346	
Std. Dev.	0.0085		0.0075		0.0082	

Table 17: Tan δ Values for the Laminates S, M and L

The temperature range above which Tan δ is higher than 0.3, is an important characteristic for good damping materials [193]. The Table 17 shows the damping properties of the laminates S, M and L. The values quoted are the Tan δ values of the dry samples of the three laminates. The average Tan δ values show that there is no significant difference between laminates M and L, while the damping property of laminate S is significantly less than the former two. The smaller resin-rich areas in laminate S may be the explanation for these lower damping properties. Chandra et al. [188] suggested an increase in damping due

to slip in the unbound regions between fibre and matrix interface. This particular phenomenon could be attributed to the higher damping behaviour of laminates M and L which had more voids compared to S.

Low damping also indicates that S has better stiffness and strength properties. This result supports the conclusions drawn from the impact properties of the laminates S, M and L, where the impact response of the laminate S showed higher stiffness (Sections 5.3 and 5.4).

6.7.5 Effect of Moisture on the Viscoelastic Response

Absorption of moisture can reduce glass transition temperatures and mechanical properties by matrix plasticization, swelling, cracking, and fibre/matrix interface damage. DMTA analysis is therefore important, as it is a sensitive indicator of the molecular motions in the material. As indicated earlier the T_g data can be reported as the $\text{Tan } \delta$ peak, loss modulus peak, or onset of the storage modulus decrease; though there is debate about which particular value should be used.

As the same resin system was used for laminates S, M and L, major variations in the glass transition temperature were not expected. Typical dynamic mechanical properties, of the dry sample, 4-day aged sample and 61-day aged sample of laminate S are shown in Figs. 94-96 respectively. The general trend observed for all the laminates was that after 4 days of ageing a secondary transition started to appear which got more distinct as the ageing progressed.

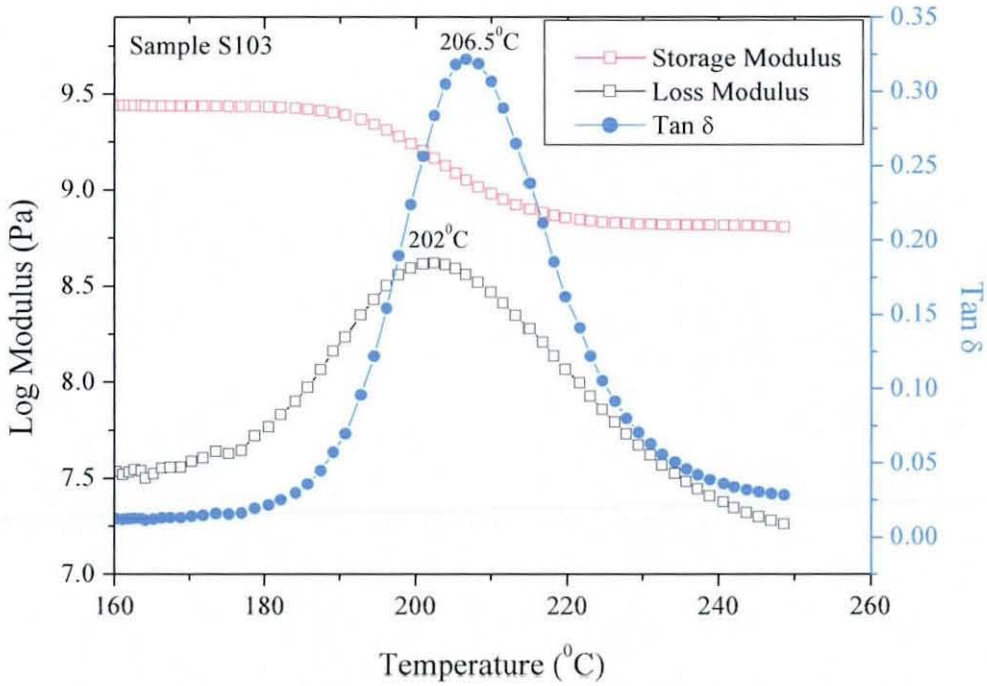


Fig. 94: Typical DMTA Test Result of Dry Laminate S

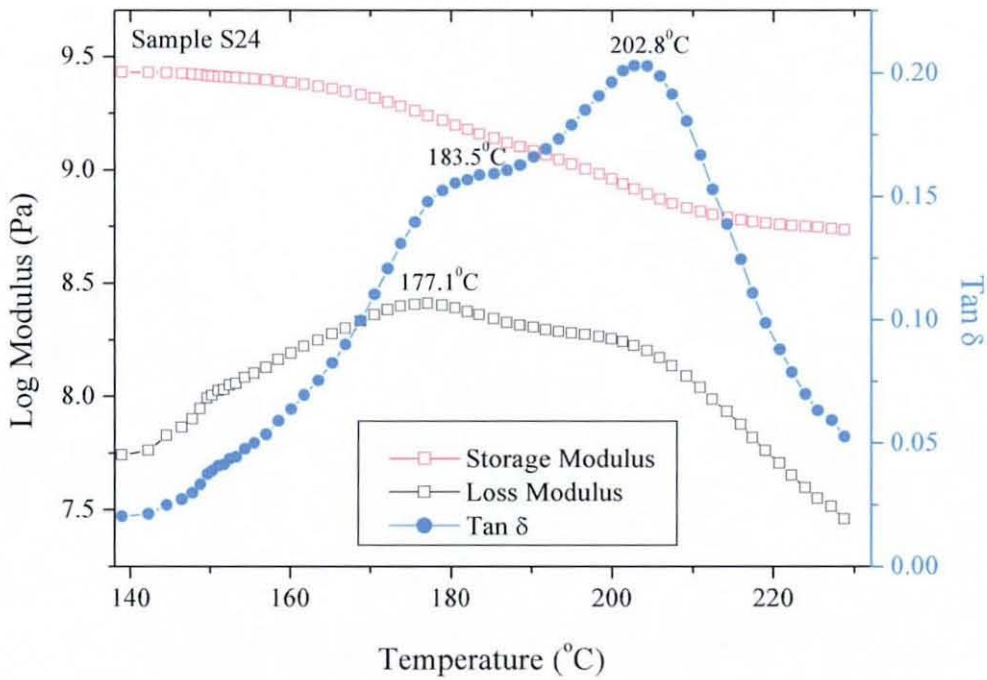


Fig. 95: Typical DMTA Test Result of Laminate S, Aged for 4 Days (%MC=0.823)

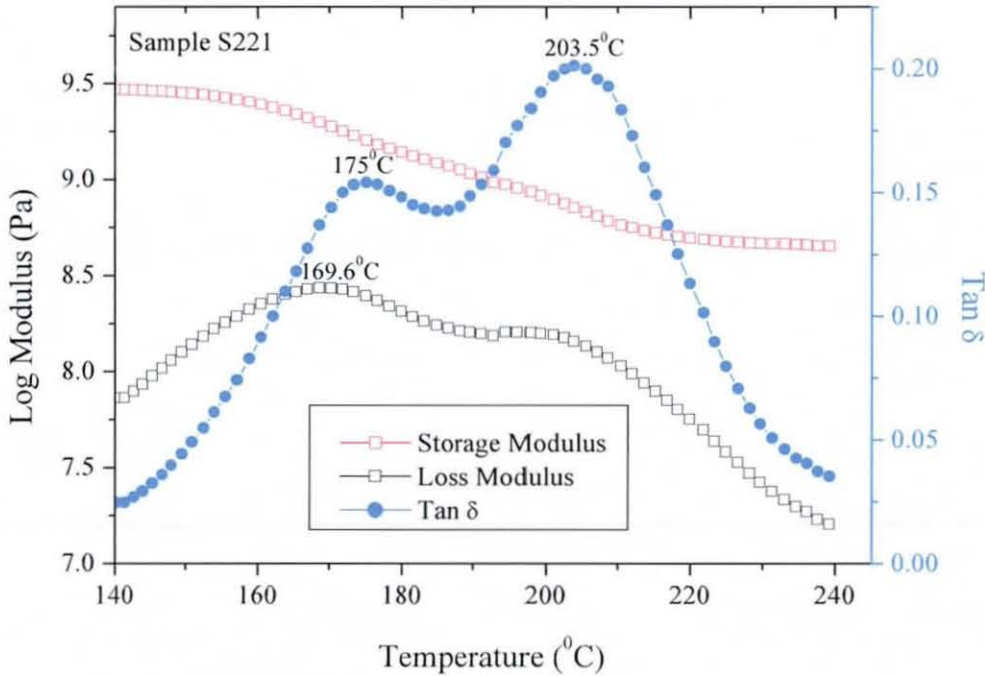


Fig. 96: Typical DMTA Test Result of Laminate S, Aged for 61 Days (%MC=1.555)

Initially it was assumed that the appearance of the secondary transition was due to degradation of the resin. In order to verify this one sample from each laminate, aged 61 days, was dried in an air-circulated oven at 180°C. The dried samples (once there was no further weight reduction) were then run on DMTA. The result for the laminate S is shown in Fig. 97. The results showed the disappearance of the secondary transition and a higher value for the T_g .

The increase in the T_g value may be attributed to further cross-linking of the resin due to the elevated temperature drying as suggested by Smith et al. [189]. The disappearance of the secondary transition peak is interesting, as it confirms that the presence of the secondary peak in the aged samples was not due to the permanent degradation of the resin. Instead it is proposed that it is due to partial hydrolysis of the samples. The secondary peak in the aged samples represents the T_g of the hydrolysed part of the sample and the other peak represents the T_g of the dry core.

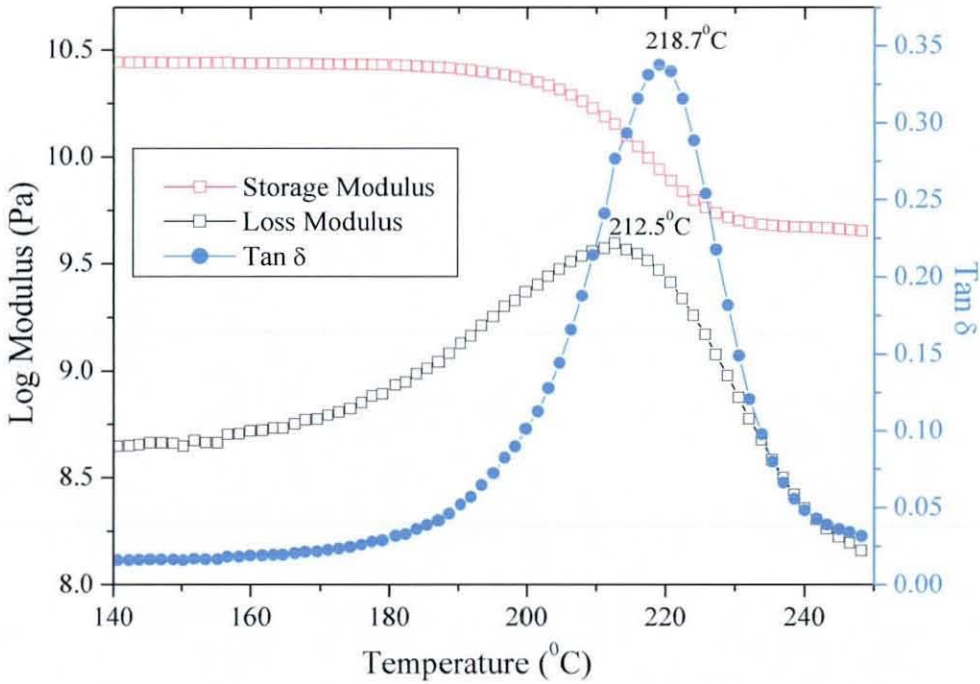


Fig. 97: DMTA Test Result of a Dried Sample (of S) after Aging for 61 Days

The effect of percentage water uptake on the storage modulus of laminates S, M and L are presented in the Figs. 98-100. The curves for the storage modulus of laminate S show little difference compared to laminates M and L, with L showing the largest variation with water uptake percentage. However, for polymer composites, storage modulus response is not very sensitive, which makes interpretation difficult.

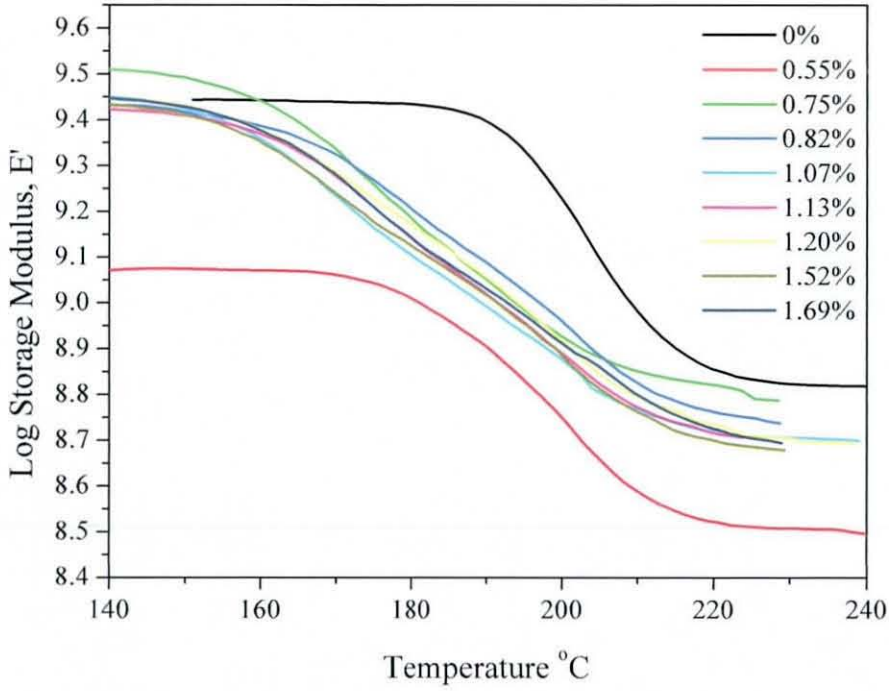


Fig. 98: Effect of Water Uptake on Storage Modulus of Laminate S

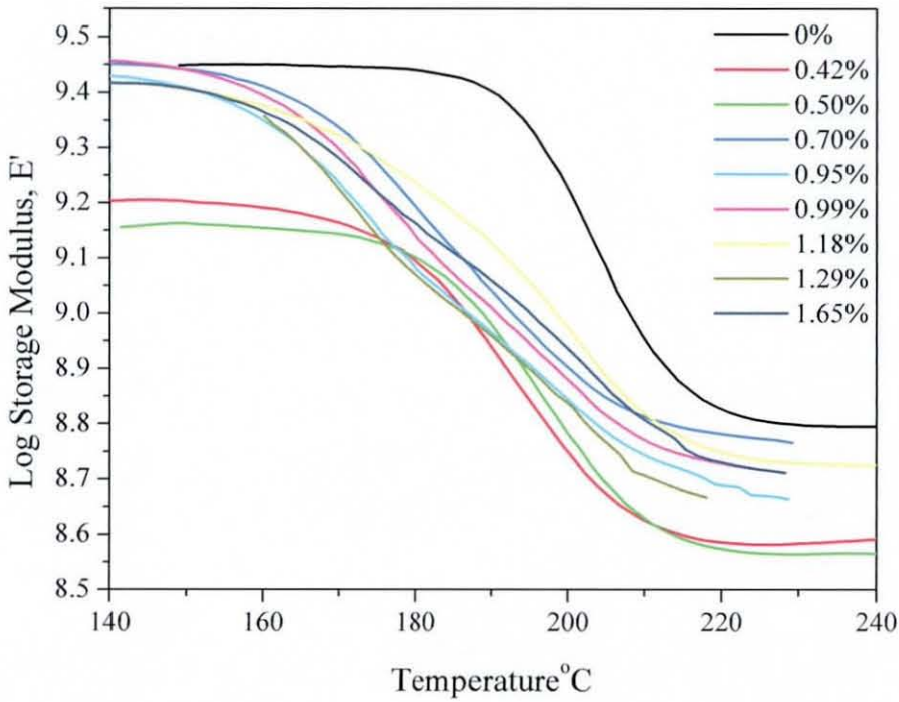


Fig. 99: Effect of Water Uptake on Storage Modulus of Laminate M

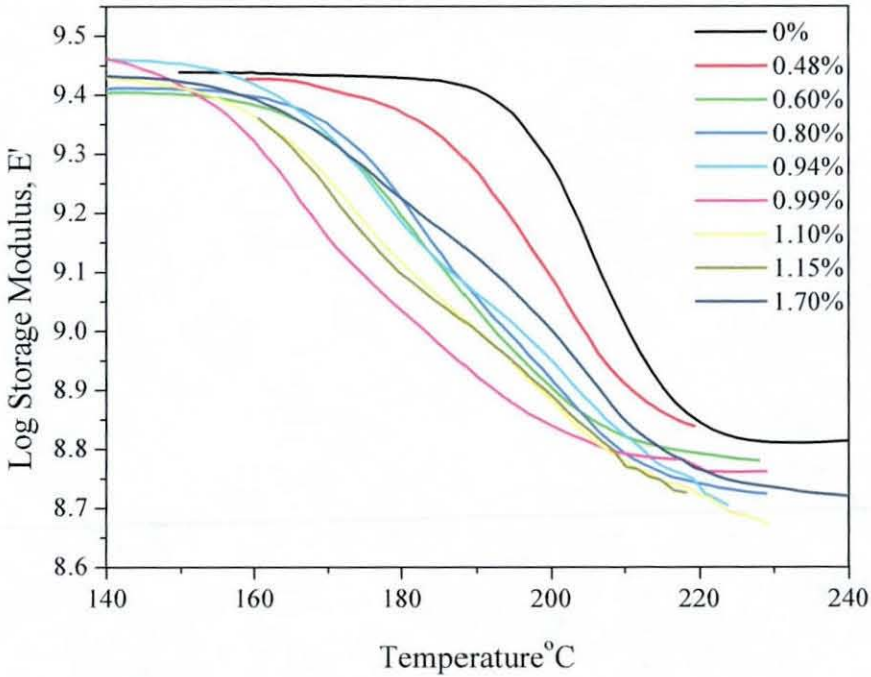


Fig. 100: Effect of Water Uptake on Storage Modulus of Laminate L

The effect of percentage water uptake on the loss modulus of laminates S, M and L are presented in the Figs. 101-103. The measurement of T_g by loss modulus peak corresponds more precisely to the temperature at which stiffness (as expressed by storage modulus) suffers significant deterioration. Results presented by Akay [194] also suggest that for advanced composites, T_g by loss modulus peak is a more consistent and appropriate index than the one based on $\text{Tan } \delta$ peak. The test results for the laminates show insignificant difference. For all the laminates the peak of the loss modulus broadens with water absorption followed by the appearance of a secondary peak.

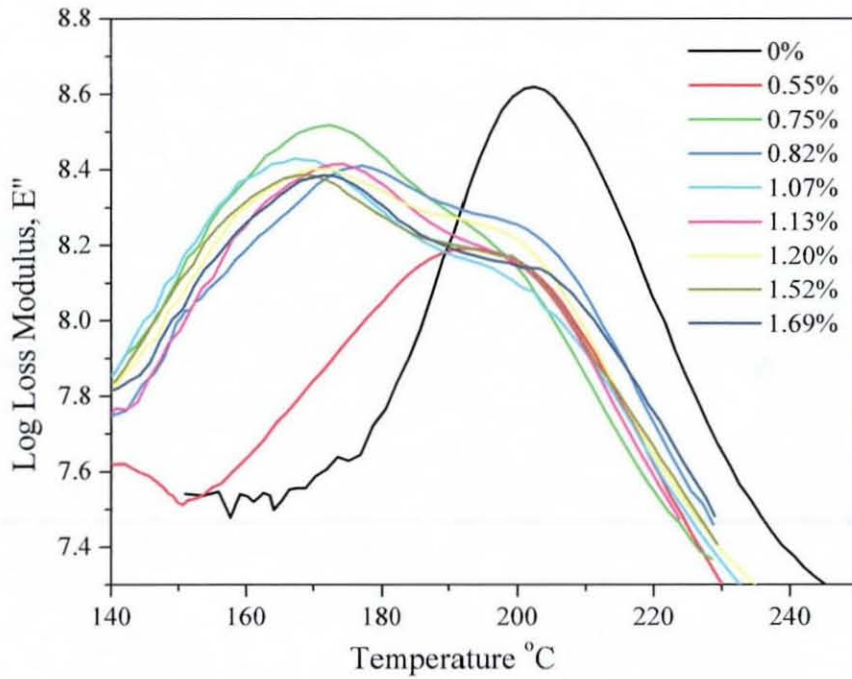


Fig. 101: Effect of Water Uptake on Loss Modulus of Laminate S

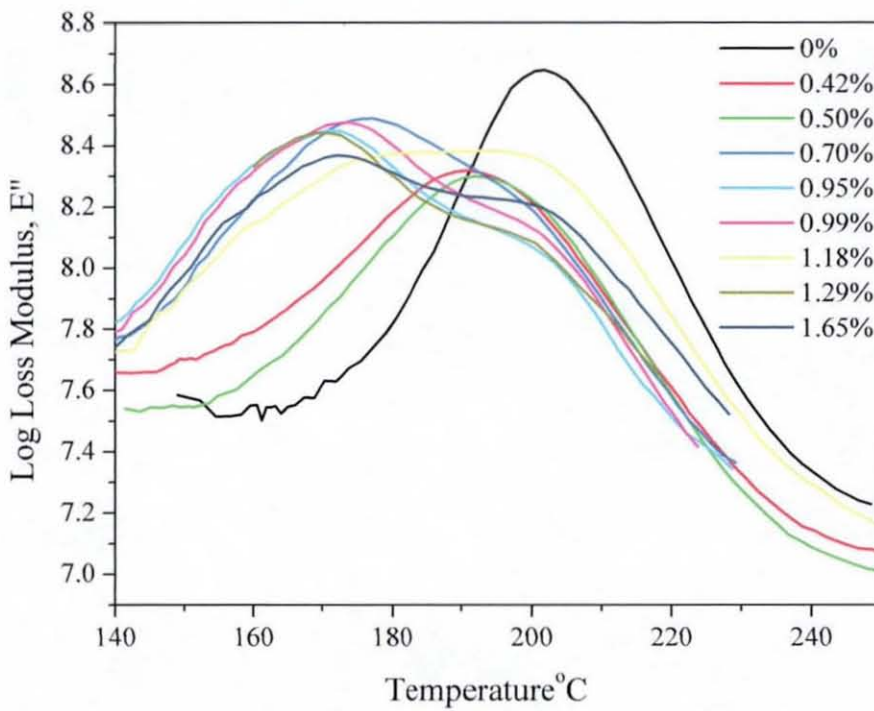


Fig. 102: Effect of Water Uptake on Loss Modulus of Laminate M

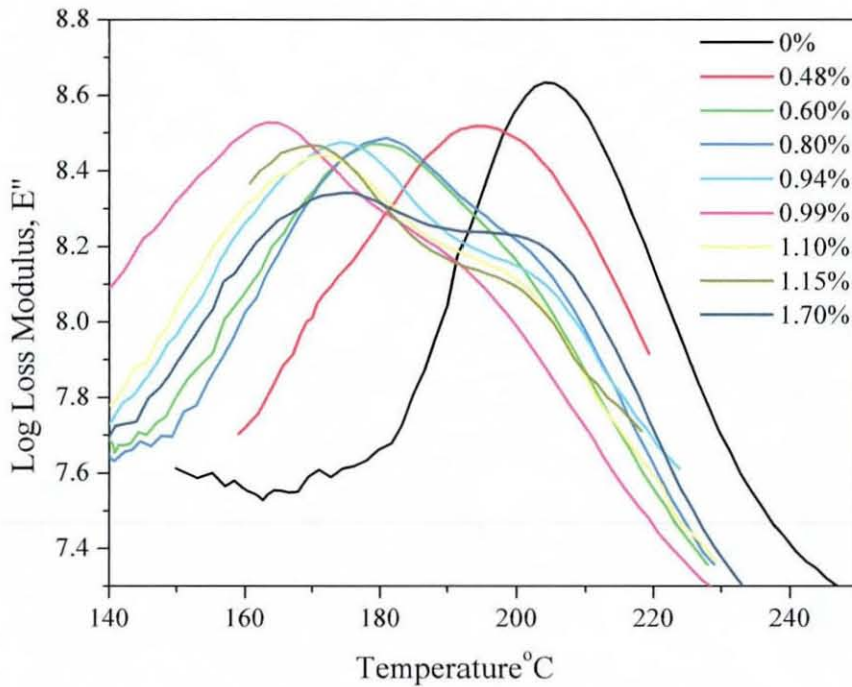


Fig. 103: Effect of Water Uptake on Loss Modulus of Laminate L

The effect of percentage water uptake on the $\text{Tan } \delta$ of laminates S, M and L are presented in the Figs. 104-106. Again, as expected, there is no significant difference in behaviour between the laminates. The $\text{Tan } \delta$ variation for the laminates follows the same trend as loss modulus – the peak broadens with increased water absorption with the appearance of a secondary peak. The value of $\text{Tan } \delta$, however, decreases significantly with water uptake percentage. As mentioned earlier this is due to partial hydrolysis of the samples.

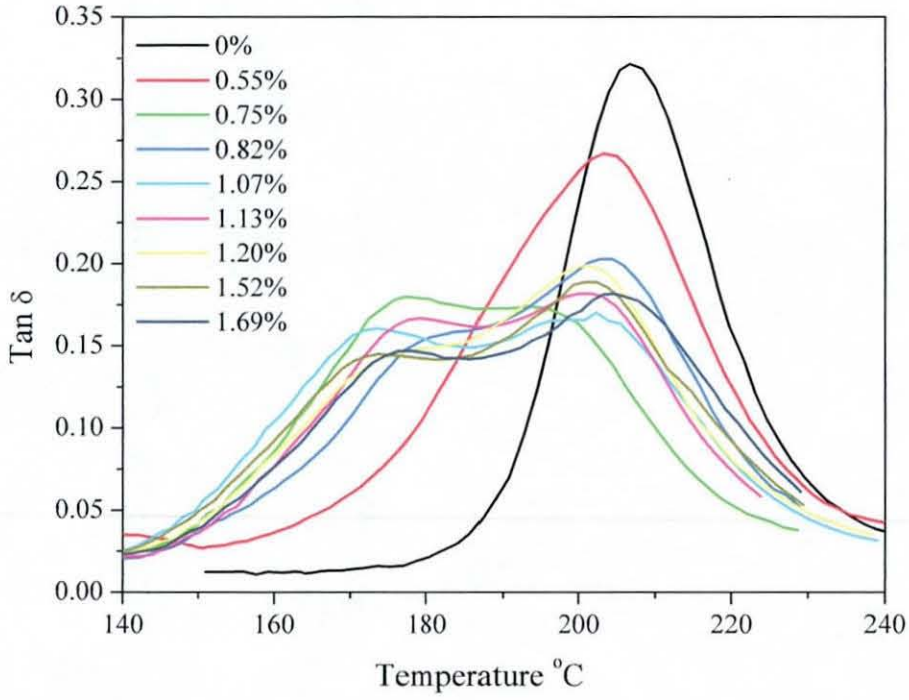


Fig. 104: Effect of Water Uptake on Tan δ of Laminate S

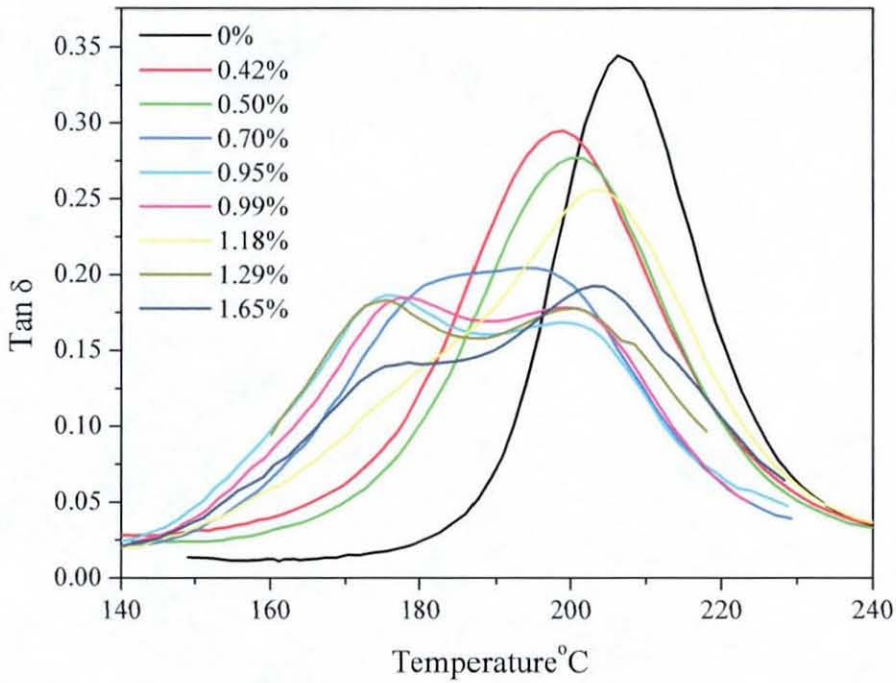


Fig. 105: Effect of Water Uptake on Tan δ of Laminate M

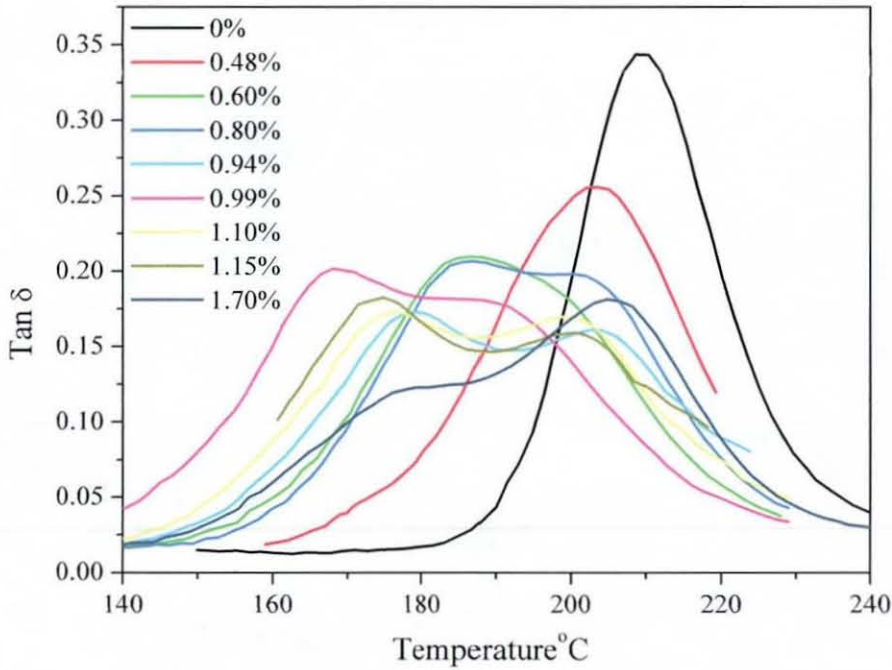


Fig. 106: Effect of Water Uptake on Tan δ of Laminate L

Fig. 107 shows the T_g measured from the loss modulus peak plotted against percentage water uptake for all the laminates. The overall trend shows a direct linear relationship between T_g and percentage water uptake, with a decrease in T_g of approximately 25°C for each 1% water uptake percentage. This reduction in T_g is because of the replacement of the strong hydrogen bonds in the epoxy network by the weaker water-related hydrogen bonds with increasing water uptake percentage. Linear fits of the results, for all three laminates, show very little difference as expected from a specific resin system. A similar outcome was reported by Maxwell and Pethrick [195].

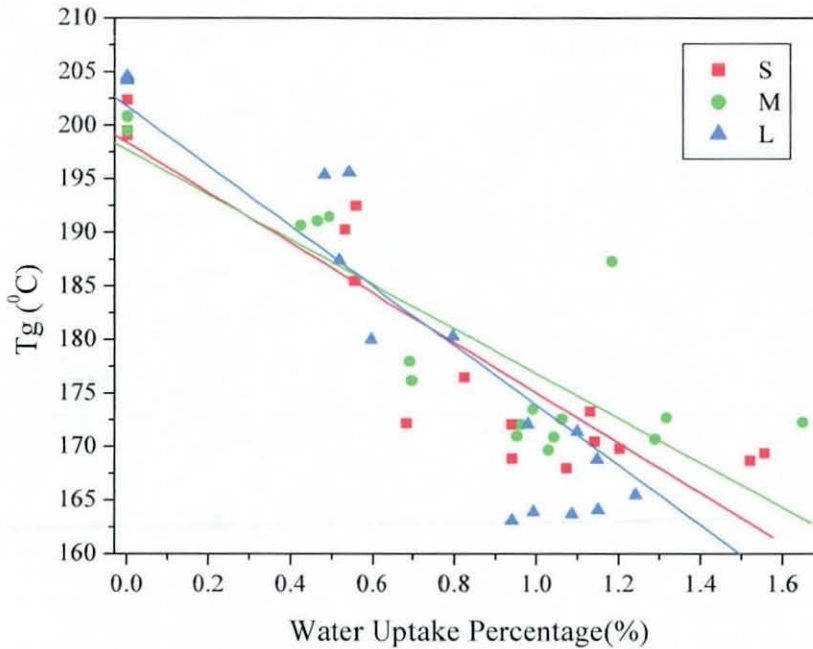


Fig. 107: Variation of Tg (Based on Loss Modulus) with Percentage Water Uptake

6.7.6 Concluding Remarks

Dynamic mechanical thermal analysis was carried out on dry and water aged samples of laminate S, M and L. There was very little difference between the laminates as the properties measured rely mainly on the resin and interface. The test results showed that the dynamic property varied with frequency of testing. The decrease in the glass transition temperature with water uptake showed a linear relationship for all the laminates. The most interesting result found was that damping behaviour of laminate L was better than laminates S and M. This result is consistent with the higher stiffness displayed by laminate S during the low energy impact and through penetration impact testing.

6.8 THERMO-HUMID EFFECT ON COMPRESSION STRENGTH

In this section, results of the compression strength of the wet unimpacted and 10, 20, 30 Joules impacted samples are presented and discussed. Four samples of each of the above impact conditions, of laminates S, M and L were tested in compression using the QMW miniature anti-buckling guide. All these samples were initially dried in an air-circulated oven till they reached a steady weight. These samples were then immersed at 70° C in a water bath. The water uptake behaviour of the samples has previously been discussed in section 6.1.

6.8.1 Thermo-humid Effect on Compression Strength of Unimpacted Samples

A measure of the unimpacted compression strength under various thermo-humid conditions provides the base-line strength for the compression strength samples. The problem associated with this testing method has been discussed in Section 5.5.1. The experience gained from the dry compression testing was applied here; which led to samples failing predominantly in the unsupported region (gap) of the anti-buckling guide although some still failed by end crushing. These failure modes have also been discussed in Section 5.5.1.

Impact Level	Compression Strength (MPa)								
	Laminate S			Laminate M			Laminate L		
	6 days	26 days	96 days	6 days	26 days	96 days	6 days	26 days	96 days
Unimpacted	231	223	255	265	252	221	229	211	230
Std. Dev.	(±16)	(±57)	(±27)	(±14)	(±22)	(±22)	(±10)	(±39)	(±12)
10 Joules	169	164	141	154	160	157	158	153	130
Std. Dev.	(±11)	(±17)	(±29)	(±8)	(±11)	(±30)	(±31)	(±9)	(±14)
20 Joules	124	122	127	121	87	118	149	119	131
Std. Dev.	(±10)	(±15)	(±11)	(±16)	(±29)	(±16)	(±9)	(±33)	(±29)
30 Joules	119	105	124	105	121	99	113	104	100
Std. Dev.	(±8)	(±17)	(±6)	(±9)	(±15)	(±11)	(±19)	(±18)	(±8)

Table 18: Summary of the Compression Test Results of 'Wet' Samples

A summary of the compression strength results is shown in Table 18. The detailed results can be found in the Appendix. Graphical presentations of this

data are shown in Figs. 108- 110 which show plots of the compression strength of unimpacted samples, of laminates S, M and L, against impact energy, at specific durations of immersion in water. The compression strengths of the unimpacted samples of S and L show no particular trend, while M shows an expected downward trend with the percentage water uptake. The large standard deviations in the compression strength of all the laminates could be attributed to two factors. Firstly, unparallel ends of a sample may have caused stress concentrations and therefore a large variation in the compression strength value. Secondly, the number of results was too few in some cases for a better statistical picture.

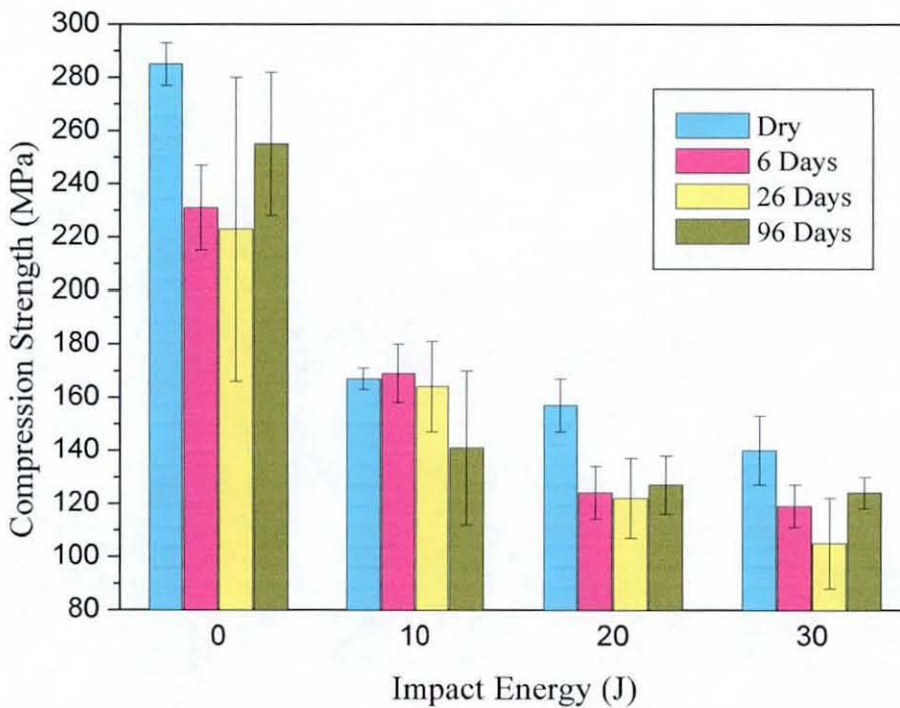


Fig. 108: Compression Strength vs. Impact Energy: Laminates S

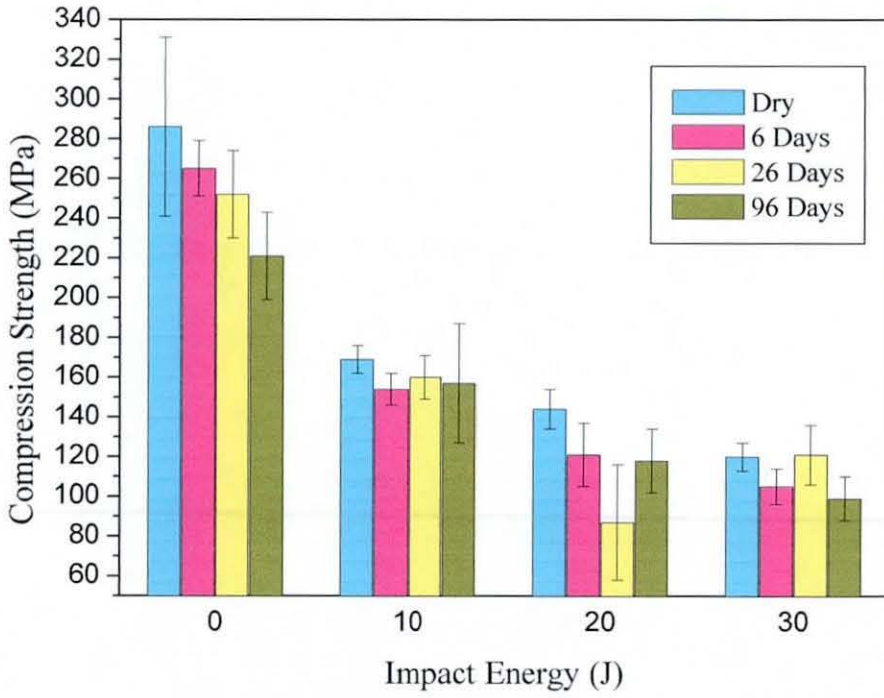


Fig. 109: Compression Strength vs. Impact Energy: Laminates M

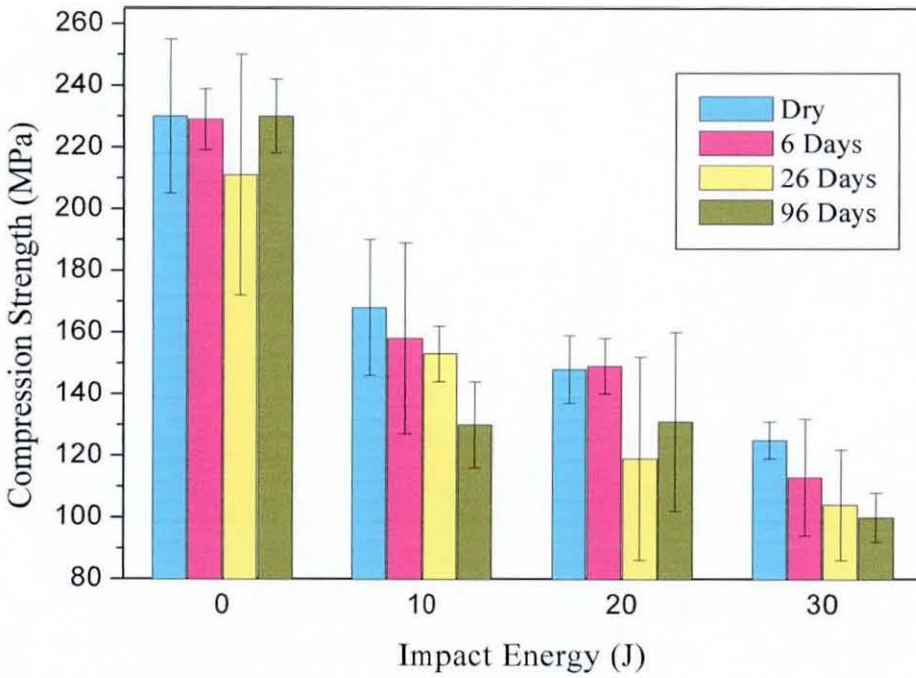


Fig. 110: Compression Strength vs. Impact Energy: Laminates L

The overall effect of percentage water uptake on the compression strength of the unimpacted samples is shown in Fig. 111. The linear fit for laminates S, M and L show a downward trend. This could be because higher water uptake by carbon-epoxy laminates weakens the fibre-matrix interface bonds. This weakening of the interfacial bonds reduces the support that fibres get from the matrix to prevent them from buckling, Rao et al. [103]. As a result the compression strength of the 'wet' samples reduces.

Fig. 111 appears to show a higher degree of compression strength reduction by the high stitch density laminate, S. As the epoxy matrix used in all three laminates was the same, the behaviour of laminate S could be attributed to possibly an increased ingress of water in the core of the laminate and a high stress concentration in the matrix around the stitching [25]. The former case was confirmed by the work of Whiteside et al. [196], where they showed that stitching yarns provide paths for accelerated moisture ingress into the core of thick laminates.

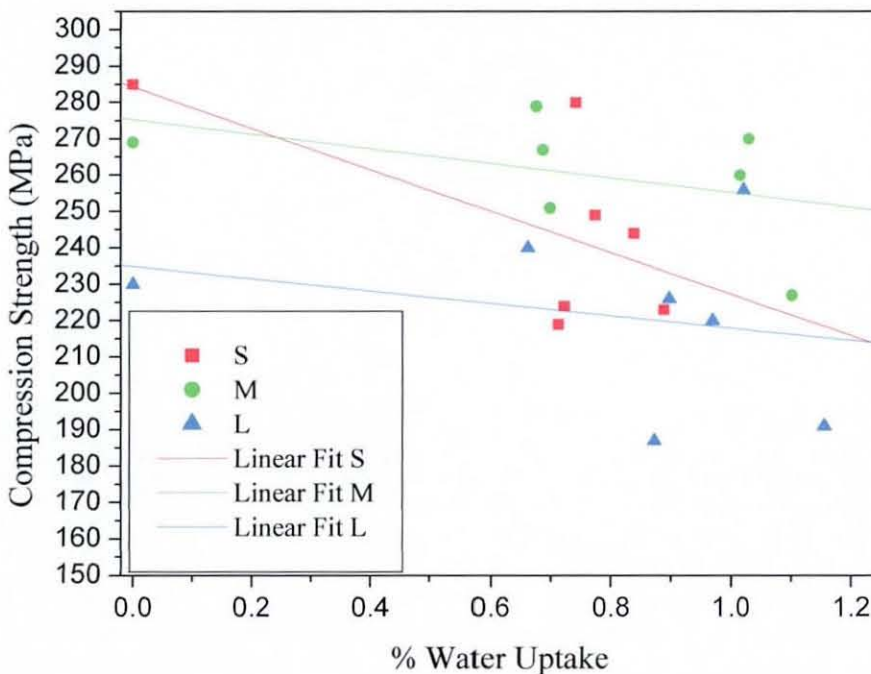


Fig. 111: Effect of Water Uptake on Compression Strength of Unimpacted Samples

In the case of high stitch density it is, therefore, expected that the 'wet' sample will have more interfacial degradation in the core area along with higher overall stress concentration due to stitching. The resultant effect could contribute to higher degradation in the compression strength for higher stitch density, which is evident from the results found in the current study.

6.8.2 Thermo-humid Effect on Compression after Impact Strength

The thermo-humid effect on 10, 20 and 30 joules impacted samples of laminates S, M and L were presented in Table 18 and Figs. 108-110. The dry CAI results, section 5.5.2, showed that the CAI strength dropped significantly as the impact energy increased. This trend was attributed to the extent of damage formed during the impact. During the thermo-humid aging of the impacted samples, further degradation of the CAI strength was observed. The damaged areas after impact presented a clear pathway for water to ingress deep inside the core of the impacted samples, which subsequently reduced the fibre-matrix interfacial bond strength. Any such weakening in the fibre-matrix interface results in less lateral support for the fibres, and premature failure of the laminates due to out-of-plane buckling.

The percentage reductions of compression strengths of unimpacted; 10, 20 and 30 joules impacted samples after a specific duration in water were calculated w.r.t. the corresponding dry compression strength for laminates S, M and L. The calculations can be found in the Appendix. The retention in compression strength due to thermo-humidity after 6, 26 and 96 days are presented in Fig. 112-114 respectively.

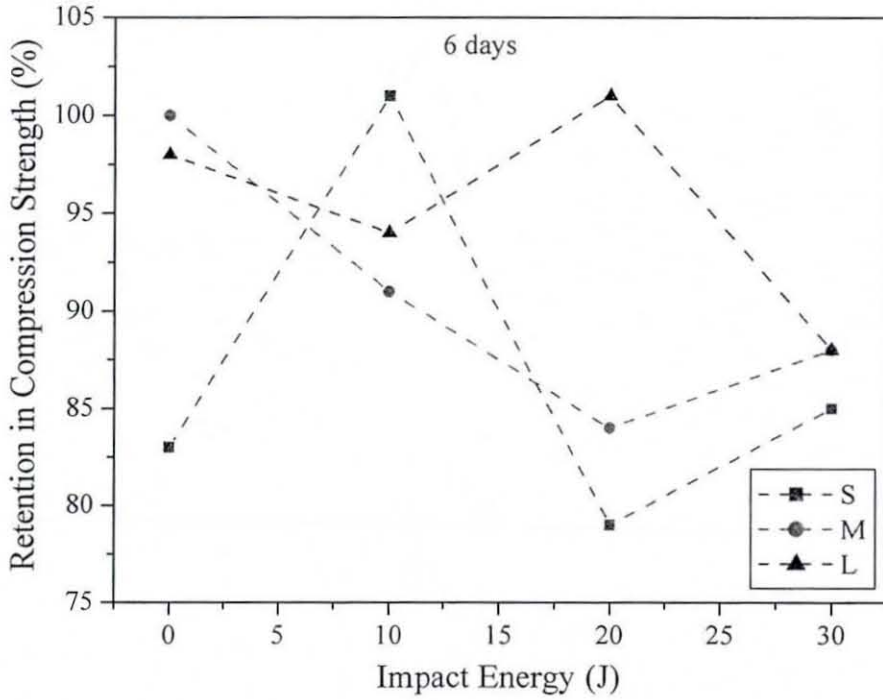


Fig. 112: % Retention of CAI Strength vs. Impact Energy after 6 Days Immersion

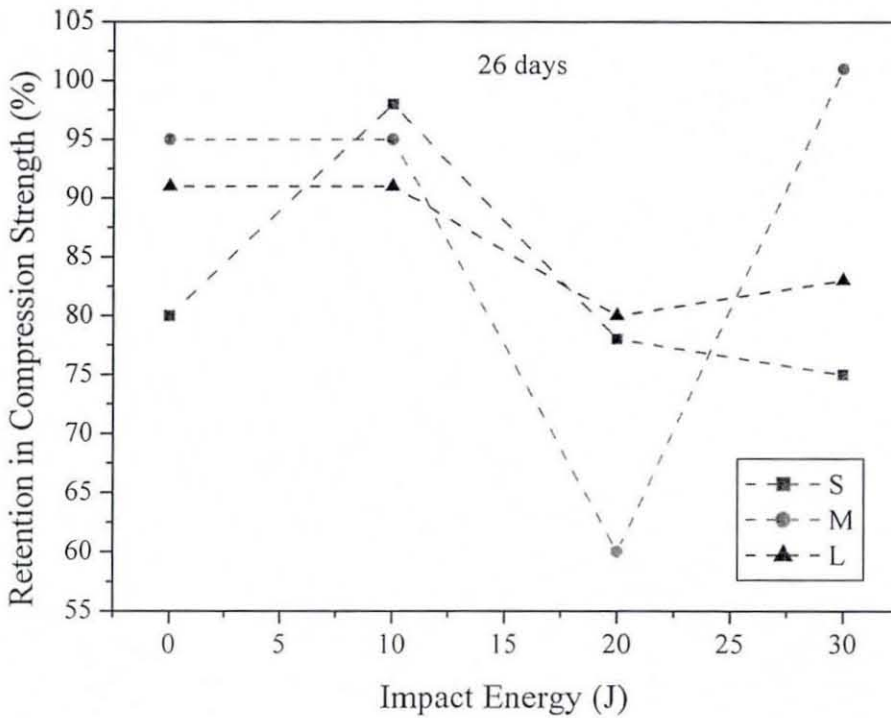


Fig. 113: % Retention of CAI Strength vs. Impact Energy after 26 Days Immersion

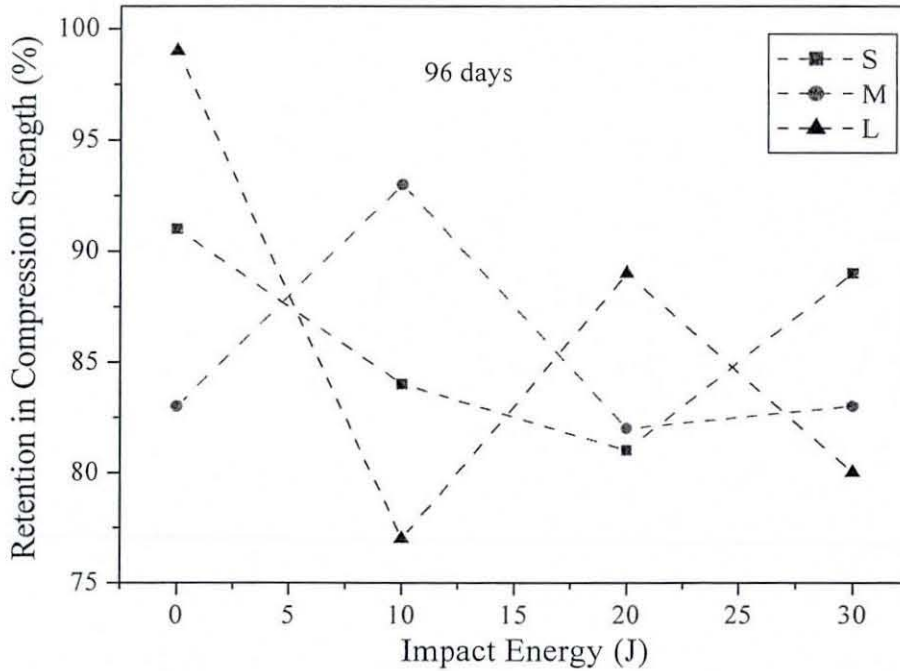


Fig. 114: % Retention of CAI Strength vs. Impact Energy after 96 Days Immersion

The large scatter observed in the percentage retention in CAI could be associated with three different factors: large variations of the compression strengths of all the laminates, variation in the damage area for a particular laminate and the trend in the water-uptake for individual laminate. These three factors are related to each other to some extent.

The individual data points, in the Figs. 115-117, showing the variation of CAI strength with percentage water uptake show that CAI strength did not always decrease as the percentage water uptake increased. On many occasions CAI strength showed increased values with water uptake. This result can be due to a number of factors, including non-uniform stress application during testing, due to misaligned specimen in the anti-buckling guide; shape of the impact damage area, waviness of the reinforcement, quantity of free water and bonded water etc. The effect of most of these factors is explained earlier except the case of free and bonded water. As fibre breakage occurred in the tensile half of the samples, it would be reasonable to assume that free water could enter and occupy the damaged area. This would have led to an increase in the percentage water

uptake value which did not have any effect on the CAI strength value but resulted in more scatter in CAI strength.

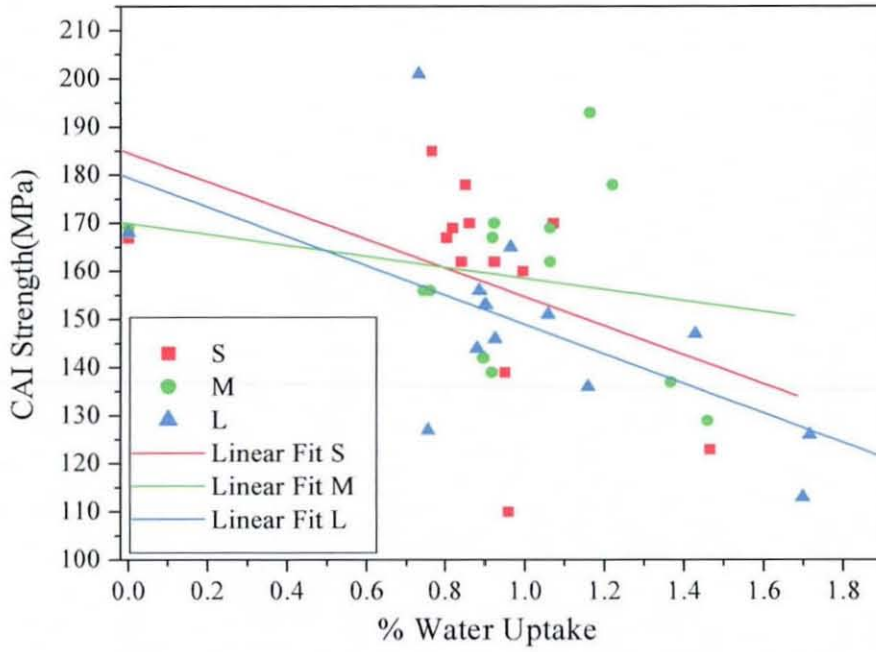


Fig. 115: Compression Strength vs. Water Uptake: 10 Joules Impacted Samples

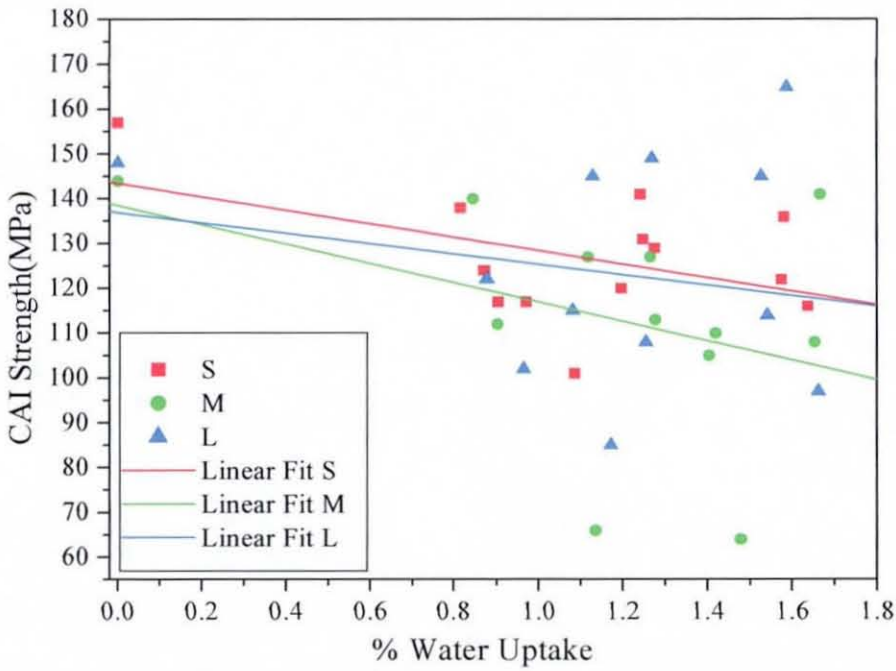


Fig. 116: Compression Strength vs. Water Uptake: 20 Joules Impacted Samples

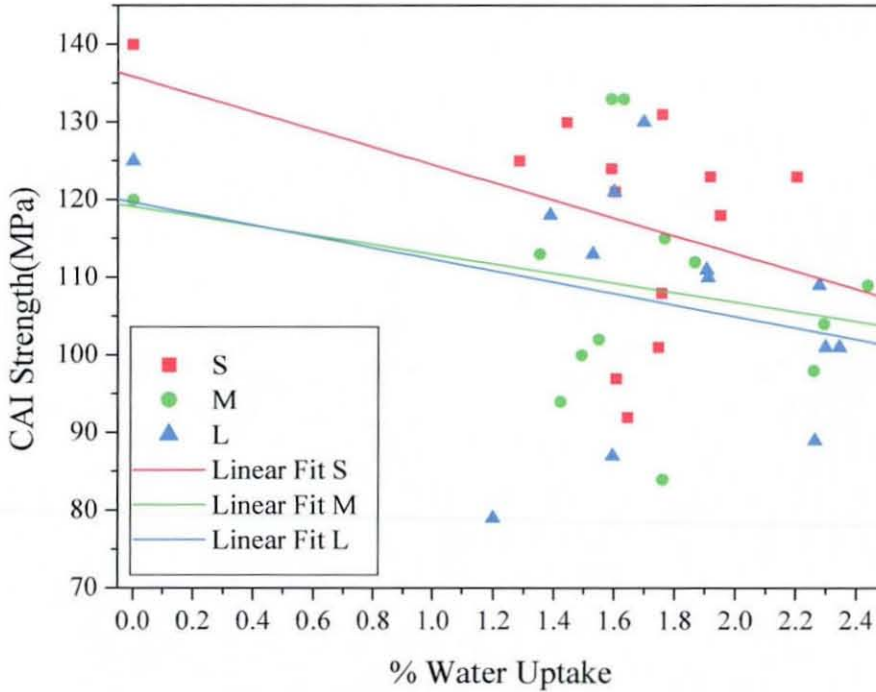


Fig. 117: Compression Strength vs. Water Uptake: 30 Joules Impacted Samples

Despite all these variables affecting the ultimate CAI strength of a sample, a trend is noticed for the 10, 20 and 30 joules impacted samples similar to the unimpacted samples which relate to stitch density. In all the cases laminate S with the highest stitch density showed a greater tendency of CAI strength degradation. As explained in section 6.8.1 this trend could be attributed to the high stress concentration in the matrix around the stitching and the increased ingress of water in the core of the laminate with high stitch density.

CHAPTER 7

CONCLUSIONS

Stitching in MWK fabrics provide through-thickness reinforcement of CFRP composites and was initially considered as a promising concept for improving damage resistance and tolerance problems. It is shown in the current study that doubling the stitch density renders slight increase in stiffness and elastic energy retention during low energy impact. More importantly, high stitch density leads to less delamination at low energy impact and more in-plane fibre fracture at higher energy impact. High stitch density is more resistant to perforation during through penetration impact and absorbs more energy. Conversely, it is shown that stitch density does not affect the damage initiation, while recovery of the dent depression is better for the laminate with low stitch density. Stitch density also has no significant effect on the ILSS (at dry, elevated temperature and after thermohumid conditioning) and that the fabric ply interfaces have low resistance to crack propagation during ILSS testing of thin laminates.

Compression and compression after impact properties are most influenced by the stitch density. Compression strength, of dry unimpacted samples, decrease with a decrease in stitch density, while the mode of failure changes from V-notched type to shear type. On the other hand, percentage retention of compression strength after impact for high stitch density is the lowest at all impact levels for both dry and aged (thermohumid) samples. This behaviour is attributed to the high stress concentration in the matrix around the stitching, and possibly an increased ingress of water in the core of the laminate leading to more interfacial degradation. Both Mode I and II fracture toughness properties of the laminates are affected by the resin-rich areas and tow waviness (due to stitch architecture), which act against each other, nullifying, to some extent, their contribution to the mechanical property.

Thermohumid property testing results show that the diffusion of water molecules into epoxy resins is largely non-Fickian and depends on two factors – availability of micro-voids (evident from Raman analysis) and the attractive forces between the water molecules and the epoxy resin matrix. Distribution of resin rich area and voids, which are dependent on stitch density, also play a significant part in water ingress in composite samples. FTIR and Raman analysis of the aged samples indicate an increase in the formation of hydrogen bonds after hydration but has no correlation with the increase in % water uptake. However, surface defects lead to more degradation and is evident from Raman mappings.

DMTA results indicate better damping property of the low stitch density. High stitch density tends to show significantly low damping, indicating better stiffness and strength properties. The storage modulus, loss modulus and $\tan \delta$ decrease significantly with percentage water uptake for all the laminates. The appearance of a secondary $\tan \delta$ peak indicates that the diffusion process for this resin system is quite slow, which leaves the core not degraded.

The evidence from this programme points out that the mechanical performance of MWK based composites, in contrast to prepregs, is not uniquely determined by the fibre volume fraction of the layers and their orientations. The extent to which these properties are affected by stitch architectures is dependent on their effect on the extent of tow waviness and axial alignment of the fibres. Fabrication techniques also decide the distribution of resin pockets and voids, which in turn influence the mechanical properties. Therefore, to maximize delamination resistance with minimal loss of in-plane mechanical properties, an optimal combination of the stitching and fabrication parameters will need to be identified. More importantly, the textile quality issues – which include homogeneity and orientation of the reinforcement fibres, gaps between the fibres etc. and the quality assessment problems, need to be solved.

CHAPTER 8

FUTURE WORK

The results presented in this study were based on commercially produced fabrics, which incorporated a variety of faults like broken/ twisted carbon fibres, broken/ missing stitching yarns etc. Furthermore, during the production of the laminates, the fabrics were cut into smaller pieces, thereby changing the stitching tension, which subsequently changed the crimp in, and gap between, the tows. It is recommended for future studies that these parameters are strictly controlled during the production stages of the fabric and of the laminates, in order to be confident that the results found are the actual behaviour of the reinforcements and are not being caused by the faults listed earlier.

A further issue raised in this study about the liquid composite moulding is the flow behaviour of the resin during manufacturing. The permeability of the reinforcements with varying stitch density requires focused analysis using displacement controlled and stress controlled measurement techniques. Fibre packing behaviour with increasing or decreasing load also needs investigation.

It would be worthwhile conducting a study into the effect of various types and sizes (number of filaments) of stitching materials. Such material may include glass, carbon, Kevlar etc.

It is also recommended that the resin-rich area and tow crimp variation with the stitch density be quantified. These were found to be competing during damage progression.

As impact properties were found to be affected by the stacking sequence significantly, it would be interesting to check the Mode I and II fracture toughness behaviour due to the change in stacking sequence.

A further study of the influence of impact test variables on the CAI test results could be of interest. Variables such as type or size of impactor, type or size of the support, thickness of the sample, number of impacts, etc. could be investigated for further characterisation of damage resistance and tolerance due to change in stitch density.

The effect of various design of anti-buckling guide on the CAI properties could also be undertaken. The CAI properties using miniaturised test fixture and other fixtures require further comparison, in order to increase the confidence in the validity of miniaturised testing.

During the long term test, it is recommended that impact behaviour after ageing is carried out. Literature surveys showed only a few such studies have ever been carried out. However, this particular property of structural composites is thought to be important.

Further study using Raman spectroscopy should be carried out. The initial results presented in this study showed that mapping of the aged sample is useful for chemical analysis. For better quality of results it is recommended that the acquisition time of the spectra be increased by at least fifty-fold. Some publications have presented the technique of measuring stress concentration using Raman Spectroscopy, which could be used to determine the stress concentration due to various stitching parameter in the MWK fabric reinforced composites.

REFERENCE

1. Mazumdar, S.K., *Composites Manufacturing: Materials, Products and Process Engineering*. 2000: CRC Press.
2. Nutt, S.R., Introduction to Constituent Materials, in *ASM Handbook*. 2001: ASM International.
3. Mills, A., Burley, G. and Backhouse, R., Innovative Materials and Manufacturing Processes for the Cost Effective Manufacture of Composite Airframe Structure. in *International SAMPE Symposium and Exhibition*. 1999.
4. Baker, A.A., Jones, R. and Callinan, R.J., *Damage Tolerance of Graphite/Epoxy Composites*. *Composite Structures*, 1985. **4**(1): p. 15-44.
5. Abrate, S., *Impact on Composite Structures*. 1998: Cambridge University Press.
6. Poe, C.C., Dexter, H.B. and Raju, I.S., Review of the NASA Textile Composite Research. in *38th AIAA/ASME/ASCE/AHS/ASC Structures, Structural Dynamics, and Materials Conference and Exhibit Adaptive Structures Forum*. 1997.
7. Jackson, W.C. and Portanova, M.A., Impact Damage Resistance of Textile Composites. in *International SAMPE Technical Conference*. 1996.
8. Bibo, G.A. and Hogg, P.J., Influence of Reinforcement Architecture on Damage Mechanisms and Residual Strength of Glass-Fibre/Epoxy Composite Systems. *Composites Science and Technology*, 1998. **58**(6): p. 803-813.
9. Mills, A., *INFACS (Fibre Placement and Structures)*. 1999, EPSRC Innovative Manufacturing Initiative.
10. Avila-Dominguez, R. Composites Manufacturing Using Non-Crimp Fabrics (NCF). in *European Society of Composite Materials*. 2001: Newsletter 4.

11. Tong, L., Mouritz, A.P. and Bannister, M.K., *3D Fibre Reinforced Polymer Composites*. 2002: Elsevier Science Ltd.
12. de Araujo, M., Hu, H. and Figueiro, R., *Multiaxial Weft Knitted Technology for Industrial Textiles*. International Textile Bulletin – Nonwovens Industrial Textiles, 1995. 41(1): p. 44-45.
13. Anon., *Copcentra MAX3 CNC*, LIBA.
14. Anon., *Multiaxial High-Tech Knitting Machine Manual*, Karl Mayer.
15. Marsh, G., *Affordability is the Focus for Aerospace Composites*. Reinforced Plastics, 2001. 45(1): p. 34-36.
16. Dow, M.B. and Dexter, H.B., *Development of Stitched, Braided and Woven Composite Structures in the ACT Program and at Langley Research Center (1985 to 1997) Summary and Bibliography*. 1997, NASA. p. 1-86.
17. Marsh, G., *Affordability Essential for Aerospace Materials*. Reinforced Plastics, 2000. 44(1): p. 32-35.
18. www.vectorply.com accessed in 2003
19. Ko, F.K., Hu, J. and Jiang, Y., *Modeling Uniaxial Tensile Properties of Multiaxial Warp Knitted Fabrics*. Textile Research Journal, 1998. 68(11): p. 828-834.
20. Ko, F.K., *Three Dimensional Fabrics for Composites*, in *Textile Structural Composites*. 1989, Elsevier Science Publisher. p. 129-172.
21. www.karlmayer.de accessed in 2003
22. Anon., *Reinforcement - Specifications for Multi-axial Multi-ply Fabrics, Part 1: Designation*. BS EN 13473-1: 2001, 2001.
23. Ko, F.K., *Processing of Textile Preforms*, in *Advanced Composites Manufacturing*, T.G. Gutowski, Editor. 1997, John Wiley & Sons Inc. p. 157-206.

24. Rongxing, Z., Hong, H., Nanliang, C. and Xunwei, F., An Experimental and Numerical Study on the Impact Energy Absorption Characteristics of the Multiaxial Warp Knitted (MWK) Reinforced Composites. *Journal of Composite Materials - Lancaster*, 2005. **39**(6): p. 525-543.
25. Mouritz, A.P., Leong, K.H. and Herszberg, I., *A Review of the Effect of Stitching on the In-plane Mechanical Properties of Fibre-reinforced Polymer Composites*. *Composites Part A: Applied Science and Manufacturing*, 1997. **28**(12): p. 979-991.
26. Mouritz, A.P. and Cox, B.N., *A Mechanistic Approach to the Properties of Stitched Laminates*. *Composites Part A: Applied Science and Manufacturing*, 2000. **31**(1): p. 1-27.
27. Mouritz, A.P., Bannister, M. K., Falzon, P. J. and Leong, K. H., *Review of Applications for Advanced Three-Dimensional Fibre Textile Composites*. *Composites Part A: Applied Science and Manufacturing*, 1999. **30**(12): p. 1445-1461.
28. Anon., *SP Systems Guide to Composites*, Technical Guide, SP Systems.
29. Leong, K., Ramakrishna, S., Huang, Z. and Bibo, G. A., *The Potential of Knitting for Engineering Composites - A Review*. *Composites Part A: Applied Science and Manufacturing*, 2000. **31**(3): p. 197-220.
30. Ko, F.K. and Kutz, J., *Multiaxial Warp Knit for Advanced Composites*. in American Society of Mechanical Engineers, Materials Division (Publication) MD. 1988.
31. Wang, Y., Li, J. and Do, P.B., *Properties Of Composite Laminates Reinforced With E-Glass Multiaxial Non-Crimp Fabrics*. *Journal of Composite Materials*, 1995. **29**(17): p. 2317-2333.
32. Truong, T.C., Vettori, M., Lomov, S. and Verpoest, I., *Carbon Composites Based on Multi-Axial Multi-Ply Stitched Preforms. Part 4. Mechanical Properties of Composites and Damage Observation*. *Composites Part A: Applied Science and Manufacturing*, 2005. **36**(9): p. 1207-1221.

33. Dexter, H.B. and Hasko, G.H., *Mechanical Properties and Damage Tolerance of Multiaxial Warp-Knit Composites*. Composites Science and Technology, 1996. **56**(3): p. 367-380.
34. Bibo, G.A., Hogg, P.J. and Kemp, M., *Mechanical Characterisation of Glass and Carbon-Fibre-Reinforced Composites Made with Non-Crimp Fabrics*. Composites Science and Technology, 1997. **57**(9-10): p. 1221-1241.
35. Bibo, G.A., Hogg, P. J., Backhouse, R. and Mills, A., *Carbon-Fibre Non-Crimp Fabric Laminates for Cost-Effective Damage-Tolerant Structures*. Composites Science and Technology, 1998. **58**(1): p. 129-143.
36. Kang, T.J. and Kim, C., Mechanical and Impact Properties of Composite Laminates Reinforced with Kevlar Multiaxial Warp Knit Fabrics. *Polymers and Polymer Composites*, 1997. **5**(4): p. 265-272.
37. Kang, T.J. and Kim, C., Energy-Absorption Mechanisms in Kevlar Multiaxial Warp-Knit Fabric Composites under Impact Loading. *Composites Science and Technology*, 2000. **60**(5): p. 773-784.
38. Shyr, T.W. and Pan, Y.H., *Impact Resistance and Damage Characteristics of Composite Laminates*. *Composite Structures*, 2003. **62**(2): p. 193-203.
39. Schrauwen, B. and Peijs, T., Influence of Matrix Ductility and Fibre Architecture on the Repeated Impact Response of Glass-Fibre-Reinforced Laminated Composites. *Applied Composite Materials*, 2002. **9**(6): p. 331-352.
40. Joffe, R. and Varna, J., Effect of Bundle Waviness on Compressive Strength and Notch Sensitivity of Non-Crimp Fabric Composites. in American Society of Mechanical Engineers, Applied Mechanics Division, AMD. 2002.
41. Edgren, F., Mattsson, D, Asp, L.E. and Varna, J., *Formation of Damage and Its Effects on Non-Crimp Fabric Reinforced Composites Loaded in Tension*. *Composites Science and Technology*, 2004. **64**(5): p. 675-692.

42. Lomov, S.V., Belov, E. B., Bischoff, T., Ghosh, S. B., Truong, T.C. and Verpoest, I., *Carbon Composites Based on Multiaxial Multiply Stitched Preforms. Part 1. Geometry of the Preform*. Composites Part A: Applied Science and Manufacturing, 2002. **33**(9): p. 1171-1183.
43. Rudd, C.D., Long, A. C., Kendall, K. N., Mangin, C. G. E., *Liquid Moulding Technologies: Resin Transfer Moulding, Structural Reaction Injection Moulding And Related Processing Techniques*. 1997: Woodhead Publishing Ltd. p. 1-64.
44. Williams, C., J. Summerscales, and S. Grove, *Resin Infusion under Flexible Tooling (RIFT): a review*. Composites Part A: Applied Science and Manufacturing, 1996. **27**(7): p. 517-524.
45. Stewart, R., *SCRIMP Offers a Cleaner Alternative*. Reinforced Plastics, 2002. **46**(5): p. 26-29.
46. Marsh, G., *Resin Film Infusion – Composites Cost Reducer*. Reinforced Plastics, 2002. **46**(2): p. 44-49.
47. Sevostianov, I.B., Verijenko, V. E., von Klemperer, C. J. and Chevallereau, B., *Mathematical Model of Stress Formation During Vacuum Resin Infusion Process*. Composites Part B: Engineering, 1999. **30**(5): p. 513-521.
48. Darcy, H.P.C., *Les fontaines publiques de la ville de Dijon*. 1856: Dalmont, Paris.
49. Ahn, K.J., J.C. Seferis, and L. Letterman, *Autoclave Resin Film Infusion Process- Analysis and Prediction of Resin Content*. Sampe Quarterly, 1990. **21**(2): p. 3-9.
50. Ahn, K.J., J.C. Seferis, and J.C. Berg, *Simultaneous Measurements of Permeability and Capillary Pressure of Thermosetting Matrices in Woven Fabric Reinforcements*. Polymer Composites, 1991. **12**(3): p. 146-152.
51. Anon., *Process Instructions Manual, ACG MTM44 - Dual Cure Epoxy Matrix*, Advanced Composites Group Ltd.

52. Park, J. and Kang, M.K., *A Numerical Simulation of the Resin Film Infusion Process*. *Composite Structures*, 2003. **60**(4): p. 431-437.
53. Gutowski, T.G., Cai, Z., Bauer, S., Boucher, D., Kingery, J. and Wineman, S., *Consolidation Experiments for Laminate Composites*. *Journal of Composite Materials*, 1987. **21**: p. 650-669.
54. Qi, B., Raju, J., Kruckenberg, T. and Stanning, R., *A Resin Film Infusion Process for Manufacture of Advanced Composite Structures*. *Composite Structures*, 1999. **47**(1-4): p. 471-476.
55. Dillon, G., P. Mallon, and M. Monaghan, *The Autoclave Processing of Composites*, in *Advanced Composites Manufacturing*, T.G. Gutowski, Editor. 1997, John Wiley & Sons Inc. p. 207-241.
56. Gutowski, T.G., *A Brief Introduction to Composite Materials and Manufacturing Processes*, in *Advanced Composites Manufacturing*, T.G. Gutowski, Editor. 1997, John Wiley & Sons Inc. p. 5-42.
57. Godbehere, A.P., *The Manufacture of Composites by Resin Film Infusion of Non-Crimp Fabrics*. 1995, PhD Thesis, Cranfield University.
58. Robitaille, F. and Gauvin, R., *Compaction of Textile Reinforcements for Composites Manufacturing. I: Review of Experimental Results*. *Polymer Composites*, 1998. **19**(2): p. 198-216.
59. Robitaille, F., Long, A.C. and Rudd, C.D., *Geometric Modelling of Textiles for Prediction of Composite Processing and Performance Characteristics*. *Plastics, Rubber and Composites*, 2002. **31**(2): p. 66-76.
60. Crookston, J.J., Long, A.C. and Jones, I.A., *Modelling Effects of Reinforcement Deformation During Manufacture on Elastic Properties of Textile Composites*. *Plastics Rubber and Composites*, 2002. **31**(2): p. 58-66.
61. Chen, B. and Chou, T.W., *Compaction of Woven-Fabric Preforms in Liquid Composite Molding Processes: Single-Layer Deformation*. *Composites Science and Technology*, 1999. **59**(10): p. 1519-1526.

62. Visconti, I.C., Langella, A. and Durante, M., *Analysis of Transversal Permeability for Different Types of Glass Fiber Reinforcement*. Applied Composite Materials, 2003. 10(2): p. 119-127.
63. Harper, J.F., Miller, N.A. and Yap, S.C., Problems Associated with the Compression Testing of Fibre Reinforced Plastic Composites. Polymer Testing, 1993. 12(1): p. 15-29.
64. Minguet, P.J., Fedro, M.J. and Gunther, C.K., *Test Methods for Textile Composites*. 1994, NASA.
65. Kyriakides, S., Arseculeratne, R., Perry, E. J. and Liechti, K. M., *On the Compressive Failure of Fiber Reinforced Composites*. International Journal of Solids and Structures, Time Dependent Problems in Mechanics, 1995. 32(6-7): p. 689-738.
66. Brookes, C.R. and Choudhury, A., *Failure Analysis of Engineering Materials*. 2002: McGraw Hill Companies Inc. p. 304-306.
67. Soutis, C., Measurement of the Static Compressive Strength of Carbon-Fibre/Epoxy Laminates. Composites Science and Technology, 1991. 42(4): p. 373-392.
68. Soutis, C., Curtis, P.T. and Fleck, N.A., *Compressive Failure of Notched Carbon Fibre Composites*. Proc R Soc London A, 1993. 440(1909): p. 241-256.
69. Miller, A.J., The Effect of Microstructural Parameters on the Mechanical Properties of Non-crimp Fabric Composites. 1996, MPhil Thesis, Cranfield University, UK.
70. Drapier, S. and Wisnom, M.R., *Finite-Element Investigation of the Compressive Strength of Non-Crimp-Fabric-Based Composites*. Composites Science and Technology, 1999. 59(8): p. 1287-1297.

71. Hogg, P.J., Prichard, J.C. and Stone, D.L., *A Miniaturised Post-Impact Compression Test*. Composites Testing and Standardisation, European Conference, ECCM-CTS, 1992: p. 357-370.
72. Hull, D., *An Introduction to Composite Materials*. 1981: Cambridge University Press.
73. Shu, W.Y. and Lin, K.F., The Effects of Additives on Curing Properties, Resin Contents and Mechanical Properties of Graphite/ Epoxy Composites. *Polymer Composites*, 1992. **13**(3): p. 213-222.
74. Drapier, S. and Wisnom, M.R., A Finite-element Investigation of the Interlaminar Shear Behaviour of Non-Crimp-Fabric-based Composites. *Composites Science and Technology*, 1999. **59**(16): p. 2351-2362.
75. Piggott, M.R., The Effect of Fibre Waviness on the Mechanical Properties of Unidirectional Fibre Composites: A Review. *Composites Science and Technology*, 1995. **53**(2): p. 201-205.
76. Matthews, F.L. and Rawlings, R.D., *Composite Materials: Engineering and Science*. 1994: Chapman & Hall.
77. Sjogren, A., Asp, L. E., Greenhalgh, E. S. and Hiley, M. J., Interlaminar Crack Propagation in CFRP: Effects of Temperature and Loading Conditions on Fracture Morphology and Toughness, in *Composite Materials: Testing, Design and Acceptance Criteria*, ASTM STP 1416. 2002, p. 235-252.
78. Kollar, L.P. and Springer, G.S., *Mechanics of Composite Structures*. 2003: Cambridge University Press.
79. Anon., ESIS – European Structural Integrity Society – Polymer and Composites Task Group.
80. Kessler, A. and Bledzki, A., Correlation between Interphase-Relevant Tests and the Impact-Damage Resistance of Glass/Epoxy Laminates with

- Different Fibre Surface Treatments. *Composites Science and Technology*, 2000. **60**(1): p. 125-130.
81. Jordan, M.W. and Bradley, W.L., Micromechanism of Fracture in Toughened Graphite-Epoxy Laminates, in *Toughened Composites: Symposium on Toughened Composites*, N.J. Johnston, Editor. 1987, ASTM STP 937.
 82. Hogg, P.J. and Bibo, G.A., *Impact and Damage Tolerance*, in *Mechanical Testing of Advanced Fibre Composites*, Editor J.M. Hodgkinson,. 2000, CRC Press. p. 211-247.
 83. Chivers, R.A. and Moore, D.R., Further Developments in the Interpretation of Signals from Instrumented Falling Weight Impact (IFWI). *Measurement Science and Technology*, 1990. **1**(4): p. 313-321.
 84. Bibo, G.A., Leicy, D., Hogg, P. J. and Kemp, M., High-temperature Damage Tolerance of Carbon Fibre-reinforced Plastics: Part 1: Impact Characteristics. *Composites*, 1994. **25**(6): p. 414-424.
 85. Cantwell, W.J., Curtis, P.T. and Morton, J., *An Assessment of the Impact Performance of CFRP Reinforced with High-Strain Carbon Fibres*. *Composites Science and Technology*, 1986. **25**(2): p. 133-148.
 86. Williams, J.G. and Rhodes, M.D., Effect of Resin on Impact Damage Tolerance of Graphite/ Epoxy Laminates, in *Composite Materials : Testing and Design*. 1982, ASTM STP 787. p. 450-480.
 87. Greenhalgh, E.S. and S. Singh, The Effect of Moisture, Matrix and Ply Orientation on Delamination Resistance, Failure Criteria and Fracture Morphology in CFRP, in *Composite materials : Testing, Design, and Acceptance Criteria*, 2002, ASTM STP 1416. p. 221-234.
 88. Hitchen, S.A. and Kemp, R.M.J., The Effect of Stacking Sequence on Impact Damage in a Carbon Fibre/Epoxy Composite. *Composites*, 1995. **26**(3): p. 207-214.

89. Strait, L.H., Karasek, M.L. and Amateau, M.F., Effects of Stacking Sequence on the Impact Resistance of Carbon Fiber Reinforced Thermoplastic Toughened Epoxy Laminates. *Journal of Composite Materials*, 1992. **26**(12): p. 1725-1740.
90. Dost, E.F., Finn, S. R., Stevens, J. J., Lin, K. Y. and Fitch, C. E., Experimental Investigation into Composite Fuselage Impact Damage Resistance and Post Impact Compression Behaviour. in 37th International SAMPE Symposium and Exhibition. 1992.
91. Cantwell, W.J. and Morton, J., *The Impact Resistance of Composite Materials - A Review*. *Composites*, 1991. **22**(5): p. 347-362.
92. Dickinson, L.C., Farley, G.L. and Hinders, M.K., *Translaminar Reinforced Composites: A Review*. *Journal of Composites Technology and Research*, 1999. **21**(1): p. 3-15.
93. Ellyin, F. and Rohrbacher, C., The Influence of Aqueous Environment, Temperature and Cyclic Loading on Glass-Fibre/Epoxy Composite Laminates. *Journal of Reinforced Plastics and Composites*, 2003. **22**(7): p. 615-636.
94. Ellyin, F. and Rohrbacher, C., *Effect of Aqueous Environment and Temperature on Glass-Fibre Epoxy Resin Composites*. *Journal of Reinforced Plastics and Composites*, 2000. **19**(17): p. 1405-1427.
95. Weitsman, Y.J. and Elahi, M., Effects of Fluids on the Deformation, Strength and Durability of Polymeric Composites - An Overview. *Mechanics of Time Dependent Materials*, 2000. **4**(2): p. 107-127.
96. Suh, D.W.K., Ku, M.K., Nam, J.D., Kim, B.S. and Yoon, S.C., *Equilibrium Water Uptake of Epoxy/Carbon Fiber Composites in Hygrothermal Environmental Conditions*. *Journal of Composite Materials*, 2001. **35**(3): p. 264-279.
97. Zhou, J. and Lucas, J.P., Hygrothermal Effects of Epoxy Resin. Part I: The Nature of Water in Epoxy. *Polymer*, 1999. **40**(20): p. 5505-5512.

98. Zhou, J. and Lucas, J.P., Hygrothermal Effects of Epoxy Resin. Part II: Variations of Glass Transition Temperature. *Polymer*, 1999. **40**(20): p. 5513-5522.
99. Wong, T.C. and Broutman, L.J., Effect of Stress on Sorption of Water in an Epoxy Resin. in Annual Technical Conference - Society of Plastics Engineers. 1985.
100. Roy, S. and Xu, W., *Modeling of Diffusion in the Presence of Damage in Polymer Matrix Composites*. *International Journal of Solids and Structures*, 2001. **38**(1): p. 115-125.
101. Patel, S.R. and Case, S.W., *Durability of a Graphite/Epoxy Woven Composite under Combined Hygrothermal Conditions*. *International Journal of Fatigue*, 2000. **22**(9): p. 809-820.
102. Roy, S., Xu, W., Patel, S. and Case, S., *Modeling of Moisture Diffusion in the Presence of Bi-Axial Damage in Polymer Matrix Composite Laminates*. *International Journal of Solids and Structures*, 2001. **38**(42-43): p. 7627-7641.
103. Rao, R.M.V.G.K., Balasubramanian, N. and Chanda, M., Factors Affecting Moisture Absorption in Polymer Composites Part 1: Influence of Internal Factors, in *Environmental Effects on Composite Materials*, Editor G.S. Springer. 1988. p. 75-88.
104. Myung, C.L. and Peppas, N.A., *Models of Moisture Transport and Moisture-Induced Stresses in Epoxy Composites*. *Journal of Composite Materials*, 1993. **27**(12): p. 1146-1171.
105. Springer, G.S., Numerical Procedures for the Solution of One Dimensional Fickian Diffusion Problems, in *Environmental Effects on Composite Materials*, G.S. Springer, Editor. 1981, Technomic Publishing Co. p. 166-199.
106. Nogueira, P., Ramírez, C., Torres, A., Abad, M.J., Cano, J., López, J., López-Bueno, I. and Barral, L., *Effect of Water Sorption on the Structure*

- and Mechanical Properties of an Epoxy Resin System*. Journal of Applied Polymer Science, 2001. **80**(1): p. 71-80.
107. Springer, G.S., *Environmental Effects*, in *Environmental Effects on Composite Materials*, G.S. Springer, Editor. 1988, Technomic Publishing Company, Inc. p. 1-34.
108. De Wilde, W.P. and Frolkovic, P., *The Modelling of Moisture Absorption in Epoxies: Effects at the Boundaries*. Composites, 1994. **25**(2): p. 119-127.
109. Blikstad, M., Sjoblom, P.O.W. and Johannesson, T.R., *Long-term Moisture Absorption in Graphite/Epoxy Angle-ply Laminates*. Journal of Composite Materials, 1984. **18**(1): p. 32-46.
110. Hahn, H.T., *Hygrothermal Damage in Graphite/Epoxy Laminates*. Journal of Engineering Materials and Technology, Transactions of the ASME, 1987. **109**(1): p. 3-11.
111. Choi, H. S., Ahn, K. J., Nam, J. D. and Chun, H. J., *Hygroscopic Aspects of Epoxy/Carbon Fiber Composite Laminates in Aircraft Environments*. Composites Part A: Applied Science and Manufacturing, 2001. **32**(5): p. 709-720.
112. Zhang, M. and Mason, S.E., *Effects of Contamination on the Mechanical Properties of Carbon Fibre Reinforced Epoxy Composite Materials*. Journal of Composite Materials, 1999. **33**(14): p. 1363-1374.
113. Bradley, W.L. and Grant, T.S., *Effect of the Moisture Absorption on the Interfacial Strength of Polymeric Matrix Composites*. Journal of Materials Science, 1995. **30**(21): p. 5537-5542.
114. Zhuang, H. and Wightman, J.P., *The Influence of Surface Properties on Carbon Fiber/Epoxy Matrix Interfacial Adhesion*. Journal of Adhesion, 1997. **62**(1-4): p. 213-245.

115. Takeda, N. and Ogihara, S., In Situ Observation and Probabilistic Prediction of Microscopic Failure Processes in CFRP Cross-Ply Laminates. *Composites Science and Technology*, 1994. **52**(2): p. 183-195.
116. Detassis, M., Pegoretti, A. and Migliaresi, C., *Effect of Temperature and Strain Rate on Interfacial Shear Stress Transfer in Carbon/Epoxy Model Composites*. *Composites Science and Technology*, 1995. **53**(1): p. 39-46.
117. Wimolkiatisak, A.S. and Bell, J.P., Interfacial Shear Strength and Failure Modes of Interphase-Modified Graphite-Epoxy Composites. *Polymer Composites*, 1989. **10**(3): p. 162-172.
118. Im, K.H., Cha, C.S., Kim, S.K. and Yang, I.Y., *Effects of Temperature on Impact Damages in CFRP Composite Laminates*. *Composites Part B: Engineering*, 2001. **32**(8): p. 669-682.
119. Potter, R.T. and Purslow, D., *Environmental Degradation of Notched CFRP in Compression*. *Composites*, 1983. **14**(3): p. 206-225.
120. Purslow, D., Effect of Environment on the Compression Strength of Notched CFRP - A Fractographic Investigation. *Composites*, 1984. **15**(2): p. 112-120.
121. Karasek, M.L., Strait, L. H., Amateau, M. F., Runt, J. P., *Effect of Temperature and Moisture on the Impact Behavior of Graphite/Epoxy Composites: Part I – Impact Energy Absorption*. *Journal of Composites Technology and Research*, 1995. **17**(1): p. 3-10.
122. Karasek, M.L., Strait, L. H., Amateau, M. F., Runt, J. P., *Effect of Temperature and Moisture on the Impact Behavior of Graphite/Epoxy Composites: Part II – Impact Damage*. *Journal of Composites Technology and Research*, 1995. **17**(1): p. 11-16.
123. Harper, J.F. and Abd Aziz, R., *The Influence of Thermohumidity on Compression After Impact Properties of Fibre Reinforced Epoxy Laminates*. *Key Engineering Materials – Experimental Techniques and Design in Composite Materials*, 2002. **5**(221-222): p. 173-184.

124. Imielińska, K. and Guillaumat, L., The Effect of Water Immersion Ageing on Low-Velocity Impact Behaviour of Woven Aramid-Glass Fibre/Epoxy Composites. *Composites Science and Technology*, 2004. **64**(13-14): p. 2271-2278.
125. Asp, L.E., The Effects of Moisture and Temperature on the Interlaminar Delamination Toughness of a Carbon/Epoxy Composite. *Composites Science and Technology*, 1998. **58**(6): p. 967-977.
126. Anon., *TORAYCA*, Toray Industries Inc. accessed from www.toray.co.jp
127. Anon., Product Information Sheet, Formax UK.
128. Anon., Technical Data Sheet, ACG MTM44 - Dual Cure Epoxy Matrix, Advanced Composites Group.
129. Foreman, A., *Personal Communication*. 2003: QinetiQ, Farnborough.
130. Mills, A., *Personal Communication*. 2003: Centre of Lightweight Composites, SIMS, Cranfield University.
131. Anon., Standard Test Methods for Density and Specific Gravity (Relative Density) of Plastics by Displacement, in ASTM D792-00. 2000.
132. Curtis, P.T., CRAG Test Methods for the Measurement of the Engineering Properties of Fibre Reinforced Plastics. 1988, RAE TR 88012. p. 1-51.
133. Anon., Standard Test Methods for Void Content of Reinforced Plastics, in ASTM D2734-94. 1994.
134. Anon., Operator's Manual - Rosand Type 5 Instrumented Falling Weight Impact Machine.
135. Anon., Plastics: Determination of Multi-axial Impact Behaviour of Rigid Plastics: Instrumented Puncture Testing, in BS EN ISO 6603-2:2000. 2000.
136. Kim, J.K., Recent Developments in Impact Damage Assessment of Fibre Composites, in *Impact Behaviour of Fibre-reinforced Composite Materials*

- and Structures, Editors S.R. Reid and G. Zhou,. 2000, Woolhead Publishing Ltd. p. 33-74.
137. Pavier, M.J. and Clarke, M.P., Experimental Techniques for the Investigation of the Effects of Impact Damage on Carbon-Fibre Composites. *Composites Science and Technology*, 1995. **55**(2): p. 157-169.
138. Anon., *Plastics: Standard Atmospheres for Conditioning and Testing*, in BS EN ISO 291:2005.
139. Gates, T.S., On the Use of Accelerated Test Methods for Characterization of Advanced Composite Materials. 2003, NASA Langley Research Center. p. 55.
140. Anon., *DMTA MK II Operator's Manual*, Polymer Laboratories.
141. Ferraro, J.R. and Nakamoto, K., *Introductory Raman Spectroscopy*. 1994: Academic Press, Inc.
142. Mertz, E. and Koenig, J.L., *Application of FT-IR and NMR to Epoxy Resins*, in *Advances in Polymer Science*, K. Dusek, Editor. 1986. p. 73-112.
143. Baranska, H., A. Labudzinska, and J. Terpinski, *Laser Raman Spectrometry: Analytical Applications*. 1987: Ellis Horwood Limited.
144. Anon., *LabSpec Software User Guide*. 1999, Dilor-Jobin Yvon-Spex.
145. Nilsson, K.F., Asp, L.E. and Sjogren, A., *On Transition of Delamination Growth Behaviour for Compression Loaded Composite Panels*. *International Journal of Solids and Structures*, 2001. **38**(46-47): p. 8407-8440.
146. Davies, P., Blackman, B.R.K. and Brunner, A.J., *Standard Test Methods for Delamination Resistance of Composite Materials: Current Status*. *Applied Composite Materials*, 1998. **5**: p. 345-364.
147. Davies, P., Moulin, C., Kausch, H. H. and Fischer, M., *Measurement of G_{Ic} and G_{IIc} in Carbon/Epoxy Composites*. *Composites Science and Technology*, 1990. **39**(3): p. 193-205.

148. Hoecker, F., Friedrich, K., Blumberg, H. and Karger-Kocsis, J., *Effects of Fiber/Matrix Adhesion on off-axis Mechanical Response in Carbon-fiber/Epoxy-resin Composites*. *Composites Science and Technology*, 1995. **54**(3): p. 317-327.
149. Baley, C., Davies, P., Grohens, Y. and Dolto, G., *Application of Interlaminar Tests to Marine Composites: A Literature Review*. 2004. **11**(2): p. 99-127.
150. Backhouse, R., *Multiaxial Non-Crimp Fabrics: Characterisation of Manufacturing Capability for Composite Aircraft Primary Structure Applications*, in School of Industrial and Manufacturing Science. 1998, Cranfield University.
151. Foreman, A., *Unpublished Work*. 2004.
152. Anon., *Fibre-Reinforced Plastic Composites: Determination of Apparent Interlaminar Shear Strength by Short-Beam Method*, in BS EN ISO 14130:1998. 1998.
153. Clark, G., *Modelling of Impact Damage in Composite Laminates*. *Composites*, 1989. **20**(3): p. 209-214.
154. Pearce, N.R.L., Guild, F.J. and Summerscales, J., *An Investigation into the Effects of Fabric Architecture on the Processing and Properties of Fibre Reinforced Composites Produced by Resin Transfer Moulding*. *Composites Part A: Applied Science and Manufacturing*, 1998. **29**(1-2): p. 19-27.
155. Yoshida, H., Ogasa, T. and Hayashi, R., *Statistical Approach to the Relationship between ILSS and Void Content of CFRP*. *Composites Science and Technology*, 1986. **25**(1): p. 3-18.
156. Foreman, A., Meeks, C., *Enhanced Damage Management in Polymer Composites*. 2002. QINETIQ/FST/CR025072.
157. Nettles, A.T., Douglas, M.J. and Estes, E.E., *Scaling Effects in Carbon/Epoxy Laminates under Transverse Quasi-Static Loading*. 1999, NASA Langley Research Center.

158. Wardle, B.L. and Lagace, P.A., *On the Use of Dent Depth as an Impact Damage Metric for Thin Composite Structures*. Journal of Reinforced Plastics and Composites, 1997. 16(12): p. 1093-1110.
159. Caprino, G. and Lopresto, V., The Significance of Indentation in the Inspection of Carbon Fibre-reinforced Plastic Panels Damaged by Low-velocity Impact. Composites Science and Technology, 2000. 60(7): p. 1003-1012.
160. Cantwell, W.J. and Morton, J., *Detection of Impact Damage in CFRP Laminates*. Composite Structures, 1985. 3(3-4): p. 241-257.
161. Hancox, N.L., An Overview of the Impact Behaviour of Fibre-reinforced Composites, in *Impact Behaviour of Fibre-reinforced Composite Materials and Structures*, S.R. Reid and G. Zhou, Editors. 2000, CRC Press. p. 1-32.
162. Delfosse, D. and Poursartip, A., *Energy-based Approach to Impact Damage in CFRP Laminates*. Composites Part A: Applied Science and Manufacturing, 1997. 28(7): p. 647-655.
163. Dorey, G. Impact Damage in Composites—Development, Consequences, and Prevention. in *Proc. 6th International Conference on Composite Materials and 2nd European Conference on Composite Materials*. 1988. London: Imperial College.
164. Zhou, G. and Greaves, L.J., Damage Resistance and Tolerance of Thick Laminated Woven Roving GFRP Plates Subjected to Low-velocity Impact, in *Impact Behaviour of Fibre-reinforced Composite Materials and Structures*, S.R. Reid and G. Zhou, Editors. 2000, Woolhead Publishing Ltd. p. 133-185.
165. Zhou, G., Lloyd, J.C. and McGuirk, J.J., *Experimental Evaluation of Geometric Factors Affecting Damage Mechanisms in Carbon/Epoxy Plates*. Composites Part A: Applied Science and Manufacturing, 2001. 32(1): p. 71-84.

166. Caprino, G. and Lopresto, V., *On the Penetration Energy for Fibre-Reinforced Plastics under Low-velocity Impact Conditions*. Composites Science and Technology, 2001. **61**(1): p. 65-73.
167. Babic, L., Dunn, C. and Hogg, P.J., *Damage Development and Its Significance in GRP Subjected to Impact*. Plastic, Rubber Processing and Application, 1989. **12**(4): p. 199-207.
168. Belingardi, G. and Vadori, R., *Low Velocity Impact Tests of Laminate Glass-Fiber-Epoxy Matrix Composite Material Plates*. International Journal of Impact Engineering, 2002. **27**(2): p. 213-229.
169. Hogg, P.J., *Personal Communication*. 2005.
170. Prichard, J.C. and Hogg, P.J., *The Role of Impact Damage in Post-Impact Compression Testing*. Composites, 1990. **21**(6): p. 503-511.
171. Larsson, F., *Damage Tolerance of a Stitched Carbon/Epoxy Laminate*. Composites Part A: Applied Science and Manufacturing, 1997. **28**(11): p. 923-934.
172. Suh, S.S., Han, N. L., Yang, J. M. and Hahn, H. T., *Compression Behavior of Stitched Stiffened Panel with a Clearly Visible Stiffener Impact Damage*. Composite Structures, 2003. **62**(2): p. 213-221.
173. Mattheij, P., Gliesche, K. and Feltin, D., *3D Reinforced Stitched Carbon/Epoxy Laminates Made by Tailored Fibre Placement*. Composites Part A: Applied Science and Manufacturing, 2000. **31**(6): p. 571-581.
174. Glaessgen, E.H. and Raju, I.S., *Effect of Stitching on Debonding in Composite Structural Elements*. in ICES'01---International Conference on Computational Engineering & Sciences. 2001. Puerto Vallarta, Mexico.
175. Anon., *Plastics: Determination of Water Absorption*, in BS EN ISO 62:1999. 1999.

176. Zhou, J. and Lucas, J.P., The Effects of a Water Environment on Anomalous Absorption Behavior in Graphite/Epoxy Composites. *Composites Science and Technology*, 1995. **53**(1): p. 57-64.
177. Musto, P., Ragosta, G. and Mascia, L., *Vibrational Spectroscopy Evidence for the Dual Nature of Water Sorbed into Epoxy Resins*. *Chemistry of Materials*, 2000. **12**(5): p. 1331-1341.
178. Noobut, W. and Koenig, J.L., Interfacial Behavior of Epoxy/E-Glass Fiber Composites under Wet-Dry Cycles by Fourier Transform Infrared Microspectroscopy. *Polymer Composites*, 1999. **20**(1): p. 38-47.
179. McMurry, J., *Organic Chemistry*. 2000: Pacific Grove.
180. Ngonu, Y., Maréchal, Y. and Mermilliod, N., Epoxy-Amine Reticulates Observed by Infrared Spectrometry. I: Hydration Process and Interaction Configurations of Embedded H₂O Molecules. *Journal of Physical Chemistry B*, 1999. **103**(24): p. 4979-4985.
181. Chen, S., Tan, L., Qiu, F., Jiang, X., Wang, M. and Zhang, H., The Study of Poly(Styrene-Co-P-(Hexafluoro-2-Hydroxyisopropyl)-[Alpha]-Methyl-Styrene)/Poly(Propylene Carbonate) Blends by ESR Spin Probe And Raman. *Polymer*, 2004. **45**(9): p. 3045-3053.
182. Ward, Y. and Mi, Y., The Study of Miscibility and Phase Behaviour of Phenoxy Blends Using Raman Spectroscopy. *Polymer*, 1999. **40**(9): p. 2465-2468.
183. Davies, P., Pomies, F. and Carlsson, L.A., *Influence of Water and Accelerated Aging on the Shear Fracture Properties of Glass/Epoxy Composite*. *Applied Composite Materials*, 1996. **3**(2): p. 71-87.
184. Wood, C.A. and Bradley, W.L., Determination of the Effect of Seawater on the Interfacial Strength of an Interlayer E-glass/graphite/epoxy Composite by in situ Observation of Transverse Cracking in an Environmental SEM. *Composites Science and Technology*, 1997. **57**(8): p. 1033-1043.

185. Adams, R.D. and Singh, M.M., The Effect of Immersion in Sea Water on the Dynamic Properties of Fibre-Reinforced Flexibilised Epoxy Composites. *Composite Structures*, 1995. **31**(2): p. 119-127.
186. Mouritz, A.P., Gallagher, J. and Goodwin, A.A., *Flexural Strength and Interlaminar Shear Strength of Stitched GRP Laminates Following Repeated Impacts*. *Composites Science and Technology*, 1997. **57**(5): p. 509-522.
187. Zhang, Z., Klein, P. and Friedrich, K., Dynamic Mechanical Properties of PTFE Based Short Carbon Fibre Reinforced Composites: Experiment and Artificial Neural Network Prediction. *Composites Science and Technology*, 2002. **62**(7-8): p. 1001-1009.
188. Chandra, R., Singh, S.P. and Gupta, K., *Damping Studies in Fiber-Reinforced Composites - A Review*. *Composite Structures*, 1999. **46**(1): p. 41-51.
189. Smith, F.C., Winkler, H. and Hogg, P.J., *Durability of Non-Crimp Fabric Composites in Aqueous Environments*. *Plastics, Rubber and Composites*, 2001. **30**(5): p. 233-242.
190. Karbhari, V.M. and Q. Wang, Multi-frequency Dynamic Mechanical Thermal Analysis of Moisture Uptake in E-glass/Vinylester Composites. *Composites Part B: Engineering*, 2004. **35**(4): p. 299-304.
191. Li, G., Lee-Sullivan, P. and Thring, R.W., *Determination of Activation Energy for Glass Transition of an Epoxy Adhesive Using Dynamic Mechanical Analysis*. *Journal of Thermal Analysis and Calorimetry*, 2000. **60**(2): p. 377-390.
192. He, L.H. and Liu, Y.L., Damping Behavior of Fibrous Composites with Viscous Interface under Longitudinal Shear Loads. *Composites Science and Technology*, 2005. **65**(6): p. 855-860.
193. Schäfer, F.U., Polyurethane-based Simultaneous Interpenetrating Polymer Networks of Controlled Microphase Morphology and High Damping

-
- Characteristics, in IPTME. 1996, PhD Thesis, Loughborough University. p. 88-92.
194. Akay, M., *Aspects of Dynamic Mechanical Analysis in Polymeric Composites*. Composites Science and Technology, 1993. **47**(4): p. 419-423.
195. Maxwell, I.D. and Pethrick, R.A., *Low Temperature Rearrangement of Amine Cured Epoxy Resins*. Polymer Degradation and Stability, 1983. **5**(4): p. 275-301.
196. Whiteside, J.B., Delasi, R.J. and Schulte, R.L., *Measurement of Preferential Moisture Ingress in Composite Wing/Spar Joints*. Composites Science and Technology, 1985. **24**(2): p. 123-145.
197. FitzGerald, S., Personal Communication, 2006, HoribaJobinYvon.

APPENDIX

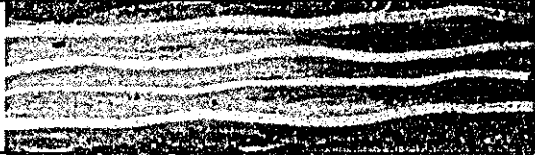
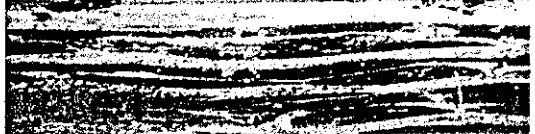
Laminate	Consumable	Cure Cycle	Initial/cure Pressure*	Cross-sectional view(Mag. ×7)
SSD2	Breather & Release	2	20/8	
SSD3	Breather & Release	1	10/10	
SSD4	Breather & Release	2	10/10	
MSD1	Release	2	10/10	
MSD2	Release	1	10/12(also at 140° & 150°C)	
MSD3	None	2	0/8	
LSD 12	None	1	20/12(also at 140° & 150°C)	
LSD 13	None	2	20/12(also at 140° & 150°C)	
LSD14	None	2	20/12	

Table 19: Optical Micro-Sections of the Compression Moulded Laminates
Perpendicular to the 0° Fibres [* = Ton Force]

Sample	Load(kN)	Thickness(mm)	Width(mm)	ILSS (MPa)	V _r
S26-1	2.600	3.20	16.00	38.086	0.556
S22-1	2.490	3.30	15.70	36.045	0.539
S23-1	2.415	3.36	17.80	30.284	0.529
S27-1	2.632	3.26	15.50	39.066	0.545
S28-1	2.590	3.24	16.68	35.943	0.549
S10-3	2.360	3.30	16.28	32.946	0.539
S11-3	2.540	3.20	16.28	36.567	0.556
S2-4	2.595	3.30	16.00	36.861	0.539
Average	2.528	3.270	16.280	35.725	
Std. Dev.	0.098	0.056	0.714	2.834	

Table 20(a): ILSS at 70° C – Laminate S

Sample	Load(kN)	Thickness(mm)	Width(mm)	ILSS (MPa)	V _r
M2-2	2.358	3.24	16.14	33.819	0.549
M3-2	2.120	3.30	16.22	29.705	0.539
M6-2	2.812	3.24	17.16	37.933	0.549
M8-2	2.624	3.20	16.00	38.438	0.556
M27-3	2.397	3.26	16.50	33.422	0.545
M3-4	2.402	3.34	16.66	32.375	0.532
M6-4	2.736	3.40	16.28	37.072	0.523
M7-4	3.144	3.38	18.66	37.387	0.526
Average	2.574	3.295	16.703	35.019	
Std. Dev.	0.322	0.072	0.871	3.144	

Table 20(b): ILSS at 70° C – Laminate M

Sample	Load(kN)	Thickness(mm)	Width(mm)	ILSS (MPa)	V _r
L10-2	2.576	3.26	17.62	33.634	0.545
L23-2	2.556	3.34	17.14	33.486	0.532
L24-2	2.832	3.34	17.36	36.632	0.532
L-X	2.335	3.26	17.16	31.305	0.545
L16-4-1	2.317	3.26	15.12	35.255	0.545
L16-4-2	2.564	3.28	15.44	37.972	0.542
L13-4	2.532	3.34	16.64	34.168	0.532
L24-4	2.960	3.32	17.40	38.430	0.535
Average	2.584	3.300	16.735	35.110	
Std. Dev.	0.220	0.039	0.945	2.441	

Table 20(c): ILSS at 70° C – Laminate L

Sample	Values at Damage Initiation						Number of Tests
	Average Force (kN)	Std. Dev. Force (kN)	Average Energy (Joules)	Std. Dev. Energy (Joules)	Average Displacement (mm)	Std. Dev. Displacement (mm)	
S (10 Joules)	3.37	0.62	1.41	0.37	0.80	0.09	16
M (10 Joules)	3.41	0.38	1.34	0.31	0.79	0.06	16
L (10 Joules)	3.51	0.55	1.43	0.20	0.85	0.12	16
S (20 Joules)	4.12	0.43	1.98	0.27	1.02	0.14	16
M (20 Joules)	4.06	0.51	1.95	0.31	1.04	0.20	16
L (20 Joules)	4.04	0.74	2.01	0.35	1.14	0.28	15
S (30 Joules)	4.56	0.57	3.53	0.29	1.41	0.22	16
M (30 Joules)	4.39	0.86	3.29	0.36	1.38	0.26	16
L (30 Joules)	4.40	0.85	2.71	0.26	1.22	0.25	15

**Table 21 (a): Force, Energy & Displacement at Damage Initiation
(During Low Energy Impact)**

Sample	Values at Peak						Number of Tests
	Average Force (kN)	Std. Dev. Force (kN)	Average Energy (Joules)	Std. Dev. Energy (Joules)	Average Displacement (mm)	Std. Dev. Displacement (mm)	
S (10 Joules)	6.56	0.20	9.72	0.05	3.60	0.06	16
M (10 Joules)	6.61	0.21	9.71	0.05	3.59	0.05	16
L (10 Joules)	6.43	0.22	9.73	0.08	3.66	0.06	16
S (20 Joules)	8.55	0.91	18.21	1.80	5.07	0.21	16
M (20 Joules)	7.51	0.46	16.52	1.79	4.96	0.27	16
L (20 Joules)	7.59	0.76	16.01	2.04	4.90	0.30	15
S (30 Joules)	7.86	0.66	20.15	2.51	5.63	0.32	16
M (30 Joules)	7.37	0.50	18.59	1.22	5.56	0.19	16
L (30 Joules)	7.31	0.62	18.86	1.58	5.63	0.20	15

Table 21 (b): Force, Energy & Displacement at Peak during Low Energy Impact

Sample No.	Force (kN)	Width (mm)	Thickness (mm)	Area (mm ²)	CAI Strength (MPa)
S2313U	50.232	53.57	3.44	184.2808	272.58
S2211U	52.455	55.06	3.32	182.7992	286.95
S2318U				0	end crush
S2216U				0	end crush
Average					279.77
STD DEV					10.16
M228U	49.758	55.12	3.25	179.14	277.76
M321U	45.92	54.89	3.31	181.6859	252.74
M326U				0	end crush
M223U				0	end crush
Average					265.25
STD DEV					17.69
L142U	46.434	54.91	3.39	186.1449	249.45
L144U	41.772	55.09	3.44	189.5096	220.42
L143U	42.324	54.9	3.38	185.562	228.09
L141U		55.13	3.4	187.442	end crush
Average					232.65
STD DEV					15.04

Table 22(a): Compression Strength of Dry Unimpacted Samples

Sample No.	Force (kN)	Width (mm)	Thickness (mm)	Area (mm ²)	CAI Strength (MPa)
S2315	30.658	54.91	3.27	179.5557	170.74
S2314	29.965	54.93	3.26	179.0718	167.34
S2715	29.108	54.74	3.29	180.0946	161.63
S2217	30.496	54.97	3.26	179.2022	170.18
Average					167.47
STD DEV					4.17
M624	27.942	54.4	3.22	175.168	159.52
M327	30.577	55.07	3.32	182.8324	167.24
M827	31.895	55.1	3.29	181.279	175.94
M224	31.364	55.01	3.28	180.4328	173.83
Average					169.13
STD DEV					7.40
L1346	31.058	55.02	3.34	183.7668	169.01
L1641	26.435	54.9	3.38	185.562	142.46
L1648	30.08	54.7	3.31	181.057	166.14
L1741	35.049	55.09	3.24	178.4916	196.36
Average					168.49
STD DEV					22.06

Table 22(b): Compression Strength of Dry 10 Joules Impacted Samples

Sample No.	Force (kN)	Width (mm)	Thickness (mm)	Area (mm ²)	CAI Strength (MPa)
S2218	28.472	54.62	3.36	183.5232	155.14
S2311	30.953	55.26	3.32	183.4632	168.72
S2618	25.944	55.01	3.27	179.8827	144.23
S2716	29.54	55.09	3.33	183.4497	161.03
Average					157.28
STD DEV					10.32
M226	24.688	54.89	3.28	180.0392	137.13
M323	25.645	55.03	3.32	182.6996	140.37
M328	25.316	54.76	3.31	181.2556	139.67
M828	28.988	55.32	3.3	182.556	158.79
Average					143.99
STD DEV					9.97
L2426	29.909	54.98	3.38	185.8324	160.95
L2328	27.002	55.22	3.35	184.987	145.97
L1646	24.277	54.83	3.29	180.3907	134.58
L1746	27.189	55.08	3.3	181.764	149.58
Average					147.77
STD DEV					10.86

Table 22(c): Compression Strength of Dry 20 Joules Impacted Samples

Sample No.	Force (kN)	Width (mm)	Thickness (mm)	Area (mm ²)	CAI Strength (MPa)
S2214	25.438	55.07	3.32	182.8324	139.13
S2215	29.047	55.18	3.34	184.3012	157.61
S2312	24.984	54.7	3.38	184.886	135.13
S2317	23.861	54.7	3.42	187.074	127.55
Average					139.85
STD DEV					12.77
M222	23.408	54.77	3.34	182.9318	127.96
M225	21.195	54.72	3.26	178.3872	118.81
M324	21.961	55.12	3.3	181.896	120.73
M325	19.967	54.75	3.27	179.0325	111.53
Average					119.76
STD DEV					6.75
L1022	23.494	54.83	3.29	180.3907	130.24
L1025	20.962	54.51	3.31	180.4281	116.18
L2324	23.164	54.62	3.37	184.0694	125.84
L2327	23.429	55.23	3.32	183.3636	127.77
Average					125.01
STD DEV					6.16

Table 22(d): Compression Strength of Dry 30 Joules Impacted Samples

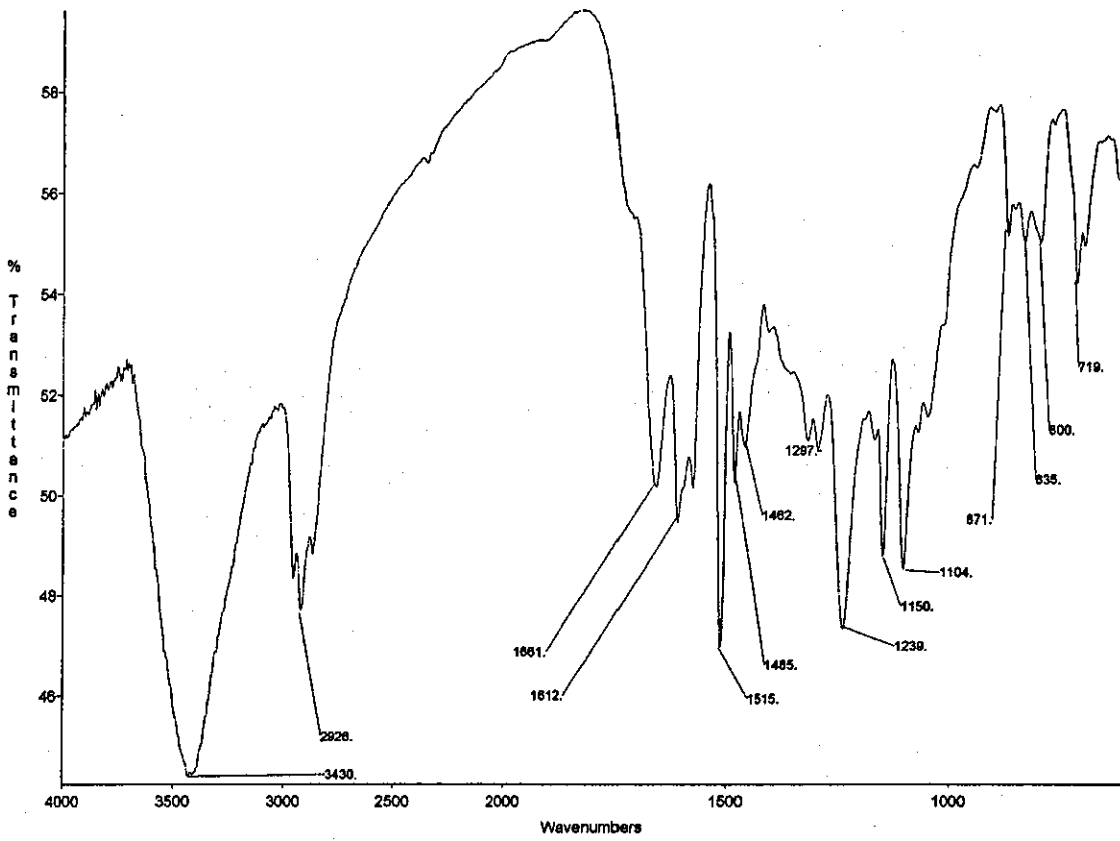


Fig. 118(a): Laminate S after 15 Days of Ageing (% w.c.= 1.369)

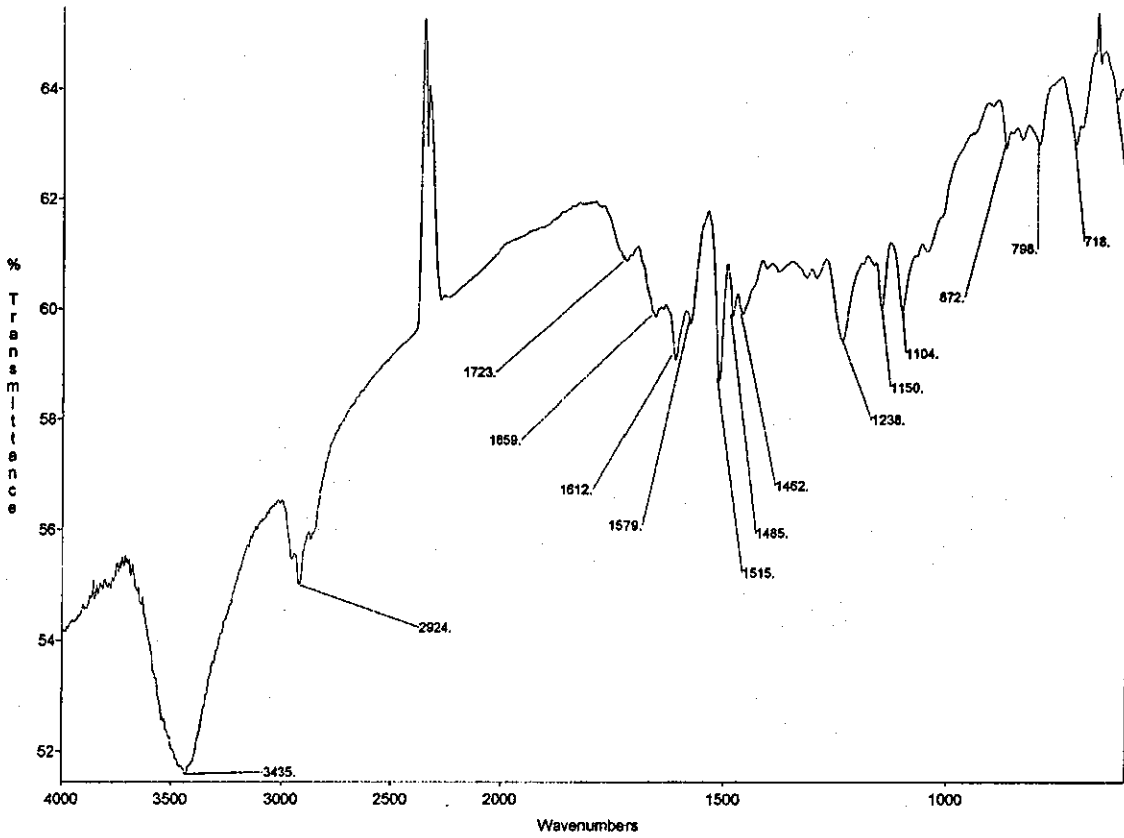


Fig. 118(b): Laminate S after 30 Days of Ageing (% w.c.= 1.09)

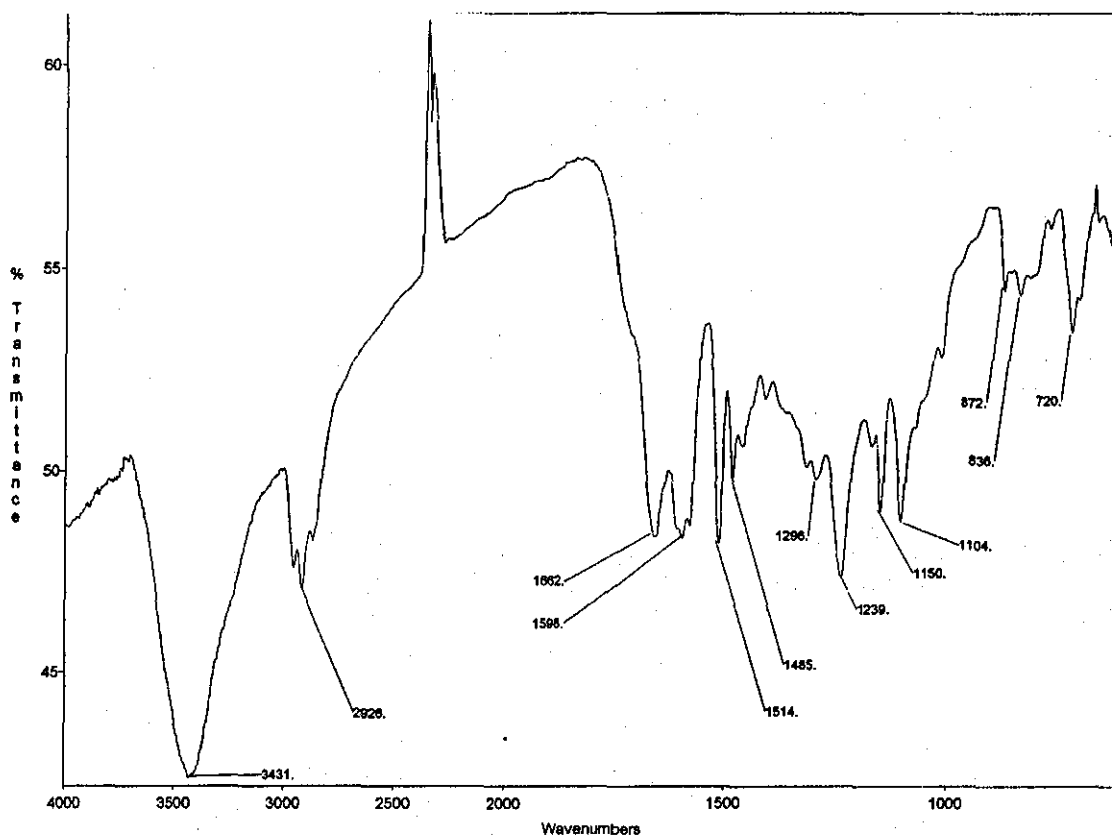


Fig. 118(c): Laminate S after 60 Days of Ageing (% w.c.= 1.118)

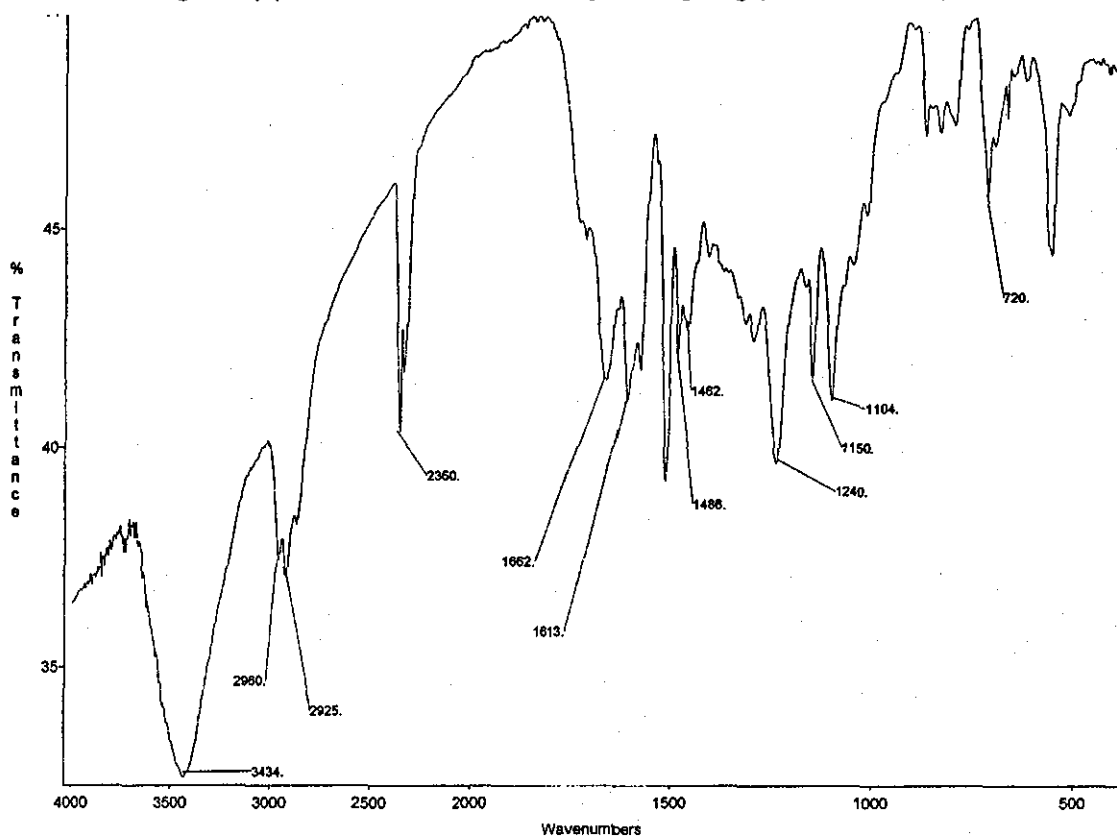


Fig. 119(a): Laminate M after 15 Days of Ageing (% w.c.= 1.201)

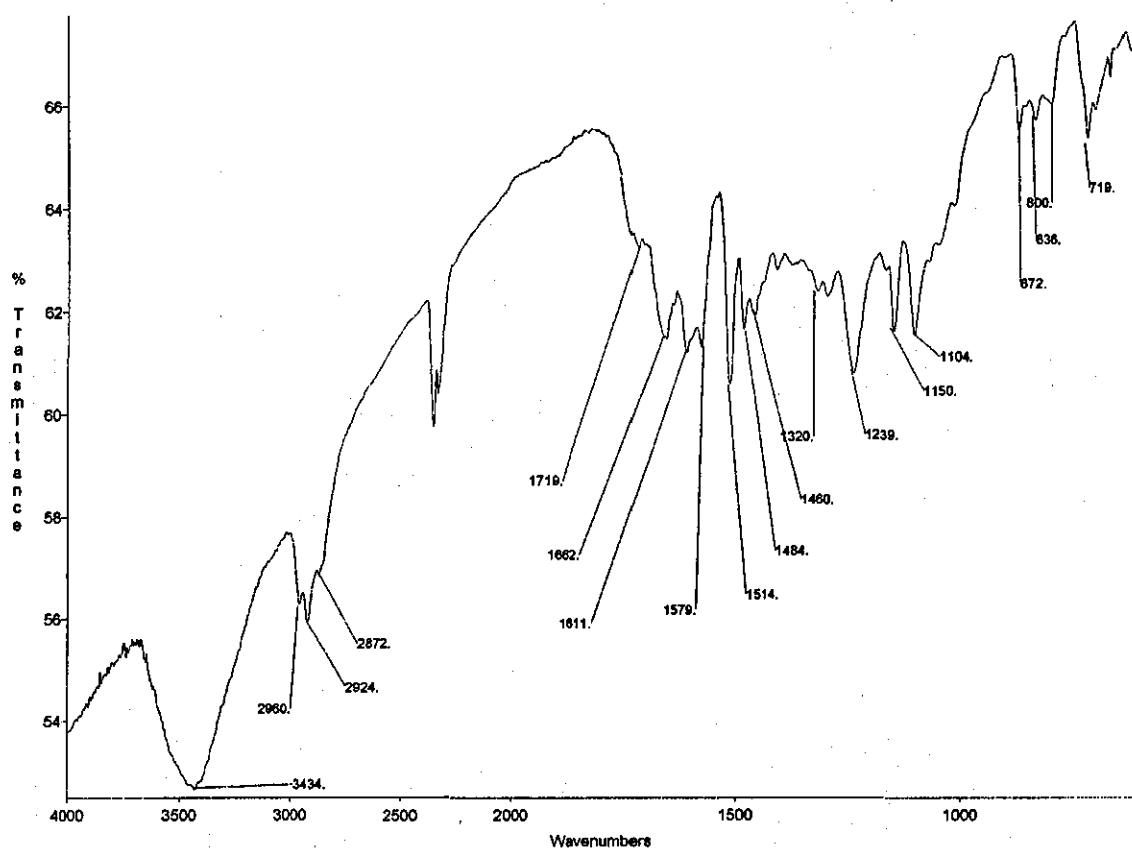


Fig. 119(b): Laminate M after 30 Days of Ageing (% w.c.= 0.969)

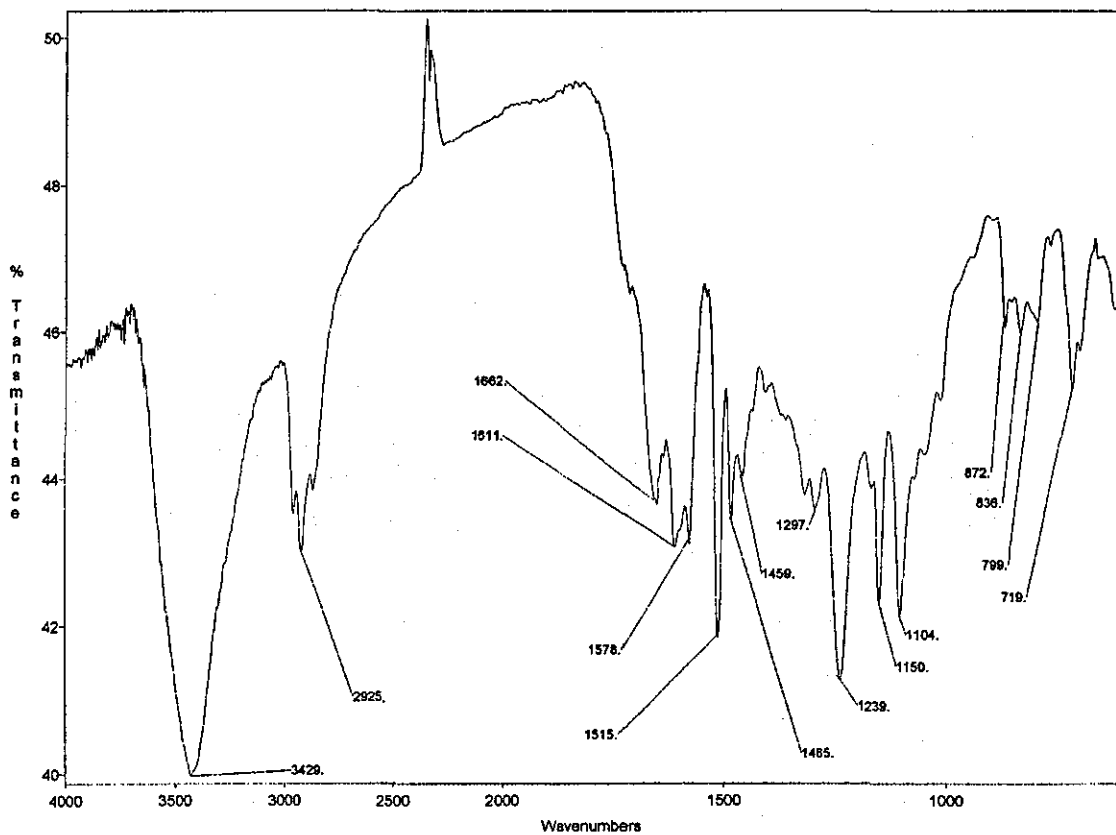


Fig. 119(c): Laminate M after 60 Days of Ageing (% w.c.= 1.046)

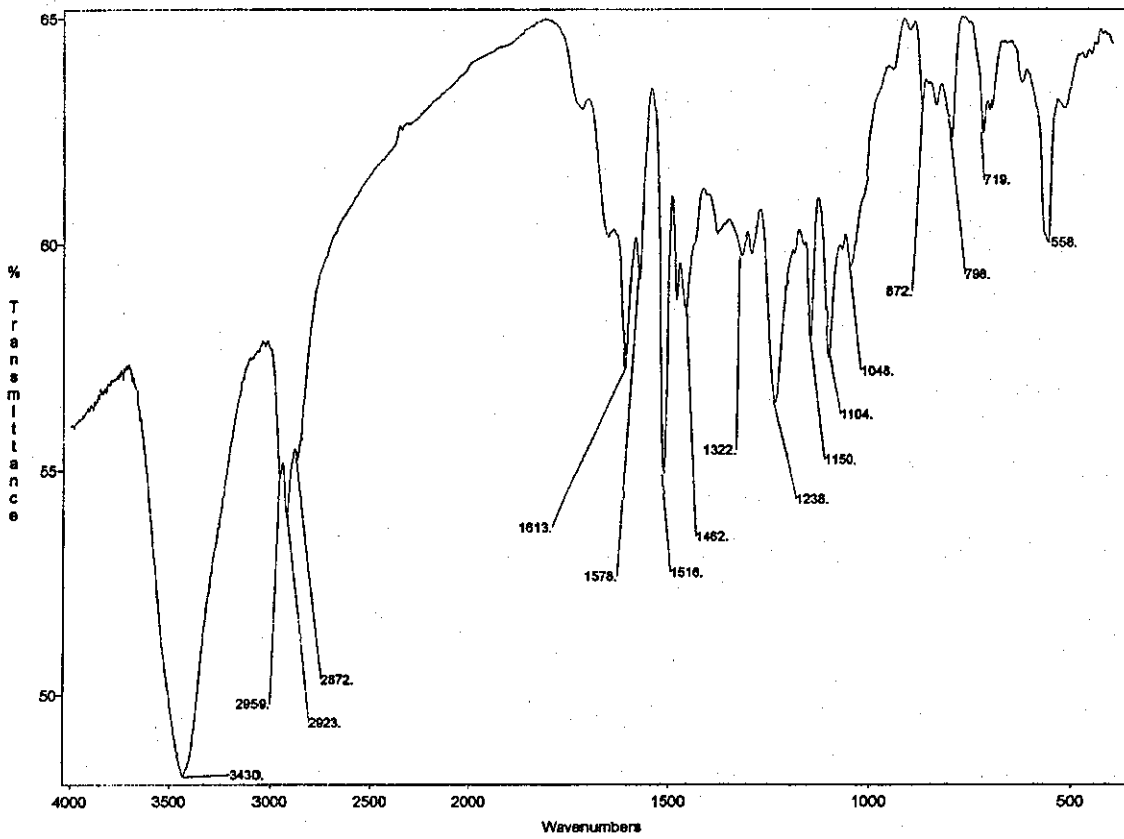


Fig. 120(a): Laminate L after 15 Days of Ageing (% w.c.= 0.971)

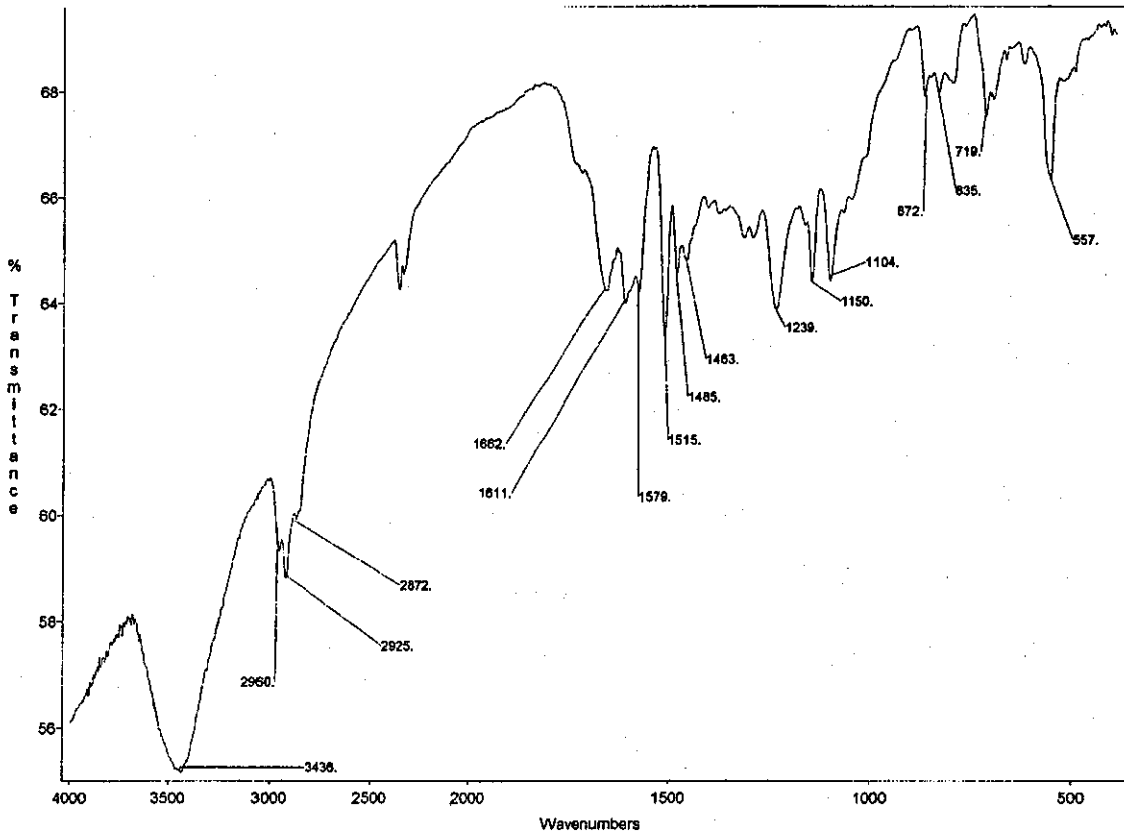


Fig. 120(b): Laminate L after 30 Days of Ageing (% w.c.= 0.913)

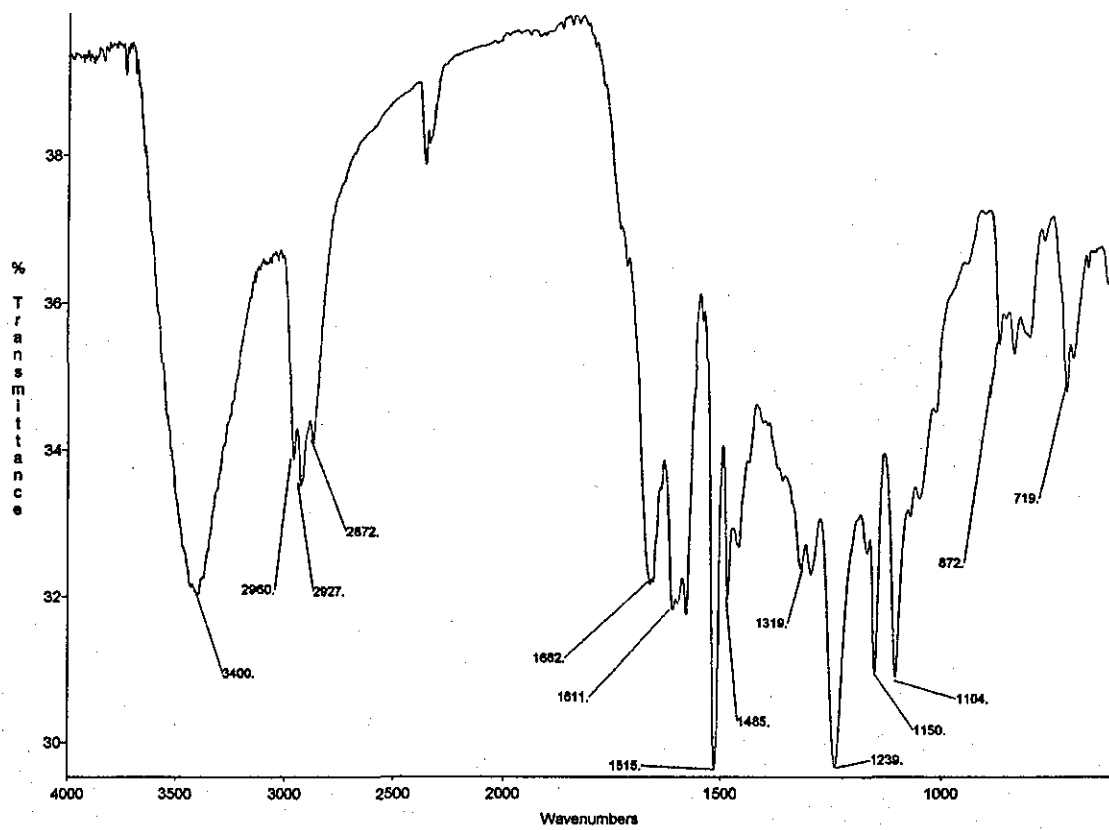


Fig. 120(c): Laminate L after 60 Days of Ageing (% w.c.= 0.959)

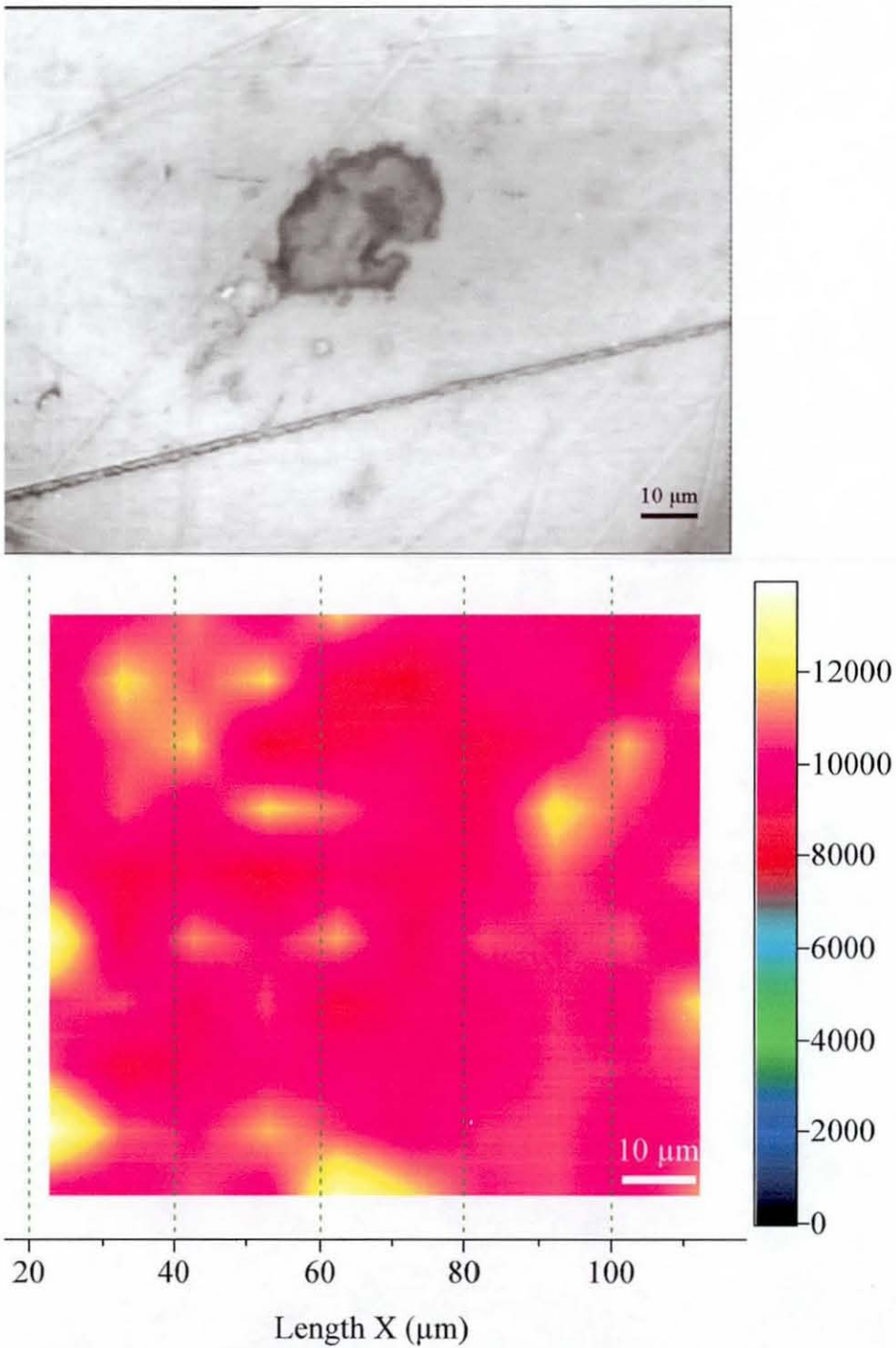


Fig. 121(a): Raman Mapping of Laminate Surface M, after 15 Days of Ageing – Optical Microscope Image of the Mapped Sample (Top) and Spatial Distribution Plot of the Intensity Values (Bottom), Map Size: 10 \times 10 Points

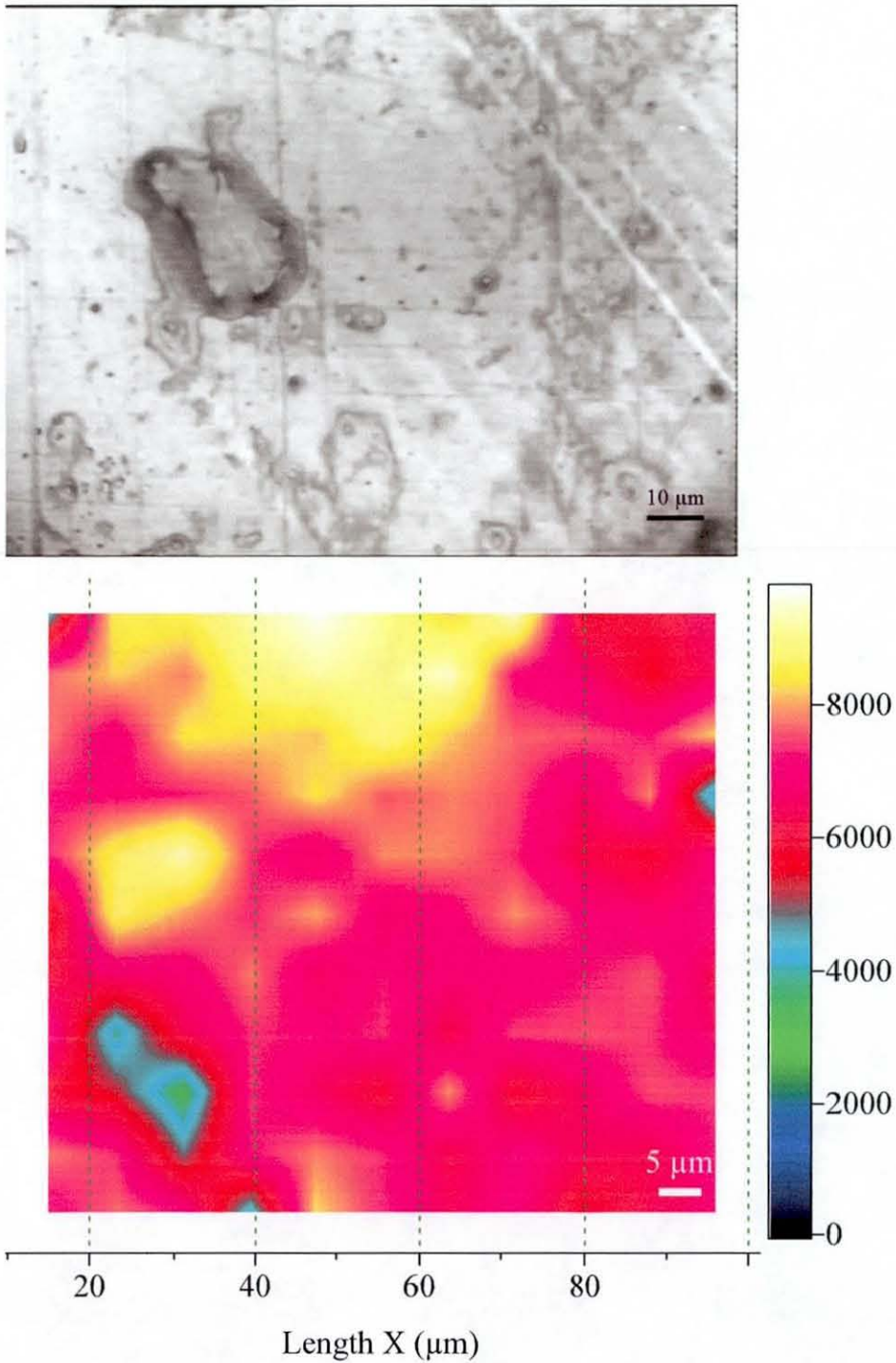


Fig. 121(b): Raman Mapping of Laminate Surface M, after 30 Days of Ageing – Optical Microscope Image of the Mapped Sample (Top) and Spatial Distribution Plot of the Intensity Values (Bottom), Map Size: 10×10 Points

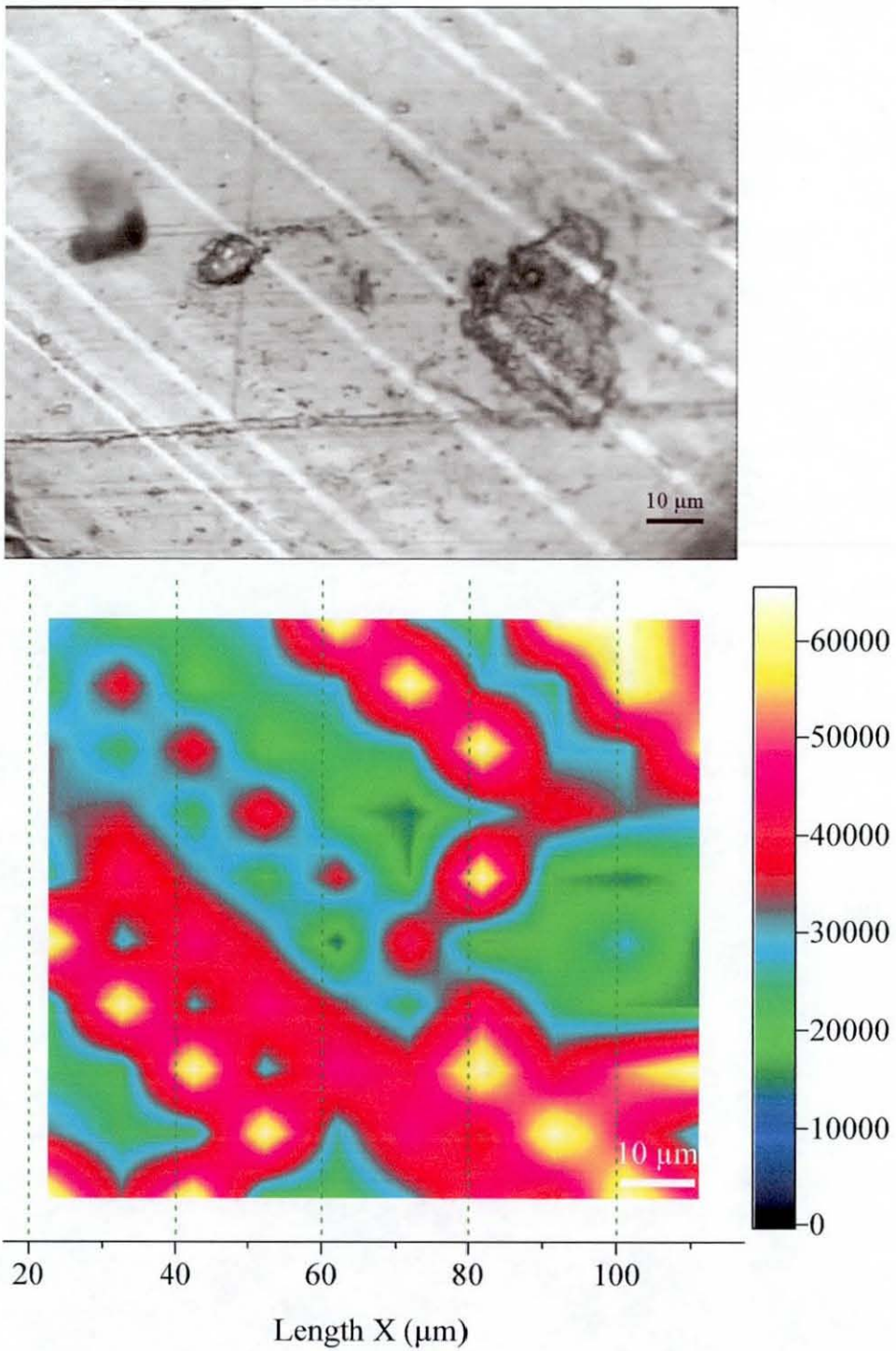


Fig. 121(c): Raman Mapping of Laminate Surface M, after 60 Days of Ageing – Optical Microscope Image of the Mapped Sample (Top) and Spatial Distribution Plot of the Intensity Values (Bottom), Map Size: 10×10 Points

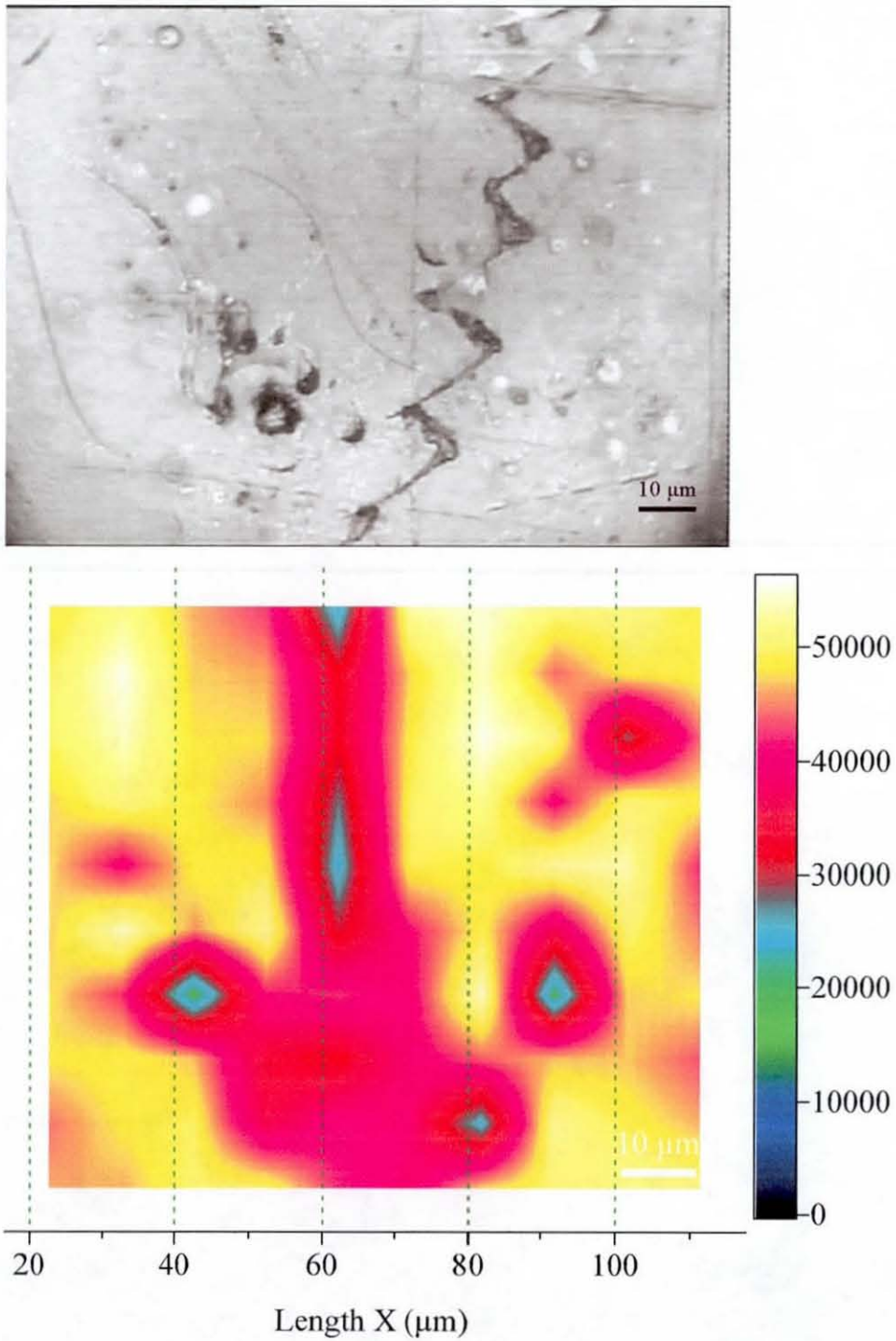


Fig. 122(a): Raman Mapping of Laminate Surface L, after 15 Days of Ageing – Optical Microscope Image of the Mapped Sample (Top) and Spatial Distribution Plot of the Intensity Values (Bottom), Map Size: 10×10 Points

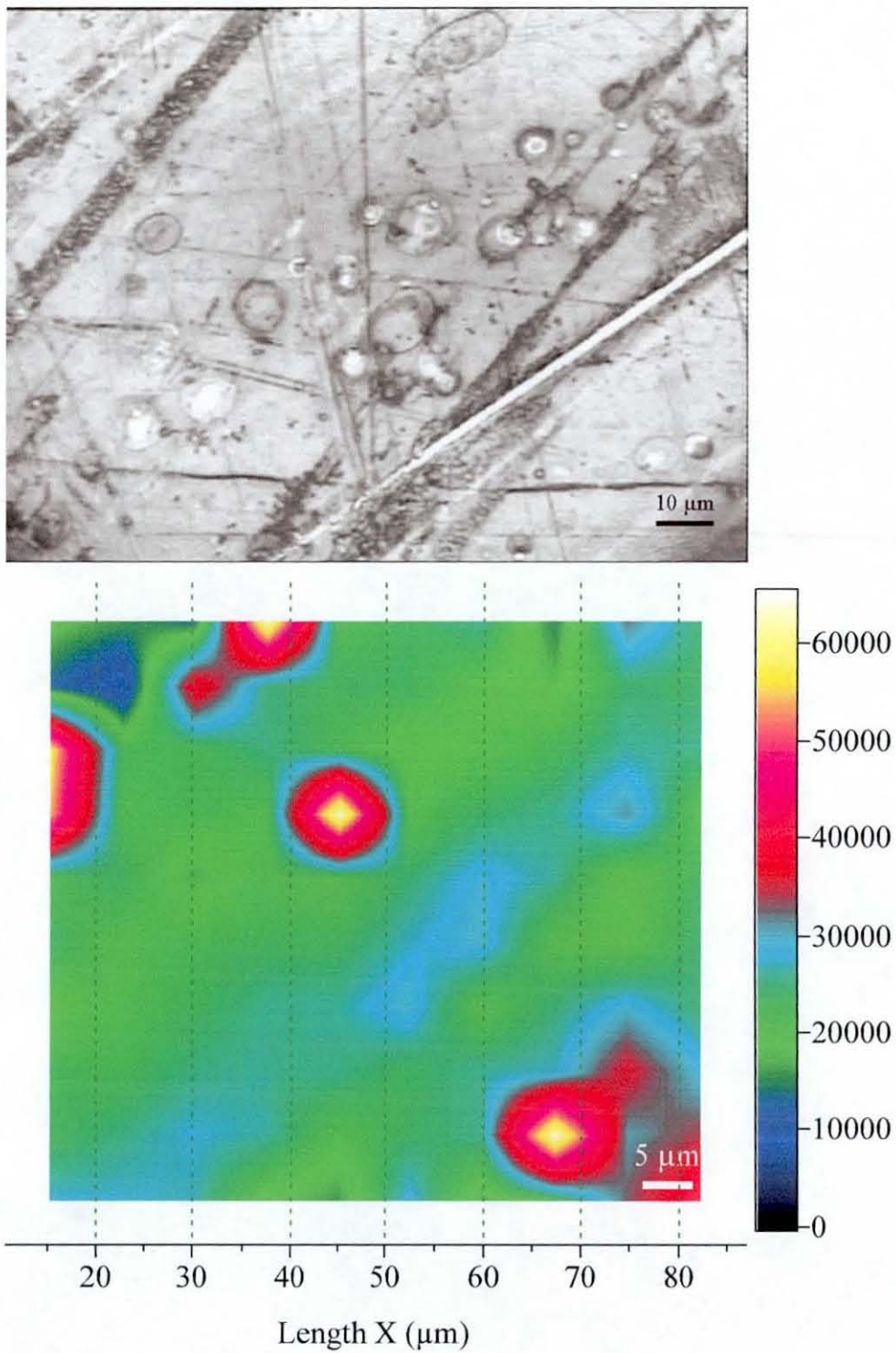


Fig. 122(b): Raman Mapping of Laminate Surface L, after 30 Days of Ageing – Optical Microscope Image of the Mapped Sample (Top) and Spatial Distribution Plot of the Intensity Values (Bottom), Map Size: 10×10 Points

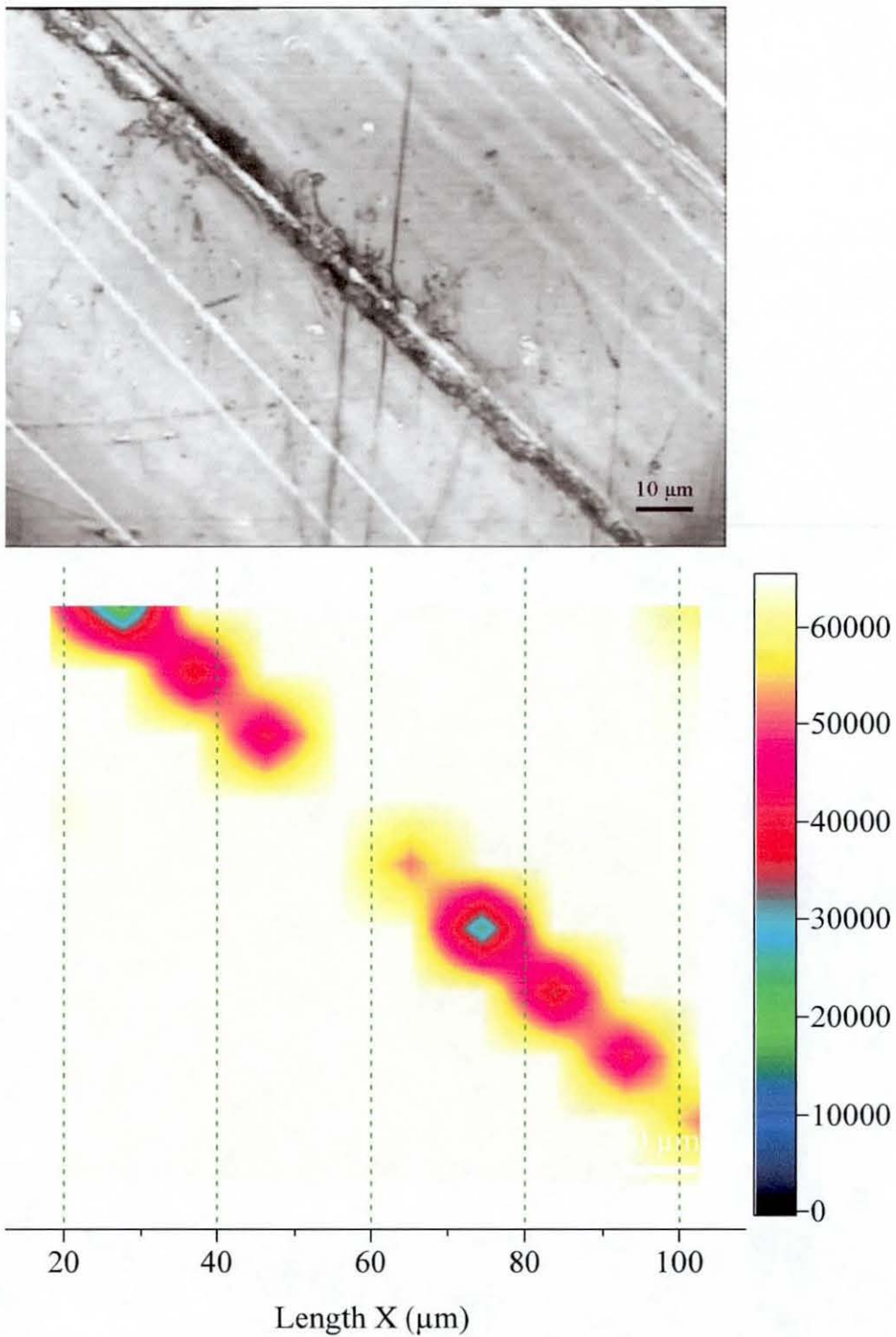


Fig. 122(c): Raman Mapping of Laminate Surface L, after 60 Days of Ageing – Optical Microscope Image of the Mapped Sample (Top) and Spatial Distribution Plot of the Intensity Values (Bottom), Map Size: 10×10 Points

Sample	Load(kN)	Thickness(mm)	Width(mm)	ILSS (MPa)	V_f
S26-1	2.552	3.35	15.55	36.742	0.531
S10-3	2.255	3.40	15.10	32.942	0.523
S22-1	1.936	3.40	15.25	28.004	0.523
S26-11	2.170	3.30	15.30	32.234	0.539
S28-1	2.098	3.30	15.05	31.682	0.539
Average	2.202	3.350	15.250	32.321	
Std. Dev.	0.228	0.050	0.197	3.122	

Table 23(a): ILSS after 12hrs of Ageing in 70° C Water– Laminate S

Sample	Load(kN)	Thickness(mm)	Width(mm)	ILSS (MPa)	V_f
M2-2	2.418	3.35	15.40	35.152	0.531
M6-4	2.138	3.45	15.60	29.794	0.515
M8-2	2.455	3.30	15.65	35.652	0.539
M2-21	2.280	3.40	15.30	32.872	0.523
M6-41	2.233	3.45	15.25	31.832	0.515
Average	2.305	3.390	15.440	33.060	
Std. Dev.	0.131	0.065	0.178	2.414	

Table 23(b): ILSS after 12hrs of Ageing in 70° C Water– Laminate M

Sample	Load(kN)	Thickness(mm)	Width(mm)	ILSS (MPa)	V_f
L24-2	2.183	3.35	15.20	32.153	0.531
L23-2	1.956	3.40	15.25	28.293	0.523
L23-21	1.964	3.40	15.30	28.316	0.523
L24-21	2.556	3.35	15.20	37.647	0.531
L13-4	2.120	3.40	15.40	30.367	0.523
Average	2.156	3.380	15.270	31.355	
Std. Dev.	0.244	0.027	0.084	3.867	

Table 23(c): ILSS after 12hrs of Ageing in 70° C Water– Laminate L

Sample	Load(kN)	Thickness(mm)	Width(mm)	ILSS (MPa)	V _f
S10-3	1.720	3.40	14.90	25.464	0.523
S11-3	2.038	3.30	14.80	31.296	0.539
S27-1	2.103	3.35	14.70	32.029	0.531
S23-1	1.610	3.45	14.90	23.490	0.515
Average	1.868	3.375	14.825	28.070	
Std. Dev.	0.240	0.065	0.096	4.237	

Table 24(a): ILSS after 24hrs of Ageing in 70° C Water– Laminate S

Sample	Load(kN)	Thickness(mm)	Width(mm)	ILSS (MPa)	V _f
M6-2	2.300	3.30	15.15	34.503	0.539
M27-3	1.872	3.30	15.25	27.899	0.539
M3-2	2.260	3.35	15.30	33.070	0.531
M7-4	2.540	3.45	16.30	33.876	0.515
Average	2.243	3.350	15.500	32.337	
Std. Dev.	0.277	0.071	0.537	3.016	

Table 24(b): ILSS after 24hrs of Ageing in 70° C Water– Laminate M

Sample	Load(kN)	Thickness(mm)	Width(mm)	ILSS (MPa)	V _f
L13-4	1.780	3.35	14.40	27.674	0.531
L23-2	1.654	3.30	15.35	24.489	0.539
L13-42	1.722	3.35	15.10	25.531	0.531
L23-22	1.856	3.40	15.00	27.294	0.523
Average	1.753	3.350	14.963	26.247	
Std. Dev.	0.086	0.041	0.403	1.498	

Table 24(c): ILSS after 24hrs of Ageing in 70° C Water– Laminate L

Sample	Load(kN)	Thickness(mm)	Width(mm)	ILSS (MPa)	V _f
S22-1	1.562	3.35	15.30	22.856	0.531
S26-1	1.798	3.35	15.15	26.570	0.531
S28-1	1.590	3.30	15.25	23.696	0.539
S27-1	1.944	3.35	15.15	28.728	0.531
S22-11	1.686	3.40	15.00	24.794	0.523
Average	1.716	3.350	15.170	25.329	
Std. Dev.	0.157	0.035	0.115	2.354	

Table 25(a): ILSS after 96hrs of Ageing in 70° C Water– Laminate S

Sample	Load(kN)	Thickness(mm)	Width(mm)	ILSS (MPa)	V _f
M7-4	2.030	3.45	15.20	29.033	0.515
M8-2	1.790	3.30	15.45	26.331	0.539
M6-2	1.940	3.35	15.15	28.669	0.531
M3-4	1.952	3.40	15.30	28.143	0.523
M6-4	2.160	3.50	15.30	30.252	0.508
Average	1.974	3.400	15.280	28.486	
Std. Dev.	0.135	0.079	0.115	1.433	

Table 25(b): ILSS after 96hrs of Ageing in 70° C Water– Laminate M

Sample	Load(kN)	Thickness(mm)	Width(mm)	ILSS (MPa)	V _f
L10-2	1.800	3.30	14.60	28.020	0.539
L10-21	1.730	3.35	15.00	25.821	0.531
L24-4	1.864	3.50	15.15	26.365	0.508
L16-4	1.766	3.40	15.15	25.713	0.523
L13-4	1.892	3.40	14.90	28.010	0.523
Average	1.810	3.390	14.960	26.786	
Std. Dev.	0.067	0.074	0.227	1.149	

Table 25(c): ILSS after 96hrs of Ageing in 70° C Water– Laminate L

Sample	Load(kN)	Thickness(mm)	Width(mm)	ILSS (MPa)	V _r
S28-1	1.682	3.30	15.20	25.150	0.539
S23-1	1.618	3.45	15.35	22.915	0.515
S2-4	1.722	3.40	15.05	25.239	0.523
S27-1	1.624	3.35	15.05	24.158	0.531
S10-3	1.722	3.45	15.05	24.874	0.515
Average	1.674	3.390	15.140	24.467	
Std. Dev.	0.051	0.065	0.134	0.966	

Table 26(a): ILSS after 264hrs of Ageing in 70° C Water– Laminate S

Sample	Load(kN)	Thickness(mm)	Width(mm)	ILSS (MPa)	V _r
M3-2	1.872	3.35	15.15	27.664	0.531
M8-2	1.710	3.30	15.40	25.236	0.539
M3-4	1.882	3.45	15.15	27.005	0.515
M27-3	1.858	3.30	15.30	27.600	0.539
M3-21	2.060	3.35	15.65	29.469	0.531
Average	1.876	3.350	15.330	27.395	
Std. Dev.	0.124	0.061	0.208	1.519	

Table 26(b): ILSS after 264hrs of Ageing in 70° C Water– Laminate M

Sample	Load(kN)	Thickness(mm)	Width(mm)	ILSS (MPa)	V _r
L13-4	1.976	3.40	15.65	27.852	0.523
L23-2	2.050	3.40	15.30	29.556	0.523
L24-2	2.020	3.40	15.50	28.748	0.523
L13-4S	1.730	3.40	14.75	25.872	0.523
L10-2	1.784	3.30	15.15	26.763	0.539
Average	1.912	3.380	15.270	27.758	
Std. Dev.	0.145	0.045	0.347	1.480	

Table 26(c): ILSS after 264hrs of Ageing in 70° C Water– Laminate L

Sample	Load(kN)	Thickness(mm)	Width(mm)	ILSS (MPa)	V_f
S2-4	1.868	3.40	15.00	27.471	0.523
S23-1	1.660	3.40	14.75	24.826	0.523
S11-3	1.728	3.35	15.10	25.620	0.531
S11-32	1.888	3.30	15.05	28.511	0.539
S2-41	1.690	3.40	15.30	24.366	0.523
Average	1.767	3.370	15.040	26.159	
Std. Dev.	0.105	0.045	0.198	1.770	

Table 27(a): ILSS after 528hrs of Ageing in 70° C Water– Laminate S

Sample	Load(kN)	Thickness(mm)	Width(mm)	ILSS (MPa)	V_f
M27-3	1.816	3.35	15.00	27.104	0.531
M7-4	1.918	3.50	15.30	26.863	0.508
M3-4	1.890	3.40	15.50	26.898	0.523
M6-2	1.918	3.30	15.65	27.854	0.539
M2-2	1.970	3.40	15.30	28.403	0.523
Average	1.902	3.390	15.350	27.424	
Std. Dev.	0.056	0.074	0.245	0.678	

Table 27(b): ILSS after 528hrs of Ageing in 70° C Water– Laminate M

Sample	Load(kN)	Thickness(mm)	Width(mm)	ILSS (MPa)	V_f
L13-4	1.772	3.40	14.80	26.411	0.523
L24-4	1.996	3.40	15.20	28.967	0.523
L24-42	2.095	3.45	14.95	30.464	0.515
L16-4	1.844	3.35	15.10	27.340	0.531
L23-2	1.916	3.40	15.35	27.534	0.523
Average	1.925	3.400	15.080	28.143	
Std. Dev.	0.126	0.035	0.214	1.587	

Table 27(c): ILSS after 528hrs of Ageing in 70° C Water– Laminate L

Sample No.	Force (kN)	Width (mm)	Thickness (mm)	Area (mm ²)	CAI Strength(MPa)
S2718U	39.74	55.07	3.29	181.1803	219
S243U	45.71	54.20	3.39	183.7380	249
S1038U	40.90	54.76	3.34	182.8984	224
S248U	bothend crush	54.98	3.42	188.0316	***
Average					231
STD Dev					16
M826U	49.88	54.75	3.27	179.0325	279
M648U	49.29	54.71	3.38	184.9198	267
M741U	46.90	55.01	3.40	187.0340	251
M628U	test failed	54.91	3.21	176.2611	***
Average					265
STD Dev					14
L2442U	41.69	54.68	3.37	184.2716	226
L1443U	40.47	54.80	3.36	184.1280	220
L1028U	42.88	54.86	3.26	178.8436	240
Average					229
STD Dev					10

Table 28(a): Compression Strength after 6 Days' Ageing of Unimpacted Samples

Sample No.	Force (kN)	Width (mm)	Thickness (mm)	Area (mm ²)	CAI Strength (MPa)
S244	29.67	54.72	3.34	182.7648	162
S245	30.10	55.01	3.38	185.9338	162
S1034	30.84	55.09	3.32	182.8988	169
S1035	33.67	54.95	3.32	182.4340	185
Average					169
STD Dev					11
M347	30.62	54.81	3.45	189.0945	162
M747	28.93	54.45	3.41	185.6745	156
M645	26.81	54.48	3.46	188.5008	142
M644	29.46	54.82	3.44	188.5808	156
Average					154
STD Dev					8
L2427	37.35	54.98	3.38	185.8324	201
L1644	23.41	54.85	3.35	183.7475	127
L2325	28.40	54.43	3.34	181.7962	156
L1345	26.50	54.48	3.34	181.9632	146
Average					158
STD Dev					31

Table 28(b): Compression Strength after 6 Days' Ageing of 10J Impacted Samples

Sample No.	Force (kN)	Width (mm)	Thickness (mm)	Area (mm ²)	CAI Strength (MPa)
S1031	21.37	54.64	3.35	183.0440	117
S1138	24.74	54.82	3.26	178.7132	138
S2818	22.37	55.10	3.28	180.7280	124
S246	21.64	54.46	3.39	184.6194	117
Average					124
STD Dev					10
M641	23.43	53.96	3.41	184.0036	127
M743	21.11	54.73	3.43	187.7239	112
M748	25.65	55.03	3.34	183.8002	140
M348	19.60	54.70	3.42	187.0740	105
Average					121
STD Dev					16
L1743	20.45	54.92	3.25	178.4900	115
L1348	20.06	55.07	3.37	185.5859	108
L2326	18.54	54.96	3.31	181.9176	102
L2428	21.90	53.55	3.36	179.9280	122
Average					112
STD Dev					9

Table 28(c): Compression Strength after 6 Days' Ageing of 20J Impacted Samples

Sample No.	Force (kN)	Width (mm)	Thickness (mm)	Area (mm ²)	CAI Strength (MPa)
S1037	22.30	54.59	3.39	185.0601	121
S1134	22.43	54.98	3.27	179.7846	125
S247	22.90	54.77	3.38	185.1226	124
S242	19.99	55.12	3.36	185.2032	108
Average					119
STD Dev					8
M344	21.18	54.98	3.43	188.5814	112
M744	18.62	54.82	3.39	185.8398	100
M825	20.00	54.95	3.23	177.4885	113
M824	16.78	55.03	3.24	178.2972	94
Average					105
STD Dev					9
L1645	15.42	54.48	3.27	178.1496	87
L1121	23.11	54.72	3.24	177.2928	130
L1441	20.38	54.85	3.30	181.0050	113
L2425	22.50	54.15	3.43	185.7345	121
Average					113
STD Dev					19

Table 28(d): Compression Strength after 6 Days' Ageing of 30J Impacted Samples

Sample No.	Force (kN)	Width (mm)	Thickness (mm)	Area (mm ²)	CAI Strength (MPa)
S2816U	40.63	54.92	3.32	182.3344	223
S2811U	43.94	54.98	3.28	180.3344	244
S1033U	26.71	55.01	3.36	184.8336	145
S1136U	49.60	55.02	3.22	177.1644	280
Average					223
STD Dev					57
M2738U	both end crush	54.95	3.23	177.4885	***
M346U	41.69	55.02	3.34	183.7668	227
M341U	47.70	54.97	3.34	183.5998	260
M643U	50.83	54.96	3.43	188.5128	270
Average					252
STD Dev					22
L1122U	top end crush	54.94	3.23	177.4562	***
L1744U	45.03	54.98	3.20	175.9360	256
L1024U	33.35	54.48	3.27	178.1496	187
L2441U	34.73	55.02	3.31	182.1162	191
Average					211
STD Dev					39

Table 29(a): Compression Strength after 26 Days' Ageing of Unimpacted Samples

Sample No.	Force (kN)	Width (mm)	Thickness (mm)	Area (mm ²)	CAI Strength (MPa)
S1137	29.78	54.83	3.25	178.1975	167
S2817	25.23	55.02	3.29	181.0158	139
S2617	32.02	54.95	3.27	179.6865	178
S2714	30.60	55.01	3.28	180.4328	170
Average					164
STD Dev					17
M742	28.91	54.65	3.41	186.3565	155
M2734	28.08	54.38	3.22	175.1036	160
M342	32.40	54.98	3.36	184.7328	175
M822	26.60	54.85	3.24	177.7140	150
Average					160
STD Dev					11
L1027	27.45	54.82	3.27	179.2614	153
L2424	25.97	55.04	3.28	180.5312	144
L1647	29.88	54.96	3.30	181.3680	165
L1442	27.24	54.98	3.29	180.8842	151
Average					153
STD Dev					9

Table 29(b): Compression Strength after 26 Days' Ageing of 10J Impacted Samples

Sample No.	Force (kN)	Width (mm)	Thickness (mm)	Area (mm ²)	CAI Strength (MPa)
S1036	23.64	54.35	3.38	183.7030	129
S241	22.64	54.91	3.37	185.0467	122
S2316	25.54	55.07	3.40	187.2380	136
S2711	18.61	55.09	3.34	184.0006	101
Average					122
STD Dev					15
M221	22.37	55.12	3.19	175.8328	127
M343	11.93	54.82	3.40	186.3880	64
M2736	11.77	55.07	3.24	178.4268	66
M646	16.89	54.27	3.40	184.5180	92
Average					87
STD Dev					29
L1341	17.63	54.82	3.31	181.4542	97
L1643	15.15	54.25	3.30	179.0250	85
L1026	25.97	54.58	3.28	179.0224	145
L2321	27.45	55.04	3.34	183.8336	149
Average					119
STD Dev					33

Table 29(c): Compression Strength after 26 Days' Ageing of 20J Impacted Samples

Sample No.	Force (kN)	Width (mm)	Thickness (mm)	Area (mm ²)	CAI Strength (MPa)
S2614	15.79	54.78	3.15	172.5570	92
S2615	16.89	54.82	3.17	173.7794	97
S2717	18.28	55.08	3.28	180.6624	101
S1135	23.01	55.18	3.21	177.1278	130
Average					105
STD Dev					17
M627	17.89	54.42	3.23	175.7766	102
M2732	23.74	55.02	3.25	178.8150	133
M647	21.51	54.83	3.42	187.5186	115
M745	25.12	54.96	3.44	189.0624	133
Average					121
STD Dev					15
L2422	21.51	54.55	3.34	182.1970	118
L1344	20.19	54.74	3.33	182.2842	111
L1347	20.08	55.22	3.32	183.3304	110
L2446	14.25	54.62	3.32	181.3384	79
Average					104
STD Dev					18

Table 29(d): Compression Strength after 26 Days' Ageing of 30J Impacted Samples

Sample No.	Force (kN)	Width (mm)	Thickness (mm)	Area (mm ²)	CAI Strength (MPa)
S2611U	43.41	54.68	3.19	174.4292	249
S2616U	40.50	54.63	3.27	178.6401	227
S2713U	51.87	54.55	3.26	177.8330	292
S1131U	43.94	54.52	3.21	175.0092	251
Average					255
STD Dev					27
M623U	38.52	54.38	3.19	173.4722	222
M821U	38.81	54.56	3.20	174.5920	222
M2733U	33.99	54.42	3.25	176.8650	192
M746U	45.91	54.79	3.40	186.2860	246
Average					221
STD Dev					22
L2448U	43.28	54.86	3.36	184.3296	235
L2444U	44.21	54.85	3.36	184.2960	240
L2447U	42.62	54.76	3.37	184.5412	231
L1021U	37.46	54.94	3.21	176.3574	212
Average					230
STD Dev					12

Table 30(a): Compression Strength after 96 Days' Ageing of Unimpacted Samples

Sample No.	Force (kN)	Width (mm)	Thickness (mm)	Area (mm ²)	CAI Strength (MPa)
S1132	19.54	54.82	3.25	178.1650	110
S2212	21.97	54.75	3.27	179.0325	123
S2612	28.38	54.62	3.25	177.5150	160
S2812	30.52	54.72	3.28	179.4816	170
Average					141
STD Dev					29
M625	23.01	54.91	3.26	179.0066	129
M227	29.46	54.07	3.23	174.6461	169
M2735	33.35	54.42	3.18	173.0556	193
M322	24.21	54.52	3.25	177.1900	137
Average					157
STD Dev					30
L2322	26.60	54.68	3.31	180.9908	147
L2445	24.59	54.64	3.32	181.4048	136
L1342	20.32	54.62	3.28	179.1536	113
L1343	23.01	54.38	3.36	182.7168	126
Average					130
STD Dev					14

Table 30(b): Compression Strength after 96 Days' Ageing of 10J Impacted Samples

Sample No.	Force (kN)	Width (mm)	Thickness (mm)	Area (mm ²)	CAI Strength (MPa)
S1133	23.11	54.82	3.21	175.9722	131
S2613	21.24	54.26	3.25	176.3450	120
S2213	21.18	54.44	3.34	181.8296	116
S2813	25.33	54.41	3.30	179.5530	141
Average					127
STD Dev					11
M626	19.27	54.88	3.20	175.6160	110
M2731	18.74	54.78	3.18	174.2004	108
M621	24.28	53.97	3.19	172.1643	141
M623	19.60	54.04	3.21	173.4684	113
Average					118
STD Dev					16
L2423	26.16	54.82	3.28	179.8096	145
L2323	18.41	54.85	3.34	183.1990	100
L2421	30.41	54.93	3.35	184.0155	165
L1023	20.45	54.84	3.27	179.3268	114
Average					131
STD Dev					29

Table 30(c): Compression Strength after 96 Days' Ageing of 20J Impacted Samples

Sample No.	Force (kN)	Width (mm)	Thickness (mm)	Area (mm ²)	CAI Strength (MPa)
S2815	21.31	54.70	3.31	181.0570	118
S2814	23.54	54.52	3.29	179.3708	131
S1032	22.37	54.07	3.35	181.1345	123
S2712	22.04	54.82	3.27	179.2614	123
Average					124
STD Dev					6
M642	19.27	54.35	3.40	184.7900	104
M2737	17.52	54.72	3.26	178.3872	98
M622	15.10	54.67	3.29	179.8643	84
M345	19.58	54.07	3.31	178.9717	109
Average					99
STD Dev					11
L2443	19.87	54.68	3.33	182.0844	109
L1642	16.20	54.81	3.31	181.4211	89
L1742	18.01	54.95	3.23	177.4885	101
L1745	17.79	54.85	3.22	176.6170	101
Average					100
STD Dev					8

Table 30(d): Compression Strength after 96 Days' Ageing of 30J Impacted Samples

Laminate S in CAI								
Impact Energy	Actual Compression Strength Value				Retention of Compression Strength w.r.t. Dry Compression Strength			
	Dry	6 days	26 days	96 days	Dry	6 days	26 days	96 days
0	280	231	223	255	100	83	80	91
10	167	169	164	141	100	101	98	84
20	157	124	122	127	100	79	78	81
30	140	119	105	124	100	85	75	89

Laminate M in CAI								
0	265	265	252	221	100	100	95	83
10	169	154	160	157	100	91	95	93
20	144	121	87	118	100	84	60	82
30	120	105	121	99	100	88	101	83

Laminate L in CAI								
0	233	229	211	230	100	98	91	99
10	168	158	153	130	100	94	91	77
20	148	149	119	131	100	101	80	89
30	125	113	104	100	100	88	83	80

**Table 31: Retention in Compression Strength Due to Thermo-Humidity
(After Various Duration in Water, at 70°C)**

